PREDICTION OF SULPHATE SCALING TENDENCY AND INVESTIGATION OF BARIUM AND STRONTIUM SULPHATE SOLID SOLUTION SCALE FORMATION

by

Mingdong Yuan

Thesis submitted for the Degree of

Doctor of Philosophy

Department of Petroleum Engineering

Heriot-Watt University

Edinburgh

July 1989

TABLE OF CONTENTS

LIST OF TABLES

LIST OF FIGURES

ACKNOWLEDGEMENTS

I wish to express my gratitude to my supervisor, Dr A. C. Todd, for his direction of this Ph.D programme and his support during my pursuit of this study.

Philip Goulding and Neil Turnbull are to be particularly thanked for my introduction to this project and for their help in various aspects of the research work: computer modelling of sulphate solubility, laboratory studies and useful discussions. Also I am grateful for their influence on my attitudes towards academic research.

I would like to thank Cliff Ogle for his careful and fine work with the scanning electron microscope and his help during my familiarisation with basic crystallography and geology.

Workshop staff, especially Allen Brown, are thanked for their work on processing labour-consuming resin coated cores and all sorts of equipment trouble-shooting work.

Liu Shengguo is acknowledged for his valuable assistance in the early part of the laboratory study.

I also wish to express my gratitude to Heather Rigg for her work on the conference papers produced during this Ph.D study and to Angela Nelson for ordering equipment parts and chemicals.

Indeed, I would like to take this opportunity to thank all the staff members and students in this Department for various help, encouragement and useful exchange of ideas on research, from which my study has greatly benefited.

ABSTRACT

Sulphate scale occurrence is one of the major production problems encountered during waterflooding processes in oilfield developments. In particular, as sea water injection is a common practice in North Sea oil operations, severe production problems are caused by sulphate scale deposition in the production facilities, also concern is arising of the potential formation damage in the near producing well bore zone due to scale precipitation. Of all the scales, barium sulphate precipitation is the most dominant scaling problem in North Sea offshore fields and it is commonly accompanied by strontium sulphate to form barium and strontium sulphate solid solution scale, which has distinct features in terms of scaling crystal morphology, size and hardness. This study was devoted to predict the scaling tendencies of barium sulphate, strontium sulphate and calcium sulphate scales and to investigate the formation damage arising from $(Ba,Sr)SO_4$ scale formation in the porous media.

A theoretically consistent model was developed in this study for predicting the sulphate scaling tendencies in single brines or due to mixing incompatible brines, such as seawater and formation water, by calculating the supersaturations and amounts of precipitation of the sulphates at temperatures and pressures covering surface and reservoir conditions. The model is able to predict competitive simultaneous coprecipitation of $BaSO_4$,$SrSO_4$ and $CaSO_4$ of which sulphate is the common ion, reflecting closely the precipitation of more than one sulphate mineral. The scaling tendencies predicted from this model agree well with field observations. The computer programme of the model is compact, optional and user-friendly. The scale prediction model is based on a solubility model which was also developed in this study from the Pitzer equation for electrolyte mean activity coefficient, an approach widely used for calculating properties of aqueous electrolyte solutions because of its sound theoretical basis and accurate representation of electrolyte properties. The predicted sulphate solubilities from the solubility model agree with the published data within the experimental measurement error.

Experimental investigation of the $(Ba,Sr)SO_4$ scale formation was carried out in static

bulk solutions and under flow influence in sandstone cores by mixing two incompatible waters. The brines used in the study were both simple artificial brines and full component synthetic North Sea water and formation waters. The rock cores were multi-pressure tapped and the pressure data recorded during the core flow tests were converted to permeability changes. The formation damage due to scaling was examined by studying the rock permeability decline as well as porosity reduction. The scaling crystals and scale distribution within a core were examined by scanning electron microscopy. The experimental results show substantial scale build-up in the cores and large permeability loss resulted from concurrently flowing North Sea water and field waters and from concurrently flowing two incompatible simple brines through cores. The scale nature and permeability damage were largely dependent on sulphate supersaturation and temperature and they were also affected by the change in the ratio between the scaling ion concentrations. The external morphology of the scaling crystals formed from mixing the sea water and formation waters differed significantly from the morphology of those crystals precipitated from the mixed simple brines, suggesting the influence of the presence of the foreign ions other than sodium and chloride ions on scale nature. It is concluded from the study that the scale formation was a rapid process initiated by heterogeneous nucleation and sustained by scaling crystal growth and deposition on the rock pore surface.

The sulphate scaling tendency prediction model and the data acquired from the experimental study on formation damage due to barium and strontium sulphate solid solution formation have potential for use in a reservoir simulation model of scale formation.

NOMENCLATURE

All the symbols used in this thesis are defined at the places where they appear. For the convenience of reference, the definitions of the symbols generally used in the thesis are together presented below.

A	Cross section area of a core
$A\phi$	Debye - Hückel parameter
B_{ij}	Second virial coefficient for single electrolyte ij
B'_{ij}	Derivative of B_{ij} in respect to solution ionic strength
C_{ij}	Third virial coefficient for single electrolyte ij
D%	Relative deviation
dk/dt	Permeability decline rate, the derivative of permeability in respect to brine injection time
$(dk/dt)_i$	Initial permeability decline rate
$(dk/dt)_m$	Maximum permeability decline rate
$E\theta_{ij}$	The component of θ_{ij} representing the higher-order electrostatic interaction between two different ions i and j of different charges but the same sign, refer to equation (2.19)
$E\theta'_{ij}$	Derivative of $E\theta_{ij}$ in respect to solution ionic strength
f^{γ}	Modified Debye - Hückel term in the Pitzer equation, refer to equations (2.10) and (2.11)
I	Solution ionic strength
k	Rock absolute permeability
K_{sp}	Thermodynamic solubility product
L	Length of a core or length of a section of a core
m	Molality, moles/1000g H_2O

MX	Electrolyte MX, usually a scaling sulphate salt
M^{2+}	Cation ion in electrolyte MX, usually Ba^{2+}, Sr^{2+} or Ca^{2+}
p	Pressure
Δp	Pressure differential
PP	Amount of precipitation
q	Flowrate
Q	Solubility
Q_{sp}	The square root of stoichiometric solubility product
r	The square root of the initial ion product of a sulphate salt over the square root of its initial stoichiometric solubility product
R	The square root of the ion product of a sulphate salt over the square root of its stoichiometric solubility product during precipitation - dissolution equilibrium
S.D%	Relative standard deviation
SP	Supersaturation
$S\theta_{ij}$	The component of θ_{ij} representing the higher-order short range interaction between two ions i and j of the same sign but excluding the interaction due to difference in ion charges
t	Brine injection time or temperature in Celsius
$t_{1/2}$	The time at which the core permeability decline rate reached half of its initial value
t_c	The time at the nominal maximum curvature point of a permeability - time curve
T	Temperature in Kelvin
X^{2-}	Anion ion in electrolyte MX, usually SO_4^{2-}
z	Ion charge
μ	Viscosity
β	Ion interaction parameters in the expression of virial coefficient B_{ij}, refer to equation (2.12)

γ_{MX}	Mean activity coefficient of electrolyte MX in an aqueous solution
ν_M	Number of cations M in one molecule electrolyte MX
ν_X	Number of anions X in one molecule electrolyte MX
ν	Sum of ν_M and ν_X
θ_{ij}	Second virial coefficient for two different ions i and j of the same sign
ψ_{ijk}	Third virial coefficient for different ions i, j and k not of the same sign

CHAPTER 1

INTRODUCTION

1.1 OILFIELD SCALE OCCURRENCE

Water-borne scale occurrence is a common problem accompanied in reservoir waterflooding processes, which are widely used to maintain formation pressure in oil recovery. As a result of scale deposition, the waterflooding performance can be severely impaired and costly measures have to be taken to tackle oilfield scaling problems. The scale may deposit at any location within an oilfield water system. Namely, water injection wells, injection well bore area, reservoir formation, near producing well bore area, producing well bores and surface water processing facility, etc. are all potential sites of scale formation. Water injectivity damage and oil productivity damage are the likely results of scale build-up in the well tubing. Also reservoir rock permeability may be impaired when scale deposition occurs in the formation, particularly oil recovery efficiency may be affected by scale formation within the near producing wellbore formation zone. The water scaling usually gets worse as water injection continues and after the injected water breaks through into the producing wells.

The scales commonly occurring in oilfields are calcium carbonate($CaCO_3$), calcium sulphate including gypsum($CaSO_4.2H_2O$) and anhydrite ($CaSO_4$), barium sulphate($BaSO_4$), strontium sulphate($SrSO_4$) as well as iron scales($FeCO_3$, Fe_2O_3) and silica scale, etc. [23,26,94] Of these scales, $CaCO_3$ and sulphates, mainly $BaSO_4$, are the scales causing most problems in North Sea offshore operations. [15,58,77,115] Barium sulphate and strontium sulphate have been found to form a completely mixed scale called barium and strontium sulphate solid solution($(Ba,Sr)SO_4$)[58,115,141] and the mixed scale of $SrSO_4$, $BaSO_4$ and $CaSO_4$ has been reported.[15,67,113] Of these scales, $CaCO_3$ is the easiest to remove by acid or chemical dissolvers, $CaSO_4$ and $SrSO_4$ are not dissolvable in

acid but can be removed by chemicals or converted to acid-dissolvable, $BaSO_4$ scale has the lowest solubility in aqueous solution and is the hardest to remove by any means.[23,26,113,147] In some North Sea oilfields, $BaSO_4$ is accompanied with $SrSO_4$ to form solid solution scale, whose nature is different from that of pure $BaSO_4$ scale or pure $SrSO_4$ scale.[15,17,26,58,141,155]

Many factors may contribute to oilfield scale deposition and different scales may be subject to different influencing factors.[26,58,77,141,146-150] Changes in water temperature and/or pressure are the common causes of scale occurrence because of subsequent alteration in the solubilities of the scaling minerals. For example, $CaSO_4$ solubility decreases with pressure drop as so does $BaSO_4$ solubility with temperature decline. Figure (1.1) is a schematic view of an oilfield under waterflooding. As seen in the figure, temperature and pressure in the water system change from one location to the other continuously. For example, a water may be stable in the reservoir formation with all the salts in it undersaturated, as it flows into the producing wellbore and up to the wellhead through the tubing, some mineral(s) may become supersaturated in the water due to temperature drop and pressure release and subsequently precipitates out from the fluid to form scale deposits on well tubing and valves,etc. The scale occurrence of $CaCO_3$ and iron compounds is also likely caused by pH change in the brine. CO_2 presence may be responsible for $CaCO_3$ scale formation. Besides the causes of scaling due to effects of temperature, pressure, pH and CO_2, the main cause of scaling is the commingling of incompatible waters. In a saline water injection operation, e.g, seawater injection into the reservoir, both the injected water and the formation water are stable within their own environments. As the saline water is being injected into the reservoir, it becomes mixed with the formation water around the injection wellbore upon their first contact, within the bulk reservoir formation, and within the near producing well zone after breakthrough of the injection water into the producing well. Figure (1.1) illustrates the commingling of incompatible waters. At the mixing, some excessive ions in the two waters, e.g, SO_4^{2-}

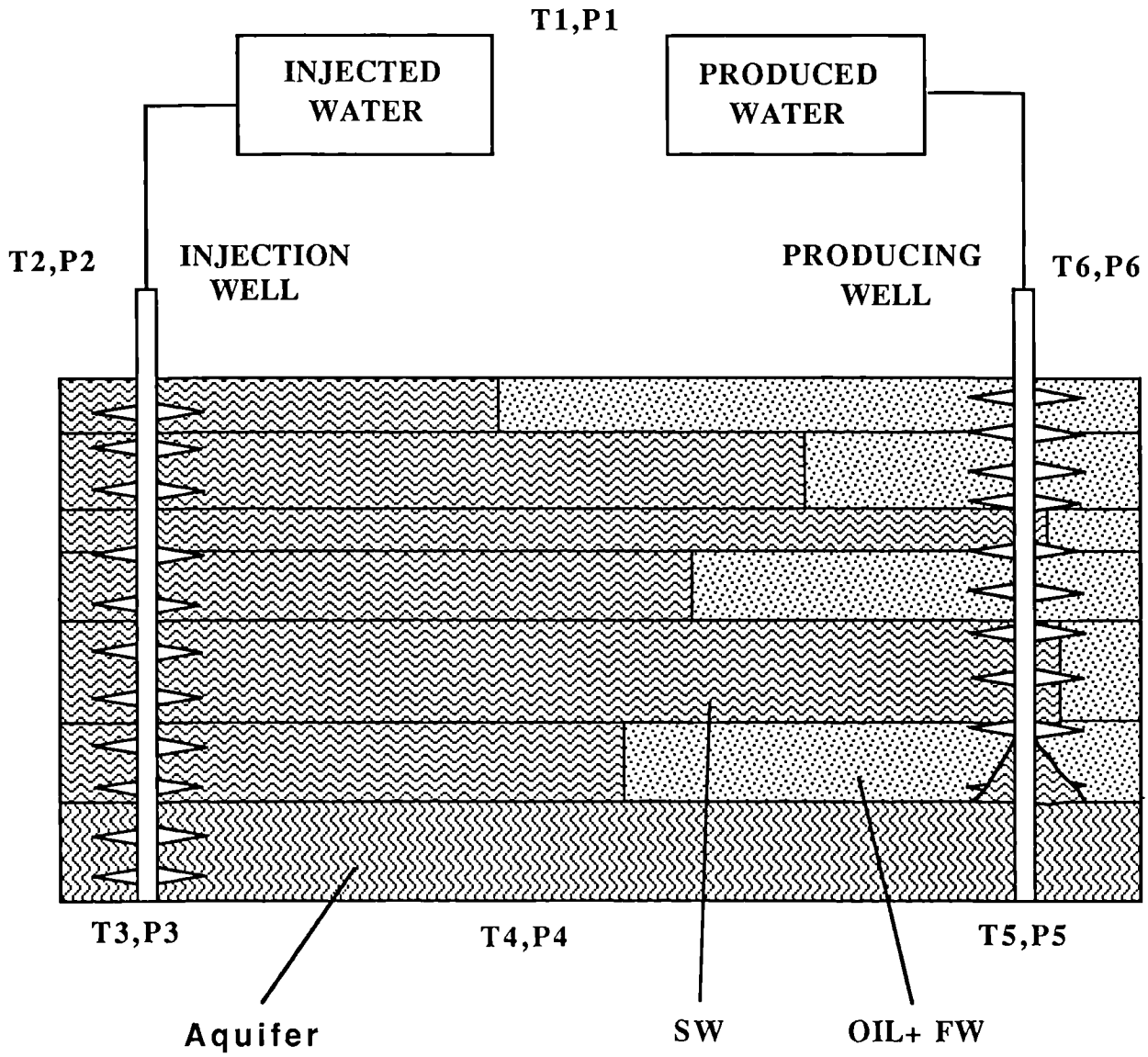

Figure 1.1 Oilfield Scale Occurrence

ions in seawater and Ba^{2+} ions in the formation water, meet to form insoluble salts supersaturated in the mixed brine and result in scale precipitation. The mixing of different waters may take place in several ways: longitudinal mixing at the front of the water displacement, lateral mixing between waters from neighbouring reservoir layers of different permeabilities, also mixing due to water coning and flow converging around the producing wellbore.

In North Sea offshore production, in which our research interest lies, the scaling problems are mainly related to sulphate scales of which $BaSO_4$ is the prime concern. As mentioned earlier in this section, $BaSO_4$ scale is the hardest and its damage the most difficult to repair. Also $BaSO_4$ is often accompanied with $SrSO_4$ to form solid solution scale. As water injection has been implemented since the early 70s and now the watercut is ever increasing in most of the North Sea fields, there is a growing concern over the deposition of $BaSO_4$ related scale in the reservoir formation and its potential damage to the formation, particularly the near producing wellbore zone. It necessitates the examination of such scaling problems to have insight into the formation damage arising from the sulphate scale formation. The findings from the investigation can be then used to help solve the $BaSO_4$ related scaling problems, to improve the effectiveness of secondary oil recovery by waterflooding and to reduce the production cost in oilfield operations.

1.2 SUMMARY OF LITERATURE RELATED TO SULPHATE SCALING PROBLEMS

This section briefly reviews the literature related to sulphate scaling problems in oilfield production. A detailed literature review on each research subject related to this study is given in Chapter 2 and Chapter 4, respectively. Since the early stage of oil production history, water scaling problems have been reported in most of the oilfields and various efforts have been made to understand, predict, prevent and remove sulphate scales.[23,24,26,39,52,130,131,147,155] Field and laboratory investigations have been carried

out to understand the nature of sulphate scale, the mechanism by which sulphate scale forms and the effect of scale formation on well injectivity and productivity and rock productivity.[22,24,42,67,113,155] Prediction of scale occurrence has advanced from simple calculations to computer modelling.[1,44,52,65,113,131,132,149] But more work reported in the literature is on how to solve the scaling problems, which can be tackled by either preventing(inhibiting) scale formation or removing the scale after it has already precipitated.[22,23,26,52,60,94,113,130,148-150] The prevention of scale formation by scale inhibitor squeeze treatment is a widely applied technique.[32,64,77,111] Scale removal by chemicals or by mechanical means is often economically impracticable and once the scale has formed the damage caused by it may never be repaired. Because scale inhibition is the major practice in oilfields, the evaluation of scale inhibitor performance has always been the major research topic on oilfield scaling. Inhibitor evaluation is based on its efficiency on stopping or retarding scale formation, its adsorption-desorption characteristics on rock pore surface and its chemical stability,etc.[15,58,64,81,111,114]

To achieve effective scale prevention or scale treatment, it is necessary to predict if any scale formation may take place in a brine or brines at certain conditions and to predict the type of scale, to understand the nature of scale,i.e, its morphology, composition, solubility and hardness,etc., to understand the mechanism by which it forms and how the scale precipitation is affected by other factors such as temperature and aqueous solution composition, and to know the potential damage the scale may cause. The studies on scale formation and scale formation prediction were intended to provide production operators with the above information or knowledge. Previous work carried out by Pucknell[113] and Goulding[42] in this Department investigated the rock permeability damage caused by $BaSO_4$ scale deposition in rock pores and some interesting aspects of $BaSO_4$ scaling were revealed from their study. An empirical model for predicting sulphate scaling tendency was also developed by Pucknell.

1.3 OUTLINE OF THIS STUDY

The work presented in this thesis is the third of the PhD programmes in scale project

existing in the Department, the previous PhD programmes were pursued by Pucknell and Goulding on $BaSO_4$ scale formation.[42,113] The present study consisits of two research areas: the development of an new computer model for predicting scaling tendencies of insoluble sulphates, and the laboratory investigation of (Ba,Sr)SO_4 solid solution formation due to mixing imcompatible brines and their damage to rock permeability. The prediction work is reported in chapters 2 and 3 and the experimental work is described in chapters 5, 6 and 7. Some of the results from this study have also been reported in three papers.[143,144,161] The purpose of carrying out an investigation of the (Ba,Sr)SO_4 scale formation was to have insight into the mechanism of forming such commonly occurred scale and the nature of the scale, and more importantly, to gain knowledge of the damage of the scaling to rock permeability, in response to the concern raised by the oil industry. From this investigation, some implications can be drawn with reference to oilfield scaling problems. As an alternative to the prediction model developed by Pucknell, the work involved in this study for predicting sulphate scaling tendency was to provide a theoretically-consistent, less empirical, accurate, comprehensively applicable and user-friendly computer prediction model in relation to the North Sea sulphate scaling problems. The new model covers the oilfield temperatures, pressures and brine compositions and is capable of predicting the simultaneous co-precipitation of different sulphates. The scaling prediction model together with the experimental data obtained from the study on (Ba,Sr)SO_4 scale formation may form the basis for developing a reservoir simulation model of formation damage arising from scale occurrence, which is one of the future goals of this scale project. The knowledge of sulphate scaling obtained from the present study may have benefit to the field work on scale prevention and treatment, and as a whole, it may be helpful in planning a successful waterflooding scheme.

The thesis consists of nine chapters, including this introductory chpater. Chapter 2 of the thesis reviews the literature on solubility prediction and scale prediction in the first section and then presents the work on developing a sulphate solubility prediction model based on Pitzer's ion interaction approach. The Pitzer's approach was extended in this study to predict the solubilities of the sparingly soluble sulphates at elevated

temperatures. Chapter 3 describes the construction of an interactive model for predicting sulphate scaling tendency, developed from the sulphate solubility prediction model. The contents in chapters 4 through chapter 7 are all related to the study of sulphate scale formation. Of the four chapters, chapter 4 presents a detailed literature review on crystallization of $BaSO_4$, $SrSO_4$ and their solid solution, the scale formation study at laboratory level and in oilfields and the resulting formation damage; chapter 5 describes the equipment, experimental methods and the composition of brines used in this study; chapter 6 proceeds to the investigation of $(Ba,Sr)SO_4$ solid solution scale formation at room temperature and chapter 7 is devoted to the investigation at elevated temperature in which the temperature effect on the scale formation is analysed and the results from the scale formation using full component sea water and field formation waters are compared to those from using the simple artificial brines. After summing up the work presented in the previous chapters, the conclusions are reached in chapter 8. Finally, recommendations for the future work on numerical modelling and experimental study of sulphate scaling are proposed in chapter 9.

CHAPTER 2

DEVELOPMENT OF A SULPHATE SCALING TENDENCY PREDICTION MODEL. 1. LITERATURE REVIEW AND SULPHATE SOLUBILITY PREDICTION

2.1 INTRODUCTION

Barium sulphate, strontium sulphate, gypsum and anhydrite are the causes of most of the scaling problems in North Sea offshore production operations, and scale prevention and treatment are widely applied for tackling the sulphate scaling problems. It is important, for successful scale prevention and treatment, to be able to identify whether any scale is likely to occur and what type of scale is occurring under certain operation conditions. An accurate prediction model for sulphate scaling tendency may produce such information. During the early stage of the on-going scale project under which this study was carried out, an empirical sulphate scaling tendency prediction model was created by Pucknell.[113] Other models for predicting sulphate solubility and scaling tendency are also reported in the literature.[35,44,50,51,52,60,65,75,117,118,130-132] Because of the inadequacies in various aspects of the previous models, which will be discussed in the literature review in the next section, it was decided to develop a prediction model in this study as an update and improvement on the existing models.

The newly developed model is able to predict the scaling tendencies of barium sulphate, strontium sulphate and calcium sulphates(gypsum and anhydrite) resulting from the mixing of injected and formation waters, as well as the effects of temperature and pressure. The competitive simultaneous co-precipitation of these sulphates, of which sulphate is the common ion, is taken into account in the model, reflecting closely the precipitation of more than one sulphate mineral. The sulphate scaling tendency may be predicted for a single fluid or solutions of mixed brines at all ratios by calculating the supersaturations and amounts of precipitation of the sulphates at temperatures and pressures covering surface and reservoir conditions. For mixed scale occurrence of

more than one sulphate, an iterative process is used for solving all the precipitation-dissolution equilibria in the solution.

The present model is based on the concept of thermodynamic equilibria between the scaling ions in a aqueous solution and their solid precipitates, which requires the knowledge of the solubilities of the sulphates at various brine compositions, temperatures and pressures representative of oilfield operation conditions. In this model, the solubilities of $BaSO_4$, $CaSO_4$ and $SrSO_4$ are regenerated from the published solubility data by the Pitzer's ion interaction approach, a widely accepted method for electrolyte solubility prediction because of its sound theoretical basis and accurate representation of the properties of aqueous electrolyte solutions.

The next section of this chapter reviews the previous work reported in published literature on electrolyte solubility prediction and on prediction of oilfield scale occurrence. The development of the sulphate solubility prediction model is then described in the rest part of the chapter, particular emphasis is put on the application of the Pitzer's approach for predicting sulphate solubilities at various solution and temperature conditions. To assess the quality of the solubility prediction by the Pitzer's approach, the predicted sulphate solubilities are compared to those measured.

2.2 LITERATURE REVIEW OF SOLUBILITY PREDICTION AND SCALE PREDICTION

2.2.1 Review of the Literature on Solubility Prediction

Aqueous electrolyte solubility prediction or calculation can be achieved in four different ways: from empirical equations, from an ion association approach, from an ion interaction approach and from a statistical mechanics approach. A number of empirical equations have been proposed for solubility calculation in various aqueous electrolyte systems.[35,60,75] These equations are usually simple and straightforward but they do not have any theoretical basis and their application is restricted to particular electrolytes, particular electrolyte solutions or particular conditions for which they were proposed.

These equations are therefore unable to predict electrolyte solubility for a wider scope such as the various brines, temperatures and pressures encountered in the oilfields. On the other hand, as statistical mechanics has advanced significantly, it has also been applied to calculate electrolyte properties such as solubility.[73,117] Though this approach has the most rigid theoretical foundation, it is still in the early stage of development and rather impractical because of the difficulty to obtain the accurate parameters, e.g, the potentials of interaction among particles, for use in the statistical mechanics calculation. The ion association theory believes that the electrolyte ions of opposite signs are not free in an aqueous solution but rather associated to each other as a sort of ion-pairs. Thus the electrolyte behaviour in an aqueous solution depends on what form of ion pair exists in the solution and the degree of ion-pairing, which are expressed by the ion association coefficients.[2,37,62] The ion association assumption has the support from experimental measurements such as conductivity measurement. The problem hindering its use is that the form and the degree of ion association vary largely depending on solution ion concentration and temperature,etc, and can not be adequately expressed, also numerous coefficients are required for various ion pairs. Due to the practical difficulties with ion association approach, it has been losing favour in solving electrolyte solution problems, especially true after the Pitzer's ion interaction approach was proposed in 1973-74.[97-99,102-104] The ion interaction theory views the ions in a solution as individual species and electrolyte or solution properties are the reflection of the interactions among the ions and the interactions between the ions and the solvent. The ion interaction approach has become a most important tool to calculate properties of aqueous electrolyte solutions since the proposal of Debye-Hückel equation in 1923.[97,99] The Debye-Hückel equation expresses the mean activity coefficient of an electrolyte as the function of solution ionic strength, assuming that the only interaction among ions in a solution is their electrostatic forces or long range Coulomb force. The equation has the form,

$$\ln \gamma_{MX} = \frac{A_\gamma \mid z_M z_X \mid I^{1/2}}{1 + b\, I^{1/2}} \qquad (2.1)$$

where γ_{MX} is the mean activity coefficient of electrolyte MX, A_γ is a constant reflecting the solution dielectric property and temperature effect and b is a general constant, I is the solution ionic strength which is universally defined as

$$I = 1/2 \Sigma m_i z_i^2 \qquad (2.2)$$

where m_i is the molality of ith ion in a solution and z_i is its charge.

The Debye-Hückel equation has proved successful in calculating electrolyte property at very low concentration near pure water but the deviation from the real mean activity coefficient increases considerably as the concentration increases.[99] The other shortcoming of the Debye-Hückel equation is that it does not account for the interactions between the different individual ions present in a solution, the so called specific ion interactions. The problems with the original Debye-Hückel equation stem from the exclusion of non-electrostatic forces, i.e, the short range forces among the ions, therefore the equation was often referred to as a limiting law, that is, it is only accurate when an electrolyte solution is very dilute and the short range forces disappear at such low concentrations.[99] To improve the accuracy of Debye-Hückel equation at higher concentrations, often a polynomial series were added to the original Debye-Hückel term, as in Pucknell's work[113], to account for the deviation of Debye-Hückel calculation from the measured data. The addition of a polynomial series to the original equation was purely empirical and only applicable to particular cases. On the other hand, many efforts have been made to develop the Debye-Hückel equation based on solution thermodynamics. The work by Mayer, Scatchard, Bronsted and Guggenheim, [51,97,99,156] et al. represented the advance at each stage of the electrolyte solution theory development towards the model truly reflecting the aqueous electrolyte properties, including solubility. The original Debye-Hückel term was either modified in or included as part of these improved models. Although the models or equations developed from the Debye-Hückel equation generally extended the range of solution concentration and took the specific ion interaction into account, their validity was still limited to low ion concentration (0.1m)[97] otherwise the expressions were very complicated including

numerous coefficients. The most recent development in the ion interaction theory was reported by Pitzer and his co-authors in a series of publications during 1973 and 1974 [97-99,102-104] and widely called Pitzer's approach or Pitzer equations. The Pitzer's approach takes a modified Debye-Hückel term to represent the long range electrostatic forces and the solvent effect and use the other terms to account for the short range forces or hard core effect, also extra terms are included to reflect the higher order electrostatic interaction between the non-equivalent charged ions of the same sign. The Pitzer's ion interaction approach is a simpler and more coherent form than the earlier models such as Bronsted and Guggenheim model.[97] At 25°C, it has been proved accurate in calculating electrolyte solution properties such as mean activity coefficient, osmotic coefficient as well as solubility in both simple or complicated multi-ion aqueous solutions with concentration range from very dilute to saturated.[51,101-105] It has also been used to calculate soluble electrolyte properties at elevated temperatures successfully.[50,51,96,100,129] The success of the Pitzer equations lies in that they accurately reflect all sorts of interactions among the ions and between the ions and the solvent. Having compared the merits and deficiencies of the different approaches in respect to sulphate solubility calculation in complicated brines, the Pitzer's ion interaction approach was eventually adopted in this study for developing a sulphate solubility prediction model to be used in the sulphate scaling tendency model. The Pitzer's approach will be described in detail in section (2.4).

2.2.2 Review of the Literature on Scaling Tendency Prediction

Most of the scaling tendency prediction methods were developed on the basis of solubility prediction.[44,50,51,113] The scale prediction models using the actual measured solubility data as their database were also reported.[1,52,149] The advantage of using the actually measured solubilities as the database is that time and effort are spared from developing a reliable solubility prediction model, also the possible error of the calculated solubility from the the measured solubility is excluded. However, with this approach are a number of shortcomings. First, the measured solubilities may not cover all the

changing temperatures, pressures and ion compositions, as the case in oilfield operations, so that either interpolation or extrapolation has to be applied or the solubility at a required condition has to be assumed the same as that at a near condition at which the measured solubility is available. Secondly, the specific ion effect may have to be neglected at some conditions due to the solubility data limitation. The solubility data themselves may be unreliable because of measurement error, especially if the database is collected from one source of measurement. Also the measured solubilities from different sources may not be consistent. On the other hand, these problems can be circumvented by using a solubility prediction model in a scaling tendency prediction model.

In the early stages of scale prediction, the scaling tendency in a brine was usually predicted by comparing the salt solubility with its concentration or its ion concentration product in the brine or by using an empirical solubility index, etc.[52,60,65,130-132] The computerised models have emerged since 1970s and gradually replaced the earlier simple calculation methods.[1,44,50,51,113,118,149] The previous models have neglected various aspects affecting scale precipitation, and as a result, large errors may occur in scale prediction at certain conditions. Early prediction methods did not consider the pressure effect on scaling.[1,52,130] Some other models were restricted to application at 25°C.[50,51,118] Another shortcoming of some of the previous models lies in the assumption of salt solubility as the unique function of sodium chloride or solution ionic strength.[1,52,60,149] Pucknell[113] did consider the specific ion effects on solubility caused by the existence of Mg^{2+} and SO_4^{2-} ions,etc. in a brine but his solution was rather empirical and not very reliable. Most of the prediction models predict scale formation of only one mineral without taking into account the effect of potential scale precipitation of other minerals in the same brines. Such a simplified treatment may lead to erratic conclusions when a common ion component is competed for by different scaling ions to form scale. For example, in a solution containing Ba^{2+}, Sr^{2+} and SO_4^{2-} ions, SO_4^{2-} ions are shared by Ba^{2+} and Sr^{2+} ions in forming $BaSO_4$ and $SrSO_4$ scales, and a separate scale prediction for either $BaSO_4$ or $SrSO_4$ produces incorrect results by assuming all the SO_4^{2-} ions in the solution are only involved in the scale formation of

one of the two sulphates. A model for predicting simultaneous co-precipitation of $BaSO_4$, $SrSO_4$ and $CaSO_4$ has been reported by Vetter et al.[149] A few questions arise from a careful examination of their paper. Inconsistent to the literal description, the flowchart of the model structure in figure 2 of the paper suggests that the effect of the less soluble sulphate such as $BaSO_4$ on precipitation of more soluble $SrSO_4$ and $CaSO_4$ was taken into account while the reverse effect such as $CaSO_4$ on $SrSO_4$ and $BaSO_4$ were neglected. Vetter's model took the measured solubilities as the database in the scale tendency prediction and the other soluble salts in the brine were assumed as sodium chloride. Besides, it seems that anhydrite was the only calcium sulphate concerned in their model. Haarberg et al[44] devised a mathematical equation for solving the equilibrated SO_4^{2-} concentration in the brine involving the coprecipitation of the different sulphates, as shown below,

$$m^2_{SO4,\,e} + A\, m_{SO4,\,e} - B = 0 \qquad (2.3)$$

where $m_{SO4,\,e}$ is the sulphate ion concentration at the equilibria of sulphate precipitation - dissolution. A is a parameter containing the initial concentrations of the precipitating ions,

$$A = -m_{SO4,i} + m_{Ca,i} + m_{Ba,i} + m_{Sr,i} \qquad (2.4)$$

and B consists of the solublity products of the sulphates at the equilibria,

$$B = Q^2_{sp,\,CaSO4,e} + Q^2_{sp,\,BaSO4,e} + Q^2_{sp,\,SrSO4,e} \qquad (2.5)$$

Equation (2.3) is seemingly very simple but the problem is that the stoichiometric solubility products of all the scaling sulphates at precipitation - dissolution equilibria are also included in the equation. These solubility products cannot be known unless the

equilibrated SO_4^{2-} concentration has been determined or vice versa. Therefore, the equation proposed by Haarberg et al cannot be solved in a straightforward manner.

2.2.3 Objectives of This Study

From the above review of the publications related to scale prediction and analysis of the previous solubility prediction methods and scaling tendency prediction models presented in these publications, it was felt necessary to develop a prediction model for sulphate scaling tendencies under oilfield conditions. This model should have the following features:

1. A solubility prediction model as its basis, which is theoretically consistent, accurate in generating the sulphate solubility, comprehensive in covering various brine compositions and oilfield conditions from subsurface to surface.

2. An interactive method to reflect the competitive simultaneous co-precipitation of more than one sulphate mineral, which is a common phenomenon in North Sea production.

3. Compact and well designed to produce fast predictions.

4. User-friendly, easy to operate with many options on concentration units and the results displayed in either numerical or graphical forms.

5. Readily to expand to include prediction for other minerals such as calcium carbonate scaling and easy to be adopted in a reservoir simulation model.

To achieve these requirements, it is considered that the Pitzer's ion interaction approach is the best for developing a solubility prediction model and an iteration method should be used to solve the precipitation-dissolution equilibria between the scaling ions

in a brine and their precipitates. The combination of the above two aspects may provide a sulphate scaling tendency prediction model of the desired quality. The development of the solubility prediction model is described in the following sections of this chapter and the model for predicting sulphate scaling will be described in chapter 3.

2.3 RELATING SOLUBILITY TO ELECTROLYTE MEAN ACTIVITY COEFFICIENT

For a sulphate salt MX in an aqueous solution, there exists a precipitation - dissolution reaction between its ions in the solution and its solid precipitate,

$$M^{2+} + X^{2-} + nH_2O \rightleftharpoons MX.\,nH_2O \qquad (2.6)$$

Here M is the cations Ba, Sr or Ca and X stands for sulphate anions. Water molecules are involved in the gypsum precipitation - dissolution only.

The solubility of MX in the solution can be then expressed as,

$$Q_{MX} = m_{M,e} \quad \text{IF } m_{M,e} < m_{X,e} \quad \text{or,}$$

$$Q_{MX} = m_{X,e} \quad \text{IF } m_{M,e} > m_{X,e} \qquad (2.7)$$

and the square root of the stoichiometric solubility product is defined as,

$$Q_{sp,MX} = (m_{M,e} \cdot m_{X,e})^{0.5} \qquad (2.8)$$

where $m_{M,e}$ and $m_{X,e}$ are the molalities of cation M and anion X at precipitation - dissolution equilibrium, respectively. When the cation concentration is equal to the anion concentration, i.e, $m_{M,e} = m_{X,e}$, The solubility Q_{MX} is the same as the square root of the solubility product $Q_{sp,MX}$ otherwise they are not identical. Q_{MX} and $Q_{sp,MX}$

are dependent on the solution ion composition, temperature and pressure. The precipitation - dissolution equilibrium constant for an electrolyte at a given temperature is called the thermodynamic solubility product. The thermodynamic solubility product of a salt is independent of the solution composition and it is related to the square root of solubility product through the mean activity coefficient,

$$K_{sp,MX} = m_{M,e}\, m_{X,e}\, \gamma_M\, \gamma_X\, \gamma^n_{H2O}$$

$$= Q^2_{sp,MX}\, \gamma^2_{MX}\, \gamma^n_{H2O} \qquad (2.9)$$

Where γ_M and γ_X are the activity coefficients of the cation M and anion X, respectively, γ_{MX} is the mean activity coefficient of sulphate MX in the solution, and γ_{H2O} is the water activity coefficient which appears only if the above equation is for gypsum.

From the above relationship, it is plain that the square root of the solubility product $Q_{sp,MX}$ for a sulphate MX in a certain solution at a given temperature can be calculated from equation (2.9) provided its thermodynamic solubility product $K_{sp,MX}$ and mean activity coefficient γ_{MX} as well as the water activity coefficient are already known. In turn, the solubility of MX, i.e, Q_{MX} and the equilibrated M and X concentrations, i.e, $m_{M,e}$ and $m_{X,e}$ can be easily calculated from $Q_{sp,MX}$. Because $K_{sp,MX}$ is a constant at a given temperature, it is the mean activity of a sulphate that relates the $Q_{sp,MX}$ or Q_{MX} to the solution composition. Therefore, determination of sulphate mean activity coefficient is the key to calculate sulphate solubility. It is believed from the literature review summarised in section (2.2) that the Pitzer equation for electrolyte mean activity is the best for calculating the sulphate mean activity coefficients at various solution ion compositions and temperatures. Accordingly, the Pitzer equation has been chosen for

predicting sulphate solubilities in this model. The next section gives the description to the Pitzer's ion interaction approach.

2.4 PITZER'S ION INTERACTION APPROACH

The Pitzer's ion interaction approach is mainly composed of three fundamental equations:[99] the equation for the excess free Gibbs energy of an aqueous electrolyte solution, the equation for osmotic coefficient of the solution and the equation for electrolyte mean activity coefficient and all of the three equations are called the Pitzer equations. The Pitzer equation for electrolyte mean activity coefficient is used for generating the sulphate solubility in the model. For a mixed electrolyte solution, its general form is expressed as,

$$\begin{aligned}\ln \gamma_{MX} = {} & |z_M z_X| f^{\gamma} + (2\nu_M/\nu) \sum_a m_a [B_{Ma} + (\Sigma m z) C_{Ma} + \\ & (\nu_X/\nu_M) \theta_{Xa}] + (2\nu_X/\nu) \sum_c m_c [B_{cX} + (\Sigma m z) C_{cX} + \\ & (\nu_M/\nu_X) \theta_{Mc}] + \sum_c \sum_a m_c m_a \{ |z_M z_X| B'_{ca} + \nu^{-1} [2\nu_M z_M C_{ca} + \\ & \nu_M \psi_{Mca} + \nu_X \psi_{caX}] \} + 1/2 \sum_c \sum_{c'} m_c m_{c'} [(\nu_X/\nu) \psi_{cc'X} + \\ & |z_M z_X| \theta'_{cc'}] + 1/2 \sum_a \sum_{a'} m_a m_{a'} [(\nu_M/\nu) \psi_{Maa'} + \\ & |z_M z_X| \theta'_{aa'}] \end{aligned} \qquad (2.10)$$

where z_M and z_X are the charges of cation M and anion X in the electrolyte MX, respectively, ν_M is the number of M ions in one MX molecule and ν_X is the number of anions and $\nu = \nu_M + \nu_X$, m is ion molality, and $\Sigma m z = \Sigma_c m_c z_c = \Sigma_a m_a |z_a|$, subscripts c and c' represent all the cations and subscripts a and a' represents all the anions in the solution.

In the Pitzer equation, the mean activity coefficient of an electrolyte in the aqueous solution is expressed as the functions of solution ionic strength(I), which is included in the modified Debye-Hückel term f^{γ}, and the molalities(m) of the individual ions present in the solution. The modified Debye-Hückel term in the Pitzer equation accounts for the long range electrostatic forces among the ions as well as the solvent effect. It has the form,

$$f^{\gamma} = - A_{\phi} \left[I^{1/2} / (1 + 1.2\, I^{1/2}) + (2/1.2) \ln (1 + 1.2\, I^{1/2}) \right] \qquad (2.11)$$

here A_{ϕ} is the Debye-Hückel constant which reflects the effect of solvent molecular interaction with the electrolyte ions and is dependent on the temperature.

The other terms in the Pitzer equation represent the short range interactions among the ions and also the higher order electrostatic forces between the ions of different charges of the same sign. The coefficients appearing in these terms are ion interaction parameters or conventionally called virial coefficients, in which B and C are the second and third virial coefficients for pure single electrolytes and their values are specific for each individual electrolyte, reflecting the short range potentials of the ions of opposite signs. θ is the second virial coefficient for mixed electrolytes, accounting for the interaction between two different ions of the same sign. The interaction among three different ions not of the same sign is represented by ψ, the third virial coefficient for mixed electrolytes. The subscripts with the virial coefficients B, C, θ and ψ stand for the ions. For instance, $B_{Na,Cl}$ represents the second virial coefficient for pure single electrolyte NaCl, $\theta_{Ca,Mg}$ is the second virial coefficient for the interaction between ions Ca and Mg and $\psi_{Na,Cl,SO4}$ stands for the third virial coefficient for the interaction among ions Na, Cl and SO_4. Third virial coefficients C_{ij} and ψ_{ijk} are constants for given ions

i,j and k at a given temperature. The second virial coefficient B_{ij} for single electrolyte ij and its derivative B'_{ij} are the functions of solution ionic strength,

$$B_{ij} = \beta^{(0)}_{ij} + (2\beta^{(1)}_{ij} / \alpha_1^2 I)[1 - (1 + \alpha_1 I^{1/2}) \exp(-\alpha_1 I^{1/2})] + (2\beta^{(2)}_{ij} / \alpha_2^2 I)[1 - (1 + \alpha_2 I^{1/2}) \exp(-\alpha_2 I^{1/2})] \quad (2.12)$$

$$B'_{ij} = dB_{ij}/dI \quad (2.13)$$

$\beta^{(0)}_{ij}$, $\beta^{(1)}_{ij}$ and $\beta^{(2)}_{ij}$ are the ion interaction parameters for the second virial coefficient B_{ij}. The $\beta^{(2)}_{ij}$ term is zero in equation (2.12) for electrolytes of univalent cation or/and anion and $\alpha_1 = 2.0$. For 2-2 or higher valent electrolytes, e.g, $CaSO_4$, $\beta^{(2)}_{ij}$ term is not zero, and $\alpha_1 = 1.2$ and $\alpha_2 = 14.0$. The B_{ij} and B'_{ij} in the above equations are for Gibbs energy expression. The other two alternatives are the second virial coefficient for activity coefficient B^{γ} and that for osmotic coefficient B^{ϕ}, their relations with the solution ionic strength are as,

$$B^{\gamma}_{ij} = 2\beta^{(0)}_{ij} + (2\beta^{(1)}_{ij} / \alpha_1^2 I)[1 - (1 + \alpha_1 I^{1/2} - 1/2\,\alpha_1^2 I) \exp(-\alpha_1 I^{1/2})] + (2\beta^{(2)}_{ij} / \alpha_2^2 I)[1 - (1 + \alpha_2 I^{1/2} - 1/2\,\alpha_2^2 I) \exp(-\alpha_2 I^{1/2})] \quad (2.14)$$

and,

$$B^{\phi}_{ij} = \beta^{(0)}_{ij} + \beta^{(1)}_{ij} \exp(-\alpha_1 I^{1/2}) + \beta^{(2)}_{ij} \exp(-\alpha_2 I^{1/2}) \quad (2.15)$$

Corresponding to the three expressions of the second virial coefficient for pure single electrolytes, the third virial coefficient for pure single electrolytes also has three forms as C, C^{γ} and C^{ϕ}. The relationships between the three C's are given here,

$$C_{MX} = C^{\phi}_{MX} / 2|z_M z_X|^{1/2} \quad (2.16)$$

$$C^{\gamma}_{MX} = 3/2\, C^{\phi}_{MX} \tag{2.17}$$

$$C_{MX} = C^{\gamma}_{MX} / 3|z_M z_X|^{1/2} \tag{2.18}$$

The second virial coefficient θ_{MN} for mixed electrolyte accounts for the interaction between two cations or two anions, that is, the subscripts MN stands for cations M and N or anions M and N. It is further composed of two terms $S\theta_{MN}$ and $E\theta_{MN}$. $S\theta_{MN}$ is a constant at a given temperature reflecting the short range interaction between the two ions while $E\theta_{MN}$ accounts for the higher-order electrostatic forces between two ions of the same sign but different charges and is the function of solution ionic strength and the ion charges.[98] θ'_{MN} is the derivative of θ_{MN} in respect of solution ionic strength and is equal to $E\theta'_{MN}$, as shown in the equations,

$$\theta_{MN} = S\theta_{MN} + E\theta_{MN} \tag{2.19}$$

$$\theta'_{MN} = d\theta_{MN}/dI = E\theta'_{MN} \tag{2.20}$$

The values of $E\theta_{MN}$ and $E\theta'_{MN}$ are dependent on the solution ion concentration and the ion charges. They can be calculated from the equation proposed by Pitzer[98].

For a pure single electrolyte solution, the Pitzer equation is reduced to a much simpler form,

$$\ln \gamma_{MX} = |z_M z_X| f^{\gamma} + m\,(2\nu_M \nu_X/\nu)\, B^{\gamma}_{MX} + m^2\,[2\,(\nu_M \nu_X)^{3/2}/\nu]\, C^{\gamma}_{MX} \tag{2.21}$$

The above equation was used in this study to determine the virial coefficients for Na_2SO_4 from its mean activity coefficients.

2.5 RELATING THE PITZER EQUATION TO SULPHATE SOLUBILITY

For sulphate MX, its thermodynamic solubility product is related to the square root of its solubility product and its mean activity coefficient by equation (2.9). Taking log forms on both sides of the equation and moving $\ln Q_{MX}$ term to the left hand side and $\ln K_{sp,MX}$ term to the right hand side, then we have,

$$-\ln Q_{sp,MX} = -1/2 \ln K_{sp,MX} + \ln \gamma_{MX} + n/2 \ln \gamma_{H2O} \qquad (2.22)$$

Replacing $\ln \gamma_{MX}$ in the equation (2.22) with the expression in the Pitzer equation (2.10), then,

$$\begin{aligned} -\ln Q_{sp,MX} = {} & -1/2 \ln K_{sp,MX} + n/2 \ln \gamma_{H2O} + |z_M z_X| f^{\gamma} + \\ & (2\nu_M/\nu) \sum_a m_a [B_{Ma} + (\Sigma m z) C_{Ma} + (\nu_X/\nu_M) \theta_{Xa}] + \\ & (2\nu_X/\nu) \sum_c m_c [B_{cX} + (\Sigma m z) C_{cX} + (\nu_M/\nu_X) \theta_{Mc}] + \\ & \sum_c \sum_a m_c m_a \{ |z_M z_X| B'_{ca} + \nu^{-1} [2\nu_M z_M C_{ca} + \\ & \nu_M \psi_{Mca} + \nu_X \psi_{caX}] \} + 1/2 \sum_c \sum_{c'} m_c m_{c'} [(\nu_X/\nu) \psi_{cc'X} + \\ & |z_M z_X| \theta'_{cc'}] + 1/2 \sum_a \sum_{a'} m_a m_{a'} [(\nu_M/\nu) \psi_{Maa'} + \\ & |z_M z_X| \theta'_{aa'}] \end{aligned} \qquad (2.23)$$

In order to calculate calculate sulphate solubility using equation (2.23), all the parameters appearing on the right hand side must be determined. Of these parameters, most of their values at various temperatures have been determined and tabulated or have been expressed in proposed equations in the public literature, but some of the parameters are only available at 25°C and their values at elevated temperatures had to be determined

in this study. The following sections describe the process of acquiring the parameters.

2.6 DETERMINING THE PARAMETERS FROM LITERATURE SOURCES

The ions of importance to the prediction of sulphate scaling tendency in oilfield brines are Na^+, Ca^{2+}, Mg^{2+}, Ba^{2+}, Sr^{2+}, Cl^-, SO_4^{2-}, etc. In this model, the effects of K^+ ions and HCO_3^- ions are treated as Na^+ and Cl^- ions, respectively. Also the trace Fe^{3+} and CO_3^{2-} are viewed as equivalent Na^+ and Cl^- ions, respectively. The explanation for such treatment will be given in sections (2.11) and (2.12). The major ions in a brine can be considered as the components of the salts of NaCl, Na_2SO_4, $MgCl_2$, $CaCl_2$, $BaCl_2$, $SrCl_2$, $BaSO_4$, $SrSO_4$, $CaSO_4$ and $MgSO_4$. Therefore, if using equation (2.23), the parameters or coefficients involved in the sulphate solubility prediction are:

A_ϕ, $-1/2\ln K_{sp,BaSO4}$, $-1/2\ln K_{sp,SrSO4}$, $-1/2\ln K_{sp,gypsum}$, $-1/2\ln K_{sp,anhydrite}$,

$\beta^{(0)}_{ij}$, $\beta^{(1)}_{ij}$, $\beta^{(2)}_{ij}$, C_{ij}, θ_{MN} and ψ_{ijk}.

Among the above parameters, A_ϕ is the Debye-Hückel parameter, K_{sp}'s are the thermodynamic solubility products of the sulphate minerals, $\beta^{(0)}_{ij}$, $\beta^{(1)}_{ij}$ and $\beta^{(2)}_{ij}$ are ion interaction parameters in the expression for the second virial coefficient B_{ij} shown in equation (2.12), C_{ij}'s are the third virial coeffcients for single electrolytes, θ_{MN}'s are the second virial coefficients for mixed electrolytes and ψ_{ijk}'s are the third virial coefficients for mixed electrolyes. In this study, subscript ij stands for electrolytes NaCl, Na_2SO_4, $MgCl_2$, $CaCl_2$, $BaCl_2$, $SrCl_2$, $BaSO_4$, $SrSO_4$, $CaSO_4$ and $MgSO_4$, subscript MN represents two different cations or two different anions out of ions Na^+, Ca^{2+}, Mg^{2+}, Ba^{2+}, Sr^{2+}, Cl^-, SO_4^{2-}, e.g, MN=Ca+Na, and subscript ijk accounts for three different

ions not of the same sign out of ions Na^+, Ca^{2+}, Mg^{2+}, Ba^{2+}, Sr^{2+}, Cl^-, SO_4^{2-}, e.g, ijk=Ca+Na+Cl.

The Debye-Hückel parameter A_ϕ and $\beta^{(0)}$ and $\beta^{(1)}$ and C for NaCl over a wide temperature range were tabulated by Pitzer et al.[105] Holmes and Mesmer[57] obtained $\beta^{(0)}$ and $\beta^{(1)}$ and C for $BaCl_2$ and $SrCl_2$ at ambient and higher temperatures by correlating osmotic coefficient using the Pitzer equation but their $\beta^{(0)}$ and $\beta^{(1)}$ values at 25°C were found incorrect by a factor of 4/3 after comparison with the 25°C values given by Pitzer[99] and testing the osmotic correlation using the Pitzer equation. Eventually, the $\beta^{(0)}$ and $\beta^{(1)}$ for $BaCl_2$ and $SrCl_2$ at 25°C were taken from Pitzer's and those at higher temperatures were collected from Holmes and Mesmer. The virial coefficients for Na_2SO_4 at temperatures other than 25°C were not available from the published literature but the mean activity coefficients of Na_2SO_4 solutions at various temperatures were tabulated by Rogers and Pitzer.[119] In this study, the least squares method(Appendix 2.1) was used with the Pitzer equation for mean activity coefficient (equation (2.21)) to determine the $\beta^{(0)}$ and $\beta^{(1)}$ and C^γ for Na_2SO_4 using the mean activity coefficients from Rogers and Pitzer. The $\beta^{(0)}$ and $\beta^{(1)}$ and C for $MgCl_2$ at 25°C were determined by Pitzer[99] and at the higher temperatures by Holmes, et al.[56] In this study, the Debye - Hückel parameter A_ϕ and the above available virial coefficients for NaCl, Na_2SO_4, $MgCl_2$, $BaCl_2$ and $SrCl_2$ were correlated with temperature and an empirical equation was produced from the temperature correlations for calculating these coefficients at various temperatures, as expressed below,

$$c_t = k_0 + k_1 t + k_2 t^2 + k_3 t^3 + k_4 t^4 \qquad (2.24)$$

where c_t is the parameter at temperature t and k_0 through k_4 are the temperature correlation coefficients of the parameter. The obtained temperature correlation coefficients are given in table (2.1).

Equations were proposed by Phutela and Pitzer[95] for calculating the virial coefficients for $CaCl_2$ and they[96] also presented equations for $MgSO_4$, these equations were used in this model for generating the virial coefficients for the two salts. The two equations are presented in table (2.1) together with the coefficients in the equations.

The virial coefficients for the three insoluble sulphates: $BaSO_4$, $SrSO_4$ and $CaSO_4$ were not found from the literature apart from their values at 25°C. This is because the virial coefficients for single electrolytes are always determined from correlating the properties of electrolytes or electrolyte solutions such as osmotic coefficient and mean activity coefficient with ion concentration in the solution using the Pitzer equations, while the three sulphates have very low solubilities in the solution so that the ion concentration ranges for the correlation are very limited. As a result, the accurate virial coefficients cannot be obtained for the three sulphates. Fortunately, $MgSO_4$ has very similar properties in an aqueous solution to those of $BaSO_4$, $SrSO_4$ and $CaSO_4$ apart from the solubility, and the virial coefficients for $MgSO_4$ can be reasonably assumed to those for the other three sulphates, as suggested by Pitzer and Rogers, et al.[99,118]

The second parts of θ_{MN} and θ'_{MN}, that is, $E\theta_{MN}$ and $E\theta'_{MN}$ in equations (2.19) and (2.20), are zeros except for ion pairs Ba-Na, Ca-Na, Sr-Na, Mg-Na and Cl-SO4, of different charges. Pitzer[98] proposed an equation for calculating $E\theta_{MN}$ and $E\theta'_{MN}$ and the equation was used in this study for calculating their values for the above cation pairs and the anion pair.

In addition to the above parameters, the water activity coefficients in the aqueous solutions are required in gypsum($CaSO_4.2H_2O$) solubility calculation as seen in equations (2.6) and (2.23). This study took the empirical equation and coefficients from Stoughton and Lietzke[133] to calculate water activity coefficient in various solution

Table 2.1 Temperature Fitting Equations for the Parameters Obtained from Published Literature

Temperature equations:

For $CaCl_2$ parameters $c_T = k_0 + k_1T + k_2T^2$

For $MgSO_4$ parameters $c_T = k_0(T/2 + 298^2/2T - 298) + k_1(T^2/6 + 298^3/3T - 298^2/2) + k_2(T^3/12 + 298^4/4T - 298^3/3) + k_3(T^4/20 + 298^5/5T - 298^4/4) + k_4(298 - 298^2/T) + k_5$

For other parameters $c_t = k_0 + k_1t + k_2t^2 + k_3t^3 + k_4t^4$

where T is temperature in Kelvin and t is temperature in Celsius. c_T or c_t is a parameter at T or t, e.g, c_t stands for $\beta^{(0)}_{NaCl}$.

Temperature coefficients:

parameter		temperature fitting coefficients					
		k_0	k_1	k_2	k_3	k_4	k_5
A_ϕ		0.3751	0.5917E-3	0.1996E-5	0.6149E-8	0.	0.
NaCl	$\beta^{(0)}$	0.5356E-1	0.1078E-2	-.8816E-5	0.3194E-7	-.489E-10	0.
	$\beta^{(1)}$	0.2586	0.7821E-3	-.8367E-6	0.4548E-8	0.	0.
	C_{MX}	0.2259E-2	-.7416E-4	0.5056E-6	-.1851E-8	.296E-11	0.
Na_2SO_4	$\beta^{(0)}$	-.4283E-1	0.3071E-2	-.2468E-4	0.1071E-6	-.1906E-9	0.
	$\beta^{(1)}$	0.9392	0.6921E-2	-.2396E-4	-.1196E-6	0.6628E-9	0.
	C_{MX}	0.4393E-2	-.1176E-3	0.2772E-6	0.1836E-9	0.	0.
$BaCl_2$	$\beta^{(0)}$	0.2434	0.9778E-3	-.8432E-5	0.1622E-7	0.	0.
	$\beta^{(1)}$	1.3690	0.5463E-2	-.1799E-4	0.1365E-6	0.	0.
	C_{MX}	-.5109E-2	-.8083E-4	0.4653E-6	-.6820E-9	0.	0.
$SrCl_2$	$\beta^{(0)}$	0.2827	0.1297E-3	-.1076E-6	-.5286E-8	0.	0.
	$\beta^{(1)}$	1.193	0.2385E-1	-.2150E-3	0.6936E-6	0.	0.
	C_{MX}	0.5929E-4	-.1006E-4	-.4794E-6	0.2083E-8	-.966E-12	0.
$MgCl_2$	$\beta^{(0)}$	0.4134E	-.3419E-2	0.4566E-4	-.2758E-6	0.5749E-9	0.
	$\beta^{(1)}$	1.0580	0.3531E-1	-.4875E-3	0.3093E-5	-.6323E-8	0.
	C_{MX}	0.3439E-2	-.7577E-4	0.5020E-6	-.1213E-8	0.	0.
$CaCl_2$	$\beta^{(0)}$	0.1161	0.1164E-2	-.1776E-5	0.	0.	0.
	$\beta^{(1)}$	3.4787	-.1542E-1	.3179E-4	0.	0.	0.
	C_{MX}	0.2920E-1	-.1354E-3	0.1344E-6	0.	0.	0.
$MgSO_4$	$\beta^{(0)}$	-1.0280	0.8479E-2	-.2337E-4	0.2158E-7	0.6840E-3	0.2150
	$\beta^{(1)}$	-0.2960	0.9456E-3	0	0	0.1103E-1	3.3646
	$\beta^{(2)}$	-13.760	0.1212	-.2764E-3	0	-.2152	-32.743
	C_{MX}	0.1054	-.8932E-3	0.2510E-5	-.2344E-8	-.8790E-4	0.6993E-2

compositions and temperature, the equation is given as,

$$\ln \gamma_{H2O} = - \frac{W}{1000} (\Sigma_i m_i) \phi \qquad (2.25)$$

where W is water molecular weight, $(\Sigma_i m_i)$ is the total molalities of all the ions in the solution, and ϕ is the solution osmotic coefficient which can be calculated by the following equation,

$$\phi = 1 - \frac{S}{3.375\, I} \{[1 + 1.5\, I^{1/2}] - 2 \ln [1 + 1.5\, I^{1/2}] - \frac{1}{1 + 1.5\, I^{1/2}} \} +$$
$$1/2\, B\, (\Sigma_i m_i) + 1/4\, C\, (\Sigma_i m_i)^2 \qquad (2.26)$$

where I is ionic strength and,

$$B = B_1/T + B_2 + B_3 \ln T \qquad (2.27)$$

$$C = C_1/T + C_2 + C_3 \ln T \qquad (2.28)$$

here B_1, B_2, B_3, C_1, C_2 and C_3 are constants and T is the temperature in Kelvin, and

$$S = 1.17202\, (\Sigma_i m_i z_i^2 / \Sigma_i m_i)\, \rho^{1/2}\, (D_{25} T_{25} / D_T\, T)^{3/2} \qquad (2.29)$$

in the above equation, z_i is the ion charge and

$$\rho = 1.00157 - 1.56096 \times 10^{-4} t - 2.69491 \times 10^{-6} t^2 \qquad (2.30)$$

$$D_T = 5321/T + 233.76 - 0.9297\, T + 0.001417\, T^2 - 8.292 \times 10^{-7} T^3 \qquad (2.31)$$

in equation (2.30) , t is the temperature in Celsius.

2.7 PARAMETERIZATION OF THE UNKNOWN COEFFICIENTS BY SOLUBILITY CORRELATIONS

Besides the parameters obtained directly or indirectly from the published literature as described in the last section, only the values at 25°C were available from the literature for the other parameters included in equation (2.23). These parameters are: the thermodynamic solubility products for $BaSO_4$, $SrSO_4$, gypsum and anhydrite, the $S\theta_{MN}$, i.e, the first parts of $\theta_{MN,}$ and ψ_{ijk} for the ions involved in the sulphate solubility prediction.

In order to determine these unknown parameters, the sulphate solubilities in various aqueous salt systems, various solution ion compositions and temperatures were collected from the published sources and their reliability was evaluated. These solubility data were then used in equation (2.23) to correlate with solution ionic strength and concentrations of the individual ions in the solution using the least squares method.(Appendix 2.1) and the parameter's values were eventually determined from the solubility correlations. It was believed that determining the unknown parameters from the sulphate solubility correlations rather than correlating the other properties of the sulphates such as mean activity coefficients could give more accurate and consistent parameters for the sulphate solubility calculation. The values of these parameters at 25°C were also determined from the solubility correlations so as to give more coherent solubility prediction, though they were available from the literature. Finally, in a similar fashion as the temperature-fittings carried out on the parameters obtained from the literature, these parameters obtained from this study were expressed in the empirical temperature equation.

2.7.1 Collection and Evaluation of Sulphate Solubility Data

As described in the last subsection, the sulphate solubilities were used in determining the sulphate thermodynamic solubility products and the virial coefficients

for mixed electrolytes using equation (2.23). After examining the equation, it was found that only the sulphate solubility data in pure water, binary and ternary aqueous salt systems were necessary for the solubility correlations. Pucknell[113] in his study collected most of the solubility data needed in the solubility correlations. Since then only a few sets of the measured solubility data on $SrSO_4$ have been reported in the published articles.[35,61,123,151] From all the sources, abundant solubility data were available for calcium sulphate, [4,6,9-12,19,30,31,36,40,45,48,53-55,59,70-72,91,93,106-108,110,125,127,128, 130,134,159,160,162,163] a reasonable amount of solubility data were collected for $SrSO_4$,[12,13,27,35,43,60,61,66,68,69,79,89,123,136,151] and the data for $BaSO_4$ were scarce in the other solutions rather than pure water and sodium chloride solutions.[8,14,27,43,66,74,85,112,120,123,135,142,145] These collected solubility data were then evaluated. The solubility data from doubtful measurements or mineral samples were discarded. For example, the $BaSO_4$ solubility data measured by Gundlach et al(1972) and Strubel(1967)[43,135] were rejected because the barite sample used in the measurement contained a high content of $SrSO_4$. Similarly, the solubilities from interpolation and extrapolation[8,145] (Blount1977 & Uchameyschvili 1966) or presented in graphic forms[66,112](Lieser1965 and Puchelt1967) were not used in the solubility correlations. Also a few data were excluded because large discrepancies from the data reported from the other sources[79,124](Seidell 1958 and Muller 1960). In a few cases[123,151](Vetter et al.1983 & Schulien 1987), a large number of sulphate solubility data reported by one source differed considerably from those measured by the others, e.g, the $SrSO_4$ solubilities measured by Vetter and co-workers were different from those reported from Davis&Collins, Jacques et al.[27,60,61] by 15 to 20%. No obvious error was found from the source papers, thus these solubility data were still included in the consequent solubility correlations. Owing to the differences in the solubilities from different sources, the quality of solubility prediction was affected, particularly for $BaSO_4$ and $SrSO_4$, which will be assessed in section (2.9). Table (2.2) shows the salt systems and the temperature and ion concentration ranges in which the sulphate

Table 2.2 The Aqueous Salt Systems in Which Solubility Correlations Were Made to Parameterise Unavailable Coefficients

Salt Systems	T(°C)	Maximum salt concentration (molal)			
		NaCl	$CaCl_2$	$MgCl_2$	Na_2SO_4
$BaSO_4$ - NaCl - H_2O	25-200	5.0	0	0	0
$SrSO_4$ - NaCl - H_2O	25-125	4.0	0	0	0
Anhydrite - NaCl - H_2O	25-200	6.0	0	0	0
Gypsum - NaCl - H_2O	25-110	6.0	0	0	0
$SrSO_4$ - $CaCl_2$ - H_2O	25-125	0	0.5	0	0
$SrSO_4$ - $MgCl_2$ - H_2O	25-125	0	0	0.5	0
Gypsum - Na_2SO_4 - H_2O	25-100	0	0	0	0.5
Gypsum - $MgCl_2$ - H_2O	25-100	0	0	1.5	0
Gypsum - NaCl - $MgCl_2$ - H_2O	28-90	4.0	0	0.3	0

solubility correlations were made to parameterize the unknown coefficients. Some sulphate solubility data in more complicated solutions were also collected from the published articles and used to test the quality of the solubility prediction. These solubility data with various concentrations were all converted by a computer programme to molal unit before being used in equation (2.23) for solubility correlation. An equation proposed by Rowe and Chou[121] was used to calculate the salt solution density in the unit conversion programme,

$$d = [\, A(T) - p\cdot B(T) - p^2\cdot C(T) + x\cdot D(T) + x^2\cdot E(T) - x\cdot p\cdot F(T) - x^2\cdot p\cdot G(T) - 1/2\; x\cdot p^2\cdot H(T)\,]^{-1} \qquad (2.32)$$

where p is the abolute pressure in kg/cm^2, T is the temperature in Kelvin and x is the weight fraction of the salts in the solution. A(T), B(T) through H(T) are the functions of temperature which can be referred to in their original paper.

The concentration conversion programme is also used in the final scaling tendency prediction model for converting different input concentration units to molal and converting the molal unit to required unit in the output.

2.7.2 Solubility Correlations in Pure Water and NaCl Solutions

Equation (2.23) was reduced to equation (2.33) for the square root of the sulphate solubility product in pure water and NaCl solutions(Appendix 2.2),

$$-\ln Q_{sp,MX} = K - 1/2\ln K_{sp,MX} + m_N S\theta + m_M m_N \psi_1 + 1/2\, m_N^2 \psi_2 \qquad (2.33)$$

where,

$$S\theta = S\theta_{MN} + S\theta_{XY}, \qquad (2.34)$$

$$\Psi_1 = \Psi_{MNX} + \Psi_{MXY}, \tag{2.35}$$

and,

$$\Psi_2 = \Psi_{MNY} + \Psi_{NXY} \tag{2.36}$$

here N is Na, X is SO_4, Y is Cl and M is Ba, Ca or Sr. K in equation (2.33) at each ion composition was calculated from the following equation,

$$\begin{aligned} K = {} & 4f^{\gamma} + (m_M + m_X)B_{MX} + m_Y B_{MY} + m_N B_{NX} + \\ & 4m_M m_X B'_{MX} + 4m_M m_Y B'_{MY} + 4m_N m_X B'_{NX} + \\ & 4m_N m_Y B'_{NY} + [(m_M + m_X)(\Sigma mz) + 2 m_M m_X]C_{MX} + \\ & m_Y [(\Sigma mz) + 2 m_M]C_{MY} + m_N [(\Sigma mz) + 2m_X]C_{NX} + \\ & 2m_N m_Y C_{NY} + m_N E\theta_{MN} + m_Y E\theta_{XY} + 4m_M m_N E\theta'_{MN} + \\ & 4 m_X m_Y E\theta'_{XY} + n/2 \ln\gamma_{H2O} \end{aligned} \tag{2.37}$$

where the subscripts M, N, X and Y refer to the same ions as in equation (2.33). m is the molality of the ion referred to by the subscript.

Equation (2.33) can be expressed as a typical first-order linear equation,

$$y = a_1x_1 + a_2x_2 + a_3x_3 + a_4x_4 \tag{2.38}$$

where ,

$x_1 = 1$ $\qquad$ $a_1 = -1/2 \ln K_{sp,MX}$

$x_2 = m_N$ $\qquad$ $a_2 = S\theta$

$x_3 = m_M m_N$ $\qquad$ $a_3 = \Psi_1$

$x_4 = 1/2\ m_N^2$ $\qquad\qquad$ $a_4 = \psi_2$

and,

$$y = -\ln Q_{sp,MX} - K \tag{2.39}$$

$\ln K_{sp,MX}$, $S\theta$, ψ_1 and ψ_2 were unknown parameters in equation (2.33) or (2.38). For each sulphate in the NaCl solutions, a set of x_1, x_2, x_3, x_4 and y in equation (2.38) were calculated from every known solution composition and corresponding solubility and then their values were substituted into equation. a_1, a_2, a_3, and a_4 , i.e, the parameters of the thermodynamic solubility product and combined virial coefficients for mixed electrolytes were eventually obtained from solving equation (2.38) using the least squares method(Appendix 2.1). The parameters determined from the sulphate solubility correlations were:

$-1/2\ln K_{BaSO4}$,

$-1/2\ln K_{SrSO4}$,

$-1/2\ln K_{Gypsum}$,

$-1/2\ln K_{Anhydrite}$,

$S\theta_{Ba,Na} + S\theta_{Cl,SO4}$,

$S\theta_{Sr,Na} + S\theta_{Cl,SO4}$,

$S\theta_{Ca,Na} + S\theta_{Cl,SO4}$,

$\psi_{Ba,Na,SO4} + \psi_{Ba,Cl,SO4}$,

$\psi_{Sr,Na,SO4} + \psi_{Sr,Cl,SO4}$,

$\psi_{Ca,Na,SO4} + \psi_{Ca,Cl,SO4}$,

$\psi_{Ba,Na,Cl} + \psi_{Na,Cl,SO4}$,

$\Psi_{Sr,Na,Cl} + \Psi_{Na,Cl,SO4}$, and

$\Psi_{Ca,Na,Cl} + \Psi_{Na,Cl,SO4}$

Two sets of $S\theta_{Ca,Na} + S\theta_{Cl,SO4}$, $\Psi_{Ca,Na,SO4} + \Psi_{Ca,Cl,SO4}$ and $\Psi_{Ca,Na,Cl} + \Psi_{Na,Cl,SO4}$ were determined from both gypsum and anhydrite solubility correlations and small differences were observed between the two sets of values from the two different correlations. It was decided that the virial coefficients obtained from the gypsum solubility correlation be used for calculating both gypsum and anhydrite solubilities in NaCl solutions because better solubility prediction for both calcium sulphates was given by using these parameters other than those from the anhydrite correlation , also insufficient solubility data were available for anhydrite solubility correlations to determine the other remaining unknown virial coefficients of calcium sulphate in the other salt systems. The above obtained parameters at different temperatures were then fitted with temperatures into the temperature-fitting equation (2.24). The quality of solubility prediction for gypsum, anhydrite, $BaSO_4$ and $SrSO_4$ will be examined in section (2.9).

2.7.3 Solubility Correlations in Na_2SO_4- (NaCL) Solutions

Similar to the process described in the last subsection, the general equation for sulphate solubility correlation (equation (2.23)) was simplified into the following form for sulphates in aqueous Na2SO4 solutions or Na2SO4 - NaCl solutions,

$$-\ln Q_{sp,MX} = K_1 + (m_Y - m_N)\, S\theta_{XY} + 1/2\,(m_M + m_X)\,(m_Y - m_N)\,\Psi_{MXY} \qquad (2.40)$$

where the subscripts M, N, X and Y refer to the same ions as in the last subsection. K_1 is the function of solution ion composition and has the form,

$$K_1 = K - 1/2\ln K_{sp,MX} + m_N S\theta + 1/2 m_N (m_M + m_X)\,\psi_1 + 1/2 m_N m_Y \psi_2 \qquad (2.41)$$

where K is calculated from equation (2.37) in the last subsection and $-1/2\ln K_{sp,MX}$, $S\theta$, ψ_1 and ψ_2 were already obtained from the solubility correlations in NaCl solutions.

The least squares method was again applied to equation (2.40) to make sulphate solubility correlations with solution ionic strength and ion molalities. The parameters determined from the solubility correlations in Na2SO4 - (NaCl) solutions are,

$S\theta_{Cl,SO4}$, $\psi_{Ba,Cl,SO4}$, $\psi_{Sr,Cl,SO4}$ and $\psi_{Ca,Cl,SO4}$

From the solubility correlation for each sulphate at a given temperature, a $S\theta_{Cl,SO4}$ was obtained, eventually, four $S\theta_{Cl,SO4}$ values at every temperature were produced from the solubility correlations for the four different sulphates and they were found not identical. Again $S\theta_{Cl,SO4}$ from gypsum solubility correlation was chosen for solubility prediction in the model because the gypsum solubility data were the most sufficient and reliable and covered wide range ion concentration. These newly determined parameters were temperature fitted, similar to those obtained from the solubility correlations in NaCl solutions.

The combined virial coefficients presented in the last subsection minus the virial coefficients obtained in this subsection then gave the single virial coefficients, e.g, $S\theta_{Ba,Na} + S\theta_{Cl,SO4}$ minus $S\theta_{Cl,SO4}$ to result in $S\theta_{Ba,Na}$. The single virial determined in this way are,

$S\theta_{Ba,Na}$, $S\theta_{Sr,Na}$, $S\theta_{Ca,Na}$, $\psi_{Ba,Na,SO4}$, $\psi_{Sr,Na,SO4}$ and $\psi_{Ca,Na,SO4}$

2.7.4 Solubility Correlations in Aqueous $MgCl_2$ or $CaCl_2$ Solutions

To obtain the virial coefficients for the mixed electrolytes containing Ca and Mg ion components, the sulphate solubility correlation was carried out from using the sulphate solubility data measured in aqueous $MgCl_2$ and $CaCl_2$ Solutions, following the similar procedure discussed in the last two subsections. First, equation (2.23) was reduced to equation (2.42) for sulphate solubility expression in the $MgCl_2$ or $CaCl_2$ salt systems,

$$-\ln Q_{sp,MX} = K_2 + m_N S\theta_1 + m_M m_N \psi_3 + 1/2\, m_N^2 \psi_4 \qquad (2.42)$$

here, subscript M refers to Ca, Ba or Sr and N denotes to Mg or Ca(*if* M *is not* Ca), and

$$K_2 = K - 1/2\ln K_{sp,MX}, \qquad (2.43)$$

$$S\theta_1 = S\theta_{MN} + 2S\theta_{XY}, \qquad (2.44)$$

$$\psi_3 = \psi_{MNX} + 2\psi_{MXY}, \text{ and} \qquad (2.45)$$

$$\psi_4 = \psi_{MNY} + \psi_{NXY} \qquad (2.46)$$

The K expression is given in equation (2.37). Then, sulphate solubilities in different concentrations at every given temperature were correlated with the solution ionic strength and ion molalities using the least squares method and the unknown parameters were determined from such correlations. The solubility correlation was not performed for $BaSO_4$ in $MgCl_2$ and $CaCl_2$ due to scarce solubility data being available. The difficulty with $BaSO_4$ solubility correlation in the salt systems other than NaCl will be given more discussion in section(2.11). The newly obtained virial coefficients are:

$S\theta_{Ca,Mg} + 2S\theta_{Cl,SO4}$, $S\theta_{Sr,Mg} + 2S\theta_{Cl,SO4}$, $S\theta_{Sr,Ca} + 2S\theta_{Cl,SO4}$, $\Psi_{Ca,Mg,SO4} + 2\Psi_{Ca,Cl,SO4}$, $\Psi_{Sr,Mg,SO4} + 2\Psi_{Sr,Cl,SO4}$, $\Psi_{Sr,Ca,SO4} + 2\Psi_{Sr,Cl,SO4}$, $\Psi_{Ca,Mg,Cl} + \Psi_{Mg,Cl,SO4}$, $\Psi_{Sr,Mg,Cl} + \Psi_{Mg,Cl,SO4}$ and $\Psi_{Sr,Ca,Cl} + \Psi_{Mg,Cl,SO4}$.

Their values at various temperatures were subsequently fitted into the proposed temperature equation (2.24). Among these combined parameters, some were split by substituting the previous determined single virial coefficients into the combined forms. Eventually, new single parameters were obtained and shown here,

$S\theta_{Ca,Mg}$, $S\theta_{Sr,Mg}$, $S\theta_{Sr,Ca}$, $\Psi_{Ca,Mg,SO4}$, $\Psi_{Sr,Mg,SO4}$ and $\Psi_{Sr,Mg,Cl}$

2.7.5 Solubility Correlations in Ternary Salt Solutions

Until now, all the sulphate solubility correlations have taken place in binary salt solutions. For determining the third virial coefficient for Na-Mg-SO_4, the sulphate solubilities in a ternary salt system containing Na, Mg and SO_4 ions were required. Consequently, gypsum solubility data in gypsum-$MgCl_2$-NaCl solutions were collected from the literature for this purpose. The gypsum solubility expression in this salt system was deduced from equation (2.23) and presented here,

$$-\ln Q_{sp,gypsum} = K_3 + 1/2 m_N m_L \Psi_{NLX} \qquad (2.47)$$

K_3 is the sum of the terms of known parameters,

$$K_3 = K - 1/2 \ln K_{sp,gypsum} + m_L B_{LX} + 4 m_L m_X B_{LX} +$$

$$4 m_L m_Y B'_{LY} + m_L [(\Sigma mz) + 2 m_X] C_{LX} +$$

$$2\, m_L\, m_Y\, C_{LY} + 4m_M m_L\, E\theta'_{ML} + 4m_N m_L\, E\theta'_{NL} +$$

$$m_L E\theta_{ML} + m_N\, S\theta_{MN} + m_L\, S\theta_{ML} + m_Y\, S\theta_{XY} +$$

$$1/2\, m_N\, (m_M + m_X)\psi_{MNX} + 1/2\, m_Y\, (m_M + m_X)\psi_{MXY} +$$

$$1/2\, m_L\, (m_M + m_X)\psi_{MLX} + 1/2 m_L m_Y (\psi_{MLY} + \psi_{LXY}) +$$

$$1/2 m_N m_Y (\psi_{MNY} + \psi_{NXY}) \qquad (2.48)$$

Where subscript N refers to Na, L for Mg, X for SO_4 and Y for Cl and K is given in equation (2.37).

As described in the previous subsections, the unknown parameters were always obtained from solubility correlations in the other aqueous salt systems but only one parameter ψ_{NLX}, i.e, $\psi_{Na,Mg,SO4,}$ is present in equation (2.47). Rearranging the equation, it becomes,

$$\psi_{NLX} = -2(\ln Q_{sp,gypsum} + K_3)/m_N m_L \qquad (2.49)$$

At a given temperature, each solubility at a certain solution concentration would result in a ψ_{NLX} value from equation (2.49) and the ψ_{NLX} parameter at that temperature was calculated by taking the average of all the values from different concentrations.

2.8 RESULTS FROM THE SULPHATE SOLUBILITY CORRELATIONS

The parameterization of the coefficients related to sulphate solubility prediction using the Pitzer equation for electrolyte mean activity coefficient was described and discussed in the last two sections. The results of the parameterization are summed up in table (2.3). The equation shown in the table is the general form of the empirical equation for calculating the parameters obtained from this study and the fitting coefficients given in

Table 2.3 Temperature Fitting Equation for the Parameters Obtained from This Study

Temperature fitting equation:

$c_t = k_0 + k_1 t + k_2 t^2 + k_3 t^3 + k_4 t^4$

where t is temperature in Celsius. c_t is a parameter at temperature t, e.g, c_t stands for $-1/2 \ln K_{sp,BaSO4}$.

Temperature coefficients:

parameter	temperature fitting coefficients				
	k_0	k_1	k_2	k_3	k_4
$-1/2 \ln K_{sp,BaSO4}$	11.69	-.2280E-1	0.2009E-3	-.5801E-6	0.8104E-9
$-1/2 \ln K_{sp,SrSO4}$	7.646	-.5670E-2	0.1803E-3	-.1227E-5	0.6418E-8
$-1/2 \ln K_{sp,gypsum}$	5.247	-.4665E-2	0.1089E-3	-.2696E-6	0.2382E-9
$-1/2 \ln K_{sp,anhydrite}$	4.662	0.1870E-1	-.1678E-3	0.1688E-5	-.4425E-8
$\Psi_{Ba,Na,SO4} + \Psi_{Ba,Cl,SO4}$	0.2578E-3	-.1796E-4	0.1934E-6	-.4816E-9	-.1596E-11
$\Psi_{Ba,Na,Cl} + \Psi_{Na,Cl,SO4}$	-0.1530	0.4542E-2	-.6968E-4	0.4378E-6	-.8177E-9
$\Psi_{Sr,Na,SO4} + \Psi_{Sr,Cl,SO4}$	-0.6899E-2	-.5673E-4	0.2341E-5	-.1374E-7	0.
$\Psi_{Sr,Na,Cl} + \Psi_{Na,Cl,SO4}$	0.1511E-1	0.1663E-3	0.1389E-4	-.5397E-6	0.3413E-8
$\Psi_{Ca,Na,Cl} + \Psi_{Na,Cl,SO4}$	0.1192E-1	-.1280E-2	0.2122E-4	-.1162E-6	0.
$S\theta_{Cl,SO4}$	0.3876	-.2830E-1	0.1007E-2	-.1465E-4	0.7409E-7
$S\theta_{Ca,Na}$	-0.3237	0.3176E-1	-.1063E-2	0.1495E-4	-.7424E-7
$S\theta_{Ba,Na}$	0.7653E-1	0.1670E-1	-.8347E-3	0.1362E-4	-.7222E-7
$S\theta_{Sr,Na}$	-0.3038	0.2621E-1	-.1020E-2	0.1592E-4	-.8272E-7
$S\theta_{Ca,Mg}$	-0.6564	0.5506E-1	-.1999E-2	0.2930E-4	-.1482E-6
$S\theta_{Sr,Mg}$	-0.7734	0.5377E-1	-.1979E-2	0.2949E-4	-.1482E-6
$S\theta_{Ca,Sr}$	-0.2627	0.1074E-1	-.1693E-2	0.2930E-4	-.1482E-6
$\Psi_{Ca,Na,SO4}$	-0.6296	0.1563E-1	-.1047E-3	0.6970E-7	0.
$\Psi_{Ca,Cl,SO4}$	0.584	-.1492E-1	0.9274E-4	0.	0.
$\Psi_{Ca,Mg,SO4}$	-1.1680	0.2984E-1	-.1855E-3	0.	0.
$\Psi_{Ca,Sr,Cl} + \Psi_{Ca,Cl,SO4}$	-3.263	0.2232	-.1556E-2	0.	0.
$\Psi_{Ca,Mg,Cl} + \Psi_{Mg,Cl,,SO4}$	-0.06179	0.7933E-3	-.1063E-3	0.	0.
$\Psi_{Sr,Mg,Cl} + \Psi_{Mg,Cl,SO4}$	0.	0.	0.1112E-3	-.1217E-5	-.4939E-8

the table are used in the equation for calculating the parameters. It can be seen from table (2.3) that some of the parameters are in combined forms. This is because there were not sufficient data available to make solubility correlations in the other salt systems which may split these combined parameters into single ones. In the solubility prediction model, these combined parameters are used together with other single coefficients after some approximate treatment has been applied to the specific ion effects in complicated waters.

2.9 QUALITY OF THE SOLUBILITY PREDICTION

It is necessary to assess the quality of the sulphate solubility prediction using the Pitzer's approach based equation (2.23). For this purpose, the sulphate solubilities in the aqueous salt systems listed in table (2.4) were calculated from equation (2.23) with the parameters given in tables (2.1) and (2.3) and then compared to the measured solubilities collected from the published literature. Of these salt systems, the measured sulphate solubilities in systems 1-9 were used in determining the parameters shown in table (2.3) while no parameterization was carried out in salt systems 10-12. It is important to assess the quality of solubility prediction by comparing the calculated solubilities with the measured data not only in the salt solutions from which the parameterization has been done but also in the solutions not being used for determining the unknown parameters. If the predicted sulphate solubilities are in good agreement with the the measured data in the aqueous salt systems like 10 to 12 in which no coefficient parameterization has been carried out, then it proves that the solubility prediction method is accurate not only in regenerating solubility data but in predicting solubilities in more complicated solutions.

In assessing the quality of the sulphate solubility prediction, two terms are often used to indicate the difference of the calculated solubilities from the measured ones. One is the relative standard deviation(S.D%), as defined in equation (2.50), and the other is the relative deviation(D%), as expressed in equation (2.51),

Table 2.4 Relative Standard Deviations of Predicted Solubilities from the Measured

No.	Aqueous systems	S.D%	No.	Aqueous systems	S.D%
1	$BaSO_4$ — NaCl	8.7	7	$SrSO_4$ — $MgCl_2$	21.1
2	$SrSO_4$ — NaCl	13.7	8	Gypsum — $MgCl_2$	2.4
3	Anhydrite— NaCl	8.2	9	Gypsum — NaCl — $MgCl_2$	3.6
4	Gypsum — NaCl	2.5	10	Gypsum — NaCl — $MgCl_2$ — Na_2SO_4	7.9
5	$SrSO_4$ — $CaCl_2$	13.3	11	$SrSO_4$ — NaCl — $SrCl_2$ — $MgCl_2$ — $CaCl_2$	8.6
6	Gypsum — Na_2SO_4	2.1	12	Gypsum — NaCl — $MgCl_2$ — $CaCl_2$	5.7

$$S.D\% = 100 \times \sqrt{\frac{1}{n}\sum_{i=1}^{n}\left(\frac{Q_{sp,measured} - Q_{sp,predicted}}{Q_{sp,predicted}}\right)^2} \qquad (2.50)$$

$$D\% = 100 \times \frac{Q_{sp,measured} - Q_{sp,predicted}}{Q_{sp,predicted}} \qquad (2.51)$$

The relative standard deviations between the sulphate solubilities calculated from using equation (2.23) in various solutions and the analysed solubilities in the same solutions reported from the literature are given in table (2.4). The anhydrite solubilities were calculated using those parameters obtained from gypsum solubility correlations except its own thermodynamic solubility product parameter $-1/2\ln K_{sp,anhydrite}$. The deviations show that, in general, the predicted sulphate solubilities are in reasonable good agreement with the actual solubilities. Analysing these deviations for different sulphates, it can be seen that the solubility prediction for gypsum is the most accurate, the predictions for $BaSO_4$ and anhydrite solubilities are the next and the solubility prediction for $SrSO_4$ is the poorest. After examining the solubility sources for each mineral, it was found that gypsum solubility data are the most abundant and reliable because the accurate measurement techniques were available, solubility data for $BaSO_4$ are not sufficient in some concentration and temperature ranges and some discrepancies exist between different sources, causing the parameters determination to be less reliable, and large variation occurred between the different data sources for $SrSO_4$. In the case of $SrSO_4$, it seems that the large deviations of the calculated solubilities from the measured data are probably attributed to the internal disagreement among the published solubility data themselves rather than any inaccuracy with the prediction method.

To visualise the quality of solubility prediction, the predicted sulphate solubilities in each salt solution are graphed along with the measured ones and their relative deviations are also displayed graphically in the following.

Solubility Prediction in Aqueous NaCl Solutions

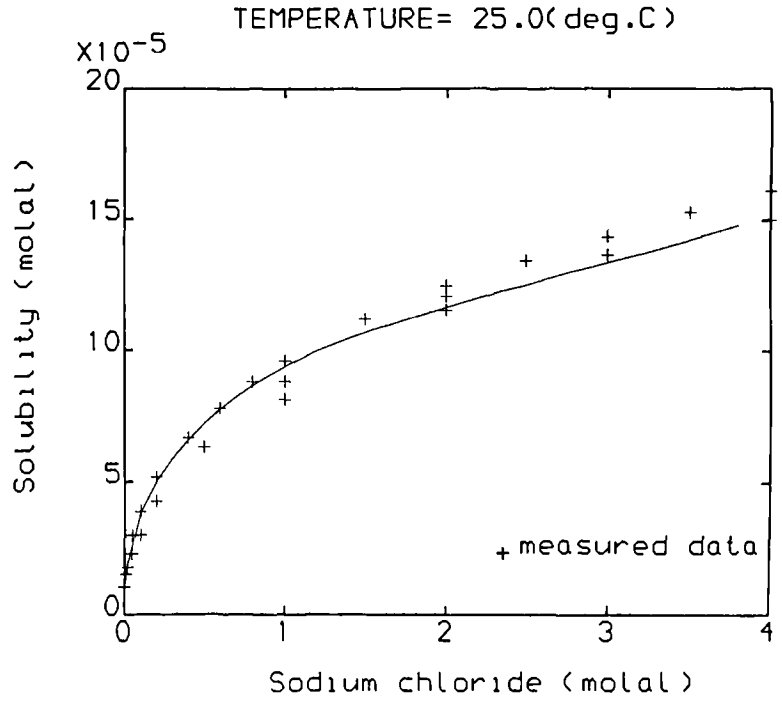

Figure 2.1 Predicted and measured barium sulphate solubilities in sodium chloride solutions. Solubility data from references 14, 27, 74, 112, 120, 135 and 142

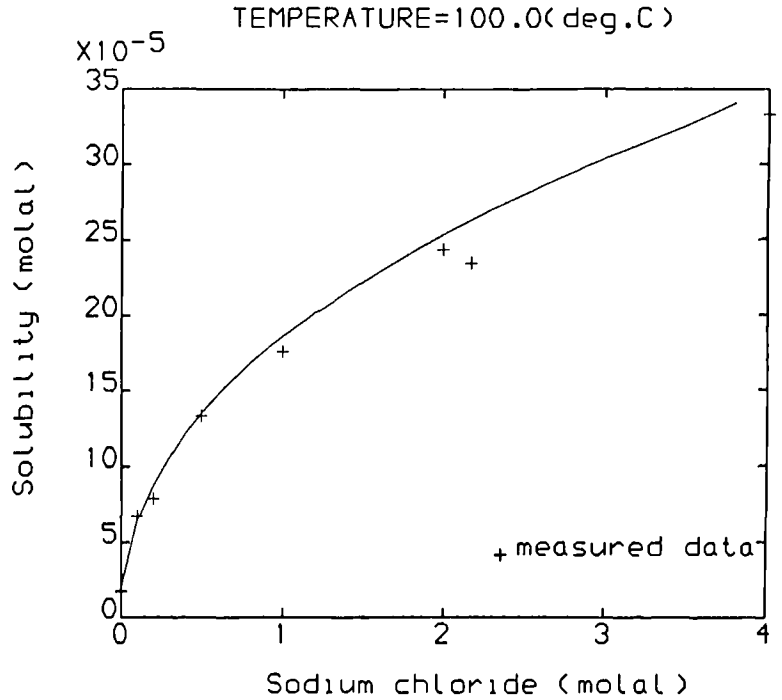

Figure 2.2 Predicted and measured barium sulphate solubilities in sodium chloride solutions. Solubility data from references 14, 27, 74, 112, 120, 135 and 142

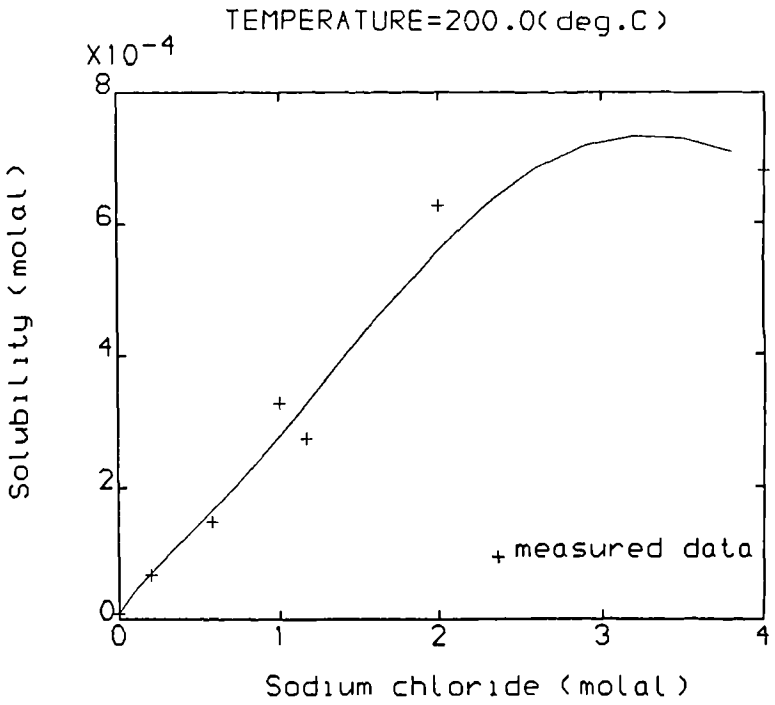

Figure 2.3 Predicted and measured barium sulphate solubilities in sodium chloride solutions. Solubility data from references 14, 27, 74, 112, 120, 135 and 142

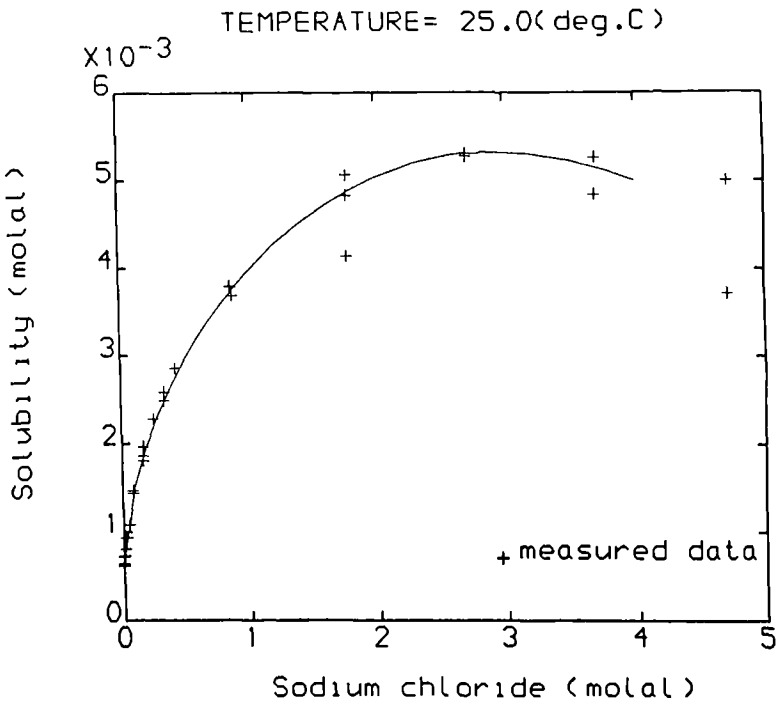

Figure 2.4 Predicted and measured strontium sulphate solubilities in sodium chloride solutions. Solubility data from references 27, 60, 61, 123, 124, 136 and 151

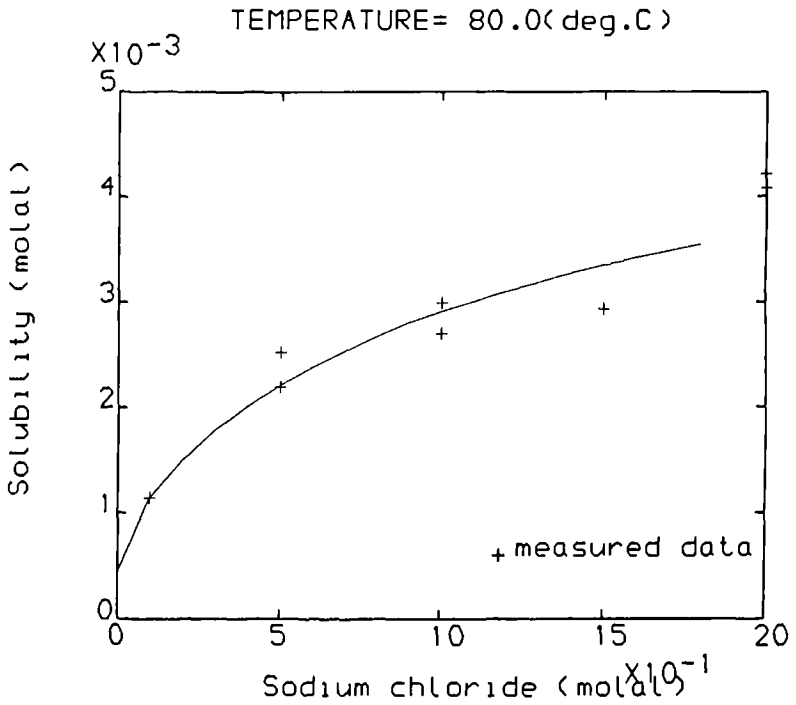

Figure 2.5 Predicted and measured strontium sulphate solubilities in sodium chloride solutions. Solubility data from references 27, 60, 61, 123, 124, 136 and 151

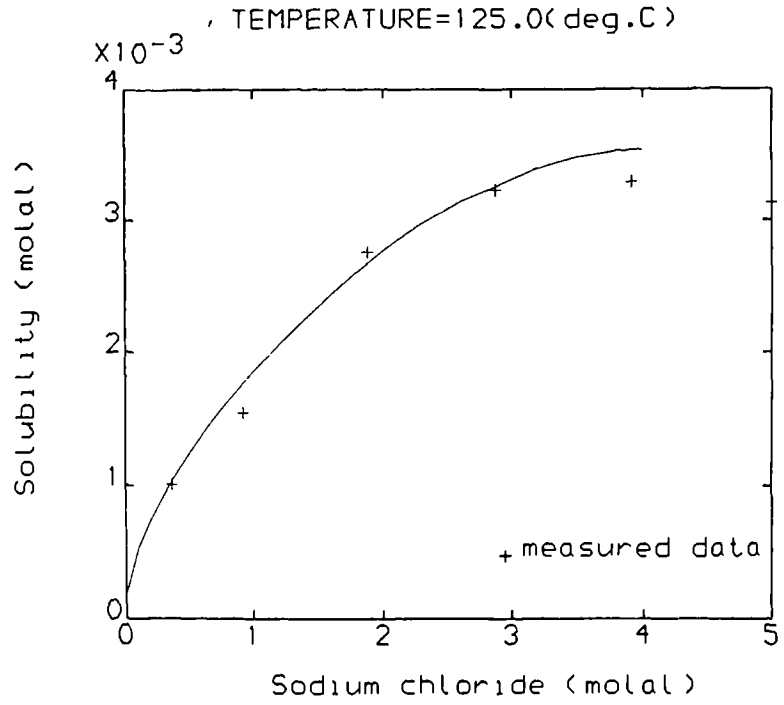

Figure 2.6 Predicted and measured strontium sulphate solubilities in sodium chloride solutions. Solubility data from references 27, 60, 61, 123, 124, 136 and 151

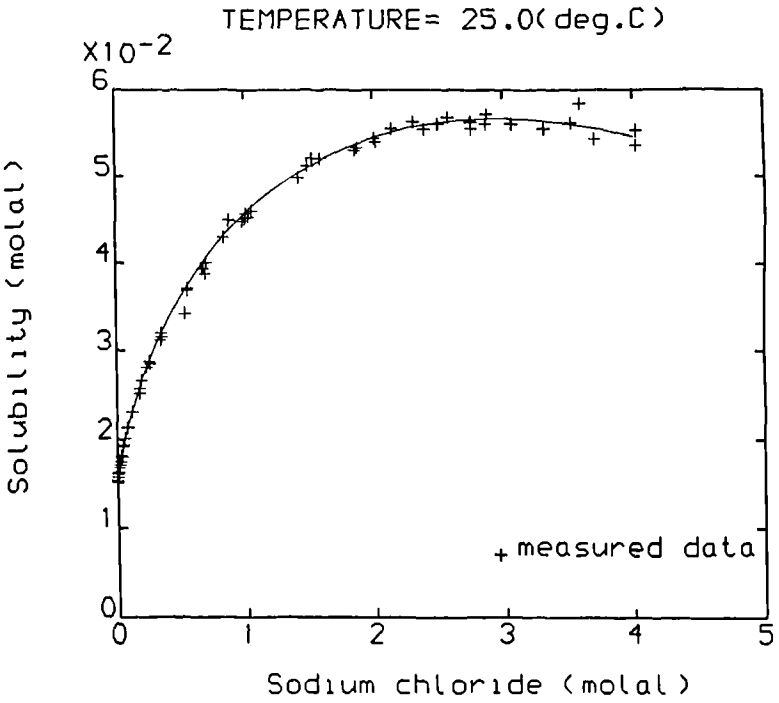

Figure 2.7 Predicted and measured gypsum solubilities in sodium chloride solutions. Solubility data from references 4, 9, 10, 11, 12, 19, 30, 40, 45, 53, 54, 55, 59, 70, 71, 72, 93, 107, 110, 124, 127, 128 and 160

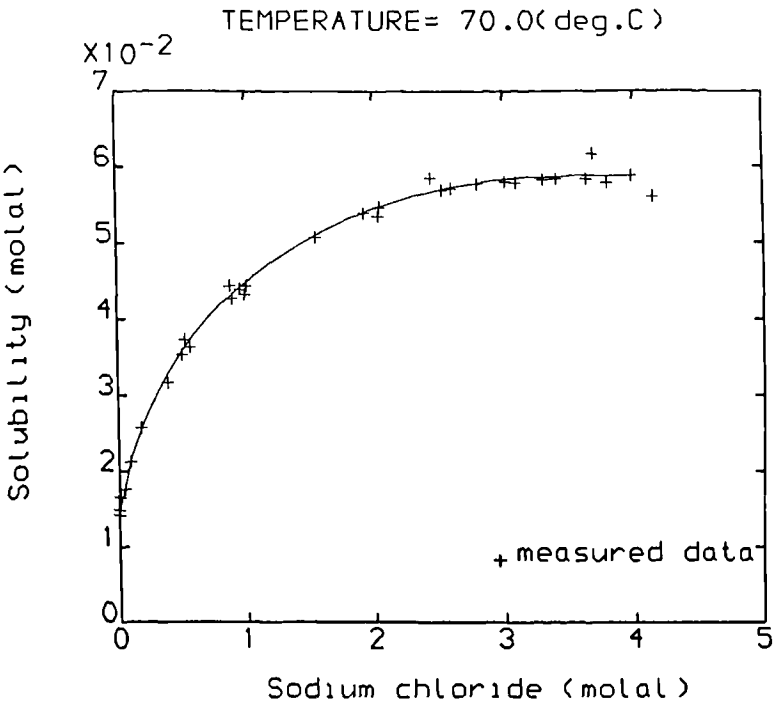

Figure 2.8 Predicted and measured gypsum solubilities in sodium chloride solutions. Solubility data from references 4, 9, 10, 11, 12, 19, 30, 40, 45, 53, 54, 55, 59, 70, 71, 72, 93, 107, 110, 124, 127, 128 and 160

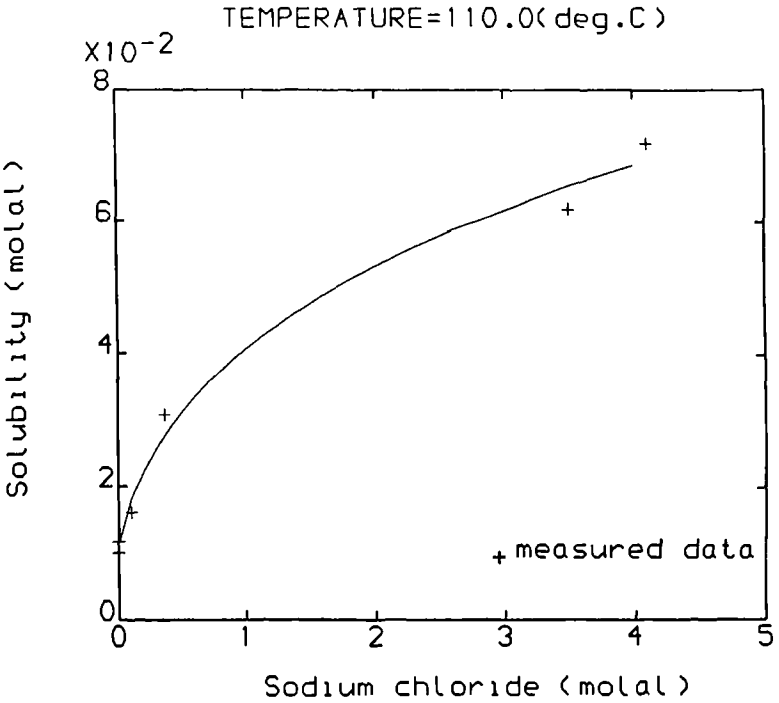

Figure 2.9 Predicted and measured gypsum solubilities in sodium chloride solutions. Solubility data from references 4, 9, 10, 11, 12, 19, 30, 40, 45, 53, 54, 55, 59, 70, 71, 72, 93, 107, 110, 124, 127, 128 and 160

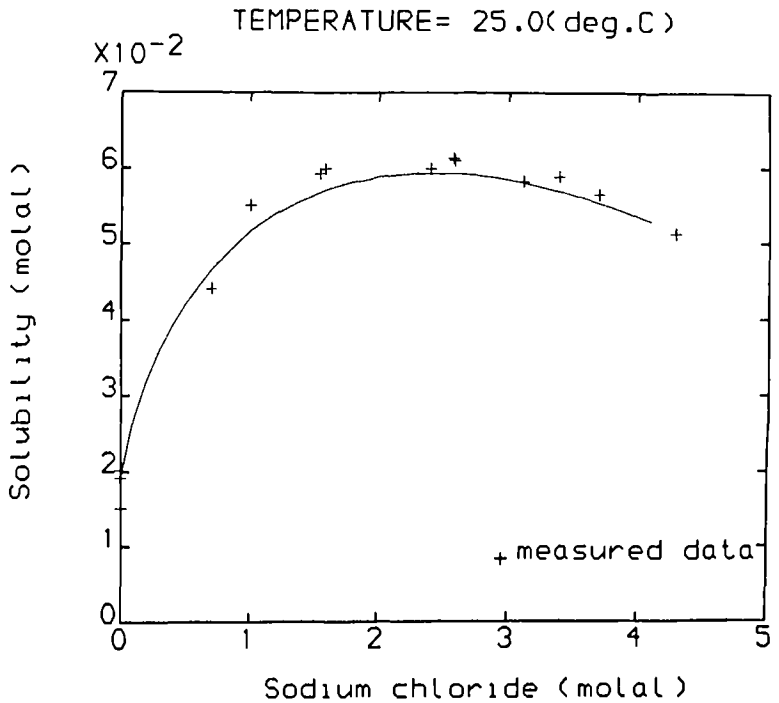

Figure 2.10 Predicted and measured anhydrite solubilities in sodium chloride solutions. Solubility data from references 9, 10, 11, 12, 30, 31, 36, 40, 45, 53, 54, 55, 70, 71, 72, 93, 107, 110, 124, 127, 134 and 159

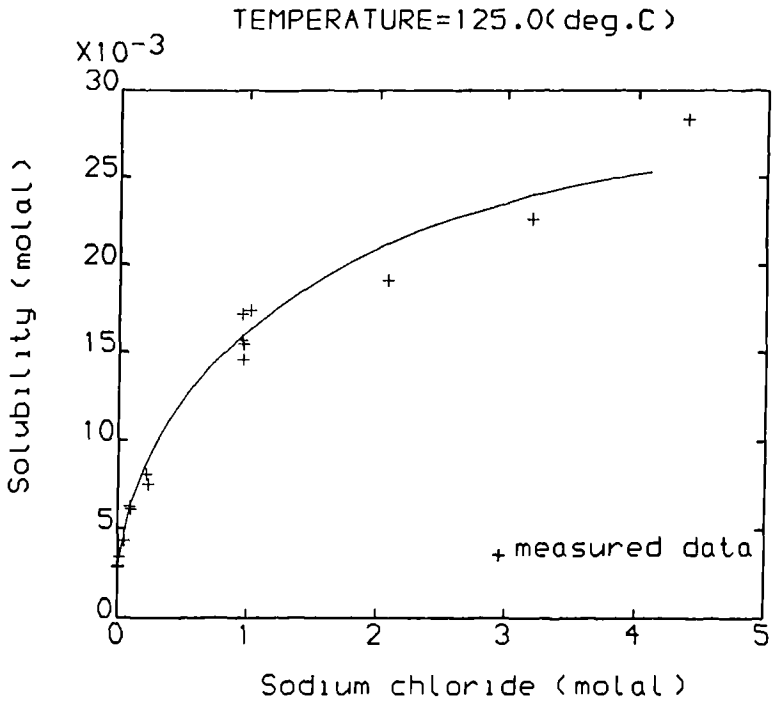

Figure 2.11 Predicted and measured anhydrite solubilities in sodium chloride solutions. Solubility data from references 9, 10, 11, 12, 30, 31, 36, 40, 45, 53, 54, 55, 70, 71, 72, 93, 107, 110, 124, 127, 134 and 159

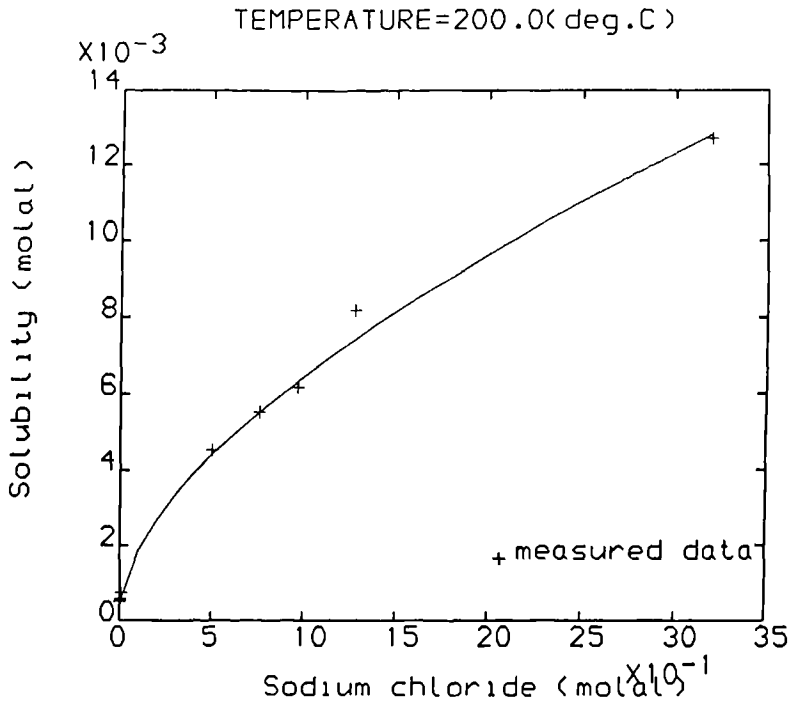

Figure 2.12 Predicted and measured anhydrite solubilities in sodium chloride solutions. Solubility data from references 9, 10, 111, 12, 30, 31, 36, 40, 45, 53, 54, 55, 70, 71, 72, 93, 107, 110, 124, 127, 134 and 159

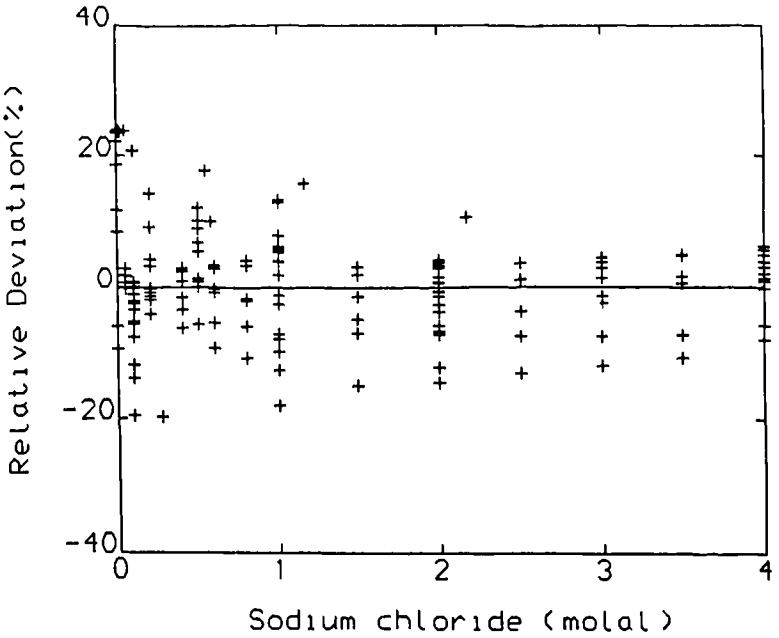

Figure 2.13 Relative deviations of barium sulphate solubility prediction in sodium chloride solutions. Solubility data from references 8, 14, 27, 43, 74, 112, 120, 135 and 142

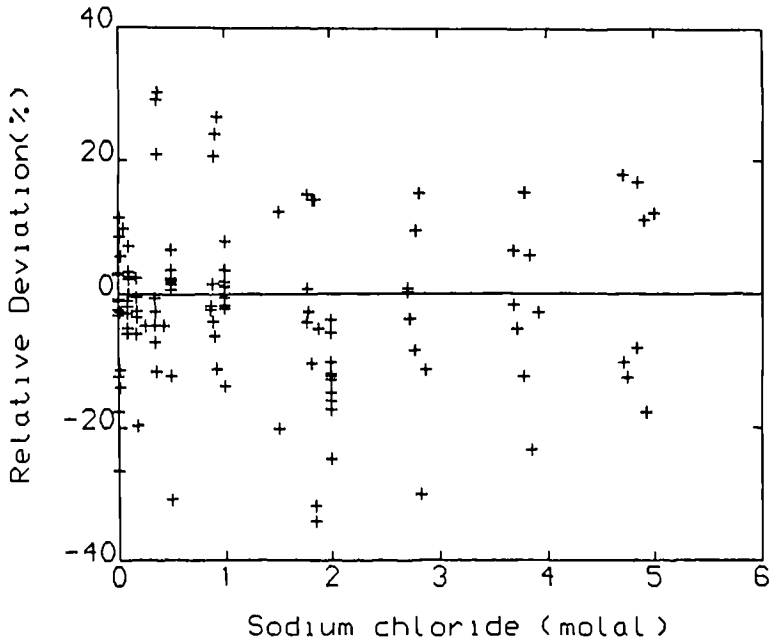

Figure 2.14 Relative deviations of strontium sulphate solubility prediction in sodium chloride solutions. Solubility data from references 27, 60, 61, 123, 124, 136 and 151

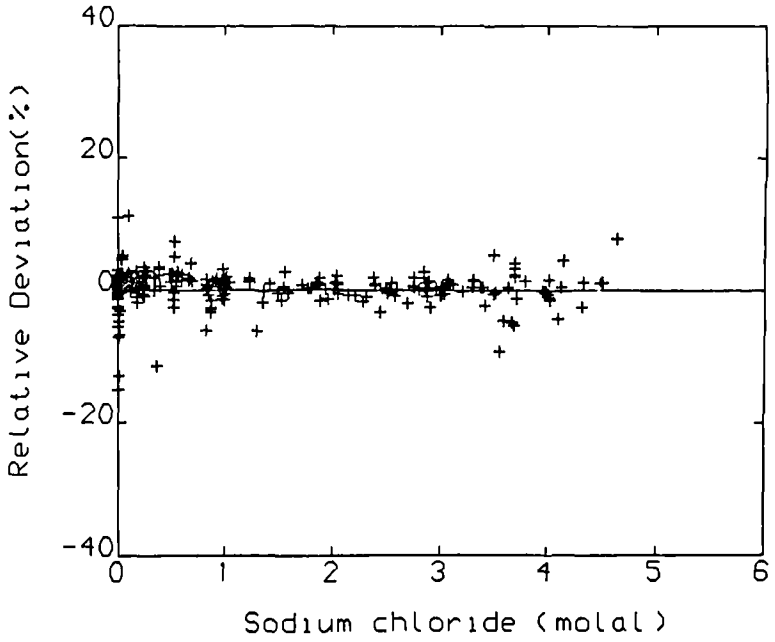

Figure 2.15 Relative deviations of gypsum solubility prediction in sodium chloride solutions. Solubility data from references 4, 9, 10, 11, 12, 19, 30, 40, 45, 53, 54, 55, 59, 70, 71, 72, 93, 107, 110, 124, 127, 128 and 160

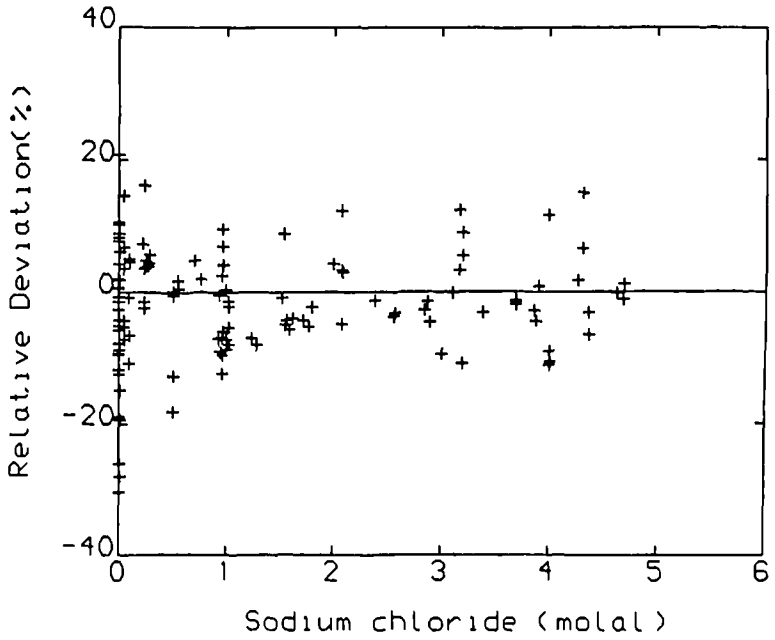

Figure 2.16 Relative deviations of anhydrite solubility prediction in sodium chloride solutions. Solubility data from references 9, 10, 11, 12, 30, 31, 36, 40, 45, 53, 54, 55, 70, 71, 72, 93, 107, 110, 124, 127, 128 and 159

The curves of the predicted sulphate solubilities versus NaCl solution concentrations with the measured data marked on the graphs are shown in figures (2.1) through (2.12). For each sulphate mineral, three graphs, indicating the quality of solubility prediction in NaCl solutions at low, medium and high temperatures, are presented. It can be seen from all the graphs that the predicted solubilities have good agreement with the published data. The deviations of the predicted from the measured solubilities are mainly caused by the discrepancy among the measured data themselves, as suggested in figures (2.4) and (2.11). Also the solubility prediction at lower temperatures are more reliable than that at higher temperatures owing to the availability of more abundant and reliable solubility data at lower temperatures. Figures (2.13) through (2.16) are the relative deviations of the predicted solubilities from those collected from literature at different temperatures. The relative deviations of $BaSO_4$ solubility prediction in NaCl solutions are within ±23% and most are not beyond ±10%. ±36% is the maximum deviation for $SrSO_4$ solubility prediction and most of the deviations are less than ±20%. Only three deviations for anhydrite solubility prediction are over 20% while mostly the deviations are not more than ±10% which are similar to the deviations for $BaSO_4$ solubility prediction in NaCl solutions. The best quality of solubility prediction in NaCl solutions is achieved for gypsum where all but a few predicted solubilities differ from the measured ones by less than ±5%. It becomes clear when looking at the graphs in figures from (2.13) to (2.16) that the large prediction deviations are always accompanied by poor solubility data, as suggested by the constrast in the prediction quality between the gypsum solubility prediction and $SrSO_4$ solubility prediction.

Solubility Prediction in the Aqueous Solutions Other than NaCl Solutions

As in the NaCl solutions, the predicted solubilities along with the measured data are plotted against the soluble salt concentrations. Figures (2.17) to (2.19) show the graphs of gypsum solubilities in aqueous $MgCl_2$ solutions at three different temperatures. Figures(2.20) through (2.22) show the gypsum solubilities in aqueous Na_2SO_4

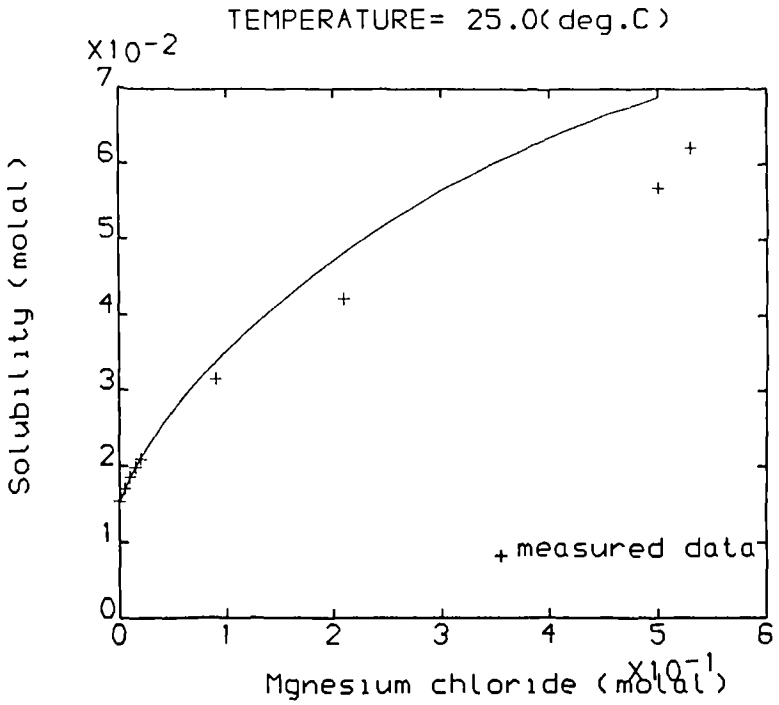

Figure 2.17 Predicted and measured gypsum solubilities in magnesium chloride solutions. Solubility data from references 36, 72, 91, 108, 124, 125 and 130

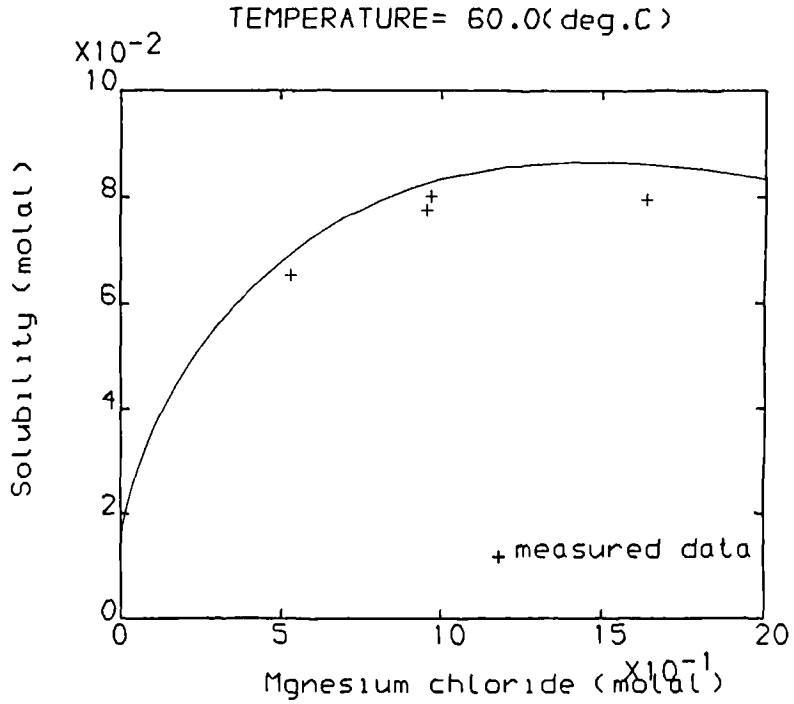

Figure 2.18 Predicted and measured gypsum solubilities in magnesium chloride solutions. Solubility data from references 36, 72, 91, 108, 124, 125 and 130

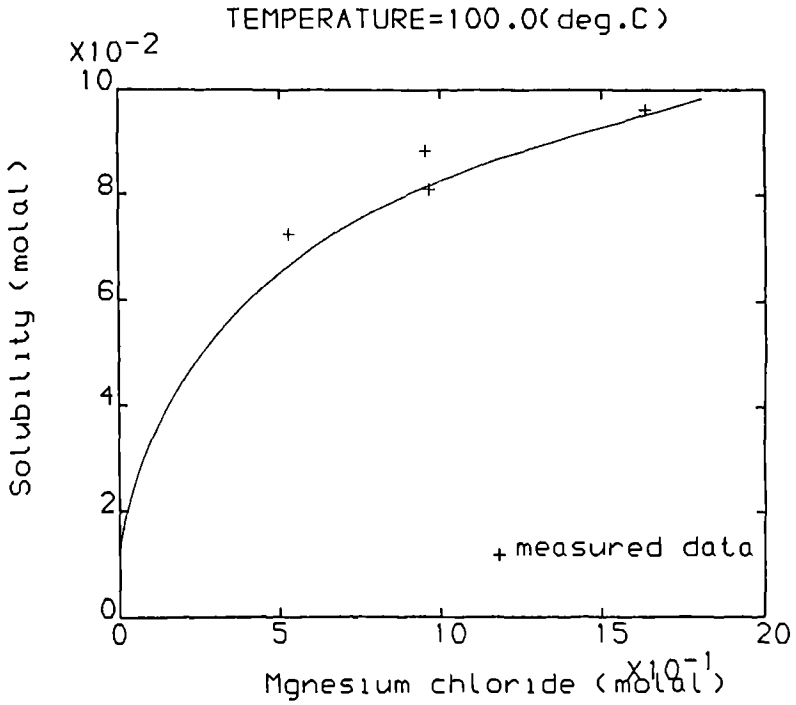

Figure 2.19 Predicted and measured gypsum solubilities in magnesium chloride solutions. Solubility data from references 36, 72, 91, 108, 124, 125 and 130

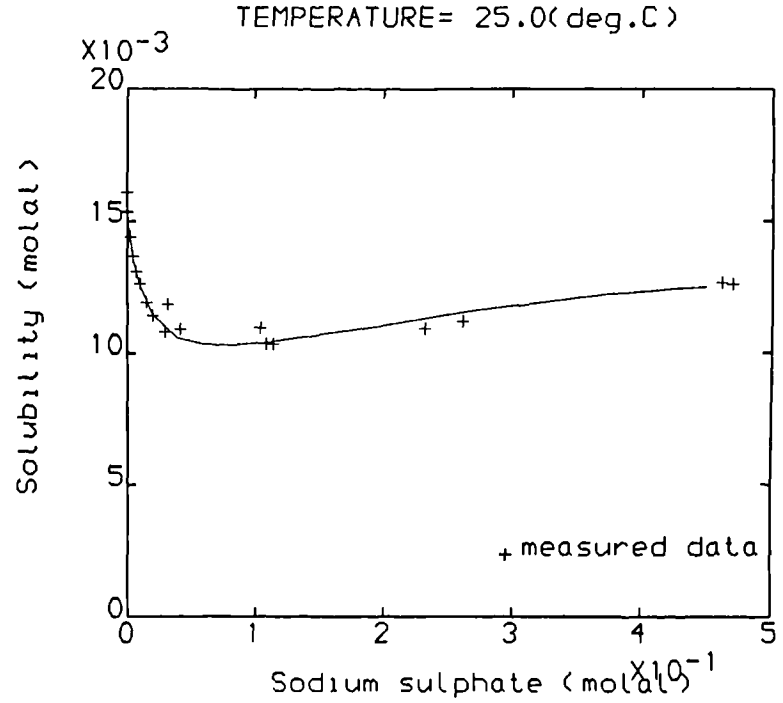

Figure 2.20 Predicted and measured gypsum solubilities in sodium sulphate solutions. Solubility data from references 6, 30, 55, 70, 130 and 160

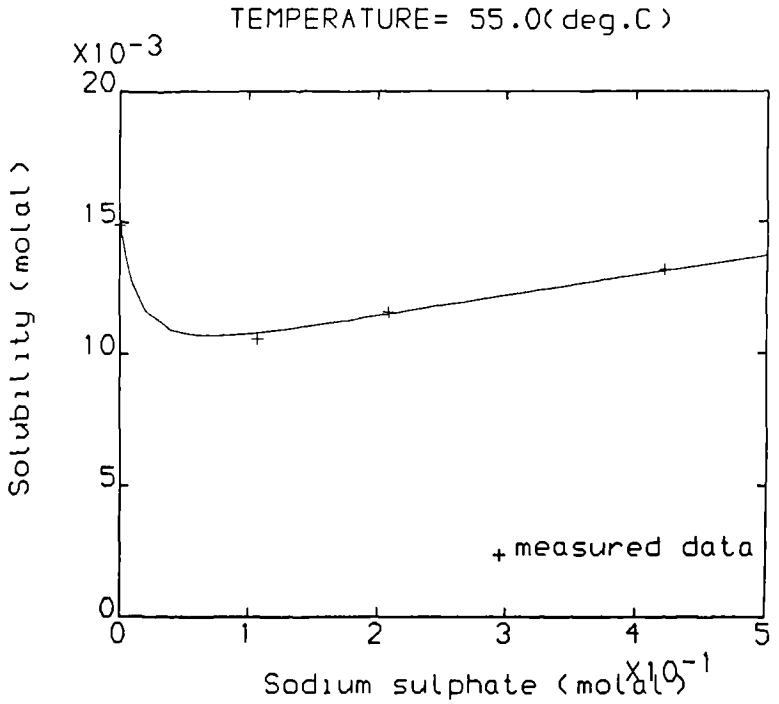

Figure 2.21 Predicted and measured gypsum solubilities in sodium sulphate solutions. Solubility data from references 6, 30, 55, 70, 130 and 160

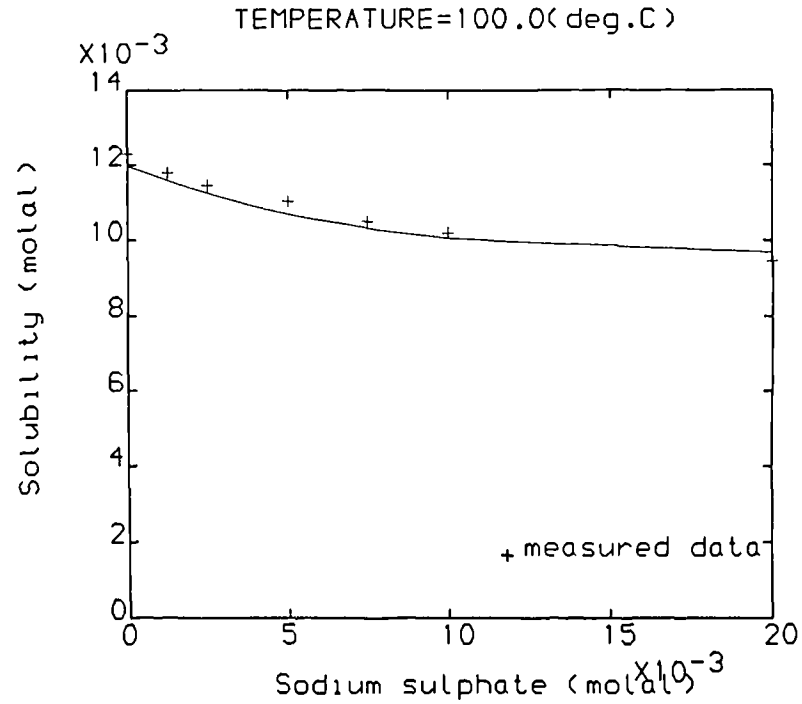

Figure 2.22 Predicted and measured gypsum solubilities in sodium sulphate solutions. Solubility data from references 6, 30, 55, 70, 130 and 160

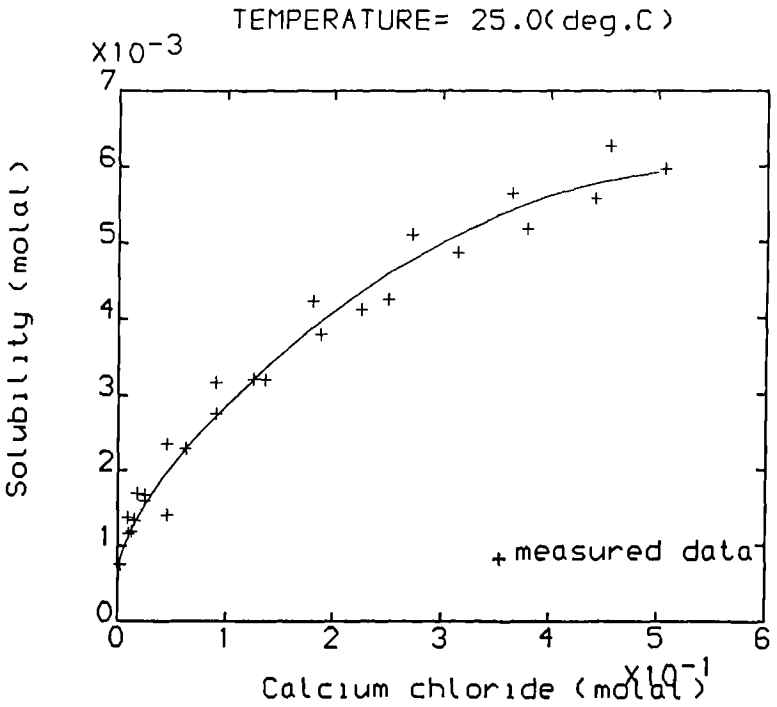

Figure 2.23 Predicted and measured strontium sulphate solubilities in calcium chloride solutions. Solubility data from references 27, 61 and 151

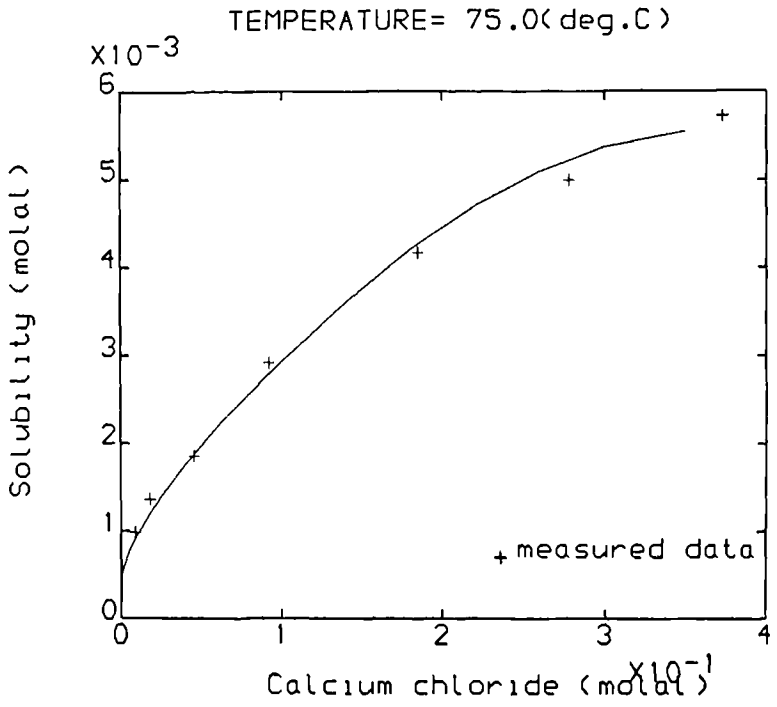

Figure 2.24 Predicted and measured strontium sulphate solubilities in calcium chloride solutions. Solubility data from references 27, 61 and 151

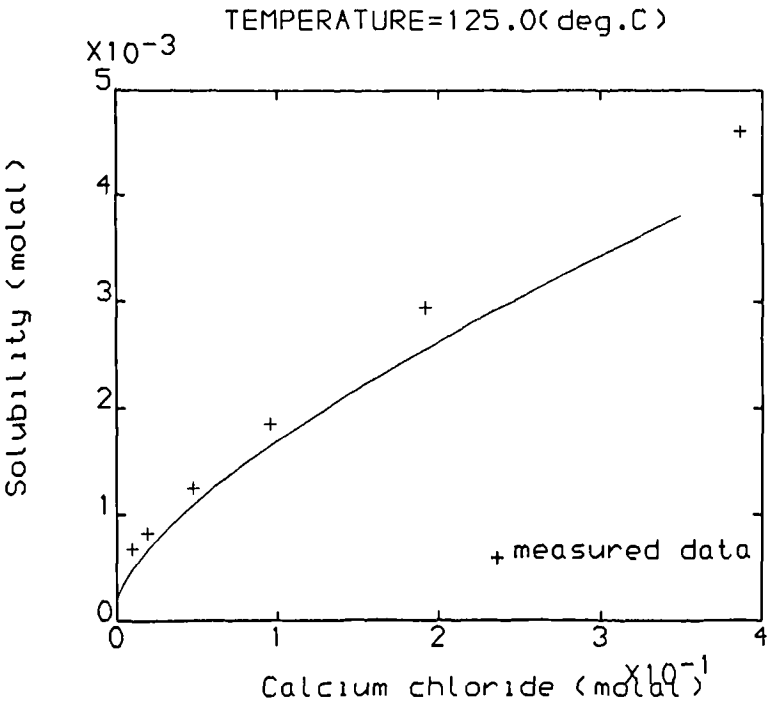

Figure 2.25 Predicted and measured strontium sulphate solubilities in calcium chloride solutions. Solubility data from references 27, 61 and 151

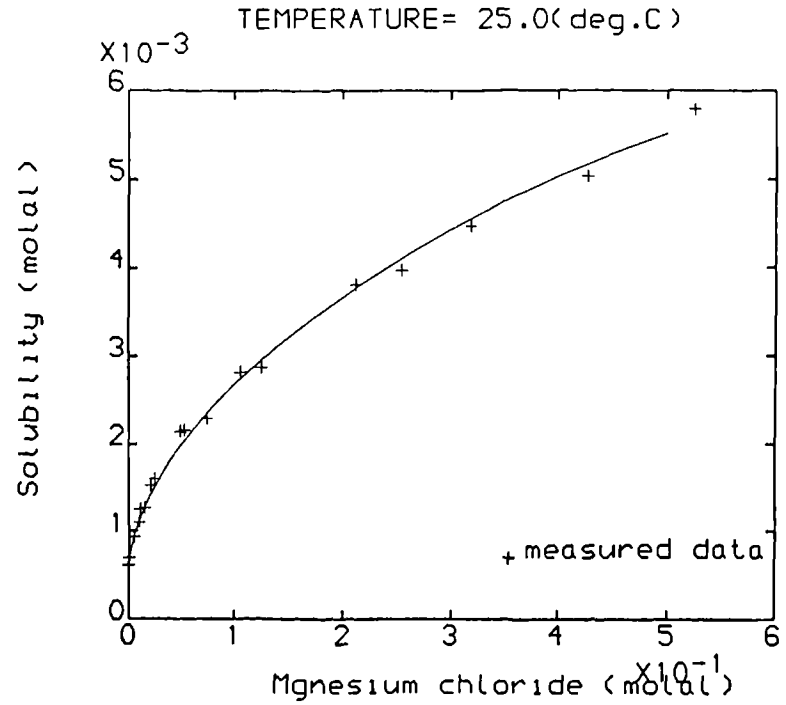

Figure 2.26 Predicted and measured strontium sulphate solubilities in magnesium chloride solutions. Solubility data from references 27 and 151

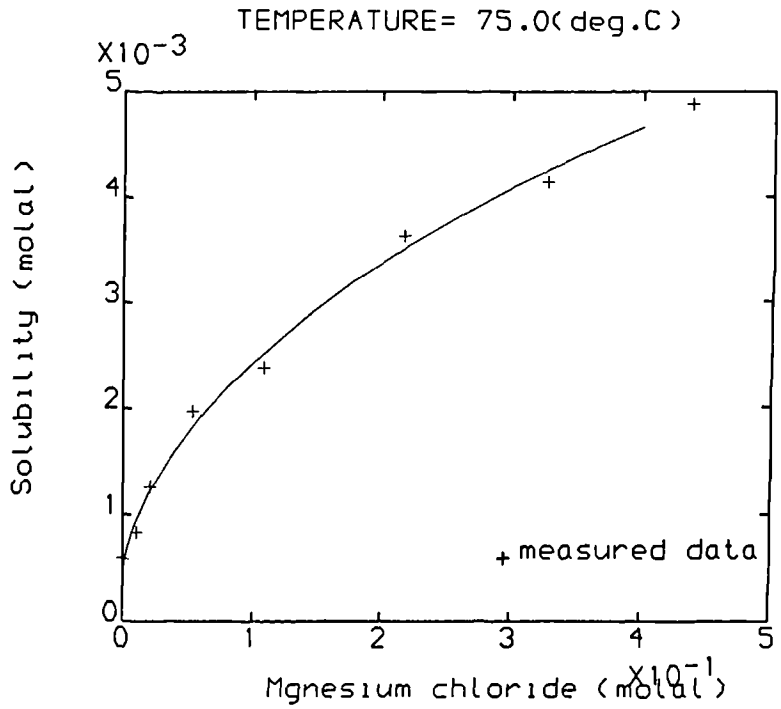

Figure 2.27 Predicted and measured strontium sulphate solubilities in magnesium chloride solutions. Solubility data from references 27 and 151

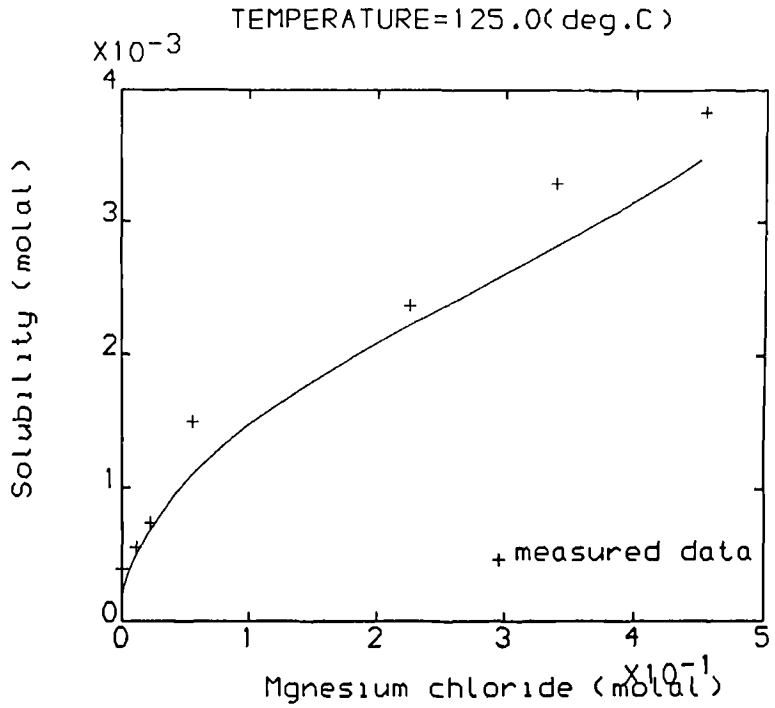

Figure 2.28 Predicted and measured strontium sulphate solubilities in magnesium chloride solutions. Solubility data from references 27 and 151

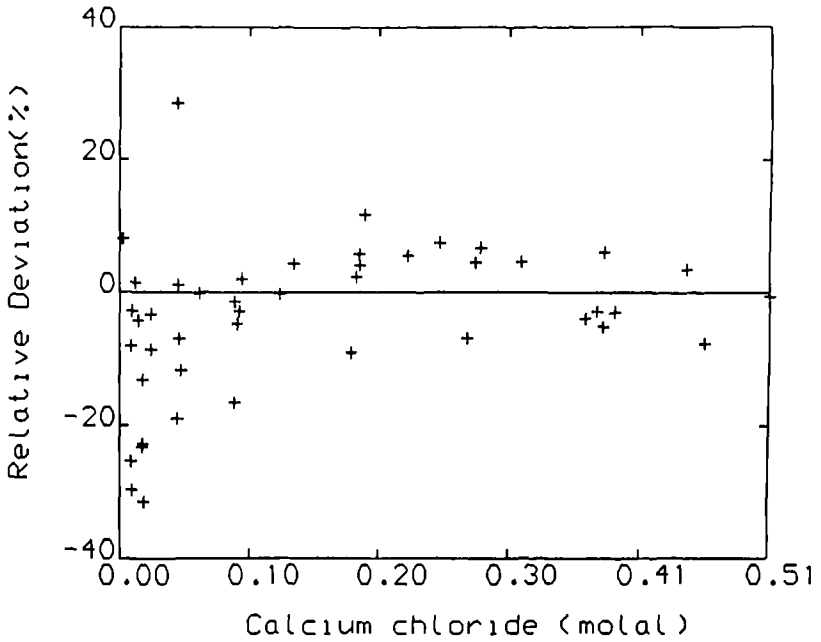

Figure 2.29 Relative deviations of strontium sulphate solubility prediction in calcium chloride solutions. Solubility data from references 27, 61 and 151

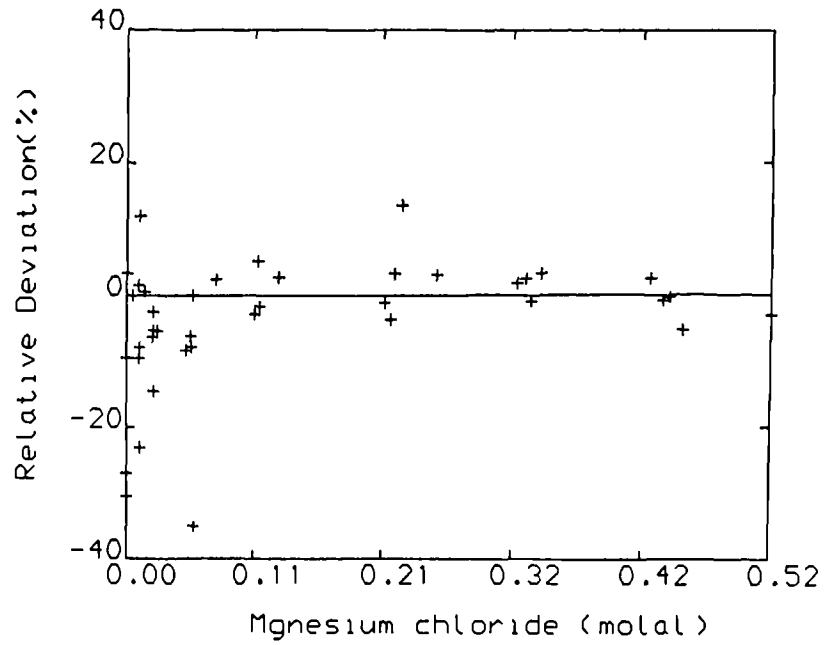

Figure 2.30 Relative deviations of strontium sulphate solubility prediction in magnesium chloride solutions. Solubility data from references 27 and 151

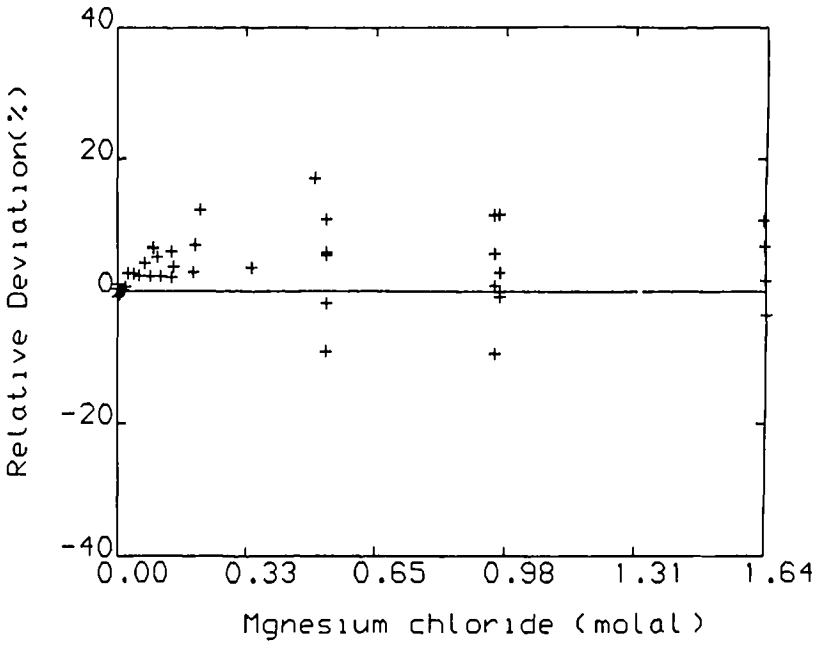

Figure 2.31 Relative deviations of gypsum solubility prediction in magnesium chloride solutions. Solubility data from references 36, 72, 91, 108, 124, 125 and 130

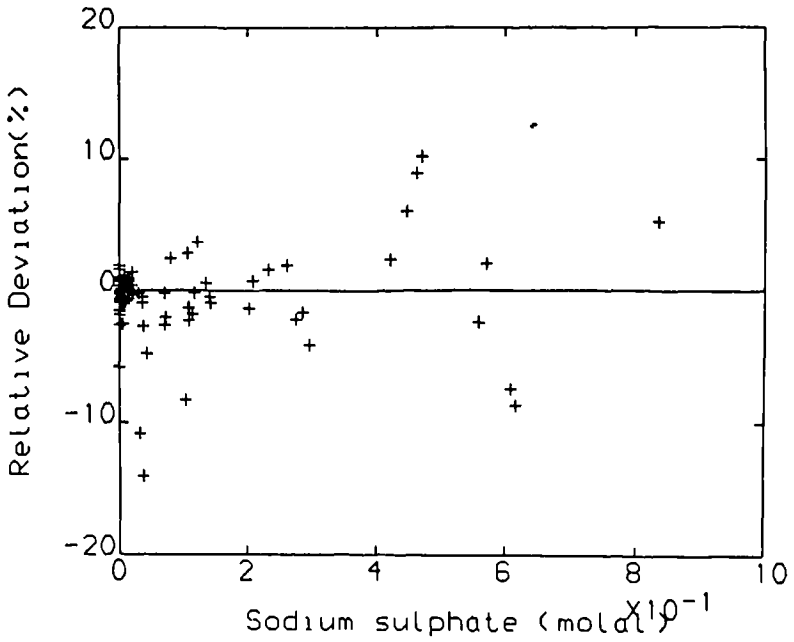

Figure 2.32 Relative deviations of gypsum solubility prediction in sodium sulphate solutions. Solubility data from references 6, 30, 55, 70, 130 and 160

solutions. The graphs of $SrSO_4$ solubilities in aqueous $CaCl_2$ solutions at three different tempratures are presented in figures (2.23) to (2.25) and those in aqueous $MgCl_2$ solutions are shown in figures (2.26) through (2.28). All the graphs indicate the general agreement of the predicted solubilities with the published data. The solubility curves in figures (2.20), (2.21) and (2.22) show the changing trend different from the curves in the other figures, which is because the SO_4^{2-} ions are in excess in the gypsum-Na_2SO_4 solutions compared to the precipitating cations Ca^{2+} and therefore the square root of their solubility product Q_{sp} is not the same as gypsum solubility in such solutions.

The relative solubility prediction deviations for gypsum and $SrSO_4$ in the above aqueous solutions are calculated and presented in figures (2.29) through (2.32), respectively. The deviations for gypsum in both $MgCl_2$ and Na_2SO_4 solutions are usually below ±10% while most of the prediction deviations for $SrSO_4$ in $CaCl_2$ and $MgCl_2$ solutions are less than ±20%.

2.10 PRESSURE EFFECT ON SULPHATE SOLUBILITY

The sulphate solubility prediction using Pitzer's ion interaction approach has proved successful in a wide range of solution ion composition and temperature from this study, as revealed in the section (2.9). Until now, the pressure effect on sulphate solubility has not be taken into account. The effect of pressure change on sulphate solubility is not as important as temperature change. But to apply the prediction model to oilfield operations, where the system pressure can be as high as 8000 psi (≈600 bars), the pressure effect on sulphate solubility must be taken into account. In theory, the Pitzer equation for electrolyte mean activity can reflect the pressure effect by correlating the virial coefficients in the equation with pressure, as treated for temperature effect.[99,100] Blount and Dickson, et al.[9,10] published their measured anhydrite solubility data in pure water and in NaCl solutions and gypsum solubility data in pure water at elevated pressures. High pressure gypsum solubility data in the other solutions than pure water

were unavailable except a scarce few data. The solubility data for $SrSO_4$ at elevated pressures were collected from two sources(Jacques&Bourland1983[60] and Schulien1987[123]). $BaSO_4$ solubilities at pressure rather than 1 bar were measured by Blount [8] and Schulien.[123] As a whole, the sulphate solubility data at elevated pressures, collected from the above sources, were sparse which makes the systematic correlations of sulphate thermodynamic solubility products and the virial coefficients with pressure using the Pitzer equation impractical. As an alternative, the pressure effect on solubility was not directly calculated from the Pitzer equation but a two step process was involved in calculating a sulphate solubility at an elevated pressure. First, the sulphate solubility was calculated using equation (2.23) assuming the pressure was ambient, then a correction was made to account for the difference in solubility at the given pressure from that at ambient pressure. There were two methods for correcting sulphate solubility due to pressure effect. One was a theoretical equation relating pressure to solubility through the volume change(ΔV) of a sulphate due to precipitation (Harned & Owen 1958)[49], as shown below,

$$\frac{\partial \ln Q}{\partial p} = -\frac{\Delta V}{RT} \qquad (2.52)$$

This equation was used by Pucknell[113] in his solubility prediction model. The difficulty with this method lies in that no accurate ΔV values were available for various solution compositions, temperatures and pressures. As a result, some empirical approaches had to be applied to determine ΔV values which were rather cumbersome and inaccurate. In Pucknell's model, the predicted solubilities using this equation were often different from the measured ones by over 25% which, in some cases, was larger than the deviation caused by pressure itself. Owing to the deficiencies with using equation (2.52), completely empirical equations were preferred in this study to reflect pressure effect on sulphate solubilities. In the proposed empirical pressure equations,

the ratio of the square root of the stoichiometric solubility product at a given pressure to that at the ambient pressure is expressed as the functions of pressure and solution ionic strength,

$$R_{BaSO4} = Exp\ ((A(p - p_r) + B(p^2 - p_r^2))\ Exp\ (C\ I^{1/2} + DI)) \quad (2.53)$$

$$R_{SrSO4} = Exp\ ((A(2.0 - T/298)(p - p_r) + B(p^2 - p_r^2))\ Exp\ (\ C\ I^{1/2} + DI)) \quad (2.54)$$

The pressure equation for anhydrite has the same formula as equation (2.53) and

$$R_{gypsum} = 1.0 + 0.69\ (R_{anhydrite} - 1.0) \quad (2.55)$$

$$R = Q_{sp}/Q_{sp,r} \quad (2.56)$$

where A, B, C and D are the pressure coefficients for each mineral, I is solution ionic strength, p and p_r refer to the elevated pressure and the reference pressure(the ambient pressure) in bars respectively, and T is temperature in Kelvin.

The reference pressure is 1 bar at temperature less than or equal to 100°C or it is equal to vapour pressure at temperature higher than 100°C. The vapour pressure of a solution at a given temperature is calculated using Pucknell's correlation[113],

$$p_r = Exp\ (\ -\ 17.0825 + 0.0613866T - 0.414799 \times 10^{-4} \times T^2\ ) \quad (2.57)$$

The pressure coefficients in equations (2.53) through (2.55) were then obtained from correlating the elevated pressure solubilities with pressure. It was assumed that in the pressure equations, apart from that for $SrSO_4$, the pressure effect on the solubility of a sulphate was the same at different temperatures, that is, the deviation of the solubility at an elevated pressure from that at ambient pressure was not affected by the solution temperature. This approximate treatment was a result of scarce solubility data at elevated

Table 2.5 Pressure Equations and Their Coefficients

Pressure equations:

R_{BaSO4}(or $R_{anhydrite}$) = $Exp((A(p - p_r) + B(p^2 - p_r^2))\ Exp(CI^{1/2} + DI))$

$R_{SrSO4} = Exp((A(2.0-T/298)(p - p_r) + B(p^2 - p_r^2))\ Exp(C\ I^{1/2} + DI))$

$R_{gypsum} = 1.0 + 0.69\ (R_{anhydrite} - 1.0)$

$Q_{sp}/Q_{sp,r} = R$

where Q_{sp} and $Q_{sp,r}$ are the square root of stoichiometric solubility products at pressure p and reference pressure p_r in bars, respectively. T is temperature in Kelvin and I is ionic strength in molal.

The maximum pressures and solution ionic strengths and pressure coefficients:

Sulphate	max p(bars)	max I(m)	A	B	C	D
$BaSO_4$	500	6.0	0.82E-3	0.27E-6	-.5468	0.1022
$SrSO_4$	414	2.0	0.18E-2	-.17E-5	0.10	-.40
$CaSO_4$	500	6.0	.50E-3	0.12E-5	-.988	0.229

Table 2.6 Relative Standard Deviations of Predicted Solubilities from Measured Solubilities at Elevated Pressures

Sulphate	$BaSO_4$	$SrSO_4$	Anhydrite	Gypsum
S.D% without pressure correction	35.84	15.31	39.10	52.62
S.D% after pressure correction	21.30	11.52	4.27	1.89

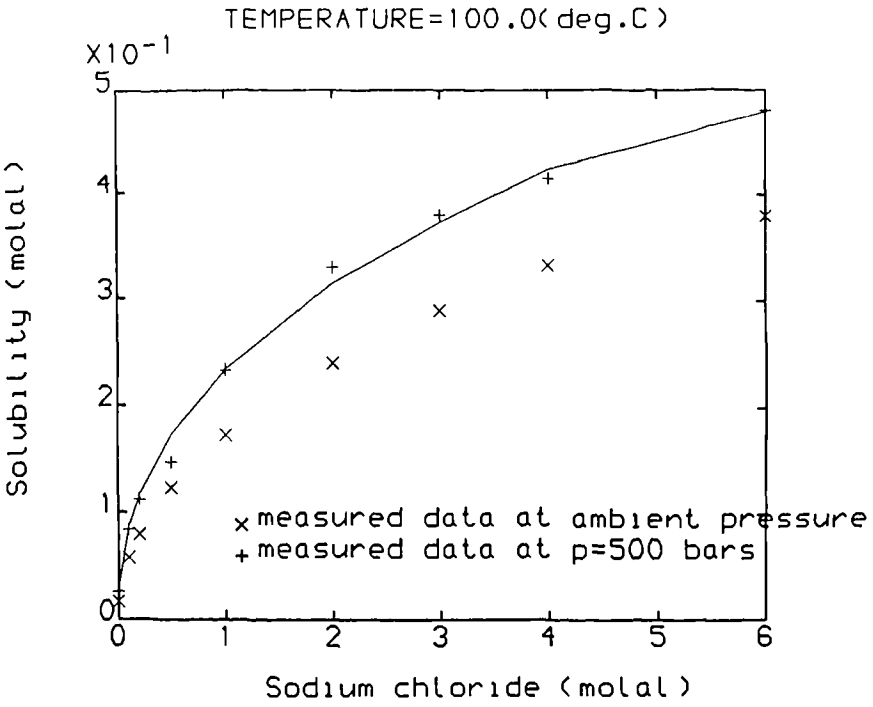

Figure 2.33 Predicted and measured barium sulphate solubilities in sodium chloride solutions at elevated pressure. Solubility data from reference 8

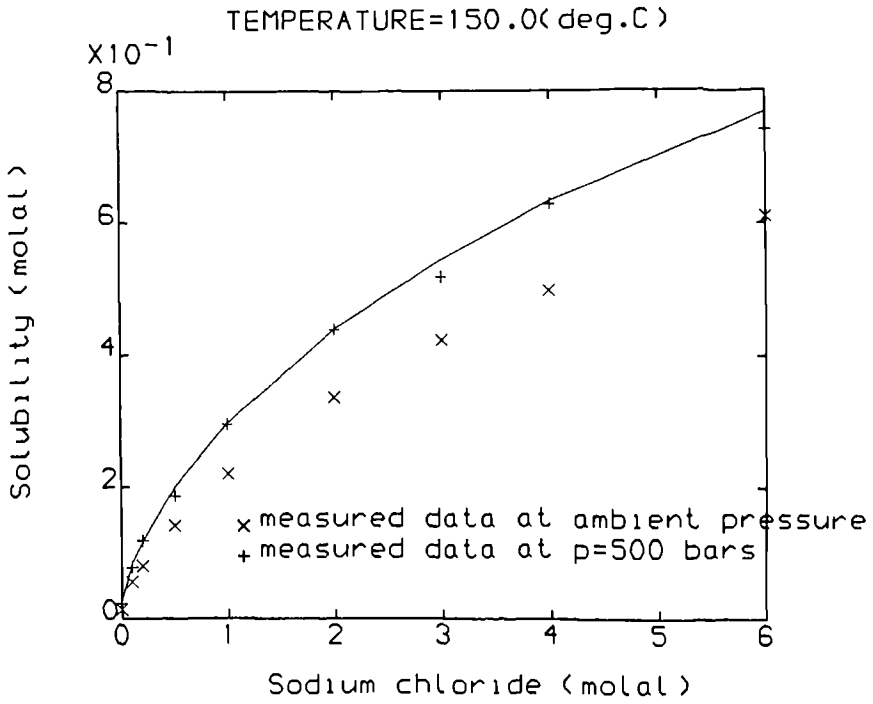

Figure 2.34 Predicted and measured barium sulphate solubilities in sodium chloride solutions at elevated pressure. Solubility data from reference 8

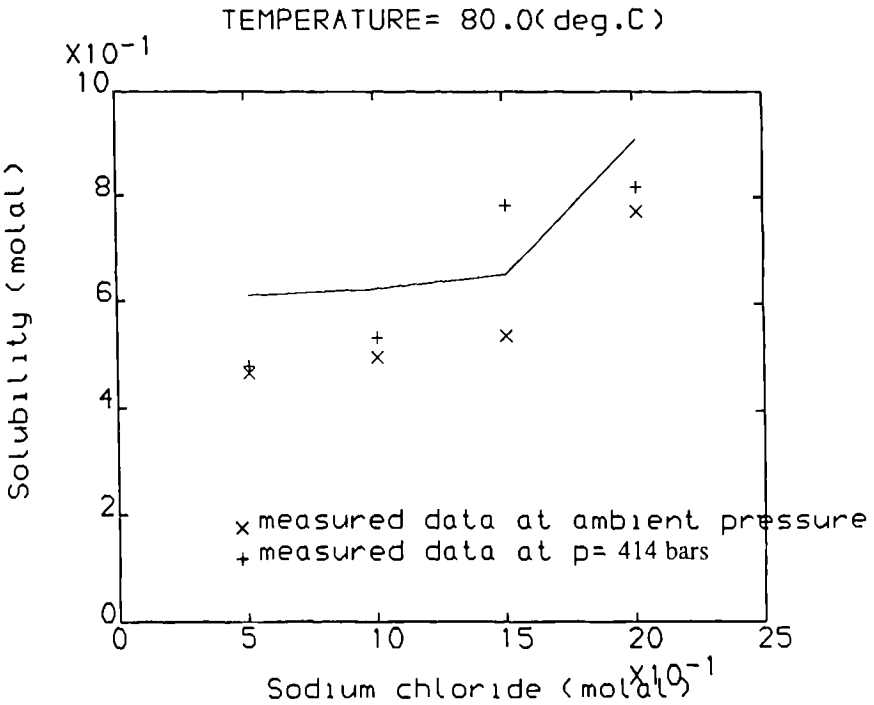

Figure 2.35 Predicted and measured strontium sulphate solubilities in sodium chloride solutions at elevated pressure. Solubility data from reference 123

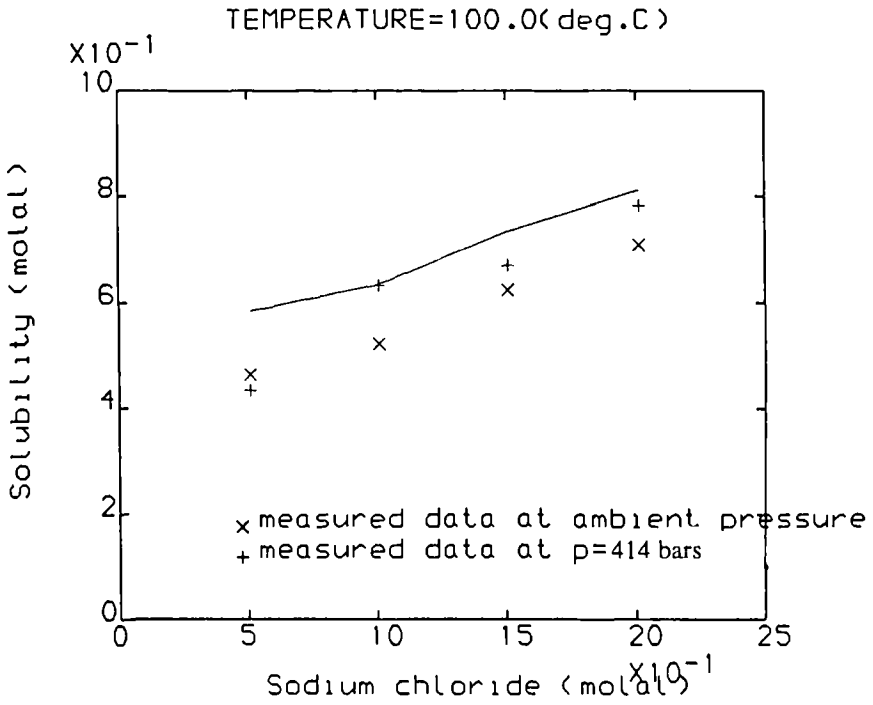

Figure 2.36 Predicted and measured strontium sulphate solubilities in sodium chloride solutions at elevated pressure. Solubility data from reference 123

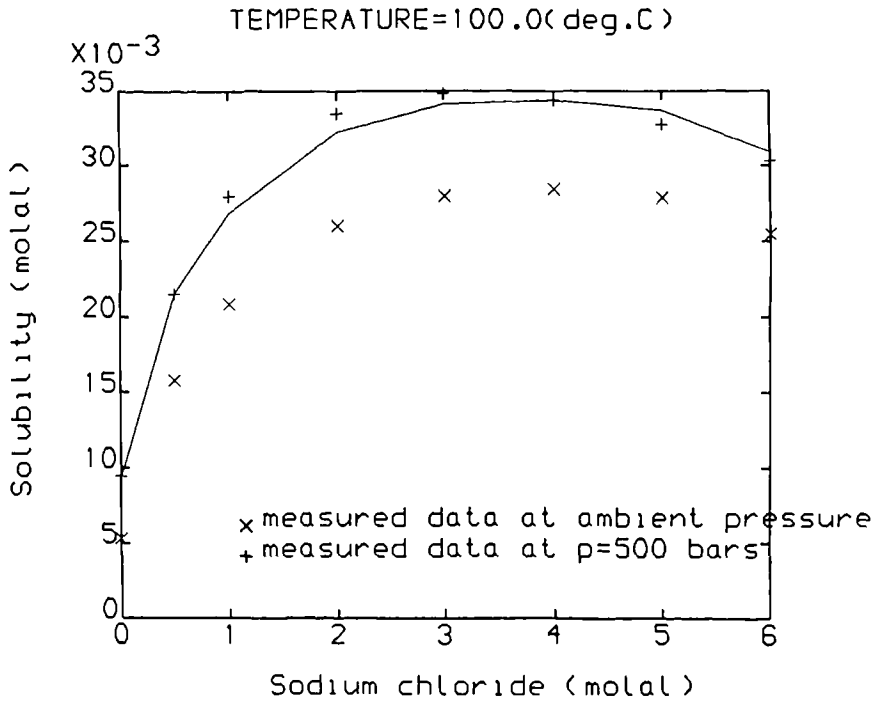

Figure 2.37 Predicted and measured anhydrite solubilities in sodium chloride solutions at elevated pressure. Solubility data from references 9 and 10

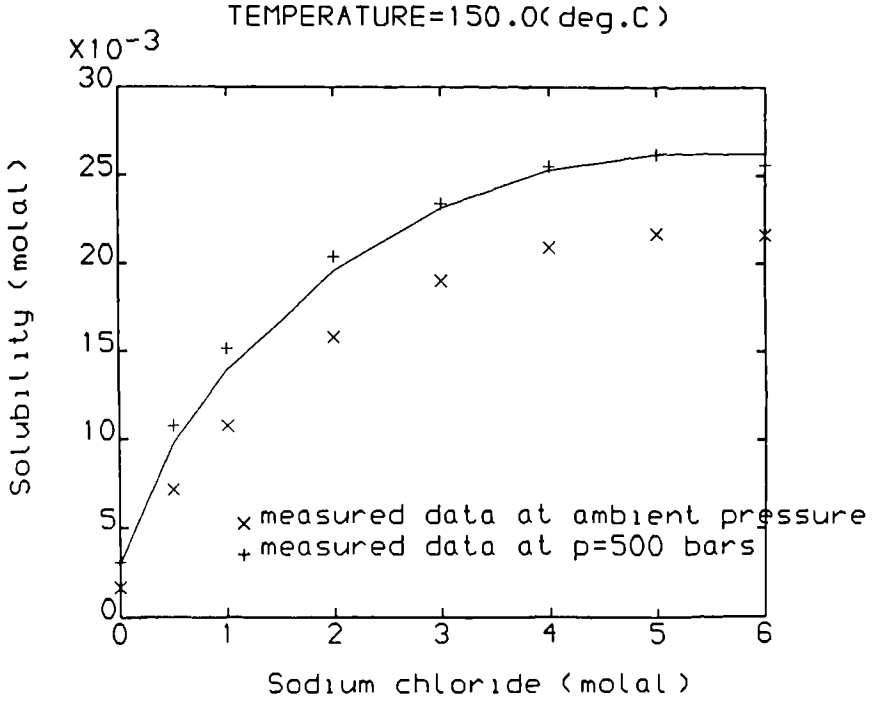

Figure 2.38 Predicted and measured anhydrite solubilities in sodium chloride solutions at elevated pressure. Solubility data from references 9 and 10

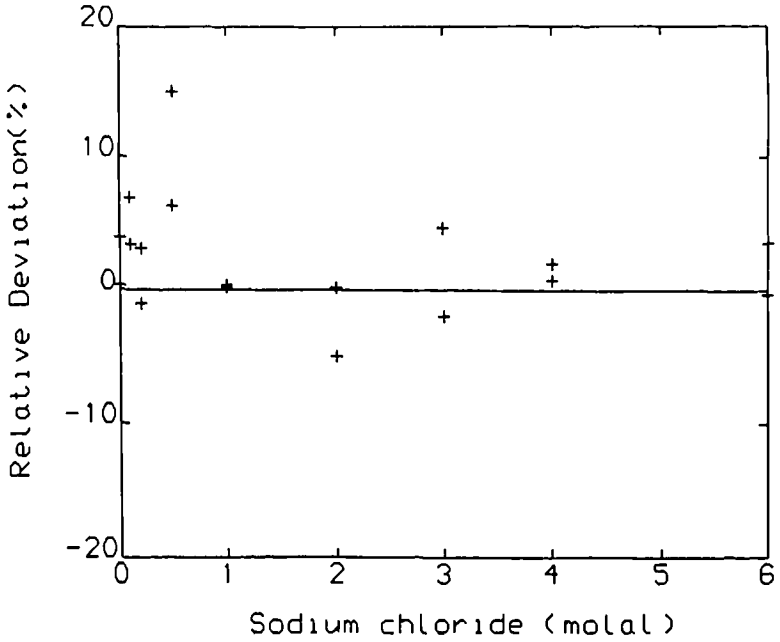

Figure 2.39 Relative deviations of barium sulphate solubility prediction in sodium chloride solutions at 500bars. Solubility data from reference 8

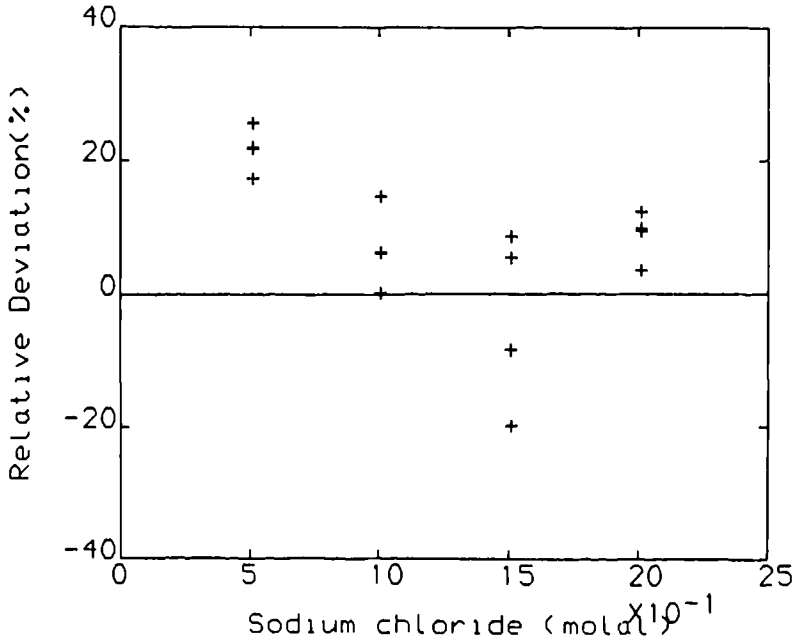

Figure 2.40 Relative deviations of strontium sulphate solubility prediction in sodium chloride solutions at 207 and 414 bars. Solubility data from references 60 and 123

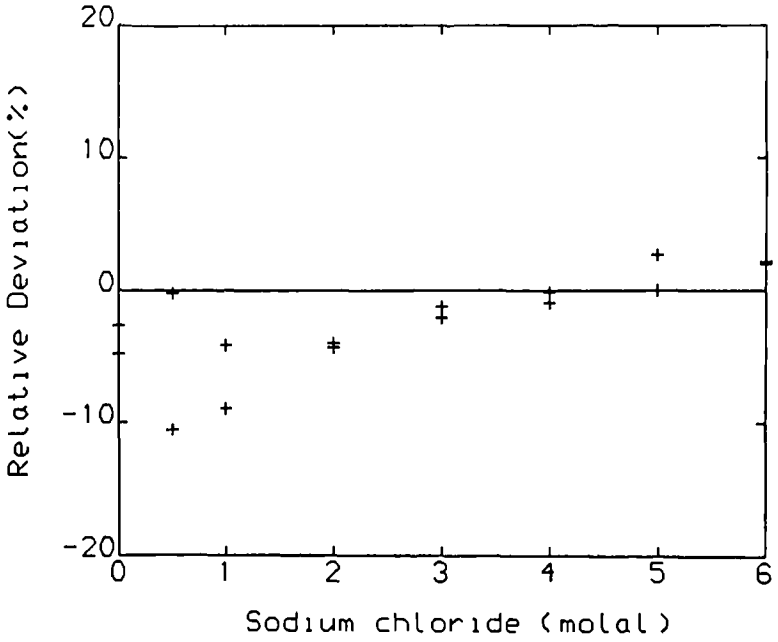

Figure 2.41 Relative deviations of anhydrite solubility prediction in sodium chloride solutions at 500bars. Solubility data from references 9 and 10

pressures and it has proved reasonably accurate. The pressure equation obtained from anhydrite solubility correlation was also used for calculating gypsum solubility at elevated pressures as shown in equation (2.55) because the gypsum solubility at elevated pressures were found only in pure water. To account for the difference in pressure effect on solubility between anhydrite and gypsum, a correction factor was added to the anhydrite pressure equation when it was used for gypsum high pressure solubility calculation, devised from comparing the pressure effect on gypsum solubilities in pure water to that on anhydrite solubilities in pure water. The proposed empirical pressure equations for the sulphates are shown in table (2.5) together with the coefficients in the equations, also the ranges of pressure and solution ionic strength in which the equations are valid are given in the table. The deviations of the calculated solubilities using the empirical equations from the published data are given in table (2.6). The predicted sulphate solubilities at elevated pressures togther with the measured data both at reference pressures and at the elevated pressures are shown in figures (2.33) through (2.38). The relative deviations of predicted solubilities at elevated pressures from those measured for $BaSO_4$, $SrSO_4$ and gypsum as functions of NaCl concentration are presented in figures (2.39) through (2.41).

2.11 THE SULPHATE SOLUBILITY PREDICTION MODEL

In sections (2.6) and (2.7), the process involved in developing a Pitzer's ion interaction approached based method for predicting sulphate solubilities at various temperatures and solution ion compositions was described. The effect of pressure change on sulphate solubilities was accounted for in section (2.10). The quality of the solubility prediction method developed from this study was also analysed in sections (2.9) and (2.10). As a whole, this method can fulfil the purpose of predicting sulphate solubilities covering oilfield brines and conditions and it can be used in the sulphate scaling tendency prediction model.

Based on equation (2.23) and equations (2.53) through (2.56), a computer model was constructed for sulphate solubility prediction which can calculate the solubility,

Table 2.7 The Ranges of Ion Concentrations, Temperature and Pressure That the Solubility and Scale Models are Applicable

t = 25 - 120°C (20-150°C) p = 1 - 500 bars

Specific ion concentrations (molal)

Na^+	4.0 (6.0)	K^+	Assumed as equivalent Na^+
Mg^{2+}	0.2 (0.5)	Fe^{3+}	Assumed as equivalent Na^+
Ca^{2+}	0.2 (0.5)	HCO_3^-	Assumed as equivalent Cl^-
Cl^-	4.0 (6.0)	CO_3^{2-}	Assumed as equivalent Cl^-
SO_4^{2-}	0.1 (0.2)		

* The figures in the brackets are the conditions under which the models can be used but the reliability is not guaranteed.

square root of solubility product of a sulphate at given solution concentration, temperature and pressure. The prediction model comprises three subprograms, each performs the solubility calculation for $BaSO_4$, $SrSO_4$ and $CaSO_4$(gypsum and anhydrite), respectively. The three subprograms are also incorporated into the scaling tendency prediction model and make the solubility calculations when they are called by the main programme.

Table (2.7) lists the specific ions whose effects on sulphate solubility are reflected, the valid ranges of the ion concentrations, and valid temperature and pressure ranges in the solubility prediction model and in the subsequently constructed scale prediction model. The other unlisted ions, i.e, K^+, Fe^{3+}, HCO_3^- and CO_3^{2-} are treated as Na^+(for cations) or Cl^-(for anions), that is, their concentrations in a solution are converted to equivalent Na^+ or Cl^- molality in the sulphate solubility prediction. The reason for such an approximate treatment was due to the lack of solubility data in the existence of such specific ions for parameterizing the virial coefficients for these ions, also they are minor or trace components in sea water or formation waters and the difference caused by their existence to sulphate solubilities from sodium chloride is very small at very low concentration. This approximation was accepted because it gives reasonably good results by taking the major ions effects into account. For $BaSO_4$ solubility prediction, due to even scarce data, its impossible to make reliable solubility correlations to take the specific ion effects into account (it was found that the use of the coefficients determined from solubility correlations using a few unreliable data may cause even larger error in calculating $BaSO_4$ solubility than ignoring the specific effects at all.). As a result, all other complicated salts in the brines are treated as equivalent NaCl in prediction of $BaSO_4$ solubility and scaling tendency in the solubility model and the scale prediction model. This approximation would not cause significant deviation because of NaCl dominance in sea water and formation waters.

To refresh the memory of the development of this solubility prediction model, the flow chart in figure (2.42) summarises the process involved in the solubility model development, as described in the previous sections.

2.12 COMMENTS ON THE SULPHATE SOLUBILITY PREDICTION

A sulphate solubility prediction model has been developed to be used as the centrepiece of the scaling tendency prediction model constructed in this study. Generally, the requirements preset for such a solubility prediction model have also been achieved. On the other hand, due to various problems associated with the model development, the current prediction model has some approximations in calculating the sulphate solubilities, as described in the last section and section (2.7). If those mentioned difficulties encountered in the construction of the model can be solved, it is certain that improvement can be made on the present solubility model to increase its accuracy and widen its applicability. In fact, all the difficulties were caused by one or other problem with the data sources. The $BaSO_4$ solubility data shortage constrains the model to neglect the effects of specific ions on its solubility. Similarly, the specific effects of some minor ions such as K^+ and HCO_3^- on $CaSO_4$ and $SrSO_4$ are also uncounted. The large discrepancies among $SrSO_4$ solubility data resulted in some uncertainty in its solubility prediction. The scarce solubility data at elevated pressures made it impossible to base the prediction model entirely on the Pitzer's approach. The other problem arises when both $BaSO_4$ and $SrSO_4$ are present in a aqueous solution and tend to co-precipitate and form so called barium and strontium sulphate solid solution. A few papers[8,17,41] have studied the $(Ba,Sr)SO_4$ solid solution and concluded that the solubility of both $BaSO_4$ and $SrSO_4$ solubilities in the solid solution would be different from the solubilities they have in their pure precipitates. Again the lack of solubility data in the $(Ba,Sr)SO_4$ solutions prevented this model to take the effect of the solid solution on the $BaSO_4$ and $SrSO_4$ solubilities into account.

CHAPTER 3

DEVELOPMENT OF A SULPHATE SCALING TENDENCY PREDICTION MODEL. 2. AN INTERACTIVE MODEL

3.1 INTRODUCTION

In the last chapter, the development of a sulphate solubility prediction model for use in the scale prediction model was described and discussed. This chapter gives the description of how an interactive prediction model for sulphate scaling tendencies was constructed from the solubility prediction model. In particular, discussion is presented on the method used for predicting scale occurrence in the case of competitive simultaneous co-precipitation of more than one sulphate mineral. The predicted supersaturations and amounts of precipitation of the sulphates in the brines are compared to the results predicted by the previous models and compared with the field observations. The case studies of the sulphate scaling tendencies in the North Sea offshore field waters are also presented in the chapter.

The scaling tendency prediction for a brine essentially is to provide two pieces of information: the supersaturation(s) of the insoluble salt(s) and the amount(s) of precipitation of the salt(s) which may result from the supersaturated brine. In this model, the salts concerned with scale precipitation are sulphates, i.e, $BaSO_4$, $SrSO_4$ and $CaSO_4$(gypsum and anhydrite). The scale precipitation in a single brine may take place if excessive scaling cations and anions are present in the solution or it may result from changes in temperature and pressure. The other cause of sulphate scale occurrence is due to mixing chemically incompatible brines. These scaling causes are considered in this model. It is rather easy to predict the scaling tendency in a brine in presence of only one of the sulphates, using the solubility prediction model with a simple iteration to calculate the concentrations of the scaling ions at equilibrium. On the other hand, if the different sulphates prone of scale coexist in the same brine, the prediction problem becomes

complicated because the scaling anions SO_4^{2-} are the common ions consumed by all the scaling cations Ba^{2+}, Ca^{2+},and Sr^{2+} in the co-precipitation of the sulphates. Vetter's model,[149] as discussed in the literature in chapter 2, only took the effect of precipitation of less soluble sulphates on the precipitation of more soluble sulphates into account while the reverse effect was neglected, which may result in large errors in scale prediction in the case that the cations of a more soluble sulphate, such as Ca^{2+} ions, are much more concentrated in the solution than the cations of a less soluble sulphate, such as Ba^{2+} or Sr^{2+} ions. Haarberg's equation(1988)[44], also described in the literature review in chapter 2 (equation(2.3)), looks simple but is complicated to solve because both the equilibrated SO_4^{2-} concentration and the sulphate stoichiometric solubility products are the unknown variables in the equation. Regarding the problems associated with Vetter's and Haarberg's methods, this study uses an iteration method to solve all the equilibria between the sulphate scaling ions in the solution and their solid precipitates by taking the sulphate supersaturations as the indicators of the equilibria.

In the next section, the basic concepts and chemical reactions involved in the sulphate scale precipitation - dissolution are introduced, followed by the description of the construction of the prediction model.

3.2 THE BASIC CONCEPTS

3.2.1 Supersaturation and Amount of Precipitation

Two terms are often used in the scale prediction model to indicate the sulphate scaling tendencies in the brines. One is the supersaturation(SP) of a sulphate in a brine and the other is the amount of precipitation of the sulphate from the brine(PP). Their definitions are given in equations(3.1) and (3.2),

$$SP_{MX} = \frac{(m_M \cdot m_X)^{1/2}}{Q_{sp,MX}} \qquad (3.1)$$

where SP_{MX} is the supersaturation of sulphate MX in the given brine at the conditions under consideration and $Q_{sp,MX}$ is the square root of the stoichiometric solubility product of the sulphate at equilibrium. m_M and m_X are the concentrations of the scaling cations Ca^{2+}, Ba^{2+} or Sr^{2+}, and scaling anions SO_4^{2-}, respectively. The subscript M refers to Ca^{2+}, Ba^{2+} or Sr^{2+} and X for SO_4^{2-}.

$$PP_{MX} = m_{M,i} - m_{M,e} \tag{3.2}$$

where PP_{MX} is the amount of precipitation of sulphate MX from an initially supersaturated aqueous solution when the precipitation - dissolution equilibrium has reached. $m_{M,i}$ and $m_{M,e}$ are the concentrations of the scaling cation M in the initial solution and in the equilibrated solution, respectively.

3.2.2 Scale Precipitation and Dissolution

When a sulphate mineral is supersaturated in a brine, that is, its SP > 1, then the sulphate will tend to precipitate out from the solution to form solid. On the other hand, if the sulphate is undersaturated in the solution (SP<1) and its solid is present in the solution, the solid will tend to dissolve into the solution. Eventually, a precipitation - dissolution equilibrium will reach between the sulphate ions in the solution and its solid precipitate, which can be shown in a precipitation - dissolution reaction,

$$M^{2+} + X^{2-} \underset{\text{Dissolving}}{\overset{\text{Precipitating}}{\rightleftharpoons}} MX\ (\text{solid}) \tag{3.3}$$

where M^{2+} stands for Ca^{2+}, Ba^{2+} or Sr^{2+} ions and X^{2-} for SO_4^{2-} ions. MX is the sulphate. Specific equations may be written for each sulphate precipitation - dissolution,

$$\underset{m_{Ba,i} - PP_{BaSO4}}{Ba^{2+}} + \underset{m_{SO4,i} - PP_{BaSO4}}{SO_4^{2-}} \rightleftharpoons \underset{PP_{BaSO4}}{BaSO_4\ (\text{solid})} \tag{3.4}$$

$$\underset{m_{sr,i} - PP_{SrSO4}}{Sr^{2+}} + \underset{m_{SO4,i} - PP_{SrSO4}}{SO_4^{2-}} \rightleftharpoons \underset{PP_{SrSO4}}{SrSO_4\,(solid)} \qquad (3.5)$$

$$\underset{m_{Ca,i} - PP_{CaSO4}}{Ca^{2+}} + \underset{m_{SO4,i} - PP_{CaSO4}}{SO_4^{2-}} \rightleftharpoons \underset{PP_{CaSO4}}{CaSO_4\,(solid)} \qquad (3.6)$$

The subscript i refers to the initial ion concentrations and PP is the amount of precipitation. If only one sulphate precipitation takes place in a solution, then the amount of the SO_4^{2-} ions precipitated from the solution equals that of the scaling cations and equals to the amount of scale precipitation, that is,

for $BaSO_4$ precipitation,

$$PP_{SO4} = PP_{Ba} = PP_{BaSO4} \qquad (3.7)$$

for $SrSO_4$ precipitation,

$$PP_{SO4} = PP_{Sr} = PP_{SrSO4} \qquad (3.8)$$

and, for $CaSO_4$ precipitation,

$$PP_{SO4} = PP_{Ca} = PP_{CaSO4} \qquad (3.9)$$

Otherwise, if all three sulphates have simultaneous co-precipitation in the solution, then the amount of the SO_4^{2-} ions precipitated from the solution is equal to the sum of the amounts of precipitation of the three different scaling cations or equal to the sum of the amounts of precipitation of three sulphate minerals,

$$PP_{SO4} = PP_{Ba} + PP_{Sr} + PP_{Ca} \quad (3.10)$$

or,

$$PP_{SO4} = PP_{BaSO4} + PP_{SrSO4} + PP_{CaSO4} \quad (3.11)$$

In the case of simultaneous co-precipitation of different sulphate minerals from an aqueous solution, the precipitation of one sulphate will shift the precipitation - dissolution equilibria of the other sulphates in the solution because the concentration of the common ions SO_4^{2-} in the solution is changing as the precipitation taking place. The precipitation - dissolution equilibrium of one sulphate in the solution can not be achieved unless the equilibria have also reached for the other two sulphates, or vice versa. Owing to the fact that the sulphate precipitations are related to each other, the effect of one sulphate precipitation on the others must be addressed in an accurate scaling prediction model.

The mathematical expressions for solving the sulphate precipitation - dissolution equilibrium in a brine in presence of one sulphate mineral and for solving the precipitation - dissolution equilibria in a brine in presence of more than one sulphate mineral are presented and discussed in the next section. By solving the equilibria, the equilibrated concentrations of the scaling ions in the brine are determined from which the sulphate supersaturations and amounts of precipitation are easily calculated.

3.3 THE ITERATIVE METHODS FOR SCALE PREDICTION

For predicting sulphate scaling tendencies in a brine of given ion composition at certain temperature and pressure, the key is to determine the concentrations of the scaling ions at equilibrium in the solution. This section describes the mathematical methods used in this model to perform such a task.

3.3.1 The Iteration for Single Sulphate Precipitation

First, consider the scale precipitation of only one sulphate mineral from a given brine. The initial solution composition is known as m_i, m_j, ..., $m_{M,i}$ and $m_{X,i}$, here m_i, m_j, ... refer to the initial concentrations of all the soluble ions and they will not change during the sulphate precipitation, and $m_{M,i}$ and $m_{X,i}$ are the initial concentrations of the scaling cation M(Ba^{2+}, Sr^{2+} or Ca^{2+}) and scaling anion X, i.e, SO_4^{2-} . The ratio of the square root of the ion product of M and X to the square root of the stoichiometric solubility product of MX in the initial solution can be calculated by,

$$r = \frac{(m_{M,i} \cdot m_{X,i})^{1/2}}{Q_{sp,MX,i}} \tag{3.12}$$

If r is less than or equal to 1, the brine is either undersaturated or saturated with sulphate MX, no precipitation will occur. In this case, the supersaturation of the sulphate is equal to r and the amount of MX precipitation is zero. On the other hand, the brine is supersaturated with sulphate MX and the sulphate will tend to form scale if r is larger than 1, finally the equilibrium will reach and the precipitation will cease. In this case, the sulphate supersaturation in the initial solution is not equal to r but given in equation (3.13),

$$SP_{MX} = \frac{(m_{M,i} \cdot m_{X,i})^{1/2}}{Q_{sp,MX,e}} \tag{3.13}$$

and the amount of sulphate precipitation at equilibrium is ,

$$PP_{MX} = m_{M,i} - m_{M,e} \tag{3.14}$$

where the subscripts i and e stand for the initial and the equilibrated states of a scaling brine, accordingly.

To determine SP_{MX} and PP_{MX}, both $Q_{sp,MX,e}$, the $Q_{sp,MX}$ at the equilibrium, and $m_{M,e}$, the equilibrated scaling cation concentration, have to be resolved. As known from

the development of the sulphate solubility prediction model in chapter 2, $Q_{sp,MX}$ is the function of the solution ionic strength and the concentrations of the ions present in the solution at a given temperature. During the precipitation of sulphate MX, the scaling ion concentrations m_M and m_X and the solution ionic strength are changing constantly, resulting in a change in $Q_{sp,MX}$. At the precipitation - dissolution equilibrium, the $Q_{sp,MX}$ becomes $Q_{sp,MX,e}$. $Q_{sp,MX,e}$ can be predicted from the solubility model if the equilibrated concentrations of M and X are known (the concentrations of the other ions are already known from the initial brine composition) or vice versa. They are related to each other by the following equation,

$$\frac{(m_{M,e} \cdot m_{X,e})^{1/2}}{Q_{sp,MX,e}} = 1 \qquad (3.15)$$

The above equation does not have analytical solution because both the numerator and the denominator are the unknown variables. An iteration is used with equation (3.15) to determine $Q_{sp,MX,e}$, $m_{M,e}$ and $m_{X,e}$,

$$R = \frac{(m_M \cdot m_X)^{1/2}}{Q_{sp,MX}} \qquad (3.16)$$

where R is an indicator of sulphate MX supersaturation change during the precipitation - dissolution process, m_M and m_X are the scaling ion concentrations during the precipitation.

At the beginning of the iteration, the initial ion concentrations of the sulphate are assumed in the sulphate solubility prediction model to give a $Q_{sp,MX}$ and R is calculated from the above equation. If R is less than or equal to 1, no further iteration is calculated. Otherwise, new m_M and m_X are calculated from their initial values and the last predicted $Q_{sp,MX}$ by the following equations,

since,

$$(m_M \cdot m_X)^{1/2} = Q_{sp,MX} \tag{3.17}$$

or,

$$(m_{M,i} - x) \cdot (m_{X,i} - x) = Q^2_{sp,MX} \tag{3.18}$$

by solving x in the above equation, thus,

$$m_M = m_{M,i} - x$$

$$m_X = m_{X,i} - x \tag{3.19}$$

By assigning the new m_M and m_X values in the solubility prediction model, a new $Q_{sp,MX}$ is predicted and a new R value calculated. Such iterative process continues until the calculated R converges to 1. At R = 1, the last predicted $Q_{sp,MX}$ is the square root of the sulphate solubility product $Q_{sp,MX,e}$ at equilibrium, and the last calculated m_M and m_X are the equilibrated concentrations of the sulphate ions, i.e, $m_{M,e}$ and $m_{X,e}$ respectively. From $Q_{sp,MX,e}$ and $m_{M,e}$ and $m_{X,e}$, the supersaturation and amount of precipitation of sulphate MX are simply calculated from equations (3.1) and (3.2).

3.3.2 Iteration for Simultaneous Coprecipitation of Sulphates

The iteration method for solving the simultaneous co-precipitation of different sulphates minerals in the solution is complicated by the interaction among the sulphate precipitations as discussed in section (3.2). The following iterative process is devised for reflect such interaction.

We assume the three sulphates, $BaSO_4$, $SrSO_4$, $CaSO_4$(gypsum or anhydrite) are co-present in an aqueous at given temperature and pressure (The calculation would be simpler but the iterative process is the same if only two of the three sulphate minerals are present in a solution). Like in the one sulphate solution, the initial concentrations of the

ions are given as m_i, m_j, ..., $m_{Ba,i}$, $m_{Ca,i}$, $m_{Sr,i}$ and $m_{SO4,i}$, here m_i and m_j refers to the concentrations of the soluble ions in the solution. The supersaturations and amounts of sulphate precipitation are expressed in equations (3.20) through (3.25), respectively,

For $BaSO_4$,

$$SP_{BaSO4} = \frac{(m_{Ba,i} \cdot m_{SO4,i})^{1/2}}{Q_{sp,BaSO4,e}} \tag{3.20}$$

$$PP_{BaSO4} = m_{Ba,i} - m_{Ba,e} \tag{3.21}$$

For $SrSO_4$,

$$SP_{SrSO4} = \frac{(m_{Sr,i} \cdot m_{SO4,i})^{1/2}}{Q_{sp,SrSO4,e}} \tag{3.22}$$

$$PP_{SrSO4} = m_{Sr,i} - m_{Sr,e} \tag{3.23}$$

and, for $CaSO_4$,

$$SP_{CaSO4} = \frac{(m_{Ca,i} \cdot m_{SO4,i})^{1/2}}{Q_{sp,CaSO4,e}} \tag{3.24}$$

$$PP_{CaSO4} = m_{Ca,i} - m_{Ca,e} \tag{3.25}$$

The amount of SO_4^{2-} precipitated,

$$PP_{SO4} = PP_{BaSO4} + PP_{SrSO4} + PP_{CaSO4} \tag{3.26}$$

The SO_4^{2-} ions remaining in the aqueous solution,

$$\begin{aligned} m_{SO4} &= m_{SO4,i} - PP_{SO4} \\ &= m_{SO4,i} - (PP_{BaSO4} + PP_{SrSO4} + PP_{CaSO4}) \end{aligned} \tag{3.27}$$

where the subscripts i and e refer to the initial and the equilibrium state of the brine, respectively. Like the precipitation of single sulphate mineral in the brine, the equilibrated concentrations of the scaling cations and SO_4^{2-} ions must be determined at first in order to calculate SP and PP for the sulphates. In the simultaneous co-precipitation, the concentration of SO_4^{2-} ions in the brine is not only related to one sulphate precipitation but all the three. In the following, the iterative process is presented for determining the Q_{sp} of the three sulphates and SO_4^{2-} concentration at precipitation - dissolution equilibria.

First, the ratio of the square root of ion product for each sulphate to the corresponding square root of the sulphate solubility product during the precipitation - dissolution is given here,

$$R_{BaSO4} = \frac{(m_{Ba} \cdot m_{SO4})^{1/2}}{Q_{sp,\,BaSO4}} \tag{3.28}$$

$$R_{SrSO4} = \frac{(m_{Sr} \cdot m_{SO4})^{1/2}}{Q_{sp,\,SrSO4}} \tag{3.29}$$

$$R_{CaSO4} = \frac{(m_{Ca} \cdot m_{SO4})^{1/2}}{Q_{sp,\,CaSO4}} \tag{3.30}$$

Again, R reflects a sulphate mineral supersaturation during the precipitation - dissolution process. For an initially supersaturated sulphate mineral, the R at equilibrium should be a constant of 1 and the R will be a constant less than 1 if a sulphate is initially (and always) undersaturated. In the iteration, therefore, the R values for the sulphates are used as the indicators of the precipitation - dissolution equilibria. For every iteration, the calculation starts from the most insoluble $BaSO_4$ and ends at the most soluble $CaSO_4$.

At the beginning of the iteration, the initial concentrations of Ba^{2+} and SO_4^{2-} are assigned in the sulphate solubility prediction model with the concentrations of the other

ions to predict a $Q_{sp,BaSO4}$, the Ba^{2+} and SO_4^{2-} concentrations and the predicted $Q_{sp,BaSO4}$ are then substituted into equation (3.28) to calculate R_{BaSO4}. If the calculated R_{BaSO4} is less than 1 then $BaSO_4$ is undersaturated and the Ba^{2+} and SO_4^{2-} concentrations are not changed after this round of calculation, otherwise, the $BaSO_4$ precipitation and the new concentrations for Ba^{2+} and SO_4^{2-} ions are calculated from the their initial concentrations and the predicted $Q_{sp,BaSO4}$. After $BaSO_4$ calculation, the newly determined Ba^{2+} and SO_4^{2-} ion concentrations together with the initial concentrations of other ions are input into the sulphate solubility prediction model to predict $SrSO_4$'s Q_{sp} and R_{SrSO4} is calculated from equation (3.29). If the R_{SrSO4} is larger than 1, then SrSO4 precipitation is taking place and the Sr^{2+} and SO_4^{2-} ion concentrations are recalculated from the predicted $Q_{sp,SrSO4}$ after the precipitation. The predicted Ba^{2+}, Sr^{2+} and SO_4^{2-} ion concentrations are used in the subsequent calculation for $CaSO_4$ precipitation and new Ca^{2+} and SO_4^{2-} concentrations after the precipitation are calculated. Because of the possible precipitation of $SrSO_4$ and $CaSO_4$ after $BaSO_4$ precipitation calculation, the SO_4^{2-} ion concentration may be reduced, resulting in the precipitation - dissolution equilibrium of $BaSO_4$ towards dissolution, thus another iteration must be carried out to calculate $BaSO_4$ supersaturation and to compare it with the last calculated value. The concentrations of SO_4^{2-}, Ba^{2+}, Sr^{2+} and Ca^{2+} ions resulting from the calculations for $BaSO_4$ and $SrSO_4$ and $CaSO_4$ precipitations in the last iteration are substituted into the the sulphate solubility prediction model, while the concentrations of the other soluble ions remaining unchanged, to result in a new $Q_{sp,BaSO4}$ and R_{BaSO4} is again calculated from equation (3.28). If the new R_{BaSO4} is different from the last calculated value then from the newly predicted $Q_{sp,BaSO4}$, the Ba^{2+} and SO_4^{2-} ion concentrations in the solution are adjusted from the previous values and the amount of $BaSO_4$ precipitation recalculated. Similarly, the iteration proceeds to

calculate $SrSO_4$ and $CaSO_4$ precipitations consecutively, reflecting the change in the concentrations of Ba^{2+} and SO_4^{2-} ions in the brine. The scaling ion concentrations and amounts of precipitation are readjusted after each calculation. The iterative process continues until the supersaturations of all the three sulphates calculated from the present round of iteration are the same as those produced from the last iteration. At the end of the iterative process, the precipitation - dissolution equilibria for all the sulphates have been established and the sulphate scaling tendencies in the given brine are indicated by their supersaturations and amounts of precipitations resulting from the final iteration.

3.4 THE CONSTRUCTION OF AN INTERACTIVE MODEL

The last section is devoted to the iterative process involved in the sulphate scaling tendencies prediction. From the mathematical expressions described in the last section, a computer model was constructed for predicting the scaling tendencies of the sulphates due to mixing of incompatible waters as well as temperature and pressure effects. The main programme of the model mainly consists of three subprograms for predicting solubilities for $BaSO_4$, $SrSO_4$ and $CaSO_4$, respectively, one subprogram for converting the brine concentration units and one subprogram for graphical output. The composition(s) of the brine(s) for prediction can be read either from a datafile or from computer screen. The composition may be represented in ions or/and salts. Eight different units for ion or salt concentrations are optional for the input brine composition and three most commonly used concentration units (mg/l, mg/1000g water and molal) are optional for output of the predicted results. The brine composition is converted to molal before the prediction, if any imbalance between the cation concentrations and the anion concentrations exists in a brine, the programme will check it and add equivalent Na^+ or Cl^- to make up it. For the prediction of scaling due to mixing brines, the compositions of the mixed brines at all ratios are calculated and subsequently the scale prediction is carried out for each mixed brine composition. The prediction temperature(s) and pressure(s) are required from the screen. Then the programme proceeds to the iterative process, calling the three subprograms consecutively to

calculate the solubilities for the sulphates. From exit of the iteration, the supersaturations and amounts of precipitation of the sulphates from the brine or mixed brines are determined, also the square roots of the stoichiometric solubility products $Q_{sp,MX}$ and the sulphate solubilities are obtained as the results. The output of predicted results is optional, they may be either written to datafiles or displayed in graphical forms or both carried out together. After the prediction for the given brine or brines, the programme may go to another brine or brines and restart the prediction process again.

The flowchart in figure (3.1) shows the prediction process described above.

3.5 ASSESSMENT OF THE SCALE PREDICTION

The scaling tendency prediction model was tested by comparing the predicted brine supersaturations in both single brines and mixed brines with the field observations. The brine compositions and the analysed or observed results(generally referred to as field observations in the thesis) were collected from the published literature. The predicted results are presented in tables (3.1) and (3.2) for sulphate scaling tendencies in single and mixed brines, respectively. In table (3.1), the figures in the columns under each sulphate name are the predicted supersaturations for the sulphate in the given brines at assigned temperatures and pressures. For the mixed brines, the figures shown in table(3.2) are the predicted highest possible sulphate supersaturations when two concerned brines mix at given conditions.

3.6 CASE STUDIES OF SCALE PREDICTION

In the case studies of sulphate scaling tendencies, first the predicted results from this model are compared to the results predicted from the Vetter's model[149] as well as Pucknell's model,[113] then the sulphate scaling tendencies due to mixing North Sea water and the Forties formation water are examined by means of the present scale prediction model.

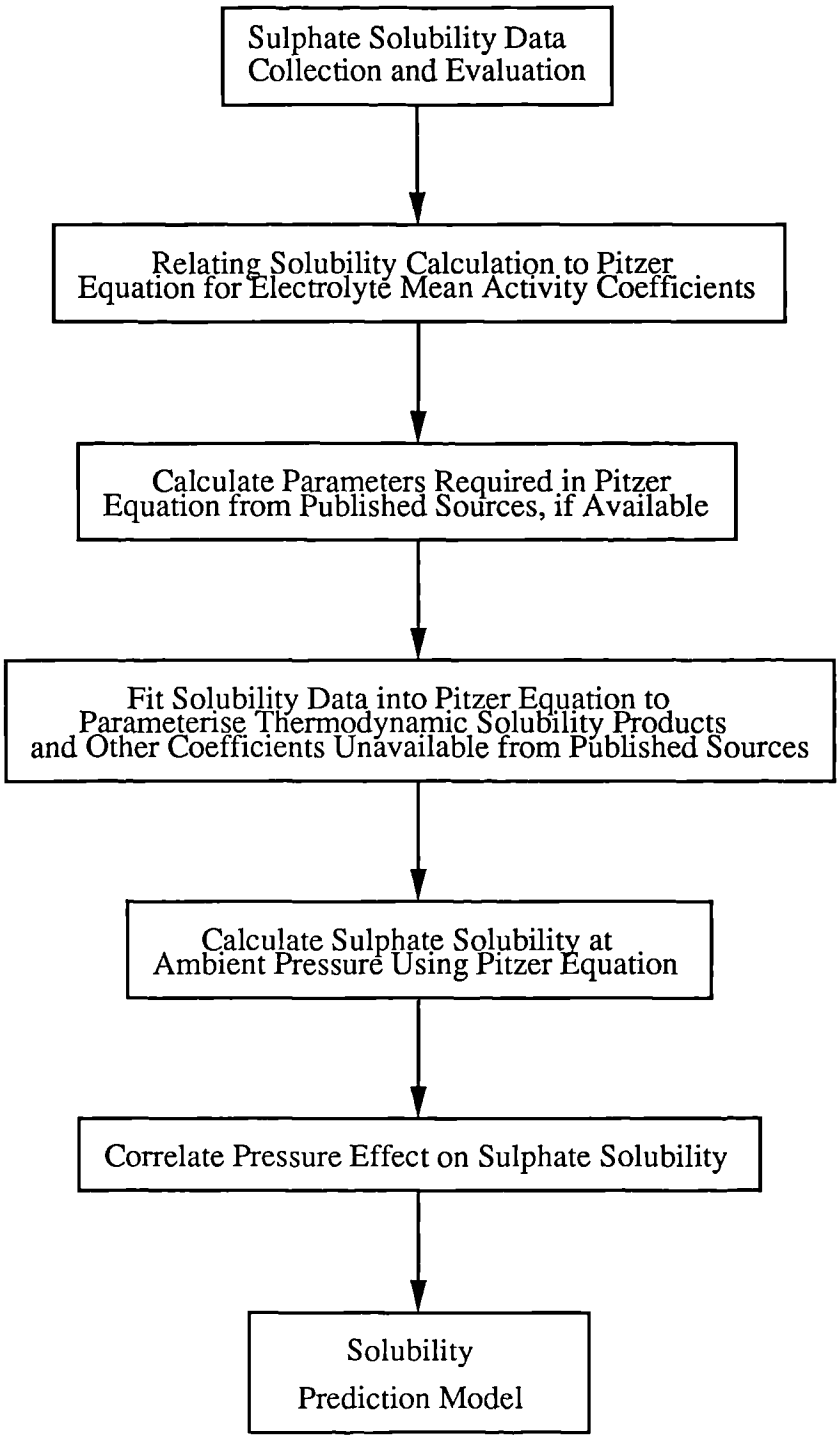

Figure 2.42 Construction of Solubility Model

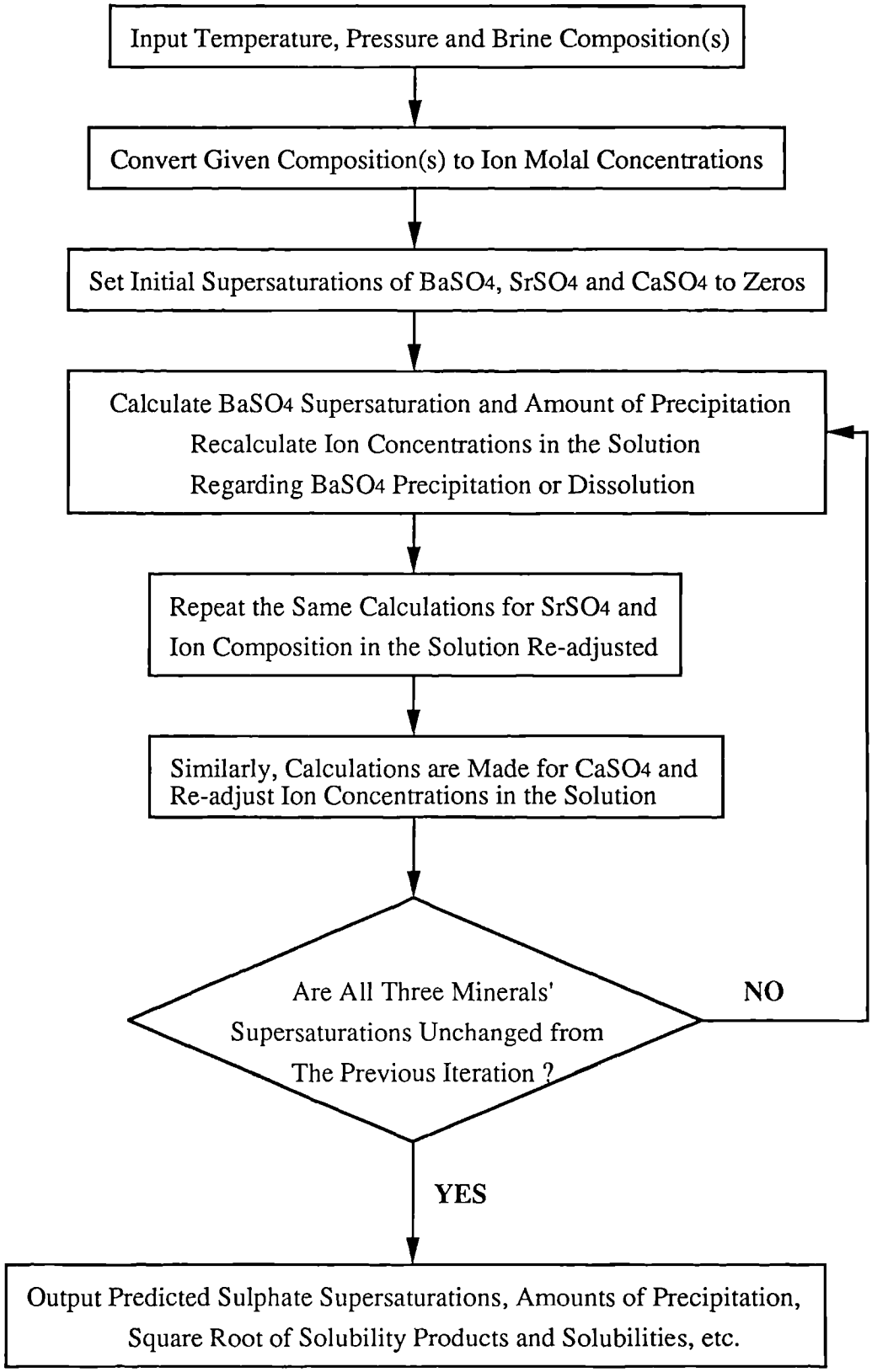

Figure 3.1 Sulphate Scaling Tendency Prediction Model

Table 3.1 Predicted Supersaturations for Single Brines

Literature Source	Brine	T(°C)	P(bars)	$BaSO_4$	$SrSO_4$	Gypsum	Anhydrite	Field Observation
Jacques &	A	110	170	—	1.04	0.41	0.78	$SrSO_4$ scale borderline
Bourland.[60]	B	110	170	—	1.70	0.63	1.19	$SrSO_4$ scale
	C	110	170	—	0.72	0.26	0.51	no scale
		25	1	—	—	1.04	0.86	
Skillman,	1	100	1	—	—	1.19	2.22	calcium
et al.[130]	2	25	1	—	—	1.00	0.87	sulphate
		100	1	—	—	1.07	1.88	scale
		25	1	—	—	1.40	1.30	
Hausler.[52]	1	100	300	—	—	1.21	2.20	gypsum
	2	25	1	—	—	1.52	1.39	scale
		100	300	—	—	1.30	2.30	

Table 3.2 Predicted Supersaturations for Mixed Brines

Literature Source	Brines	T(°C)	P(bars)	$BaSO_4$	$SrSO_4$	Gypsum	Anhydrite	Field Observation
Mitchell et al.[77]	North sea and Forties waters	25	1	35	1.7	0.55	0.46	$BaSO_4$+ $SrSO_4$ scale
		100	300	15	2.0	0.50	0.88	
Lindlof& Stoffer[67]	Arab-D1+ sea water	25	1	7.8	1.8	1.3	1.2	$SrSO_4$+ $BaSO_4$+ $CaSO_4$ scale
		100	300	3.1	2.2	1.1	1.8	
	Arab-D2+ sea water	25	1	7.2	2.1	1.7	1.8	
		100	300	2.8	2.7	1.3	2.4	
	Arab-D1+ Wasia water	25	1	4.1	0.93	0.72	0.66	$SrSO_4$ scale
		100	300	1.6	1.2	0.65	1.08	
	Arab-D2+ Wasia water	25	1	3.2	0.87	0.81	0.80	
		100	300	1.3	1.1	0.66	1.1	
Essel& Carlberg[32]	Mishrif and Gulf waters	25	1	8.7	1.6	0.87	0.80	$SrSO_4$ scale
		110	300	3.2	2.3	0.80	1.4	
Case[24]	Supply water1+ prod. water	25	1	—	—	0.41	0.35	No scale
		100	300	—	—	0.40	0.70	
Read& Ringen[115]	Sea water + Formation water	70	1	21	1.4	0.40	0.55	$SrSO_4$+ $BaSO_4$+ $CaCO_3$ scale

3.6.1 Comparison of the Predicted Sulphate Scaling Tendencies from This Model with Those from the Other Models

Vetter et al[149] predicted sulphate scale precipitation caused by commingling of injection waters and reservoir waters. The water compositions are shown in table (3.3). The same waters were used for predicting the sulphate precipitation using the present model and Pucknell's model. Vetter's results are shown in figures (3.2) and (3.3) (the type of calcium sulphate scale was not declared in their paper, it is assumed to be anhydrite rather than gypsum after comparing their results with ours.). The results predicted from this model with the same fluids are illustrated in figures (3.4) to (3.7) and the predicted sulphate precipitation from Pucknell's model are given in figures (3.8) and (3.13). The predictions for $BaSO_4$ from Vetter's model and from this model agree with each other well in all the cases. From mixing of injection water 1 with the reservoir water, both the new model of Vetter's and this model predict no $SrSO_4$ scaling but lower anhydrite precipitation is predicted from this model. From mixing injection water 2 with the reservoir water, larger amount of $SrSO_4$ and much less $CaSO_4$ precipitations are predicted in this model in contrast to the new model of Vetter's. A question arises when comparing the predicted results for $CaSO_4$ precipitation from Vetter's new model and their old model. The amount of precipitation of $CaSO_4$ predicted from their new model, which was supposed to include the competition of less soluble Ba^{2+}, Sr^{2+} for SO_4^{2-} with Ca^{2+}, is more than that predicted from their old model, which predicted $CaSO_4$ scale formation regardless of the SO_4^{2-} concentration reduction in the brine owing to $BaSO_4$ and $SrSO_4$ precipitation. This seems contrary to the likely result. In the present model the sulphate scaling tendency of gypsum is predicted as well and the results for $CaSO_4$ and $SrSO_4$ are remarkedly different from those assuming anhydrite as the potential calcium scale, as seen from comparing figure (3.4) with (3.6) and comparing figure (3.5) with (3.7). Such differences suggest that the prediction for the sulphate scaling tendencies could mislead if the type of calcium sulphate scale is

Table 3.3 Compositions of the Reservoir and Source Waters[149]

Water Component (mg/L)	Reservoir Water 1	Source Water 1	Source Water 2
$NaHCO_3$	500	1,000	200
NaCl	250,000	180,000	1,000
Na_2SO_4	<1.0	3,000	1,000
KCl	1,000	<1.0	<1.0
$MgCl_2$	2,000	1,500	500
$MgSO_4$	<1.0	400	300
$CaCl_2$	60,000	5,000	800
$SrCl_2$	2,000	<1.0	<1.0
$BaCl_2$	750	<1.0	<1.0
$FeCl_3$	1,100	<1.0	<1.0

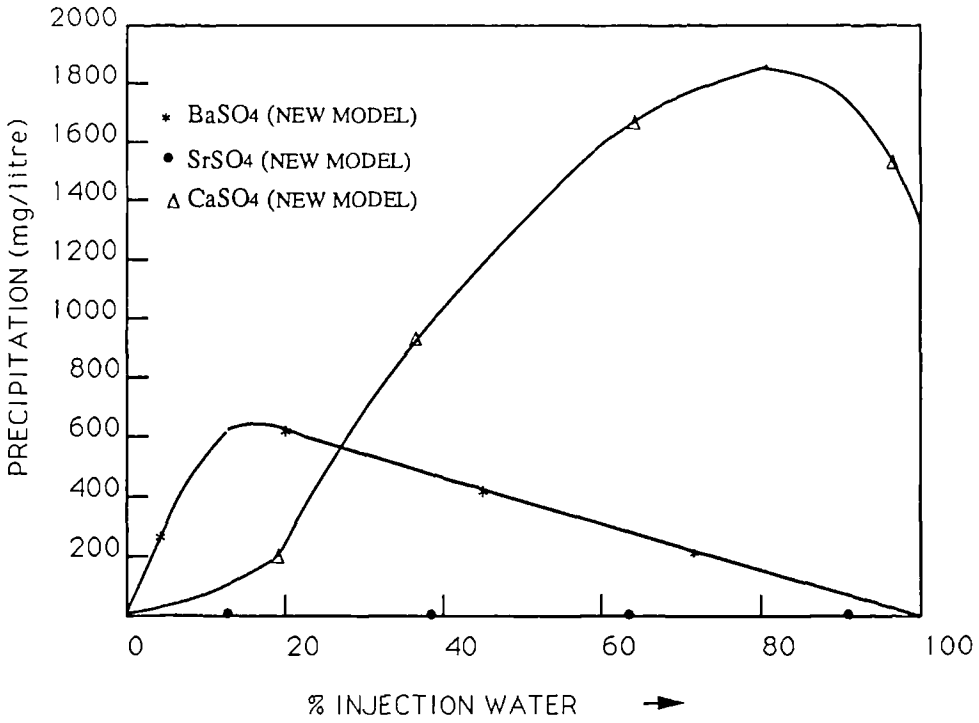

Figure 3.2 Predicted sulphate precipitations due to mixing reservoir water 1 and source water 1, Vetter's model. Water compositions in Table (3.3). Reproduced from figure 5 of reference 149

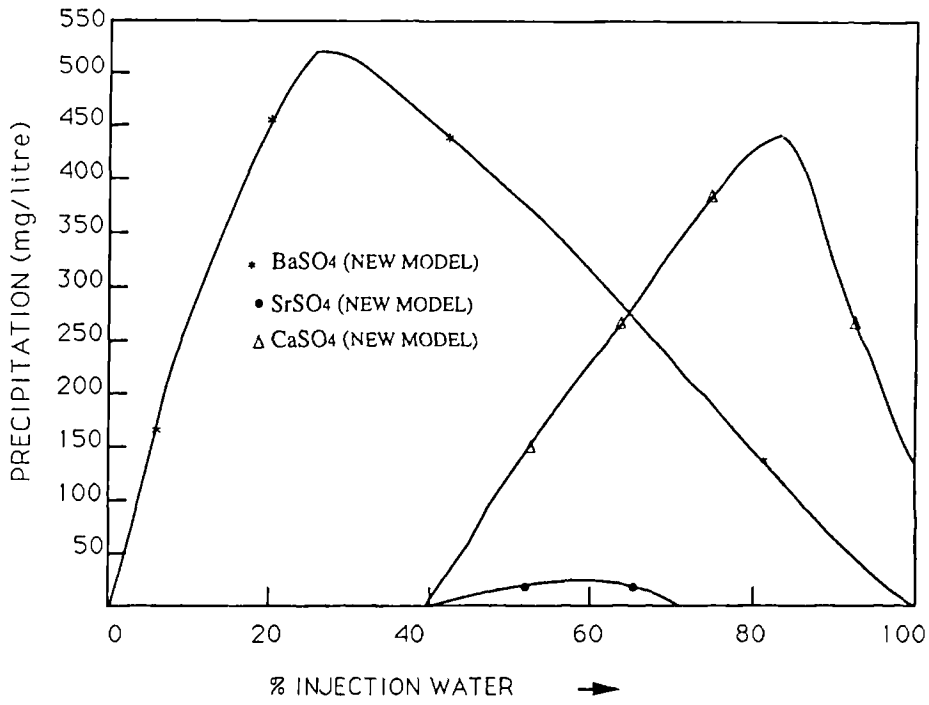

Figure 3.3 Predicted sulphate precipitations due to mixing reservoir water 1 and source water 2, Vetter's model. Water compositions in Table (3.3). Reproduced from figure 6 of reference 149

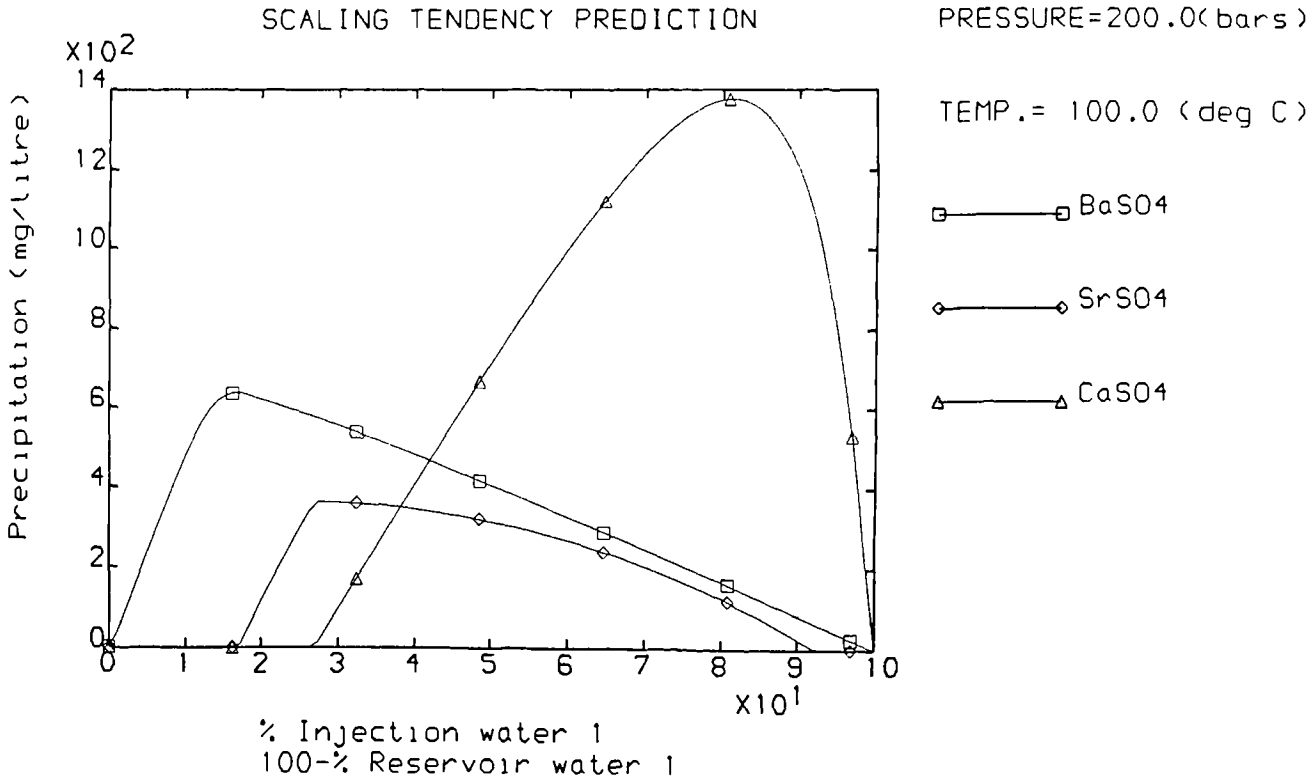

Figure 3.4 Predicted $BaSO_4$, $SrSO_4$ and anhydrite precipitation due to mixing reservoir water 1 and source water 1, the current model. Water compositions in table (3.3)

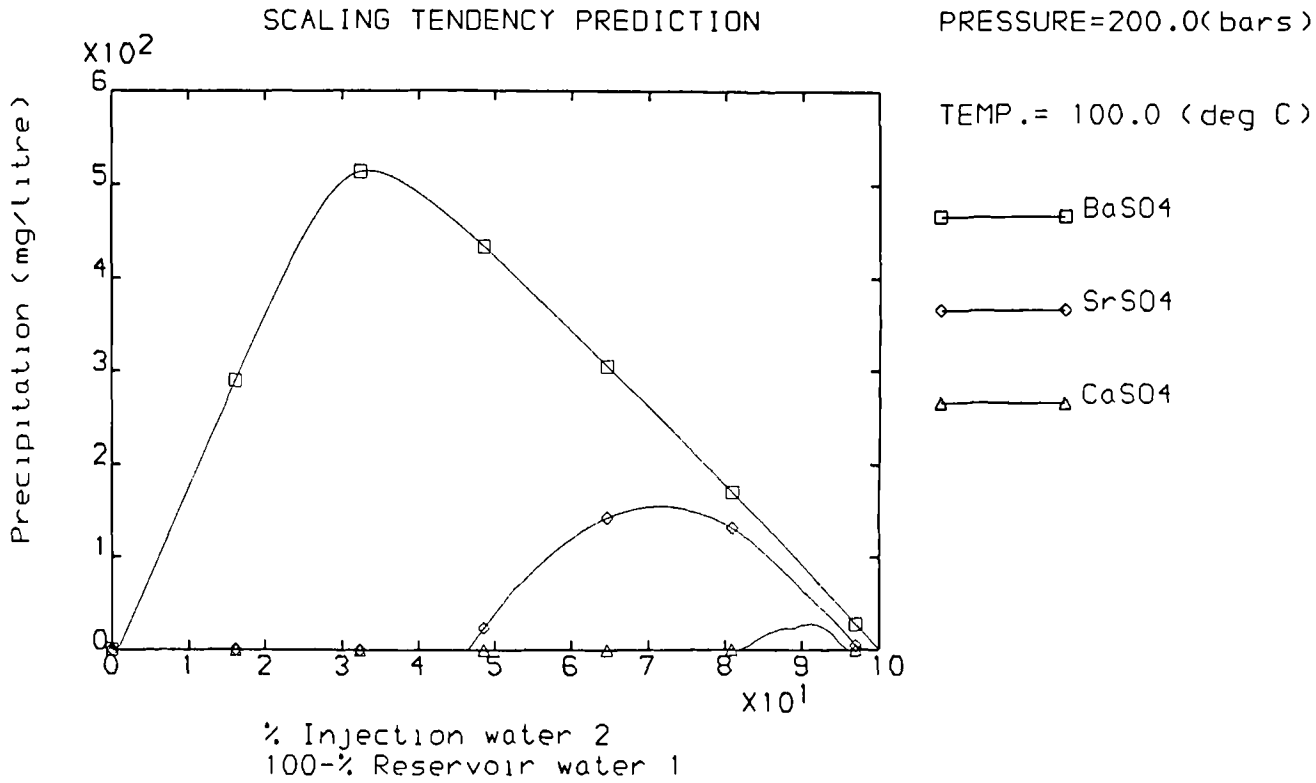

Figure 3.5 Predicted $BaSO_4$, $SrSO_4$ and anhydrite precipitation due to mixing reservoir water 1 and source water 2, the current model. Water compositions in table (3.3)

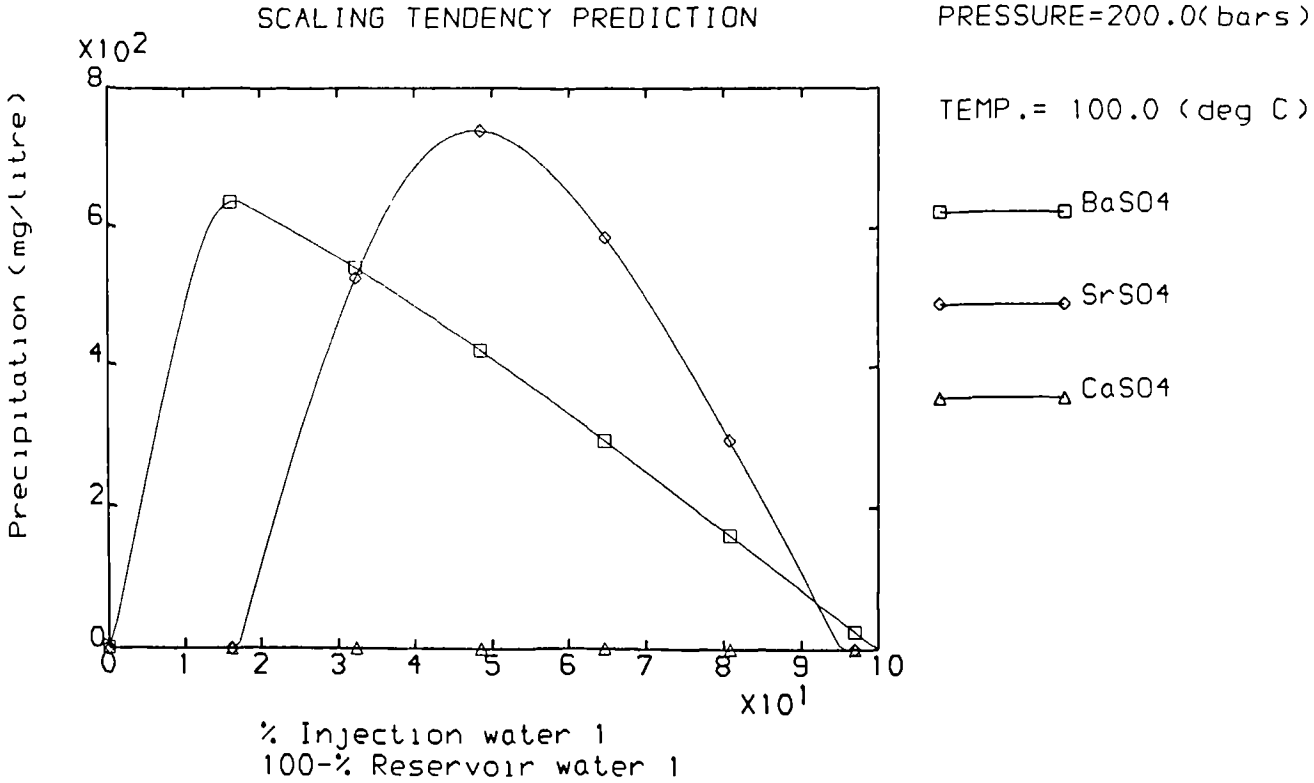

Figure 3.6 Predicted $BaSO_4$, $SrSO_4$ and gypsum precipitation due to mixing reservoir water 1 and source water 1, the current model. Water compositions in table (3.3)

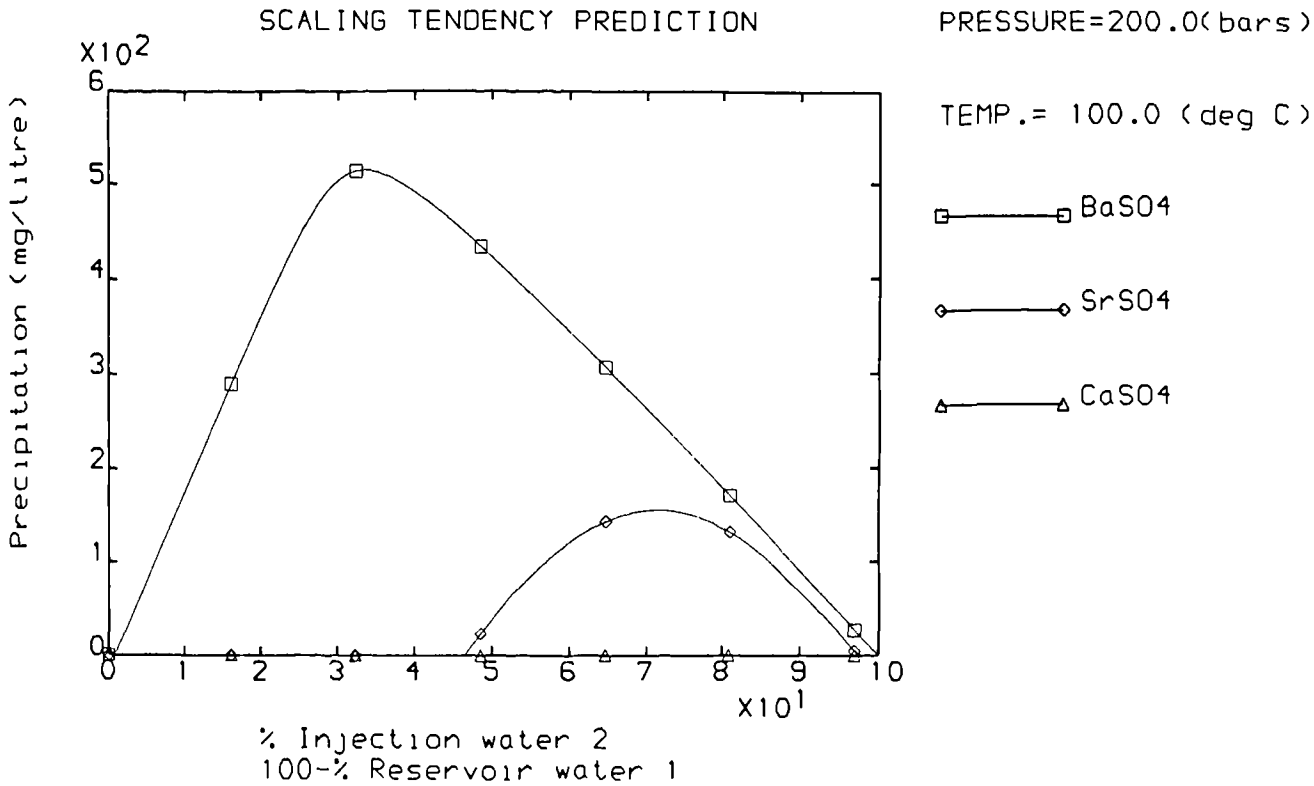

Figure 3.7 Predicted $BaSO_4$, $SrSO_4$ and gypsum precipitation due to mixing reservoir water 1 and source water 2, the current model. Water compositions in table (3.3)

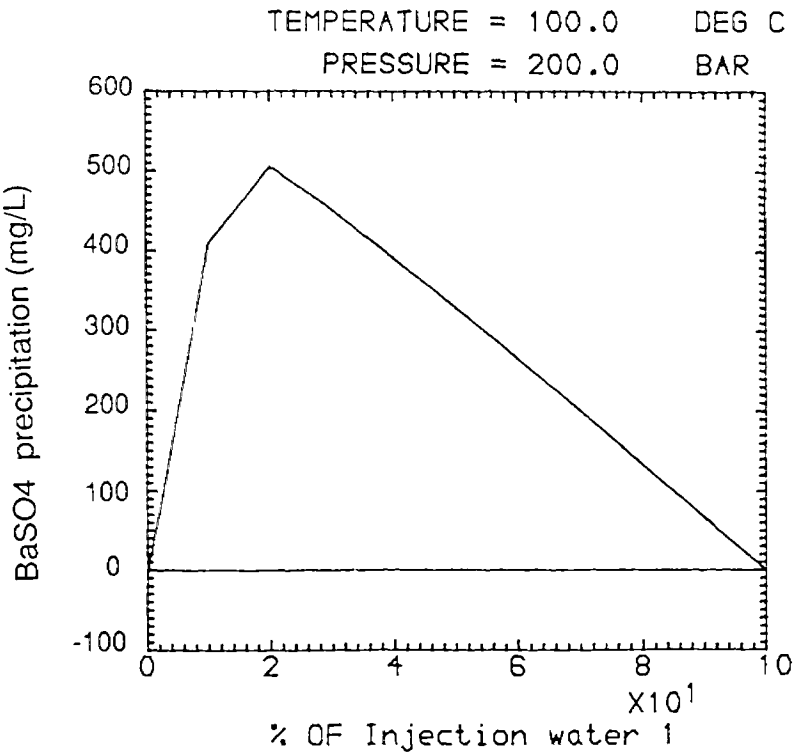

Figure 3.8 Predicted barium sulphate precipitation due to mixing reservoir water 1 and source water 1, Pucknell's model. Water compositions in table (3.3)

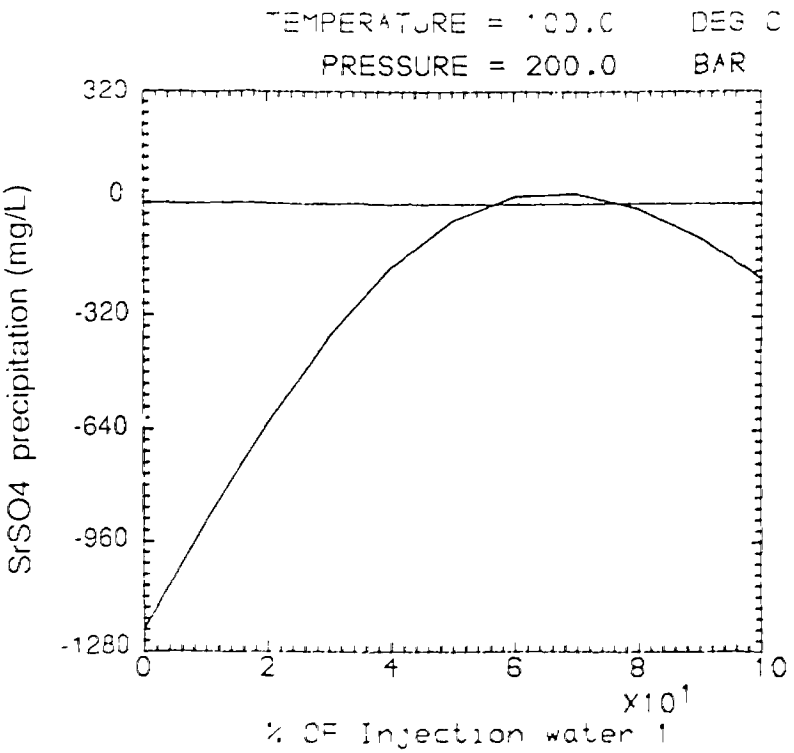

Figure 3.9 Predicted strontium sulphate precipitation due to mixing reservoir water 1 and source water 1, Pucknell's model. Water compositions in table (3.3)

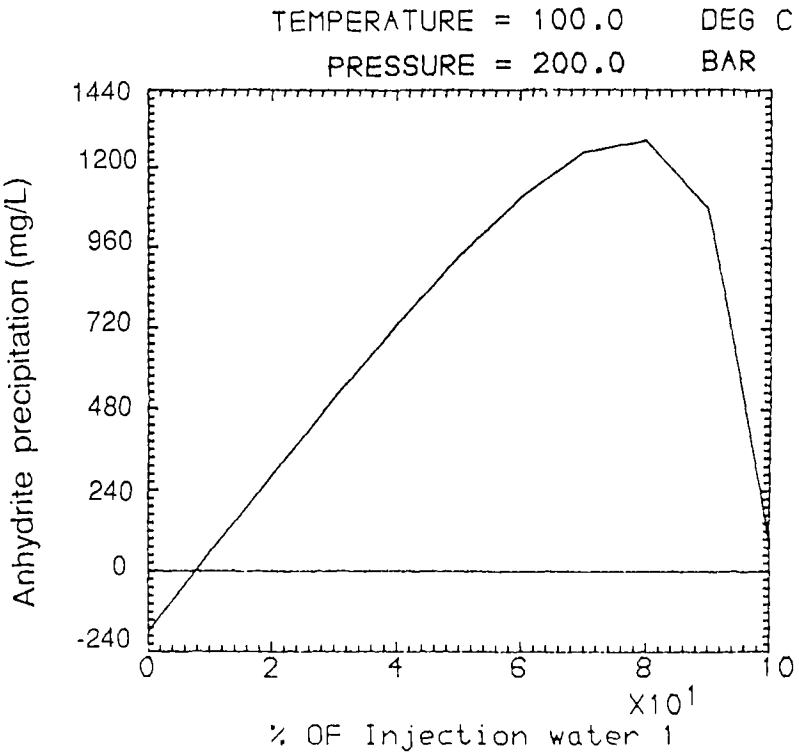

Figure 3.10 Predicted anhydrite precipitation due to mixing reservoir water 1 and source water 1, Pucknell's model. Water compositions in table (3.3)

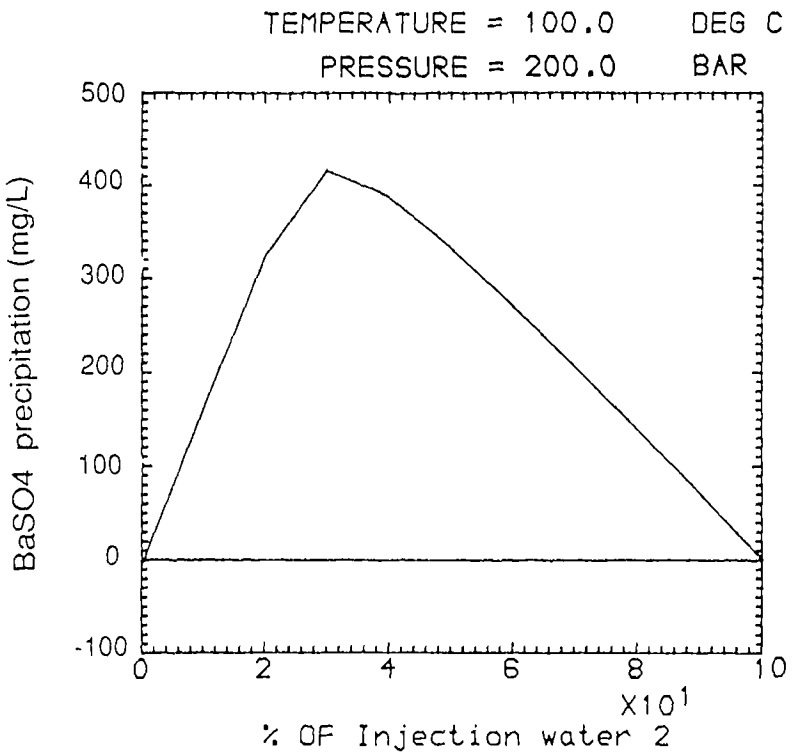

Figure 3.11 Predicted barium sulphate precipitation due to mixing reservoir water 1 and source water 2, Pucknell's model. Water compositions in table (3.3)

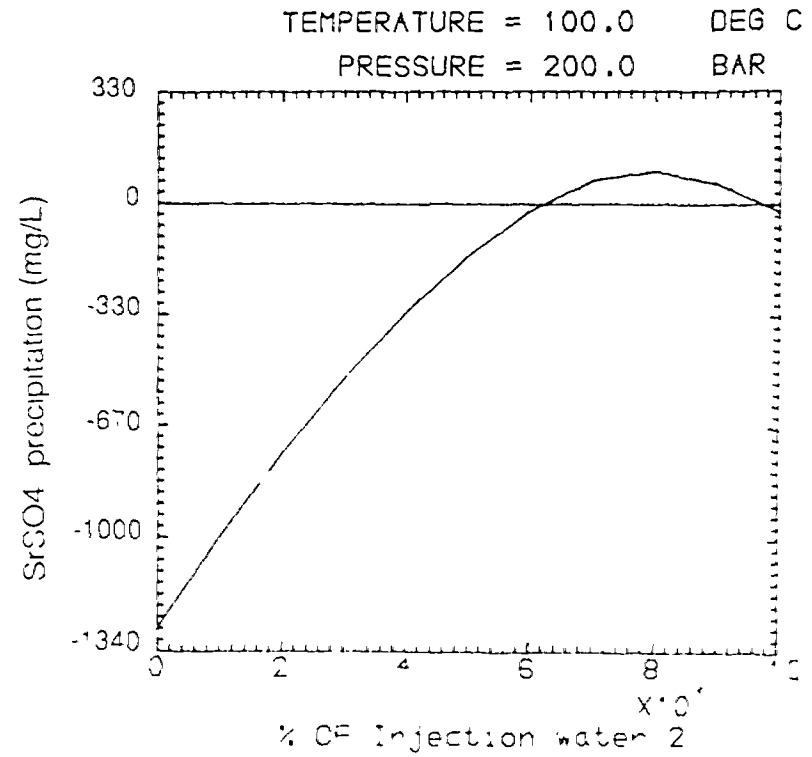

Figure 3.12 Predicted strontium sulphate precipitation due to mixing reservoir water 1 and source water 2, Pucknell's model. Water compositions in table (3.3)

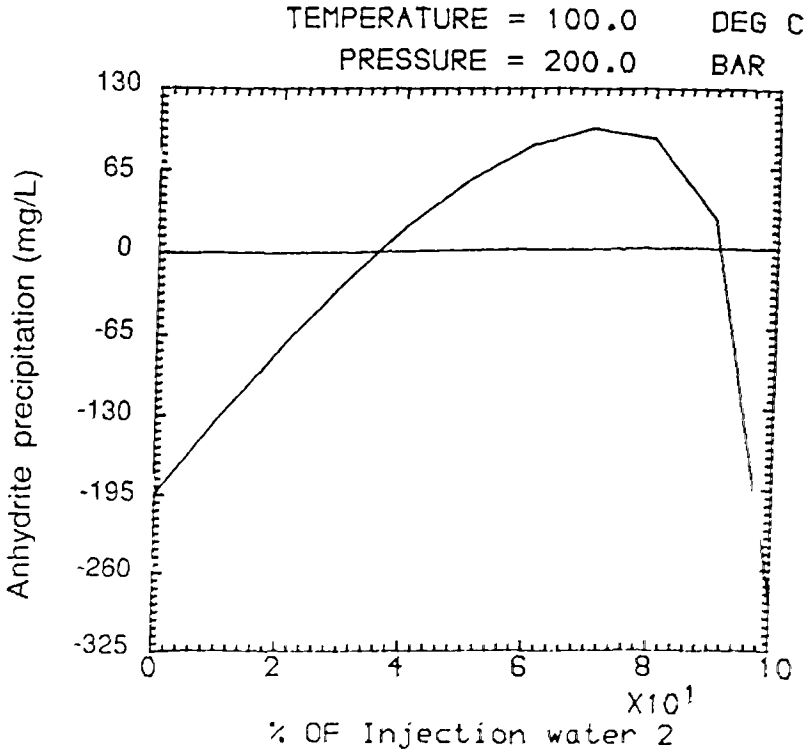

Figure 3.13 Predicted anhydrite precipitation due to mixing reservoir water 1 and source water 2, Pucknell's model. Water compositions in table (3.3)

uncertain and wrongly assumed. Compared with the predicted results from Pucknell's model, as shown in figures (3.8) through (3.13), with the predictions from the present model, as illustrated in figures (3.4) and (3.5), both models predict that gypsum is stable in the mixed waters at given temperature and pressure, Pucknell's model predicts smaller amounts of precipitation of both $BaSO_4$ and $SrSO_4$ scales than that predicted from this model as a result of either mixing reservoir water and source water 1 or mixing reservoir water and source water 2, and less anhydrite precipitation is predicted in the mixed reservoir and source water 1 while more anhydrite scale precipitation is predicted when mixing the reservoir water and source water 2 by Pucknell's model. The differences in the scale prediction results between the two models are usually about 10 to 20% and they are considered as the result of using different solubility models, also the differences may be the result of having taken the simultaneous coprecipitation of more than one sulphate mineral into account in the current model.

3.6.2 Prediction of Sulphate Scaling Tendency in North Sea Oil Operations

Forties is one of the major oilfields in the North Sea offshore production area. The compositions of the Forties formation water and the North Sea injection water are given in table (3.4). The sulphate scaling tendency in the mixed injection water and formation water was predicted using the present model at different temperature and pressure conditions. The predicted results are illustrated in figures (3.14) through (3.26). Figures (3.14) and (3.15) show the predicted supersaturations of $BaSO_4$, $SrSO_4$ and $CaSO_4$ at the temperatures and pressures assembling both surface and reservoir conditions, and figures (3.16) and (3.17) show the predicted sulphate precipitation corresponding to figures (3.14) and (3.15). From the graphs in figures (3.14) through (3.17), we can see that $BaSO_4$ is most likely to form scale while $CaSO_4$ is always stable in the mixed brines. Figures (3.16) and (3.17) also indicate that mixed $BaSO_4$ and $SrSO_4$ scale (so called solid solution) probably forms at certain mixing ratios between the injected water and the formation water. In fact, the $(Ba,Sr)SO_4$ solid solution scale

Table 3.4 Compositions of North Sea Water and Forties Formation Water[77]

Ions	North Sea Water (mg/L)	Forties Water (mg/L)
Na	11,000	30,200
Ca	403	3,110
Mg	1,320	480
K	340	430
Ba	0	250
Sr	0	660
Cl	19,800	53,000
SO_4	2,480	0
HCO_3	135	360

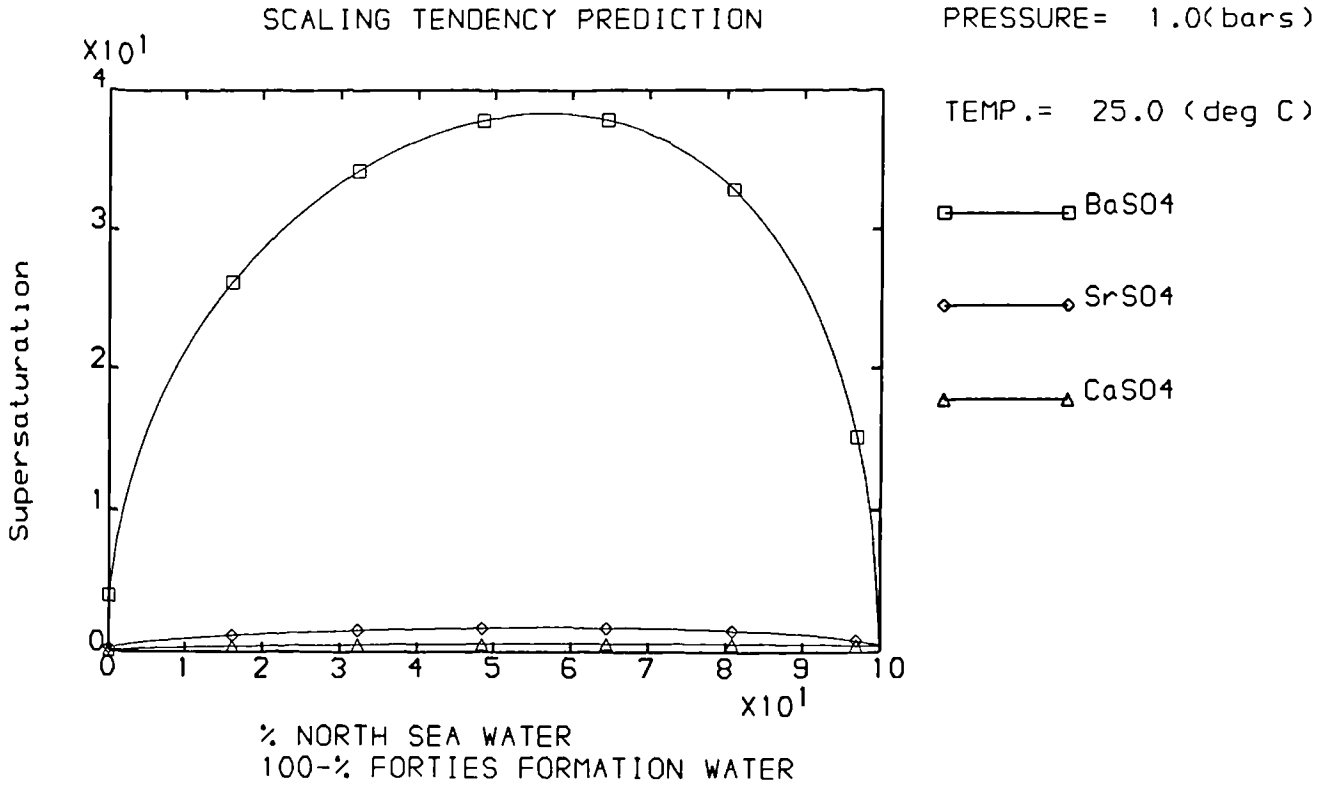

Figure 3.14 Predicted sulphate supersaturations due to mixing North sea water and Forties water at surface conditions. Water compositions in table (3.4)

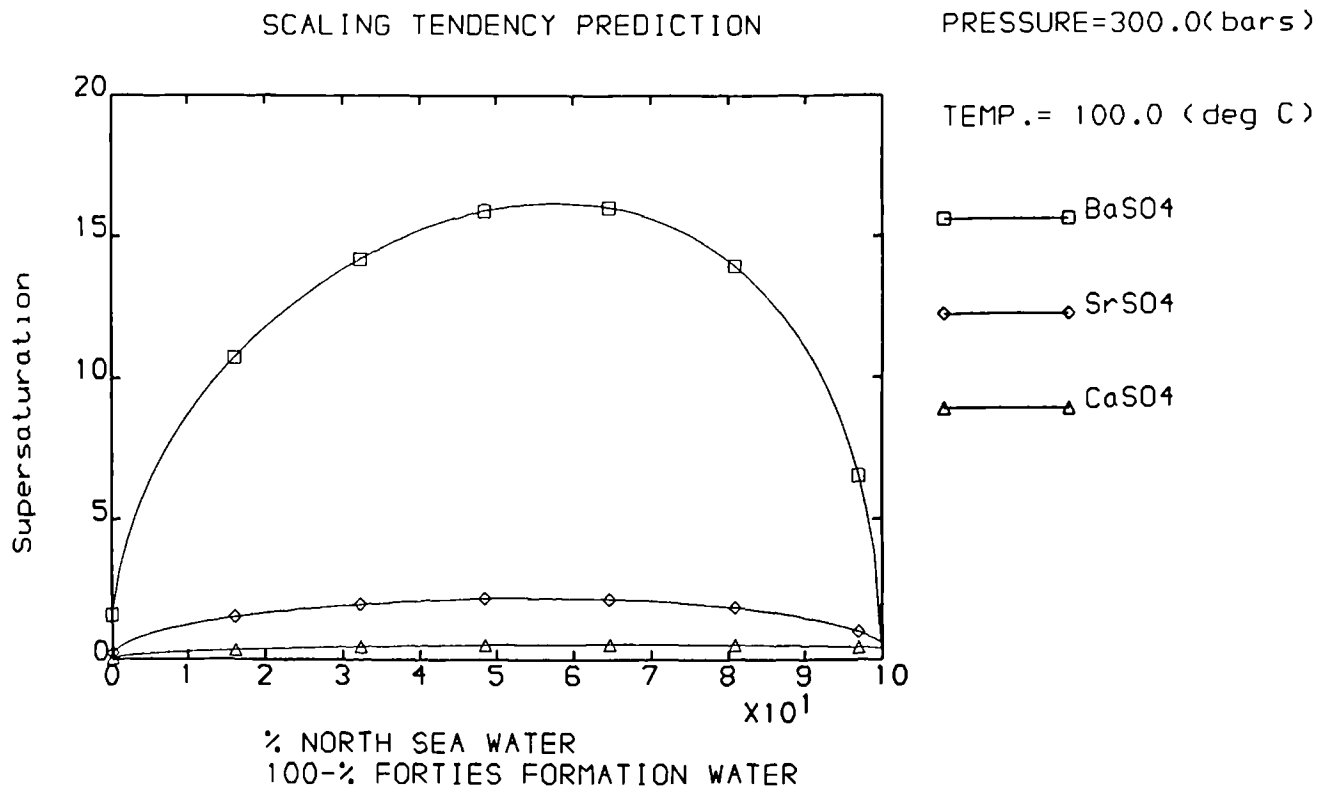

Figure 3.15 Predicted sulphate supersaturations due to mixing North sea water and Forties water at reservoir conditions. Water compositions in table (3.4)

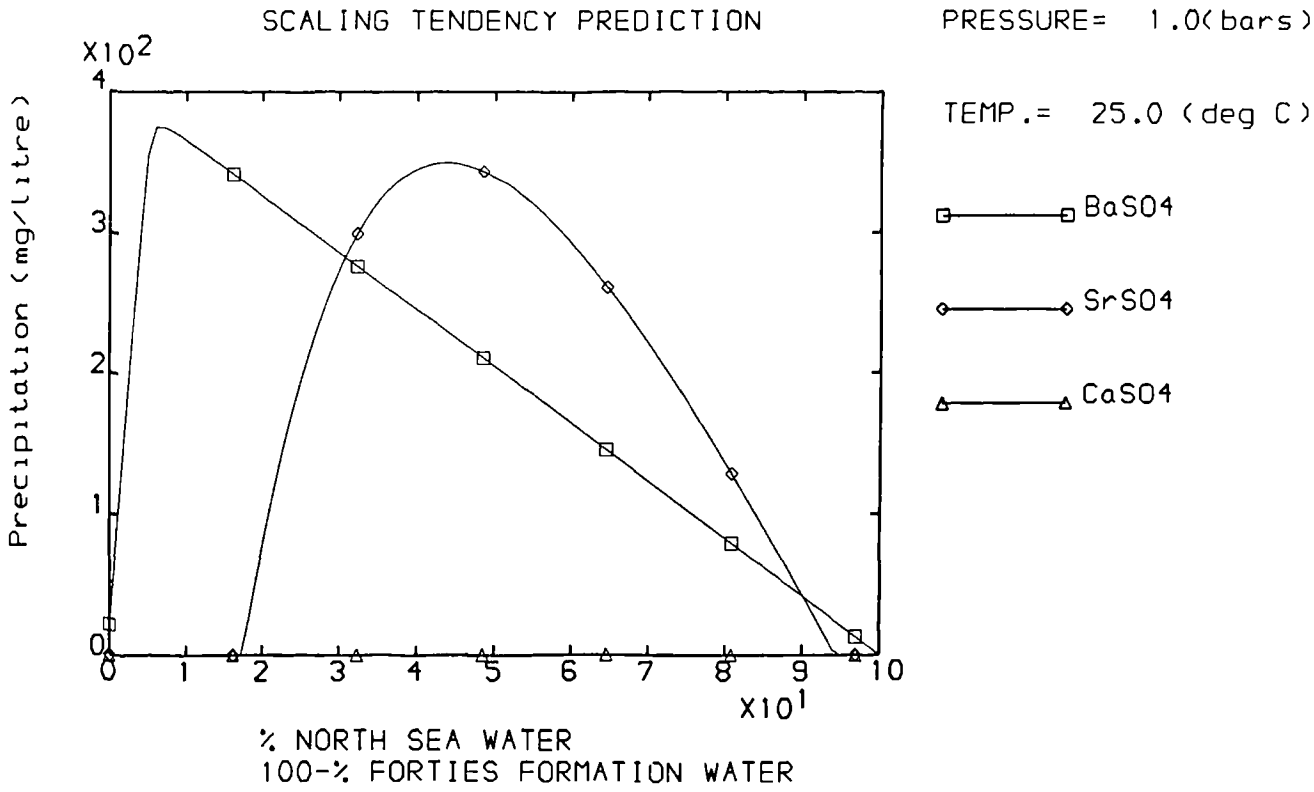

Figure 3.16 Predicted sulphate precipitations due to mixing North sea water and Forties water at surface conditions. Water compositions in table (3.4)

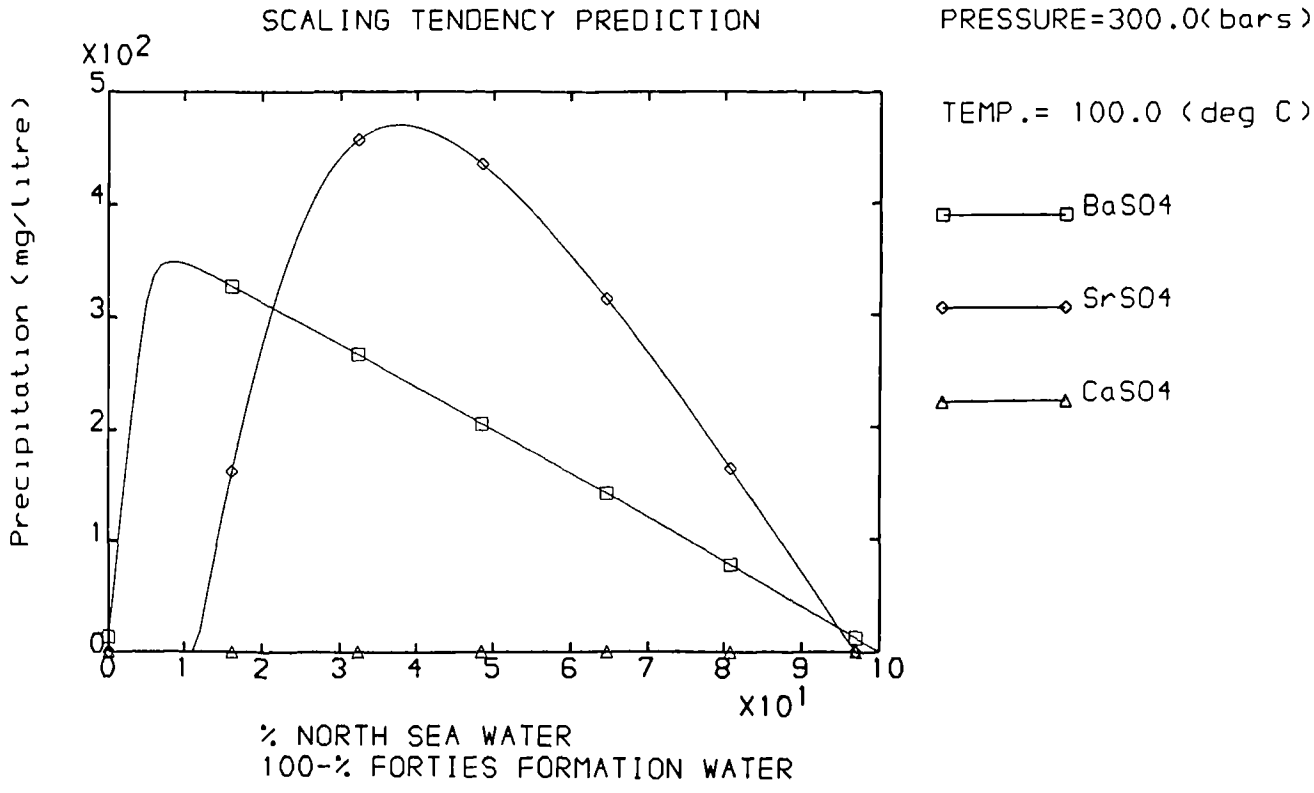

Figure 3.17 Predicted sulphate precipitations due to mixing North sea water and Forties water at reservoir conditions. Water compositions in table (3.4)

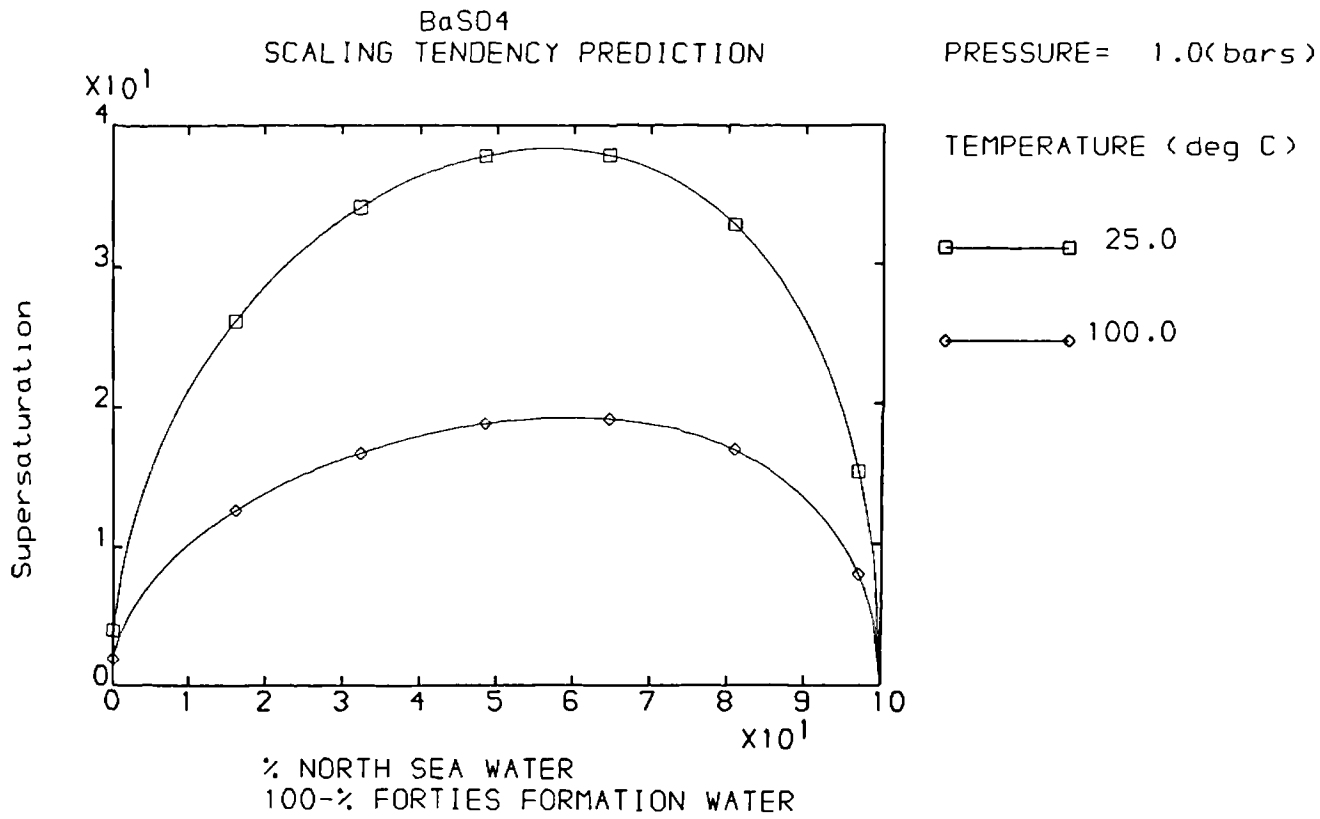

Figure 3.18 Predicted barium sulphate supersaturations due to mixing North sea water and Forties water at different temperatures. Water compositions in table (3.4)

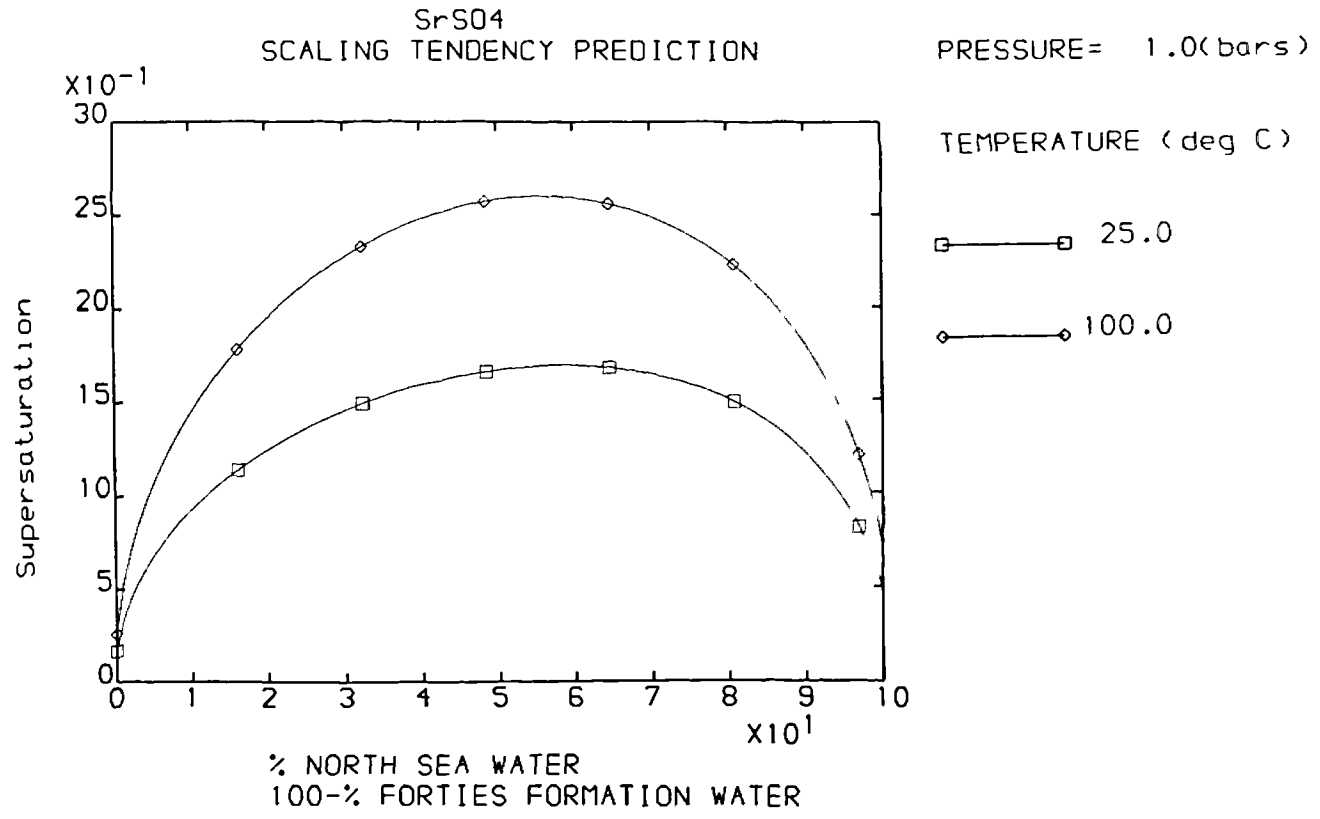

Figure 3.19 Predicted strontium sulphate supersaturations due to mixing North sea water and Forties water at different temperatures. Water compositions in table (3.4)

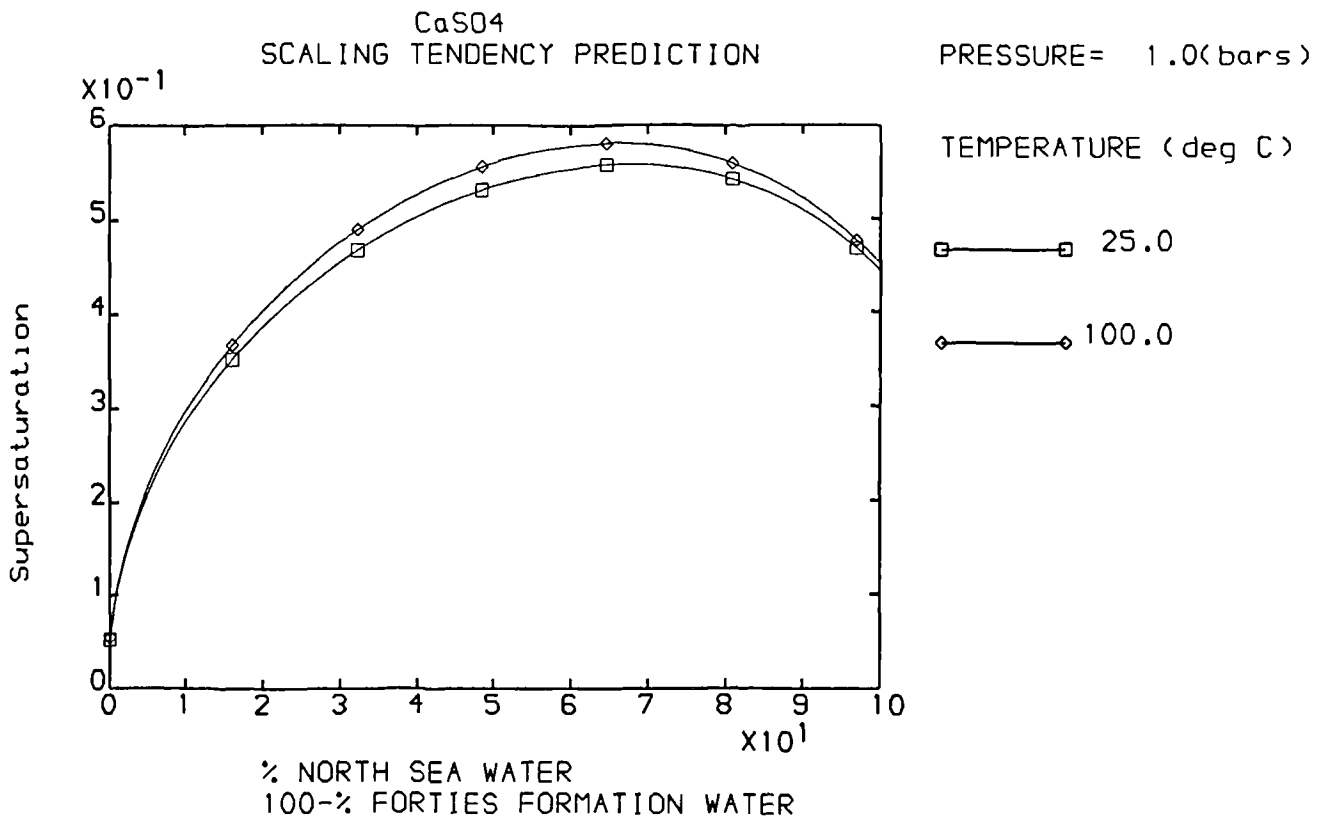

Figure 3.20 Predicted gypsum supersaturations due to mixing North sea water and Forties water at different temperatures. Water compositions in table (3.4)

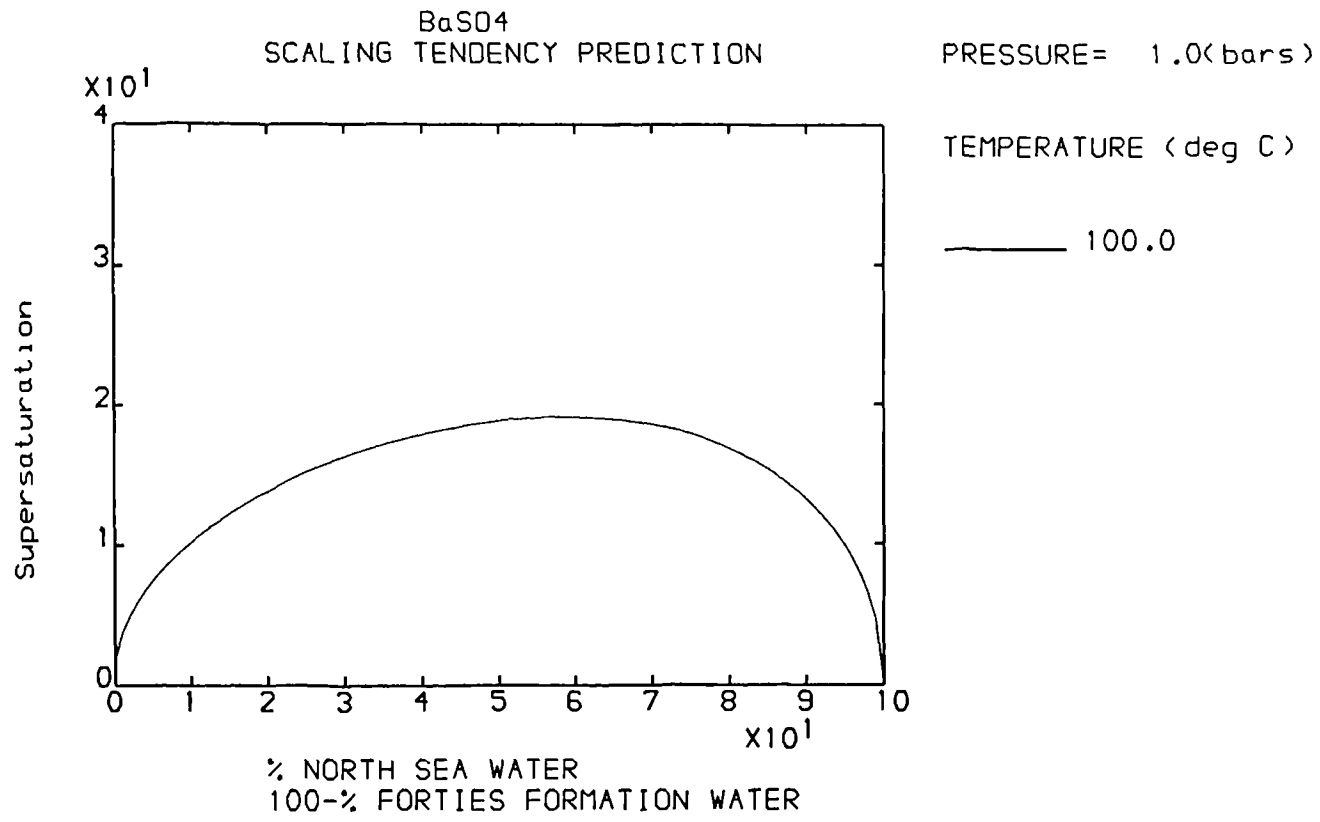

Figure 3.21 Predicted barium sulphate supersaturation due to mixing North sea water and Forties water at ambient pressure. Water compositions in table (3.4)

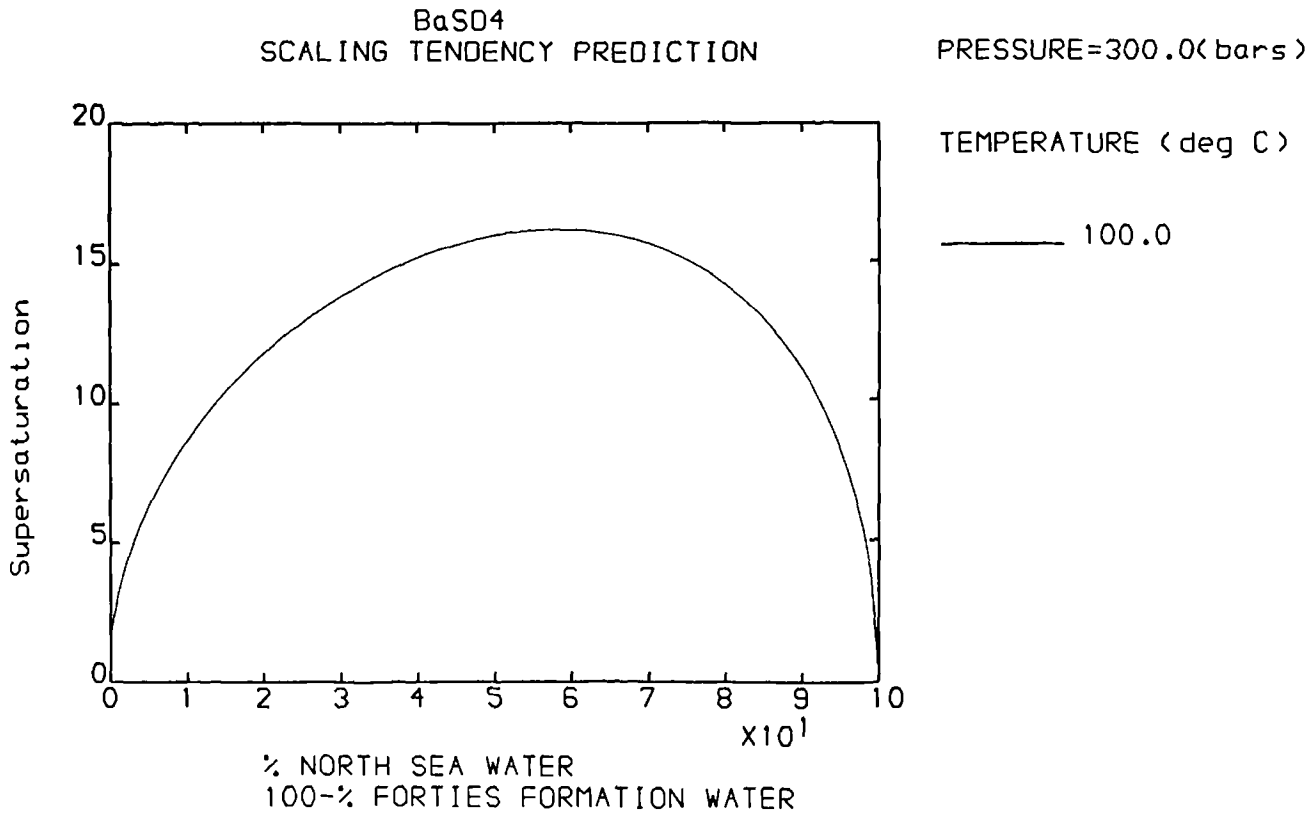

Figure 3.22 Predicted barium sulphate supersaturation due to mixing North sea water and Forties water at elevated pressure. Water compositions in table (3.4)

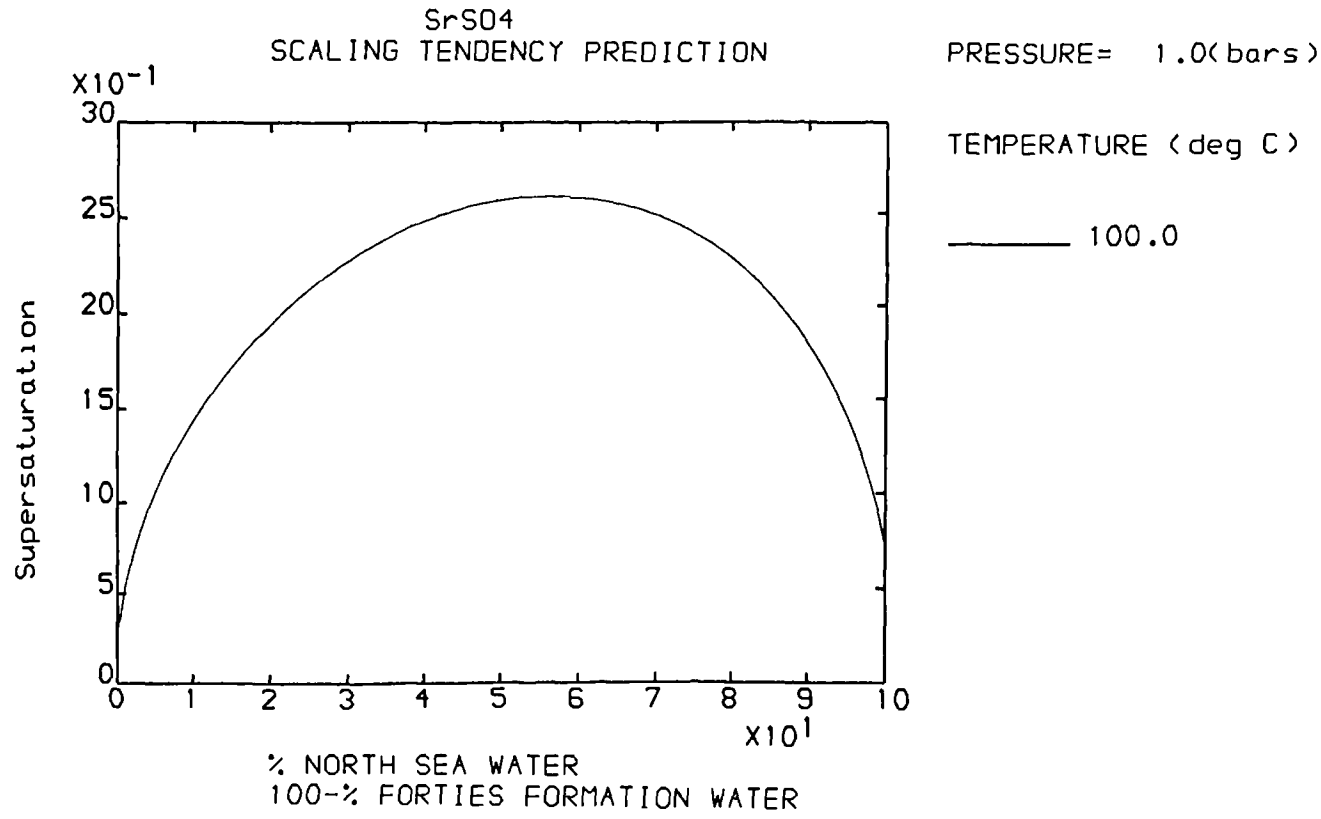

Figure 3.23 Predicted strontium sulphate supersaturation due to mixing North sea water and Forties water at ambient pressure. Water compositions in table (3.4)

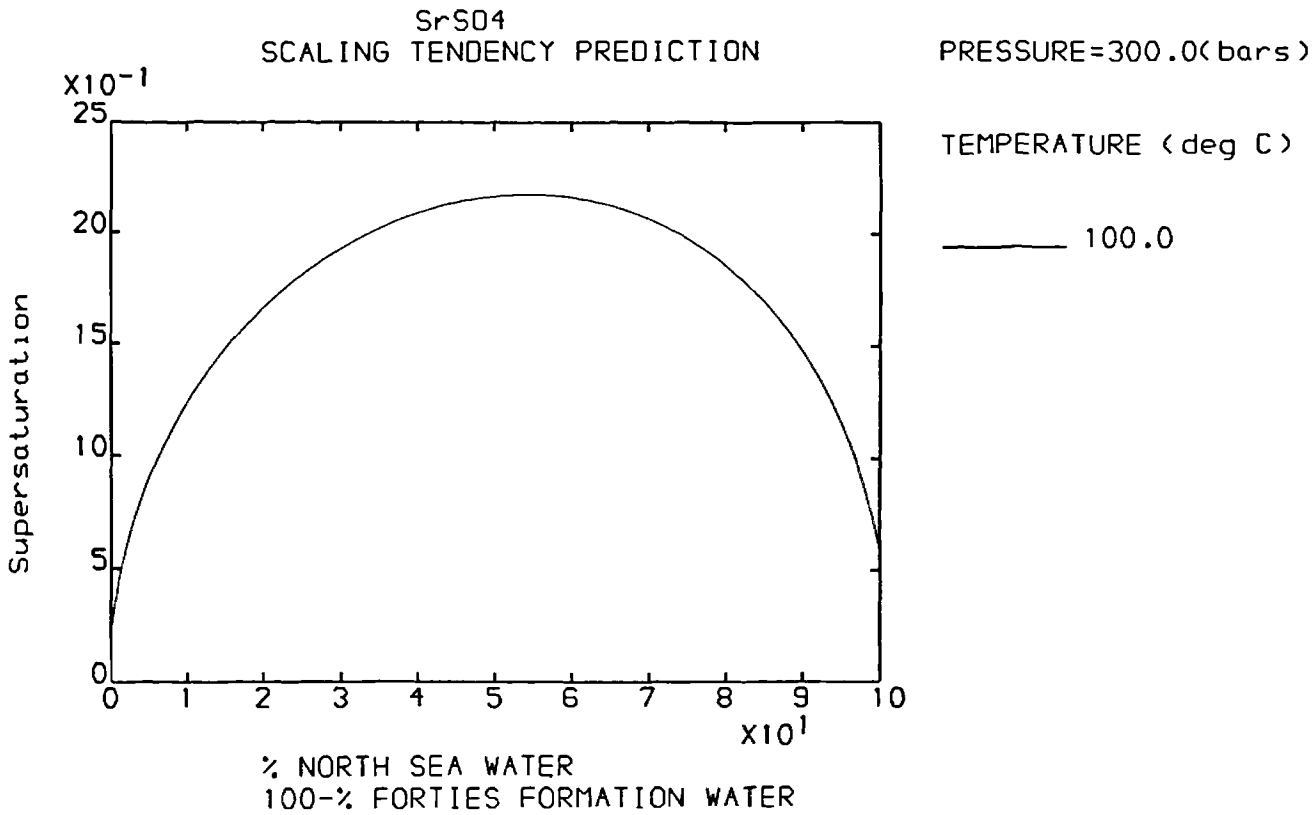

Figure 3.24 Predicted strontium sulphate supersaturation due to mixing North sea water and Forties water at elevated pressure. Water compositions in table (3.4)

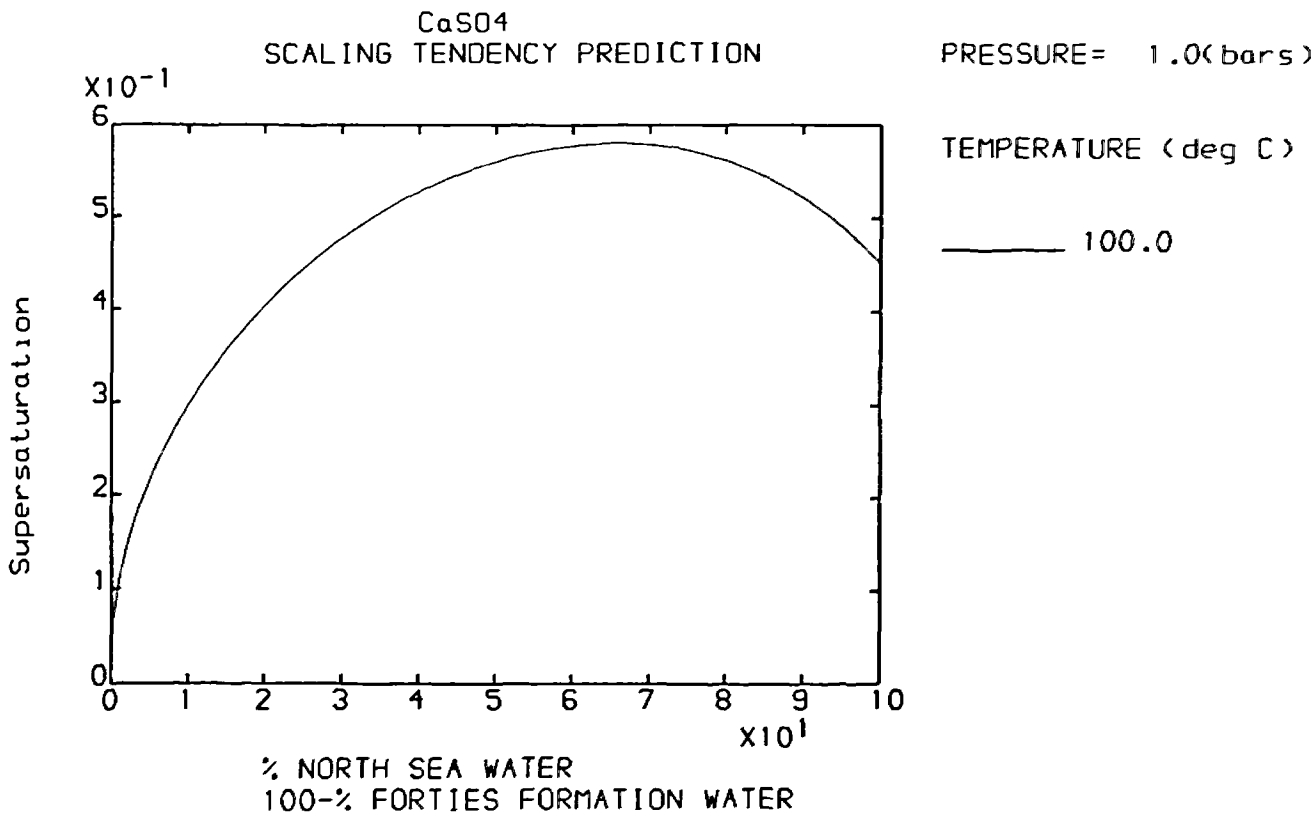

Figure 3.25 Predicted gypsum supersaturation due to mixing North sea water and Forties water at ambient pressure. Water compositions in table (3.4)

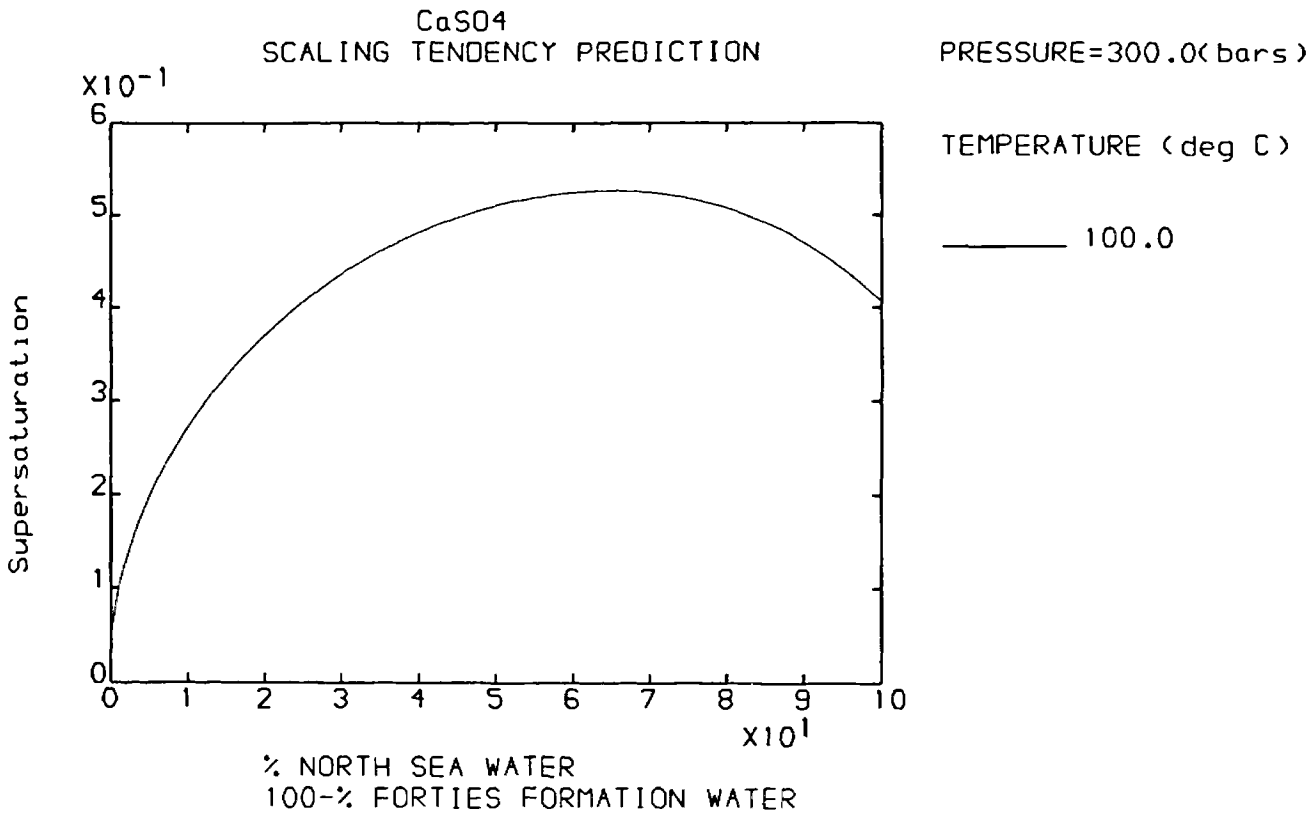

Figure 3.26 Predicted gypsum supersaturation due to mixing North sea water and Forties water at elevated pressure. Water compositions in table (3.4)

is a concern of the scale occurrence in the Forties operations.[58,77,141] Comparing figures (3.14) to (2.16) and (3.15) to (3.17), it is interesting to note that the maximum precipitation mixing ratio is not identical to the maximum supersaturation mixing ratio. For example, at 100°C and 300 bars, the largest amount of $BaSO_4$ scale would form soon after seawater is injected into the formation (seawater : formation water = 8 : 92 in volume) as shown in figure (3.17), but $BaSO_4$ is the most supersaturated when 56% sea water mixes with 42% formation water as indicated in figure (3.15). The temperature effect on the sulphate scaling tendencies is demonstrated in figures(3.18) to (3.20). Increase in temperature generally lowers the $BaSO_4$ scaling tendency but causes $CaSO_4$ and $SrSO_4$ more likely to precipitate from the brine thus less $BaSO_4$ and more $SrSO_4$ scale will form at higher temperatures in this field. The pressure increase universally makes all the sulphate minerals more soluble or less scaling-prone, as indicated from the comparison made between figures (3.21) and (3.22), between (3.23) and (3.24) and between figures (3.25) and (3.26). Hence, sulphate formation may simply result from the pressure drop, for example, as the produced water flows from the reservoir through the well tubing up to the producing wellhead.

3.7 COMMENTS ON THE SCALE PREDICTION MODEL AND ITS APPLICATION

So far a prediction model for sulphate scaling tendency has been developed in this study from a solubility prediction model which is based on the Pitzer's ion interaction approach. The method and process for the model construction were described in sections (3.2), (3.3) and (3.4) of this chapter. Its advantages, important features and reliability have also been assessed in this chapter and in chapter 2. This model is considered as an update and an improvement on the previous scale prediction models, having overcome one or other shortcomings existing in the other models. Apart from the progress made in this model, some limits are still accompanied with the present model and they may be overcome in future work. The temperature range within which the model is applicable is 25 to 150°C, that is adequate in most North Sea operations but

must be extended to a higher upper limit in some other oilfields, particularly onshore fields. The specific ion effects on $BaSO_4$ scaling are ignored and the specific effects of some minor ions such as K^+ and HCO_3^- on $CaSO_4$ and $SrSO_4$ scale formation are also neglected because of insufficient solubility data available for solubility correlation, as discussed in chapter 2. For the the same reason, the possible effect of barium and strontium sulphate solid solution precipitation on $BaSO_4$ and $SrSO_4$ solubilities are not identified in the model. Also, owing to the time limitation and the complexity, the calcium carbonate scale formation is excluded from this model. If more sulphate solubility data are available in the required aqueous salt systems and more efforts are made in the future, it is hoped that the problems associated with this model can be solved and the model can be made more accurate and more comprehensive in scale prediction.

To develop a simulation model for reservoir scale occurrence and its damage to the formation, a number of questions have to be answered. First, is there any scale occurring at certain locations within the reservoir? Secondly, if any, how fast does the scale form? Thirdly, what is the relationship between the scale quantity precipitated in the rock and its damage to the formation productivity? A scaling prediction model may be helpful in answering these questions even though it cannot directly predict the scaling rate. The type of scale potentially forming in the reservoir may be predicted from this model. The model also gives the maximum quantity of scale which could form from a brine. The sulphate supersaturations can be predicted from this model. The supersaturation is one of the key factors determining the scaling rate. Together with the knowledge acquired from laboratory experiments on sulphate scale formation and the field observations, the relationship between water composition, sulphate supersaturation, scaling rate, amount of scale formed in the porous media and its damage to permeability and porosity may be revealed and consequently the reservoir modelling of scale formation can be achieved.

CHAPTER 4

REVIEW OF PREVIOUS INVESTIGATIONS OF CRYSTALLISATION AND SCALE FORMATION OF BARIUM SULPHATE, STRONTIUM SULPHATE AND THEIR SOLID SOLUTION

4.1 INTRODUCTION

In order to have an overview of the previous work that was related to barium sulphate and strontium sulphate scale formation, this chapter summarises the literature dealt with the crystallisation of the sulphates and their scale precipitation, with the stress on the laboratory investigations. Pucknell[113] and Goulding[42] have reviewed some of the previous investigations on $BaSO_4$ study in their theses but it was felt the reviews were inadequate and often restricted to a narrow area of the previous work. This chapter intends to give a broad view of the previous research on sulphate crystallisation, scale formation and formation damage due to the scale precipitation, not only limited to $BaSO_4$ scaling but also including $SrSO_4$ and $(Ba,Sr)SO_4$ solid solution. The first part of the chapter describes the natural occurrence of barite and celestite, the sulphate nucleation, crystal growth, crystal morphology and the kinetics of crystallisation as well as the crystal composition of $(Ba,Sr)SO_4$ solid solution and its relation with the composition in the aqueous solutions. The rest of the chapter reviews the sulphate scale occurrence in the oilfields and the laboratory study of the sulphate scale formation and its damage to porous media.

4.2 CRYSTALLISATION OF $BaSO_4$, $SrSO_4$ AND $(Ba,Sr)SO_4$ SOLID SOLUTION

Previous investigations gave most of attention to $BaSO_4$ and barite(or barytes, the

natural occurrence of $BaSO_4$), considerably less study has been carried out on $SrSO_4$ and celestite(or celestine, the $SrSO_4$ mineral), and little work has been done in the area of barium sulphate and strontium sulphate solid solution. This section reviews the previous research on $BaSO_4$, $SrSO_4$ and $(Ba,Sr)SO_4$ solid solution crystallisation. It comprises four subsections, each reviews a specific topic related to $BaSO_4$, $SrSO_4$ and their solid solution and the crystallisation of the sulphate minerals both in nature and in laboratory. Subsection (4.2.1) describes the structure and morphology of BaSO4 and $SrSO_4$ crystals. The natural occurrence of barite and celestite is reviewed in the next subsection, followed by the review on the laboratory study on $BaSO_4$ and $SrSO_4$ morphology in the subsection (4.2.3). Finally, the kinetics of crystal growth of $BaSO_4$, $SrSO_4$ and $(Ba,Sr)SO_4$ solid solution is reviewed in the subsection (4.2.4)

4.2.1 The Structure and Morphology of Perfect Barium Sulphate and Strontium Sulphate

The perfect single crystal of barium sulphate(barite) is a tabular of orthorhombic crystal symmetry,[29,46] as illustrated in figure(4.1). It has four distinct crystal forms: 001,102,110 and 011, as defined in Miller indices. The crystal symmetry of a strontium sulphate (celestite) crystal is also orthorhombic, the same as that of barium sulphate, and its typical habit is prismatic as also shown in figure(4.1).[29,46] The distinct forms of the crystal are 001, 010, 011, 110 and 102. The atom structure of barium sulphate is shown in figure (4.2) and strontium sulphate is isostructural with barium sulphate. Barium in the crystal can be replaced by strontium in the crystal lattice to form a continuous solid solution series from barite to celestite but intermediates are rare.[16,29,47]

4.2.2 Natural Occurrence of Barite and Celestite

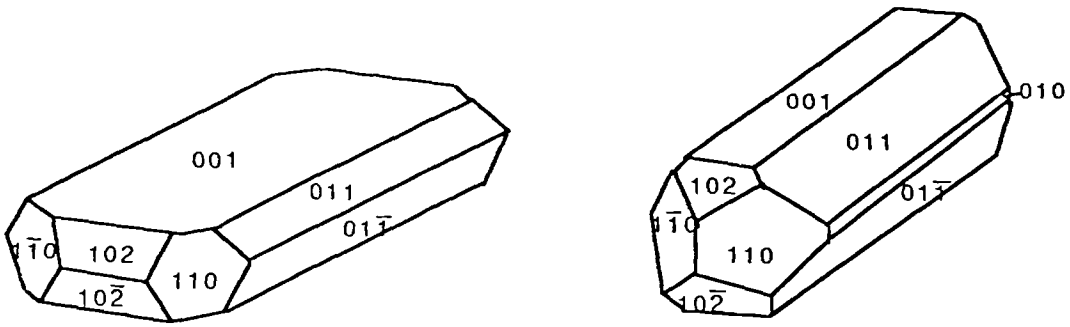

$BaSO_4$ $SrSO_4$

Figure 4.1 Crystal Symmetries of Barium Sulphate and Strontium Sulphate[29]

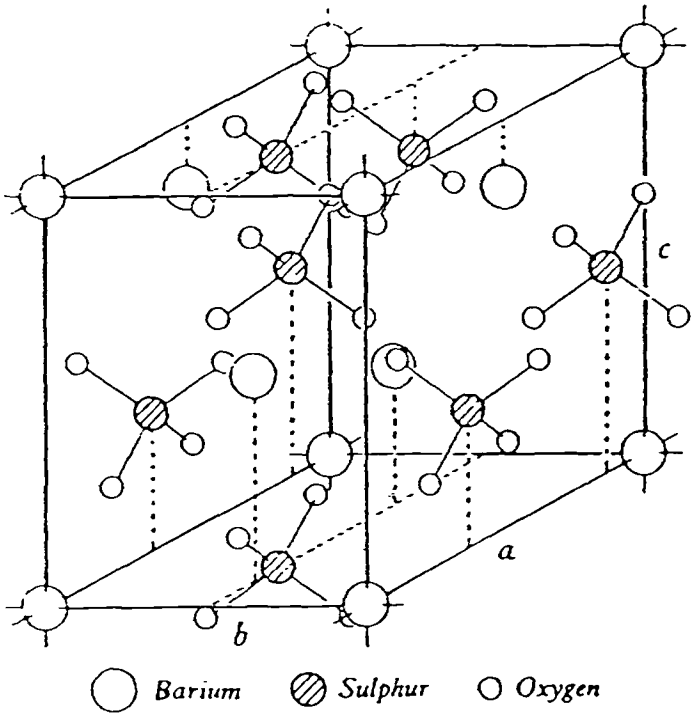

Figure 4.2 Perspective view of the structure of barium sulphate, from ref.29

a. Barite and celestite minerals

Barite is more often found in natural deposits than celestite, although both of them have approximately equal abundance in the earth.[17] Natural barite and celestite crystals are usually 100μm (micrometer) to 200μm in length.[155] Barite commonly occurs in well-formed crystals, mostly tabular and sometimes prismatic. It also occurs as globular concretions and as fibrous, lammeller, granular and earthy aggregates.[29,46] Clusters of plenty crystals are observed, which assume rosette shapes and are so called 'desert roses'.[29,46] Celestite occurs in fibrous or rounded aggregates and also as well-formed crystals with tabular(001) or prismatic habit.[29,46] Usually, barite crystal contains up to 6 to 7 molar percent of Sr and celestite contains not more than 4 molar percent of Ba in its crystals in nature, though as high as 16 percent Sr was reported existing in barite.[155]

b. Barium sulphate and strontium sulphate scales

Barite scale deposits have been found in oilfields world wide.[20,26,58,146,155] The general shape and crystal growth of $BaSO_4$ scale is similar to the natural barite mineral.[155] Like the natural barite, barium sulphate often contains a small amount of strontium sulphate in the form of solid solution rather than a mechanical mixture of two scales.[58,155] The natural $BaSO_4$ scale is typical of prismatic or tabular-shaped crystals on the order of 100 to 200μm.[155] Strontium substitution in $BaSO_4$ clearly altered the crystal habits along certain atom planes such as (113) and (203).[155] On the other hand, pure strontium sulphate scale has not been found in oilfields and relatively few cases of scale mainly composed of $SrSO_4$ were reported from the Middle East region.[32,67,126]

4.2.3 Laboratory Studies on Barium Sulphate and Strontium Sulphate Morphology

Barium Sulphate Morphology

The morphology of barium sulphate crystals precipitated from aqueous solutions have been looked at by a number of researchers since the 1940s.[7,33,34,90,138-140,153,154] The crystal nucleation and crystal growth in the solutions were carried out using different methods, mainly, the rapid precipitation by direct mixing Ba^{2+} rich solution and SO_4^{2-} rich solution, precipitation by slow dropping Ba^{2+} rich solution or SO_4^{2-} rich solution into the opposite ion rich solution, and slow precipitation of $BaSO_4$ from hydrolysis of SO_4^{2-} ions into Ba^{2+} excess solution as well as recrystallisation of barite from a brine by thermal cycling. The solution conditions and temperature were adjusted within a study or changed from one investigation to the other by different researchers. The $BaSO_4$ initial concentration for the crystal growth ranged from 0.0001m to 1.0m. Ba^{2+} to SO_4^{2-} concentration ratio varied in some studies within the range of 1 to 10. Most of the tests were conducted at ambient temperature but high temperature tests also reported. In some experiments, foreign ions such as K^+, NH_4^+, Mg^{2+}, etc. were added into the solutions in which $BaSO_4$ crystal growth was taking place.[33,154] Some tests were conducted in acid environment and the others in neutral condition. The time allowed for crystal growth was also a factor looked at in a few investigations.

Various crystal habits were observed in these experiments, such as prismatic, tabular and rectangular or less regular spherical and dendritic shapes. Suito and Takiyama[138] observed transition of crystal morphology from spherical, spindle to diamond and finally reaching rectangular particulars as $BaSO_4$ concentration reduced from 1.0m towards 0.0001m. Porous $BaSO_4$ crystals were also formed in certain solutions with foreign ions presence,[28,33] but Fischer and Ben Rhinehammer[34] in their later experiment found that foreign ions resulted in more perfection in crystal morphology and smaller size and they believed the contrary result was caused by different solution mixing method. Blount(1974)[7] found that the crystals produced in poorly cleaned flasks were smaller and less perfect. The crystal particle size differed from 0.1μm to 2mm in length.[18,140] The crystals precipitated from rapid mixing were usually small, about 1 to 20μm [7].

Blount [7] grew $BaSO_4$ crystals of 800μm long by slow adding Na_2SO_4 solution into $BaCl_2$ solution or vice versa and Brower[16] precipitated barite crystals of 50-500μm size from recrystallisation by thermal cycling.

The crystal habits and particle size are complex functions of a number of factors. The effect of supersaturation on crystal nucleation and crystal growth was one of the most important factors.[7,34,86,90,138,155] Walton and Hlabse[153] pointed out that homogeneous nucleation took place only when $BaSO_4$ concentration was above 0.01m, otherwise the nucleation was believed heterogeneous. Lower initial $BaSO_4$ concentration normally resulted in larger crystals of more perfection.[34,86,90,155] Okada and Magar(1955)[90] contradicted the findings by the other authors, they found from room temperature tests that particle size was proportional to $BaSO_4$ concentration if it was below 0.01m, and the crystal particle size was proportional to $BaSO_4$ concentration at the boiling point throughout the whole range of $BaSO_4$ concentration they used. Fischer(1951)[33] concluded that the aging of $BaSO_4$ crystals in contact with mother liquid did not result in any significant change in crystal size nor perfection unless the particle size at the start of aging period was less than 1μm, which lead to Ostwald ripening. As a rule of thumb, temperature increase resulted in more perfect crystals of larger size.[26,33,34] Different results emerged from the crystal growth in the presence of foreign ions from different studies.

Fischer(1951)[33] noted bumps formed on the crystal face which was believed to be the foreign electrolyte deposition and he also found incorporation of foreign ions in the irregular crystals. Walton and Walden(1946)[154] proved that $BaSO_4$ coprecipitated with K^+, NH_4^+ and Na^+ were solid solution by substituting Ba^{2+} with these foreign ions on one to one basis and they also found $BaSO_4$ coprecipitated from aqueous solution always contained a quantity of water, which was present as solid solution by a group of three water molecules replacing one $BaSO_4$ in the crystal lattice. Fischer and Ben Rhinehammer(1953)[34] precipitated $BaSO_4$ with the inclusion of various foreign ions in

the sulphate solution at the time of precipitation and they found that the foreign ions frequently cause an increase in crystal perfection , an increase in crystal particle size uniformity and, at higher concentrations, a decrease in the crystal size. Blount(1974)[7] found no noticeable change in the size of crystals by adding ferric chloride to a solution and precipitation of barite from a 2m HCl solution resulting in the formation of finer grained precipitate. Others[28,33] concluded that foreign ions inhibited $BaSO_4$ crystal growth, resulting in smaller and less regular crystals, also the porous nature of $BaSO_4$ crystals were attributed to foreign ions present in the $BaSO_4$ precipitation. The pH effect was studied by Fischer and Ben Rhinehammer(1953)[34] and they noticed crystal size increase with pH increase in the solution but the perfection decrease in the meantime and they also found that 100% $BaCl_2$ excess in the solution markedly decreased the crystal perfection.

The forming of clusters of $BaSO_4$ crystals were observed by Brower.[16] Nielsen(1961)[87] reported that when the initial ionic product of Ba^{2+} and SO_4^{2-} less than $10^{-4}moles^2/litre^2$, the number of $BaSO_4$ particles produced in direct mixing had no distinct change either with change in $BaSO_4$ concentration or with the duration of the precipitation. This finding was in accord with the theory of heterogeneous nucleation[152] which predicts that the total number of precipitate particles is limited to the number of impurity particles present in the solution. Compared to the barites in nature, the $BaSO_4$ crystals formed in the laboratory were generally smaller and exhibiting different habits.[26,155]

Strontium Sulphate Morphology

Few investigations have been made on strontium sulphate morphology as only five papers were found on this subject. Campbell and Nancollas [21] prepared 10-15μm size rhombic crystals of strontium sulphate in their study of kinetics of strontium sulphate crystal growth. Brower[16] synthesised strontium sulphate crystals by recrystallisation

from brine solution by thermal cycling. The largest celestite crystals obtained by this method were 80μm. Blount [7] conducted experiment on strontium sulphate crystal growth at 94°C by slow dropping sodium sulphate solution into strontium chloride solution or vice versa. The $SrCl_2$ concentration in the solution were from 0.001 to 0.1m and Na_2SO_4 from 0.005 to 0.02m. HCl ranging from 0.001 to 0.67m was added in the solution. The crystals formed were of various sizes with distinctive external morphology and the largest crystal was 1.2mm long. Small crystal aggregates were common. In general, $SrSO_4$ crystals were larger than those of $BaSO_4$, which agreed with the order of increasing solubility from $BaSO_4$ to $SrSO_4$. Precipitation of unseeded supersaturated aqueous solutions of $SrSO_4$ was carried out by Suhnel and Handlirova(1984).[137] The initial $SrSO_4$ concentration in their experiment varied from 1.10^{-3} to 2.10^{-2}m. 50ml of $SrCl_2$ solution was thermostated at 25°C and 50ml of the equimolar solution of Na_2SO_4 was added quickly under continuous agitation. The crystals formed were of a few micrometers with distinct edges and faces. Sarig(1974)[122] grew $SrSO_4$ crystals from 0.015m solution by mixing equal volume, equal concentration $SrCl_2$ and Na_2SO_4. The crystal precipitation was allowed for 24 hours either at static or with vigorous stirring. Single, well-developed and uniform crystals, about a few micrometers in length, were precipitated from the solutions. Growth steps were distinctly visible on some crystallographic faces. Stirring did not change the habit of the single crystals, except that smaller crystals by an order of magnitude were precipitated onto the large crystals.

Barium and Strontium Sulphate Solid Solution: Morphology and Composition

As mentioned in subsections (4.2.1) and (4.2.2), barite often contains a few percent strontium and a small amount of barium also sometimes exists in celestite in nature and a complete series of solid solutions can be formed from barium sulphate and strontium sulphate, though the intermediate compositions are rare in nature. A few investigations

were carried out on the formation of (Ba,Sr)SO_4 solid solution, their composition as well as the effect of strontium replacement of barium in the crystal on the morphology.(Brower1973, Blount1974, Hanor1968 and Gordon et al. 1954).[7,16,41,47]

Brower[16] stated that a complete series of solid solutions between barium sulphate and strontium sulphate in which Ba^{2+} and Sr^{2+} ions substitute one another in the orthorhombic crystal were synthesised by precipitation from aqueous solution. In his study, the solid solutions were recrystallised from brine by thermal cycling between 35 and 185°C. The initial brine was the mixture of 5-7mg of $BaSO_4$ powder and 12ml solution of 0.05m in strontium chloride and 5m in sodium chloride. The electron probe microanalysis showed that the solid solutions were homogeneous within detection limits. The crystals were measured 50-200μm and the molar ratio of Sr to Ba was 1:4 in the solid solutions.

Blount [7] also prepared uniform barium sulphate and strontium sulphate solid solution crystals by slowly dropping 0.0005 to 0.02m Na_2SO_4 solution into 0.001 to 0.1m $SrCl_2$+$BaCl_2$ solution (Sr/Ba ratio = 0.03 to 0.15). $SrCl_2$+$BaCl_2$ solution was acidified with 0.01 to 0.67molars of HCl and heated to 94°C before Na_2SO_4 solution was added. Sr/Ba ratios in the formed solid solution crystals varied between 1/30 to 1/80 of the Sr/Ba ratio in the solution. The crystal size was not mentioned but a crystal about 0.05mm was shown in a picture in the paper. Most of the crystals had the external morphology similar to that of pure $BaSO_4$ or $SrSO_4$ crystals. At higher strontium contents, many crystals had a distorted barrel like appearance.

A different approach was used in the co-precipitation of barium sulphate and strontium sulphate by Gordon et al.[41] The solid solution crystals were formed at 83°C by the hydrolysis of methyls sulphate in 20% methanol and 80% water medium containing $SrCl_2$+$BaCl_2$. On the contrary to the findings by Brower and Blount, they reported that within the initial ratios of barium to strontium concentration from 1.3 to 2700, strontium appeared to be heterogeneously distributed throughout the solid solution phase.

The results from the different investigations all indicated that precipitation of $(Ba,Sr)SO_4$ solid solution tended to remove Ba from aqueous solution at a faster rate than removing Sr. As a result, the content of Sr in the crystal was low but it increased with the crystal digestion time. To relate the Sr/Ba ratio in aqueous solution to that in the solid phase or to relate the initial Sr/Ba ratio in the aqueous solution at the starting of precipitation to that in the later stage of the precipitation, a distribution coefficient λ was often referred to.[7,41,47] When the solid phase is in equilibrium with the ions in the aqueous solution,

$$Sr_f/Ba_f = \lambda \frac{N_{SrSO4}}{N_{BaSO4}} \qquad (4.1)$$

where Sr_f and Ba_f are the final molal concentrations of the species in the aqueous solution. N is the molal fraction in the solid. The other expression is Doerner-Hoskin relation for relating the initial concentrations of Ba and Sr to their final concentrations in the aqueous solution,[41,47]

$$(Ba_i/Ba_f) = (Sr_i/Sr_f)^{\lambda} \qquad (4.2)$$

Brower considered that the $(Ba,Sr)SO_4$ solid solution series was ideal in behaviour, that is, λ was equal to the ratio of the thermodynamic solubility product of $BaSO_4$ to that of $SrSO_4$. Gordon et al found λ was about 33. Most of the Sr present barites synthesised by Blount had λ values between 33 and 66 and he suggested that the solid solutions were non-ideal because λ should be 390 for the ideal solid solutions, according to the ratio of the thermodynamic solubility products of $BaSO_4$ and $SrSO_4$ at his experimental condition (95°C). Gordon et al also stated that λ was affected by experimental conditions such as the different methods of precipitation and stirring during

crystal growth.

4.2.4 Kinetics of Crystal Growth of Barium Sulphate, Strontium Sulphate and Their Solid Solution

An Overview

The kinetic factor of nucleation and crystal growth of scale-forming minerals was considered more important in determining the course of the precipitation process than the models based on equilibrium solubilities(Nancollas and Liu1975).[82] During oilfield production, reservoir fluids are always in a state of moving from one location to the other. The brine composition changes as the injected water mixes with the formation water, as the environment surrounding the brine changes or due to changes in the other conditions such as pH and pressure. The kinetics of crystal growth of the scaling minerals plays a key role in determining where the scale deposition occurs, how fast the scale precipitation in a brine, and how much a scale would form in a particular location in a field. Therefore, in order to know the mechanism by which the sulphate scales occur, the kinetics of sulphate crystallisation has to be understood at first.

The crystallisation involves two steps: crystal nucleation(or initiation) and crystal growth. The nucleation can be heterogeneous, where there is a substrate or particle to help lower the energy barrier and serving as nucleus for crystal growth, or homogeneous, where the nucleation is spontaneous. Most of the nucleations occurring in nature were heterogeneous(Walton 1966).[152] The nucleations of barium sulphate and strontium were usually heterogeneous unless their supersaturations were above a critical value (Gardner and Nancollas 1983)[38]. Walton and Halbe(1963)[153] pointed out that barium sulphate nucleation was heterogeneous if the initial supersaturation of $BaSO_4$ was less than one hundred times of the solubility and Nielsen[87] considered the initial ionic product of barium and sulphate ions equal to $10^{-4}moles^2/litre^2$ to be the critical value(cited from Walton and Halbe1963), judging from the dependence of crystal particle number on barium sulphate concentration and the duration of precipitation. For

precipitation of strontium sulphate, homogeneous nuleation takes place only in the solution at least 50% supersaturated and immediate spontaneous crystallisation starts at 75% original supersaturation (Campbell and Cook 1935).[20] Suhnel and Handlirova(1984)[137] studied seeded growth of $SrSO_4$ crystals under continuous stirring and they found that the nucleation in the aqueous was controlled by the heterogeneous nucleation mechanism when the supersaturation was less than 16. According to their critical values, most of the barium sulphate and strontium sulphate scale depositions should be initiated by a heterogeneous nucleation process.

Kinetics of $BaSO_4$ Crystallisation

Collins and Leineweber[25] investigated the kinetics of nucleation and growth of barium sulphate crystals in homogeneous precipitation using both electrical conductivity and light scattering measurements. The nucleation appeared probably heterogeneous even though the solution was not seeded with crystals or particles. This proved the extremely difficulty in inducing homogeneous nucleation, as stated by Nancollas and Purdie(1963).[83] Collins and Leineweber also found that the $BaSO_4$ crystal growth was controlled by the diffusion from bulk solution to crystal surface. Nancollas and his coworkers studied seeded $BaSO_4$ crystal growth at 25°C as well as elevated temperatures(Gardner&Nancollas1983, Nancollas&Liu1975, Nancollas&Purdie1963 and Nancollas&Reddy1974)[38,82,83,84], mainly by means of conductivity measurement. They found that the $BaSO_4$ crystal growth was surface reaction controlled and followed a second-order rate equation after an initial surge. The rate equation for equal initial Ba^{2+} and SO_4^{2-} concentrations may be expressed as,

$$-dm/dt = k.s.(m-m_o)^n \qquad (4.3)$$

where m is the $BaSO_4$ molar concentration, t is the precipitation time, m_o is the

$BaSO_4$ molar concentration at precipitation equilibrium (i.e. the solubility), k is the rate constant and s is a function of the number of growth sites available for deposition. n is normally equal to 2 but for the initial surge period, n is as large as 20 (Nancollas and Purdie 1963)[83].

When either barium ions or sulphate ions are in excess in the aqueous solution, the rate equation has the form,

$$-dm/dt = k'.s.[(m_{Ba^{2+}})^{1/2}.(m_{SO_4^{2-}})^{1/2} - K^{1/2}_{sp,BaSO4}/f_X]^2 \quad (4.4)$$

in the equation, k' is the rate constant, smaller than k in equation (4.3) and dependent on which ion is in excess. $K_{sp,BaSO4}$ is the thermodynamic solubility product of $BaSO_4$ and f_X is the activity coefficient of the divalent ions. The initial growth surge could result in up to 30% of total precipitation reaction (Nancollas and Reddy 1974).[84] The initial surge was considered to be the result of secondary nucleation taking place on the crystal seeds while the crystal growth was proceeding.(Nancollas and Purdie1963).[83] The duration and extent of the surge may be reduced or even eliminated by increasing the number of growth sites available initially or lowering the degree of supersaturation.

Gardner and Nancollas (1983)[38] raised the temperature for $BaSO_4$ crystal growth to between 105 and 150°C. The formation of $BaSO_4$ crystals was controlled by a surface reaction and was independent of fluid dynamics at the solid-liquid interface. The rate of growth was proportional to the square of the supersaturation, in agreement with the results previously established at ambient temperature. The only difference observed at elevated temperatures was that the initial growth surge disappeared, attributing to the increased growth rates at higher temperatures which competed favourably with any concurrent nucleation process.

All the crystal growth processes investigated by Nancollas and co-workers were of surface reaction controlled mechanism, while the crystal growth by Collins and Leineweber(1956)[25] was found to be diffusion controlled but the initial supersaturation

in their experiment was as high as 32. The surface control process involves the formation of an adsorbed surface layer of hydrated Ba^{2+} and SO_4^{2-} ions.(Nancollas & Purdie 1963)[83] It was suggested that diffusion of ions from solution to the growing crystal surface may be important at high $BaSO_4$ supersaturation while, at conditions close to equilibrium, surface reactions were rate-limiting.(Gardner and Nancollas 1983).[38]

In addition, the growth rate of barium sulphate by using $Ba(OH)_2 + H_2SO_4$ was compared to that of using $BaCl_2 + Na_2SO_4$ to investigate the effect of other ions, i.e, Na^+ and Cl^- , on the $BaSO_4$ growth. No apparent difference was observed on the growth rate.(Nancollas 1968)[80]

Kinetics of $SrSO_4$ Crystallisation

Campbell and Cook (1935)[20] investigated the spontaneous crystallisation of strontium sulphate and their results were already discussed in the overview of this subsection. The crystal growth of $SrSO_4$ in aqueous solution with seed crystals were studied by Campbell and Nancollas(1969).[21] The results were similar to those for $BaSO_4$ crystallisation observed by Nancollas and co-workers, as described in the last paragraph, that is, the growth of the crystals followed an equation in which the rate of crystallisation was proportional to the square of the relative $SrSO_4$ supersaturation in the solution and this stage was often superseded by an initial growth surge. The growth rate of $SrSO_4$ was slow in comparison with that of $BaSO_4$ crystals. similarly, the following rate equation was conformed to by the crystal growth of equal initial Sr^{2+} and SO_4^{2-} concentrations,

$$-dTm/dt = k.s.(m-m_o)^n \qquad (4.5)$$

where Tm represents the total concentration of strontium sulphate and the parameters have the same meanings as in the equation (4.3). For the initial surge, n = 13, then n=2 throughout the crystal growth. Also, if Sr^{2+} or SO_4^{2-} ions were in excess, the rate of crystallisation followed the next equation,

$$-dTm/dt = k'.s.[(m_{Sr^{2+}})^{1/2}.(m_{SO4^{2-}})^{1/2} - K^{1/2}_{sp,SrSO4}/f_2]^2 \qquad (4.6)$$

where Tm is the total $SrSO_4$ concentration in the solution and f_2 is the activity coefficient for the divalent ions. Unlike the situation of the barium sulphate growth, here k' is the same as k in equation(4.5) for equivalent concentrations. It implies that the excess of either Sr^{2+} or SO_4^{2-} ions has no effect on the subsequent growth rate. In addition, changes of ionic strength introduced by using $Sr(OH)_2 + H_2SO_4$ in place of $SrCl_2 + Na_2SO_4$ for the precipitation of the $SrSO_4$ crystals were without effect on growth rates, the same as seen in barium sulphate crystal growth.

Suhnel and Handlirova(1984)[137] studied seeded growth of $SrSO_4$ crystals under continuous stirring. The concentration of $SrSO_4$ in the solution used in the precipitation was from 0.01 to 0.02m. The nucleation in the aqueous was controlled by the heterogeneous nucleation mechanism when the supersaturation was less than 16. The growth of $SrSO_4$ crystals in the solution of supersaturations less than 5.6 was of second order with respect to the concentration and at 25-45°C the process was controlled by the surface reaction mechanism. Nielsen(1969),[88] on the other hand, investigated crystallisation of $SrSO_4$ and $BaSO_4$ in highly supersaturated solutions. In the precipitation, homogeneous nucleation was followed by diffusion controlled crystal growth. He stated that after a supersaturated solution had been made by rapid mixing of two stable solutions, there was often a period where no change could be observed. The number of particles formed was a function of the ionic product, i.e, $[Sr^{2+}].[SO_4^{2-}]$, differing from that of a heterogeneous nucleation. Unseeded crystallisation of $SrSO_4$

from aqueous solutions of 0.01 to 0.02m initial $SrSO_4$ concentrations under stirring was studied by Packter(1974).[92] The nucleation occurred during induction periods and continuous regular growth then took place on the nuclei formed during these periods. The induction periods were very prolonged in the solutions of low supersaturation(from 1.2 to 3), and then over the range of supersaturation from 3 to 30, they decreased with increasing supersaturation from about 5000 seconds to less than 2 seconds. The crystal growth was rate-controlled by the rate of deposition of metal salt ions onto the growing crystal surfaces. The rate followed a second-order equation in respect to the residual excess solute ion concentration in the solution, as proposed by Campbell and Nancollas.[21]

Kinetics of $(Ba,Sr)SO_4$ Crystallisation

Gardner and Nancollas[38] studied barium sulphate crystal growth in the presence of strontium ions in the aqueous solution. Trace Sr^{2+} ions ($(1.0 - 10)x10^{-5}$molar) were included in the barium sulphate solutions. It was noted that the growth rate of $(Ba,Sr)SO_4$ solid phase was considerably slower than that for pure $BaSO_4$ crystal and the final equilibrated solid phase had an effective solubility which was approximately 30% lower than that for pure barium sulphate, i.e, more $BaSO_4$ precipitated from the solution in the presence of Sr^{2+} ions before reaching the equilibrium than without Sr^{2+} ion presence. Hanor[47] pointed out that precipitation of $(Ba,Sr)SO_4$ tends to remove Ba from aqueous solution at a faster rate than it removes Sr and Blount [7] also suggested that the earlist formed portion of the $(Ba,Sr)SO_4$ crystal had a higher Ba content.

4.3 FORMATION DAMAGE ARISING FROM BARIUM SULPHATE, STRONTIUM SULPHATE AND THEIR SOLID SOLUTION SCALE PRECIPITATION

Water scaling problems have accompanied oilfield production since its early days and the difficulties caused by scale occurrence in oil operations have been reported constantly in oilfields around the world. In particular, barium sulphate and it related scale deposition is one of the major production problems in most of the North Sea offshore fields.[58,77,115] Due to the importance of solving the scaling problems in petroleum industry, numerous investigations have been carried out to understand, predict, prevent and treat scale formation. The results obtained from these investigations were well reviewed by Cowan and Weintritt(1976)[26] and Case(1976)[23] in their books. Pucknell[113] thoroughly reviewed the literature on $BaSO_4$ scaling problems. Oilfield scale deposition was traditionally considered as the problems occurring in the well bottom holes, well tubing, valves, heaters and other water handling facility, only Weintritt and Cowan(1967)[155] showed some interest in scale precipitation in rock. In recent years, as water flooding has been ever increasingly implemented and the incompatibility between the injected water and the formation water is recognised as the main scaling cause, particularly in the North Sea oil operations, more and more concern has arisen about scale deposition in the reservoir formation and its potential damage to the rock productivity and some research activity has been directed to this problem.[5,42,44,77,94,113,115] As related to the present study, this section reviews the work aimed at the formation damage due to scale deposition.

The earliest study of the rock permeability impairment by scale formation was conducted by Weintritt and Cowan.[155] In their test, a core saturated with formation water was subsequently flooded with the injection water. No scale precipitation was found in the rock core after flowing the injection water through the core and this result was confirmed by Mitchell et al.[77] This finding is understandable because such a small amount of formation water was mixed with the injection water, even if any scale precipitation occurred in the core it would be so little to be visible. Mitchell et al.[77] and Read & Ringen[115] did the scale formation tests by flowing both artificial North Sea water and formation water concurrently through the aluminium core plugs at 70°C and pressure drops were observed during the tests. The tested core samples were then

examined by scanning electron microscopy and the scaling crystals were found deposited on the rock pore surface. The scale composition was not mentioned by Mitchell and the scale was (Ba,Sr)SO_4 and $CaCO_3$ from the test by Read and Ringen. In the earlier period of the present scale project, Pucknell[113] and Goulding[42] carried out laboratory investigation of the formation damage due to barium sulphate scale formation at ambient temperature and pressure. Pucknell confirmed that $BaSO_4$ scale would occur in the rock as the result of continuous flowing two incompatible waters through a core. On the basis of the Pucknell's work, Goulding systematically studied the barium sulphate scale formation both in the static bulk solutions and under dynamic flow in the rock cores by mixing two simple brines, one was sulphate ion rich and the other barium ion rich. He found that the brine ionic strength and $BaSO_4$ supersaturation had large effects on the scaling crystal morphology and the extent of rock permeability.

CHAPTER 5

EXPERIMENTAL INVESTIGATION OF SULPHATE SCALE FORMATION: AN OVERVIEW

5.1 INTRODUCTION

The purpose of the present experimental investigation of sulphate scale formation was to understand the mechanism of the scale occurrence and its damage to rock permeability by acquiring the following information,

i. The Nature of Sulphate Scale

a. scaling crystal morphology,
b. the scaling sites on the rock pore surface and the positioning of the scaling crystals in the pore space, and
c. the scale distribution along the length of the core.

ii. The Kinetics of Scale Formation

a. nucleation of scaling crystals,
b. crystal growth,
c. crystal precipitation and deposition on the rock pore surface, and
d. crystal growth after deposition.

iii. The Rock Permeability and Porosity Damage Due to Scaling

a. the permeability curve pattern,
b. the permeability decline rate,

c. the extent of permeability damage,

d. the extent of rock porosity damage, and

e. the relation between the permeability decline and porosity reduction or scale quantity

iv. The Factors Influencing the Scaling and Permeability Damage

a. the brine $BaSO_4$ and/or $SrSO_4$ supersaturations,

b. the scaling ion concentration ratio,

c. initial rock permeability and porosity,

d. the temperature effect, and

e. hydrodynamic forces.

These pieces of information obtained from the laboratory test were analysed individually or in combination. The relations between the different aspects of the sulphate scale formation and their dependence on the influencing factors were then revealed. The implications to oilfield scale occurrence were drawn from the findings, which may be helpful in planning waterflooding projects and in implementing scale prevention or scale treatment techniques. The results can also provide data for future reservoir modelling of sulphate scaling.

In this chapter, first, the scope of the present laboratory study is outlined. Then the brines used in the study are described. After that, the experimental equipment and instruments used in conducting the static beaker test and dynamic core flow test are presented. The injection face and the multi-pressure tapped core holder are described, followed by the description of the experimental methods and procedures. Next, the analytical techniques used for the core flow brine effluent samples, the crystal samples, the scaled core samples and porosity, etc. are introduced. Finally, the experimental results are briefly summarised.

5.2 THE SCOPE OF THE LABORATORY STUDY

Dynamic core flow tests as well as static bulk solution tests (beaker tests) were carried out in this study to investigate $(Ba,Sr)SO_4$ solid solution scale formation and its damage to the rock permeability as well as porosity, due to mixing of incompatible waters.

The formation damage arising from $(Ba,Sr)SO_4$ solid solution scale formation was the main concern in the investigation. The beaker test (or jar test) of scale precipitation served in this study as a useful means to provide comparison with the scale formation results obtained from the dynamic core flow tests and a means to provide some guidance in preselection of the brine composition for use in the consequent core tests. From comparing the size and morphology of the scaling $(Ba,Sr)SO_4$ crystals grown in the rock pores under flow influence with those of the crystals precipitated in a static bulk solution, the effects of rock surface property, the rock porous structure and the hydrodynamic forces on the scaling crystal precipitation and deposition may be revealed.

Two brines were used in each test, one was Ba^{2+} and Sr^{2+} ions rich, resembling the North Sea field formation water, and the other contained excess of SO_4^{2-} ions, resembling the North Sea water. The scale formation in the static bulk solution was achieved by rapid direct mixing the two incompatible waters and the mixing of two brines in the core was realised by concurrently flowing the two waters through the core plug to study the scale precipitation in the porous media. Most of the brines used in the mixing were simple artificial brines, that is, only the scaling ions and sodium chloride were present in the solutions, in order to systematically investigate the solid solution scale formation and the influencing factors without complication of the other ion components. Also synthetic full component North Sea water, Forties formation water and South Brae formation water were used to illustrate the scaling problems close to the oilfield reality. The experiments were carried out at both ambient temperature(20°C) and elevated temperature(70°C) and no back pressure was applied to the core flow tests. The $(Ba,Sr)SO_4$ solid solution scale formation and the formation damage caused by the scale

precipitation were subject to a number of factors, the influencing factors investigated in this study were,

i. supersaturation of $(Ba,Sr)SO_4$ in the aqueous solution,*

ii. concentration ratio of Ba^{2+} to Sr^{2+} in the brine,

iii. concentration ratio of $(Ba^{2+} + Sr^{2+})$ to SO_4^{2-} in the brine,*

iv. initial rock permeability,

v. initial rock porosity,**

vi. temperature change, and

vii.hydrodynamic forces.

The factors listed above marked with * were only examined in the ambient temperature experiments and that marked with ** was only examined at elevated temperature. The affecting factors were looked at in the experiments by changing the brine composition, selecting rock cores of different initial permeabilities or porosities, and changing the experimental conditions.

5.3 DESCRIPTION OF THE BRINES USED IN THE STUDY

This section gives a description of the compositions and the compositional characteristics of the brines used in the $(Ba,Sr)SO_4$ scale formation. The brine composition is referred to as the actual salt or ion concentrations in a brine while the brine compositional characteristics is represented by the solution ionic strength(I), scaling sulphate supersaturation(s) in the brine(SP), and the concentration ratio between the scaling ions(ICR). The solution ionic strength is defined by equation (2.2) in chapter 2 and the sulphate supersaturation is defined by equation (3.1) in chapter 3. For convenience of reference, their definitions are given here again,

$$I = 1/2 \, \Sigma \, m_i \, z_i^2 \qquad (5.1)$$

where m_i usually refers to the molality(mole/1000g solvent) of any ion i in the brine and z_i is its charge but for the convenience of preparing the brines, the solution ionic strength was measured in molarity (mole/litre solution, slightly differs from molality) in this study. The solution ionic strength is a reflection of the brine total salinity.

$$SP_{MX} = \frac{(m_M \cdot m_X)^{1/2}}{Q_{sp,MX,e}} \qquad (5.2)$$

where m_M is the concentration of the scaling cations M (Ba^{2+} or Sr^{2+}) and m_X is that of scaling anions X (SO_4^{2-}), $Q_{sp,MX,e}$ is the square root of the stoichiometric solubility product of the sulphate MX at equilibrium. MX here refers to $BaSO_4$ or $SrSO_4$. The supersaturation reflects the degree of oversaturation of a sulphate in a brine under the given conditions and indicates the driving force for the sulphate to form solid scale in the brine.

The ion concentration ratio ICR was used in this study to represent the ion concentration ratio in an aqueous solution between barium and strontium or between the scaling cations(barium and strontium ions) and the sulphate anions.

The compositions and characteristics of the simple artificial brines used in this study are presented in tables (5.1) and (5.2), respectively. (The brines marked with * are those only tested in the ambient temperature investigation). The brines were made up by dissolving the regent grade chemicals into the distilled water and the solution ionic strength was adjusted by adding NaCl into the solution. The brines were divided into three groups BS, BSH and BSS according to their compositional characteristics and each group in turn comprised a few brines differing in the concentration ratio of Ba^{2+} to Sr^{2+}. The $BaSO_4$ supersaturation was 15 and the molar ratio of (Ba^{2+} + Sr^{2+}) to SO_4^{2-} was 2 in all the four BS brines but the molar ratio of Sr^{2+} to Ba^{2+} in the different BS brines varied from 0.1 to 1000. The brines BSH1 and BSH2 were the same as the brines BS1 and BS2, respectively, apart from that the $BaSO_4$ supersaturation was 30 in

Table 5.1 Compositions of Simple Brines

Brine		Salt concentrations (moles/litre solution at 20°C)			
		NaCl	$BaCl_2$	$SrCl_2$	Na_2SO_4
BA	Ba/Sr rich	0.495	0.00218	0.	0.
	SO_4 rich	0.495	0.	0.	0.00218
BS0	Ba/Sr rich	0.496	0.00295	0.00030	0.
	SO_4 rich	0.496	0.	0.	0.00162
BS1	Ba/Sr rich	0.495	0.00218	0.00218	0.
	SO_4 rich	0.495	0.	0.	0.00218
BS2	Ba/Sr rich	0.461	0.00031	0.03072	0.
	SO_4 rich	0.461	0.	0.	0.01552
BS3	Ba/Sr rich	0.378	0.00010	0.09756	0.
	SO_4 rich	0.378	0.	0.	0.04884
BSS0	Ba/Sr rich	0.486	0.00208	0.00020	0.
	SO_4 rich	0.486	0.	0.	0.00228
BSS1	Ba/Sr rich	0.485	0.00154	0.00154	0.
	SO_4 rich	0.485	0.	0.	0.00308
BSS2	Ba/Sr rich	0.466	0.00022	0.02172	0.
	SO_4 rich	0.466	0.	0.	0.02194
BSS3	Ba/Sr rich	0.419	0.00007	0.06898	0.
	SO_4 rich	0.419	0.	0.	0.06906
BSH1*	Ba/Sr rich	0.489	0.00436	0.00436	0.
	SO_4 rich	0.489	0.	0.	0.00436
BSH2*	Ba/Sr rich	0.422	0.00061	0.06144	0.
	SO_4 rich	0.422	0.	0.	0.03102

Table 5.2 Compositional Characteristics of Simple Brines

Brine group 1 (BS brines)

Solution ionic strength	0.5M
$BaSO_4$ supersaturation	15(20°C) / 8.3(70°C)
Molar ratio $(Ba+Sr)/SO_4$	2

BS brines	molar ratio Sr/Ba	$SrSO_4$ supersaturation
BS0	0.1	0.12 / 0.14 (20°C / 70°C)
BS1	1.0	0.37 / 0.46
BS2	100	3.8 / 4.6
BS3	1000	11.9 / 14.2

Brine group 2 (BSS brines)

Solution ionic strength	0.5M
$BaSO_4$ supersaturation	15(20°C) / 8.4(70°C)
Molar ratio $(Ba+Sr)/SO_4$	1

BSS brines	molar ratio Sr/Ba	$SrSO_4$ supersaturation
BSS0	0.1	0.12 / 0.14 (20°C/70°C)
BSS1	1.0	0.38 / 0.46
BSS2	100	3.8 / 4.6
BSS3	1000	11.9 / 14.7

Brine group 3 (BSH brines)*

Solution ionic strength	0.5M
$BaSO_4$ supersaturation	30(20°C) / 16.7(70°C)
Molar ratio $(Ba+Sr)/SO_4$	2

BSH brines	molar ratio Sr/Ba	$SrSO_4$ supersaturation
BSH1	1.0	0.75 / 0.92 (20°C/70°C)
BSH2	100	7.5 /9.1

Brine BA

Solution ionic strength	0.5M
$BaSO_4$ supersaturation	15(20°C) / 8.3(70°C)
Molar ratio Ba/SO_4	1

BSH brines rather than 15 as in BS brines. The BSS brines differed from the corresponding BS brines only in that the molar ratio of (Ba^{2+} + Sr^{2+}) to SO_4^{2-} was 1 in BSS brines while it was 2 in BS brines. In order to study the transition of scale nature from pure $BaSO_4$ precipitation to (Ba,Sr)SO_4 solid solution, a brine made of Ba^{2+} and SO_4^{2-} ions without any Sr^{2+} ions was also tested both under static condition and dynamic flow condition, parallel to the tests for brines BSS. This brine was labelled as BA and its composition and the compositional characteristics are also given in tables (5.1) and (5.2), respectively. Each labelled simple brine in tables (5.1) and (5.2) was actually made from mixing two opposite brines during a test, one contained excess of Ba^{2+} and Sr^{2+}, and the SO_4^{2-} ions were in excess in the other brine. The composition and characteristics of a labelled brine, e.g. BS1, therefore referred to those in the initial state of the mixed brine.

Similarly, the full component North Sea water, the full component Forties formation water and South Brae formation water were synthesised by dissolving all the required salts into the distilled water. The salts were regent grade chemicals. The composition and compositional characteristics of the full component field waters are shown in tables (5.3) and (5.4), respectively. From their compositions, we can see that the North Sea water contains excess of SO_4^{2-} ions while the two formation waters are rich in Ba^{2+} and Sr^{2+} ions. As the injected sea water commingles with either of the formation waters, the (Ba,Sr)SO_4 solid solution scale is likely to precipitate from the mixed fluids. For convenience, the 50:50(equal volume) mixed North Sea water and Forties water is labelled as water 1 and the 50:50 mixed North Sea water and South Brae water is labelled as water 2 in the thesis.

5.4 EXPERIMENT EQUIPMENT

5.4.1 The Apparatus for Static Beaker Test

The salts used for preparing the brines were regent grade chemicals. They were:

Table 5.3 Compositions of Full Component Field Waters

Ions (mg/L)	North sea water	Forties water	South Brae water
Na	10,890	29,370	41,900
K	460	372	1,700
Mg	1,368	504	102
Ca	428	2,809	779
Sr	8	574	369
Ba	0	252	2180
Cl	19,700	52,360	68,000
SO_4	2,960	11	5
HCO_3	124	496	2,140
Fe-III	0	0	4
Ionic strength(M)	0.72	1.58	2.00

Table 5.4 Compositional Characteristics of 50:50 Mixed Field Waters at 70°C

Specifications	Water 1*	Water 2*
Solution ionic strengh (M)	1.15	1.36
$BaSO_4$ supersaturation	22.7	63.9
$SrSO_4$ supersaturation	2.0	1.6
Sr/Ba molar ratio	3.72	0.27
(Ba+Sr)/SO_4 molar ratio	0.28	0.65

* Water 1 is the equal volume mixture of North sea water and Forties formation water. Water 2 is the equal volume mixture of North sea water and South Brae formation water.

NaCl, KCl, $BaCl_2.2H_20$, $SrCl_2.6H_20$, $CaCl_2.6H_20$, $MgCl_2.6H_20$, $FeCl_3$, Na_2SO_4 and $NaHCO_3$. 250ml scrupulously clean glass jars were used for preparing the brines and for scaling crystal growth. The 0.45μm filter papers and a Millipore vacuum filtration system was used to filter the precipitated $(Ba,Sr)SO_4$ crystals from the brines. A humidity oven was used to store the crystal samples on the filter paper and finally, a Scanning Electron Microscopy (SEM) was used for microscopic study of the scaling crystals.

5.4.2 The Material and Equipment for Core Tests

Core Material

The rock cores used in the core flow tests were Clashach sandstone outcrop quarried from the Elgin area of Scotland. The rock was quite clean with a very low clay content. Most parts of the rock consisted of well cemented grains of quartz with some feldspars and micas. The rock absolute permeability varied from a few tens up to a couple of thousands of millidarcies and the porosity ranged from 12 to 24% of the bulk core volume, which provided a wide range of choice in terms of initial rock perm-poro characteristics. Figure (5.1) shows a scanning electron micrograph of an unscaled Clashach core sample. In this study, the core plugs were drilled from the Clashach rock blocks labelled 15, 16, 25, 27, 28, 29, 32 and 33. In general, the inlet line pressure increase was observed when a core was initially flowed with distilled water at a constant flowrate and the initial water effluents from the core were yellowish cloudy.

Core Holders

A clamp core holder was used for the formation damage experiments at 20°C and a steel core holder was used for the experiments at 70°C. The newly designed multi-pressure tapped steel core holder was made available only after the ambient temperature tests had completed. In the following, these two core holders are illustrated

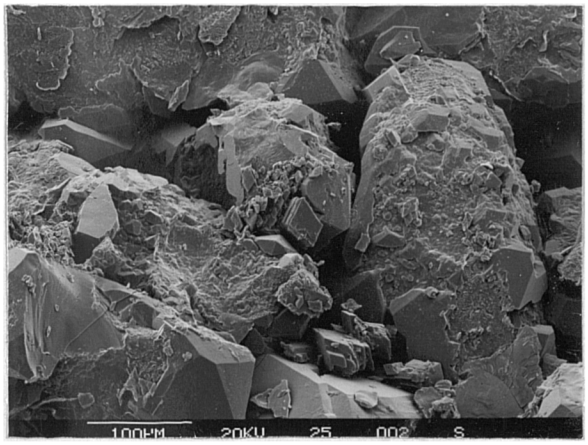

Figure 5.1 Scanning electromicrograph of an unscaled Clashach core

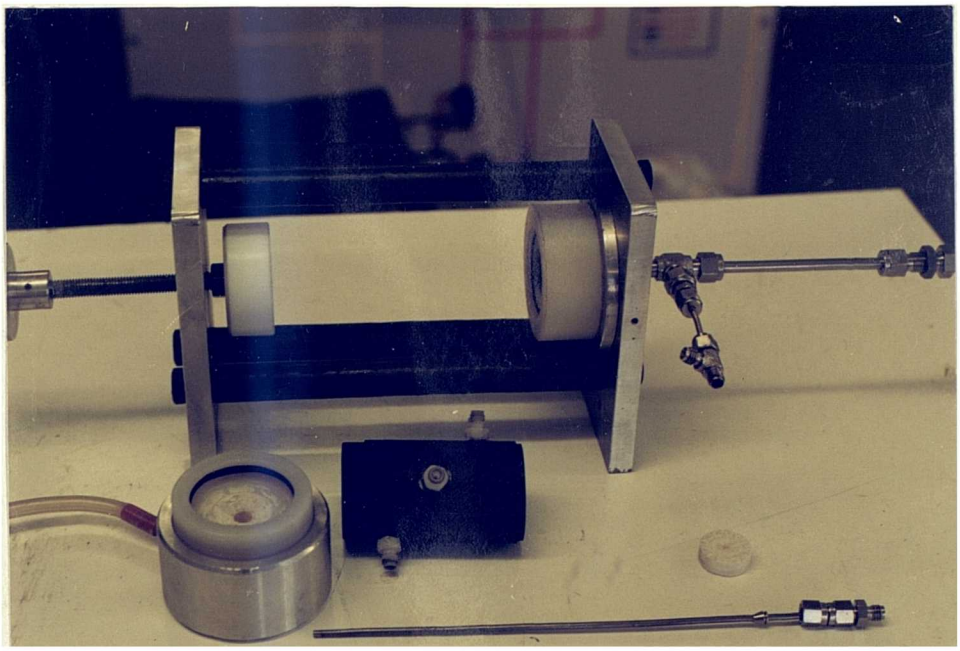

Figure 5.2 Dismantled clamp core holder and the resin bound core

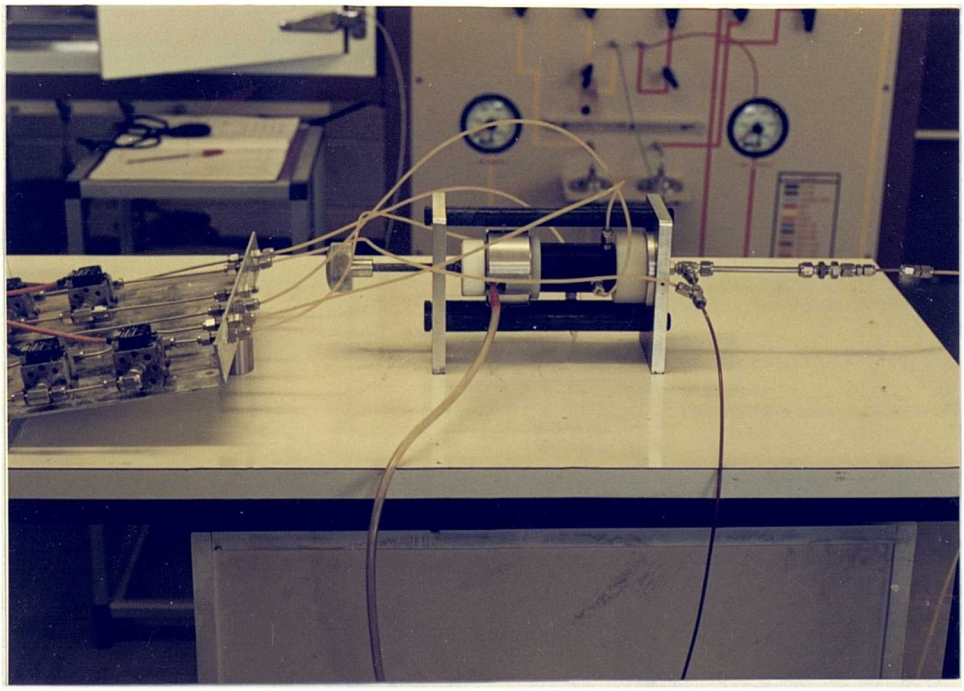

Figure 5.3 Resin bound core and clamp core holder in assembly, the blocks on the aluminium plate are differential pressure transducers

and described.

For the experiments carried out at ambient temperature, the clamp core holder was used for mounting resin cast core plugs. Figures (5.2) and (5.3) respectively show the clamp core holder without and with a core plug on it. Due to the time-consuming process of preparing the resin cast core and the pressure and temperature restriction on the resin, a steel core holder specified by the scale project was subsequently manufactured by Flowguard Co. in late 1987 which was then used in the scale formation experiments at 70°C in place of the clamp core holder. The steel core holder and its diagram are shown in figures (5.4) and (5.5), respectively. The steel core holder was multi-pressure tapped on the rubber sleeve surrounding the core plug, therefore the pressure differentials across the different sections along the length of the core could be measured during a test. The tapping holes on the rubber sleeve were spaced at 6, 28, 50 and 70 mm, starting from the front of the core. The maximum temperature specification for the core holder is 120°C and the maximum pressure the core holder can take is 4000 psi.

Injection Face

In order to mix two incompatible brines inside a core but without contact between them outside the core, an injection face, which was originally designed by Goulding,[42] was used ahead of a core front for distributing the two brines separately across the core front face. By this means the brines mixed immediately after entering the core. Figure (5.6) shows the injection faces used in both 20 and 70°C tests and the drawings of the injection face is presented in figure (5.7). As seen from figure (5.7), two patterns of flow channels were machined on the side of the injection face in contact with the core front. One pattern was made of shallow (2mm deep) grooves connecting to the centre hole, the other comprised small holes drilled through the thickness of the injection face to the other side. One brine ($Ba^{2+}$and Sr^{2+} rich) was introduced from an 1/8" inlet pipe to the centre hole and then distributed on the injection face through the grooves before flowing into the core. The other brine (SO_4^{2-} rich) was flowed through the annular of a

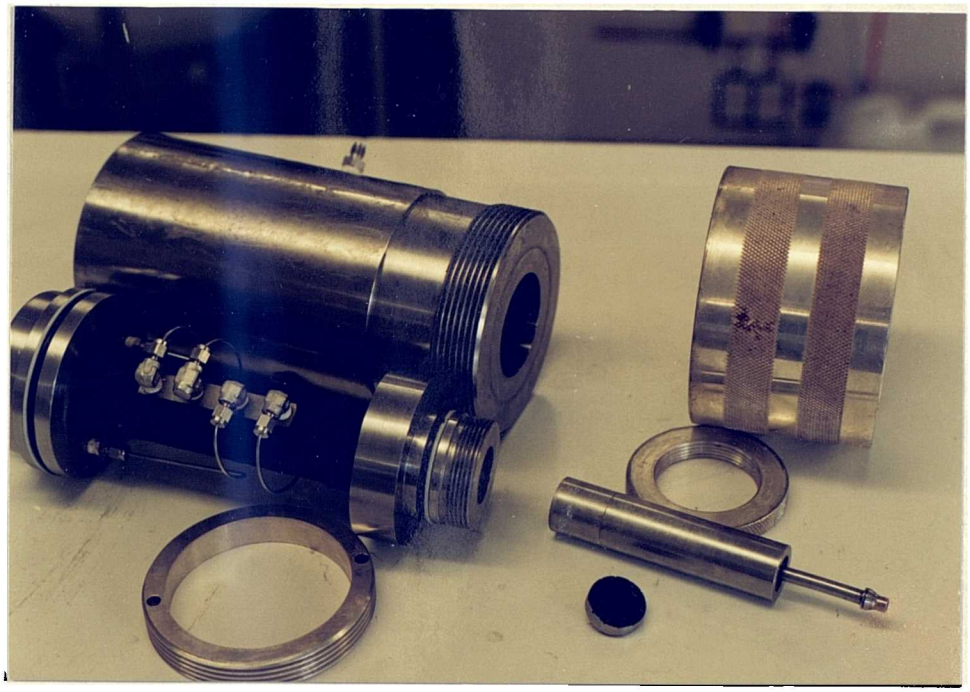

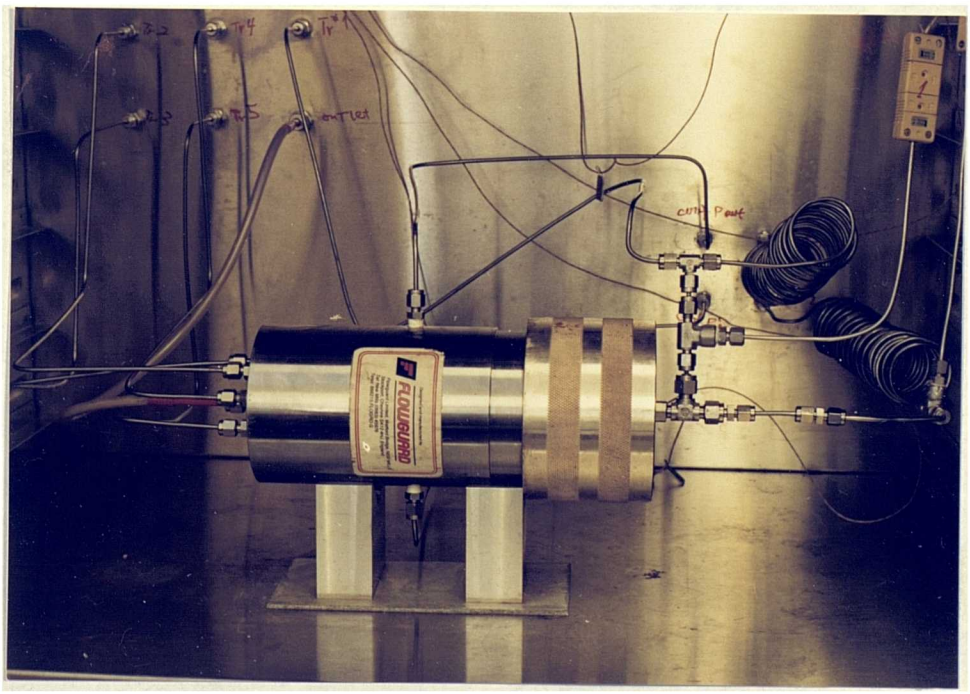

Figure 5.4 The steel core holder

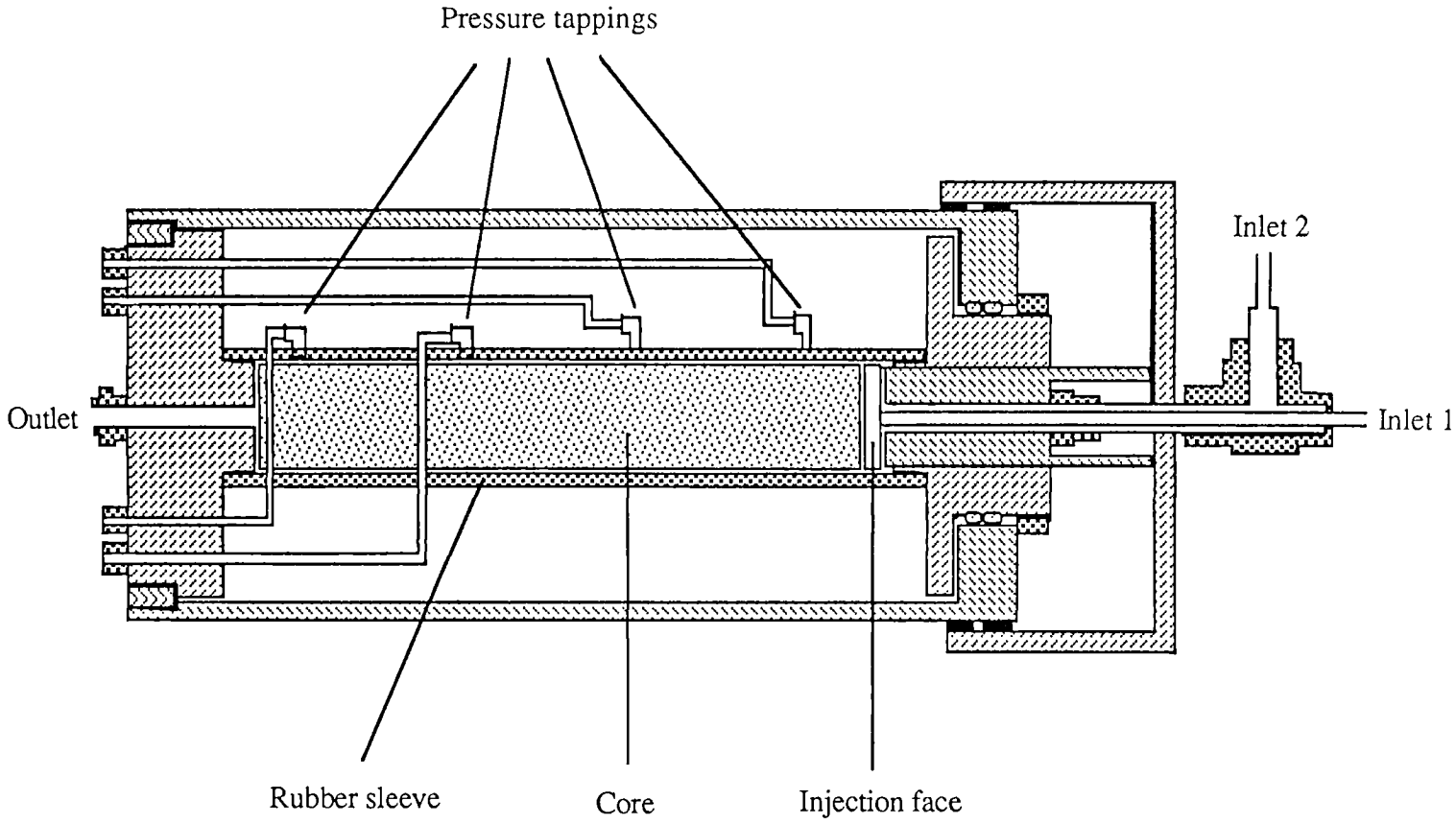

Figure 5.5 Multi-pressure Tapped Core Holder

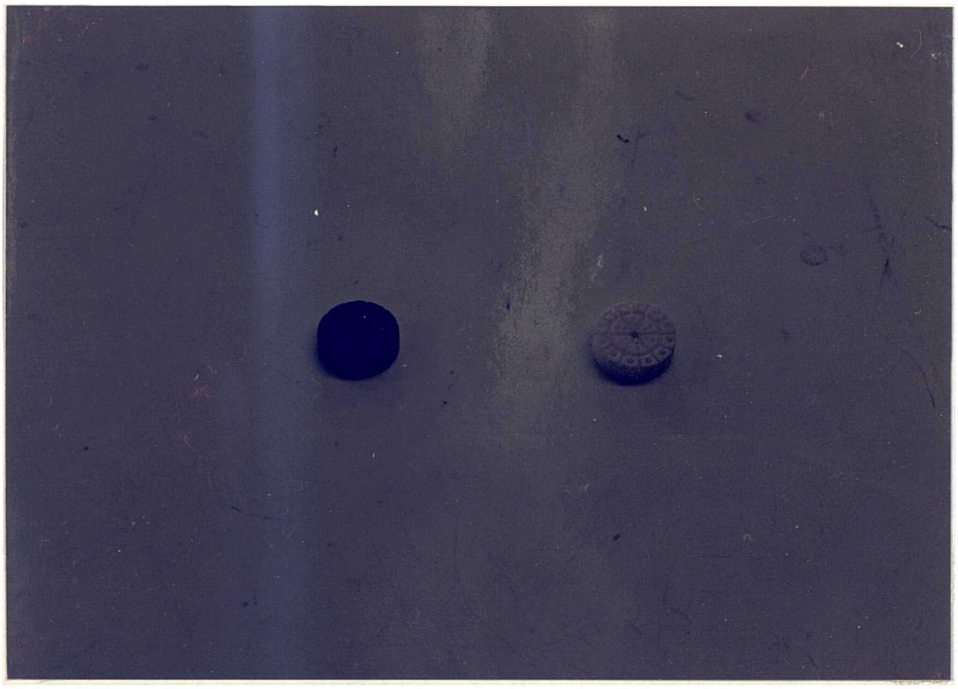

Figure 5.6 The injection faces used for room temperature core tests (white) and for elevated temperature core tests (dark)

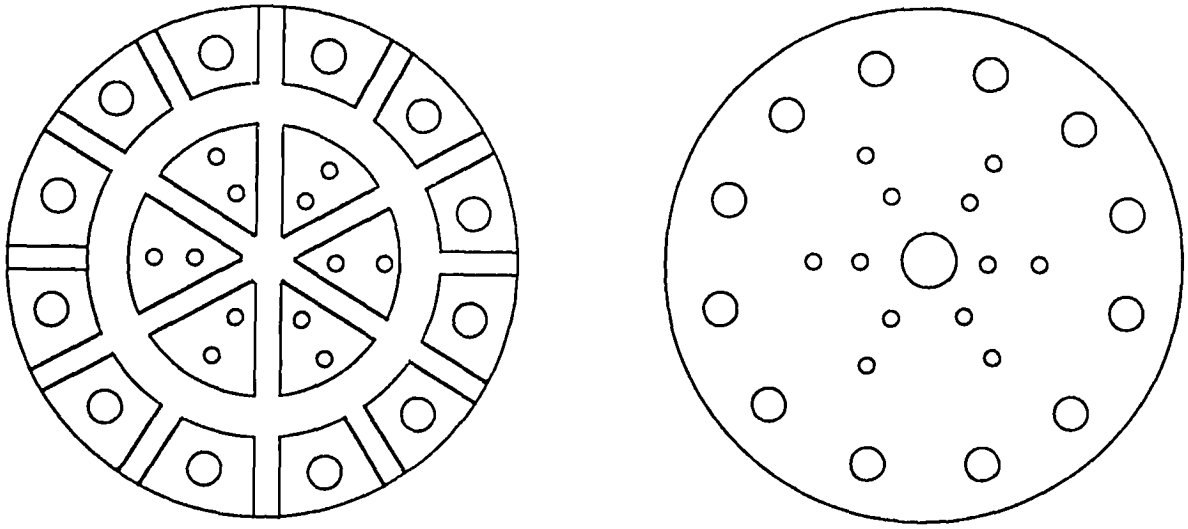

Face to core front

Back face

Figure 5.7 Injection Face

1/4" inlet pipe surrounding the 1/8" inlet to the small holes except the centre hole on the injection face. In this way, the two brines were well distributed on the core front face but isolated from each other until having entered the rock pores. The injection face for 20°C experiments was made from PTFE bar, which was soft enough to deform against the core cross face to provide a good seal between the holes and grooves while strong enough not to close the holes and grooves under flow pressure. The PTFE material was rejected for making the injection face for the elevated temperature tests because the injection face was badly deformed and the grooves and holes on it were compressed and contracted under 1000 psi confining pressure and 70° temperature. Instead, a resin made from mixing heat resistant epoxy (Araldite 2004A) and hardener (Araldite 2004B) was used to make the injection face. This injection face was tested and had more strength under stress and heat although some irreversible deformation on the general shape of the face occurred at 70°C and 1000 psi. To strengthen it, the injection face was mounted into a thin steel ring and a thin section (0.5mm) of the side of the face towards the core front was kept out of the steel ring to allow it to deform against the face of the core.

Scale Formation Rig

The front view of the scale formation core flow test rig is shown in figure (5.8) and the water supply system shown in figure (5.9). The diagram of the rig is shown in figure (5.10). The components of the rig were a nitrogen cylinder, a vacuum pump, four water tanks, two constant flow HPLC pumps, the core holders, a temperature oven, thermocouples, a confining pressure pump, 5 differential pressure transducers, a line pressure chart recorder, a data acquisition unit and a Hewlett - Packard microcomputer. The main parts of the rig are given description here.

a. water tanks

Four 20 litre glass tanks were used for storage of the distilled water and brines. Two of the tanks were filled with distilled water, the third was filled with Ba^{2+} and Sr^{2+}

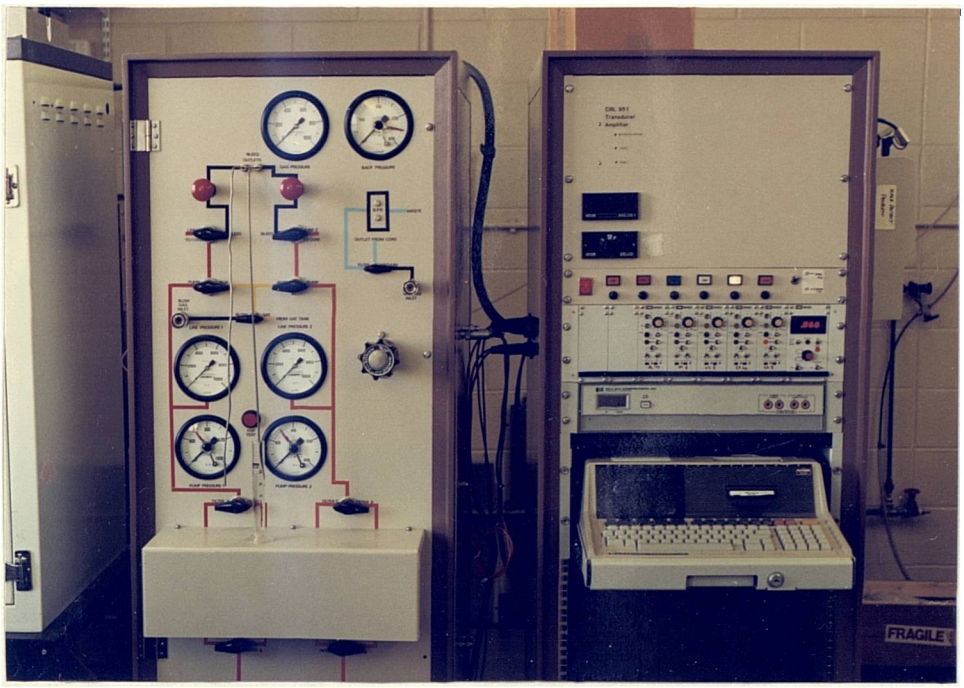

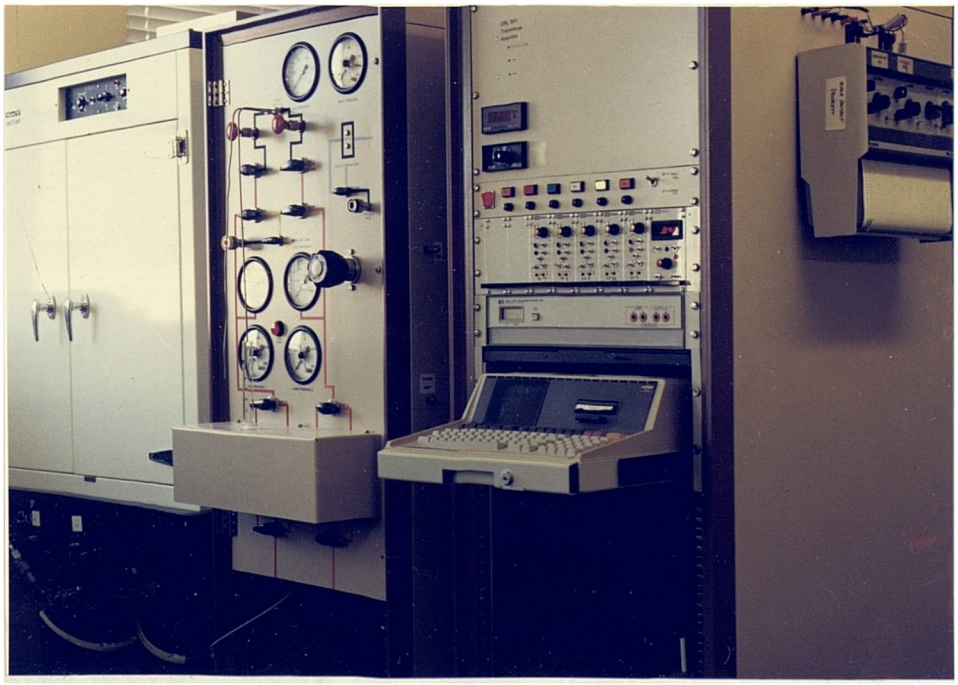

Figure 5.8 Front view of the scale formation rig: temperature oven, control module and data acquisition unit

Figure 5.9 The constant flow HPLC pumps and water supply system

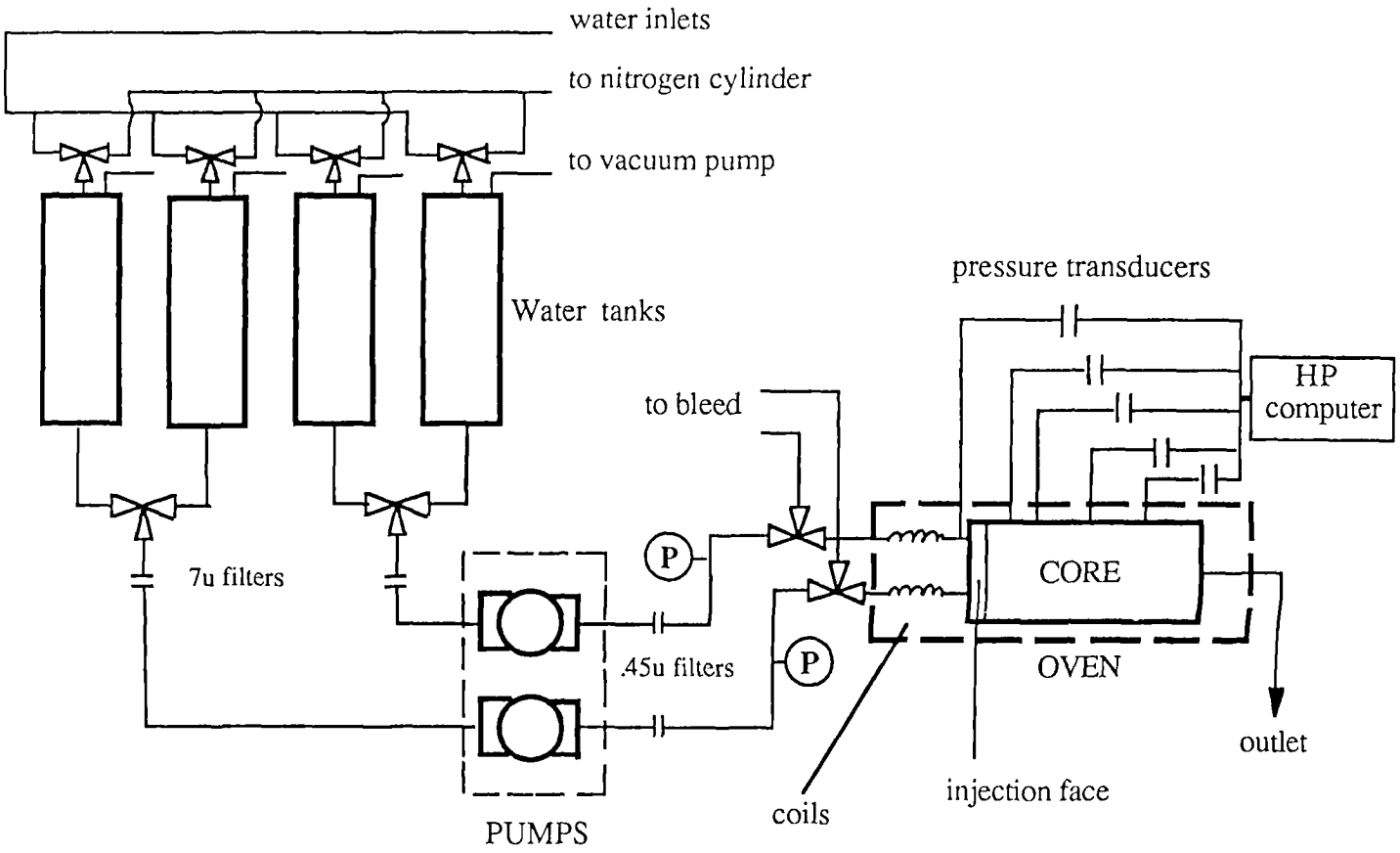

Figure 5.10 Scale Formation Rig

rich brine and the other stored SO_4^{2-} rich brine. A three way valve was connected to the top of each water tank. The tanks were first evacuated and then the waters were sucked into the tanks by vacuum and the evacuation continued until the air bubbles evaporated, then 2 psi nitrogen gas was applied to cover the water surface. A distilled water tank was connected to the tank storing Ba^{2+} and Sr^{2+} rich brine through a three way valve and the other distilled water tank was connected to the tank storing SO_4^{2-} rich brine similarly so allowing the flow to be switched from distilled water to brines or vice versa.

b. constant flowrate pumps and flow lines

Two constant flow HPLC pumps were used during a test to flow two opposite brines through a core. The pump specifications were: output pressure = 0 to 5000 psi and flowrate = 0.1 to 10.0 ml/min. The pumps were supposed to be pulseless but small pressure pulsation($\leq$ 3 psi) was often encountered during the flow tests. Two 7 μm cartridge filters were mounted on the water inlets to the pumps and again two 0.45 μm Millipore filters were equipped on the pump outlets to filter out any particles or suspensions in the waters. Two three way valves were used on the lines between the pumps and the core holder, each on one of the water pipes, to divert the waters bypass the core holder, in order to bleed air trapped in the flow lines or to check the pump flowrates. Also two pressure gauges were connected to the flow lines before the core holder to display the line pressures and to shut down the pumps if the line pressure was over the limit.

c. core holders, refer to the third paragraph of this subsection, under the headings Core Holders (p.85).

d. temperature oven and thermocouples

At the elevated temperature tests, the steel core holder was put in the oven and the test temperature was raised to 70°C. The distilled water or brines was heated up to the

temperature by flowing through 3.4 m coiled inlets in the oven before entering the core holder. Thermocouples were connected to the water inlets to indicate the water temperature.

e. differential pressure transducers

Five SE differential pressure transducers, one 1000 psi, one 500 psi, one 250 psi and two 100 psi, were used for recording the inlet line pressure and the pressure differentials along the length of a core. The 1000 psi transducer was connected to the inlet pipe in front of the core holder. The other four transducers, from the 500 psi to 100 psi ones, were sequentially connected to the ports on the core plug to give pressure readings at different points along the core length, therefore the overall pressure across the core length and the pressure differential across each section of the core, defined between 2 pressure tappings, were recorded continuously during the $(Ba,Sr)SO_4$ scale precipitation in the core.

f. data acquisition unit and HP computer

The pressures recorded by the transducers and the temperatures by the thermocouples were then passed to the HP3421 data acquisition unit which displays the temperature readings and the voltages converted from the pressure readings. The pressure data were continuously recorded in one minute intervals during a test on a tape by a HP-85 personal computer. The HP computer also served as a control unit, it would issue a command to shut down the pumps and stop data logging if the set pressure limits or maximum pressure scan number were reached.

g. pressure chart recorder

To visually observe the trend of line pressure change during a flow test, a chart recorder was installed to display the pressure at the water inlets. It was easy to see any

pressure pulsation from the chart recorded pressure curve than the numeric readings from the data acquisition unit.

5.5 EXPERIMENTAL METHODS

5.5.1 Scale Precipitation in Static Solutions

Ambient Temperature Tests

100 ml each of the two opposite brines were prepared separately by dissolving the required amounts of the salts into distilled water in the 100 ml volumetric flasks and hand shaken to make the salts completely dissolved in the solution. The two brines were then poured together into a 250 ml glass jar, followed by moderate handshaking to allow the mixing taking place. The mixed brine was then left in the jar undisturbed for at least 24 hours with cover on the jar to allow the $(Ba,Sr)SO_4$ crystals to grow in the solution. The brine was finally filtered through a 0.45 μm filter paper using a Millipore filtration system. Afterwards, the crystals on the filter paper was put in the humidity oven and eventually analysed by SEM.

Elevated Temperature Tests

The same procedure for preparing, mixing and filtering the brines as at the ambient temperature tests was used in the 70°C scale precipitation tests. The differences were: the two opposite brines were first heated up to 70°C separately in the oven and then mixed and left in the oven for the crystal growth at 70°C before being taken out of the oven to be filtered.

5.5.2 Experimental Methods Used in Formation Damage Experiments

Brine Preparation

The Ba^{2+} and Sr^{2+} ion rich brine and SO_4^{2-} ion rich brine were separately prepared by adding the required amounts of the salts into distilled water in 5 litre volumetric flasks. The salts were dissolved into the water by vigorous shaking and finally 5 litre each of the brines were made. The brines were then added to the brine storage tanks by evacuation, also the other two tanks were filled with distilled water. The newly filled waters were evacuated until no apparent air bubbles remained in the waters and then a nitrogen blanket was provided over the waters.

Core Preparation

a. For ambient temperature tests

The core plugs used in the 20°C formation damage tests were 3.5 in.(88 mm) long and 1 in. (25.4 mm) in diameter and the cores were cast in resin of 12 mm thick. 4 pressure tapping holes were drilled through the resin to the core surface, spaced at 11, 22, 44 and 66 mm starting from the front of the core. A resin moulded core ready for a test is shown in figure (5.2) and the diagram of the core is illustrated in figure(5.11).

Several steps were involved in preparing such a resin cast core. First, a one inch diameter and approximate 4.0 inch long core plug was drilled from a Clashach rock block and dried in the humidity oven. The dried core was then coated with a thin layer of 50:50 mixture of Loctite Toughbond adhesive and hardener to prevent the resin penetrating into the rock pores and left dry for half an hour. The coated core was later put into a plastic mould. The mould had a 5 mm deep and slightly more than one inch (25.4mm) diameter well centred at the bottom to hold the flat end of the core plug centred and upright. The next step was to prepare the resin for casting the core. 125 grams of epoxy(Araldite CY219) and 62.5 grams of hardener(Araldite HY219) were weighed on a scale and thoroughly mixed together with 12 ml accelerator(Araldite DY219) in a plastic beaker. The homogeneous resin was then poured into the plastic mould to fill the gap between the upright core plug and the mould to bond the core.

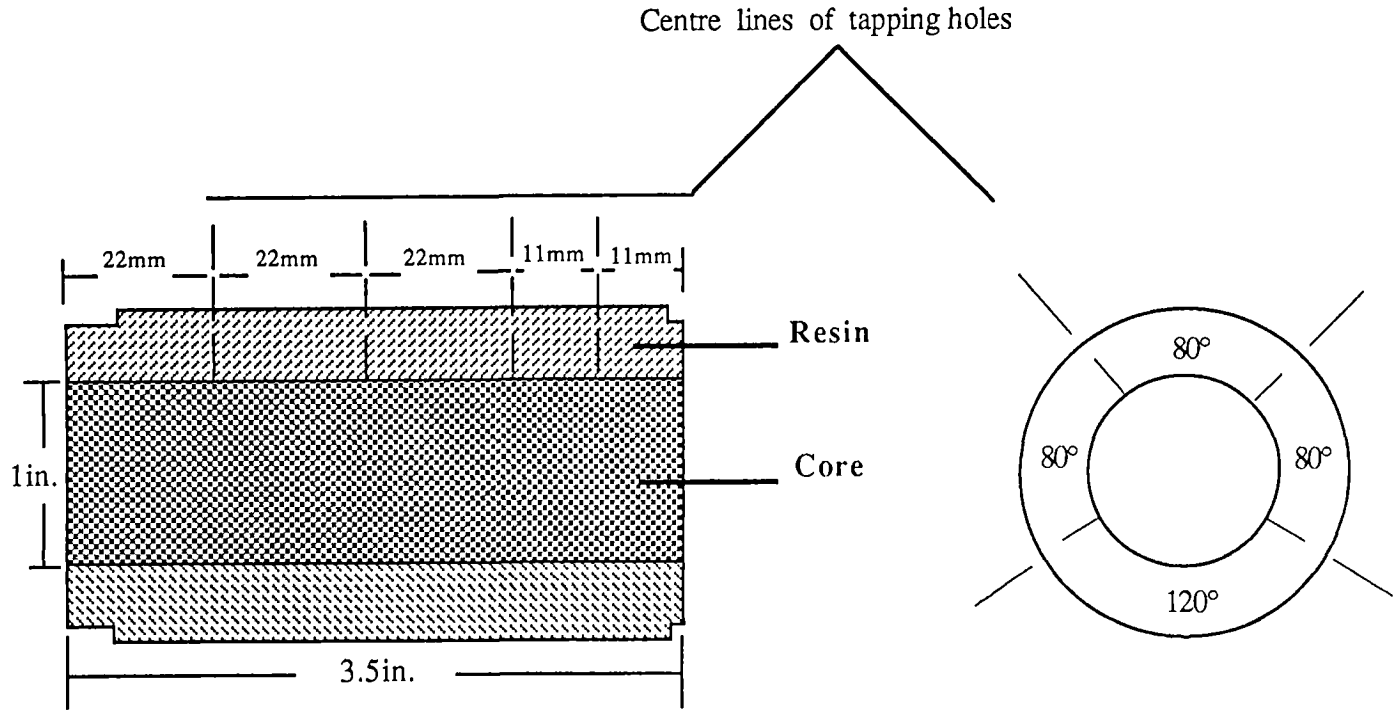

Figure 5.11 Multi-pressure Tapped Core

After that, the mould was left undisturbed at room temperature for at least 24 hours until the resin had hardened. Then, the resin bound core plug was hammered out of the mould. Both ends of the core plug were trimmed to be square to the sides of the core and to give 88 mm core length. The cast resin was later machined to 50 mm in diameter which gave the resin around the core plug a thickness of about 12 mm. Afterwards, the resin was further turned down 1 mm both in the 3 mm front section and in the 12 mm rear section for circumferential seal on the clamp core holder. Finally, four pressure tapping holes were drilled on the resin through to the rock core surface and 1/16" NPT conversion fittings were fitted into the holes for connecting with the pressure transducers. The tapping ports were positioned at 11, 22, 44 and 66 mm starting from the core front and had the radial spacings of 80° between the two nearest tappings.

The distance spacings and the radial angle spacings of the tappings on the resin core were different from those for the core used with the steel core holder, in which the distance spacings of the tappings on the core were 6, 28, 50 and 70 mm from the core front into the core depth and all the tapping holes aligned in a straight line on a metal strip built in the rubber sleeve.

Before a core flow test, the resin bound core was dried in the humidity oven and then mounted on the clamp core holder by pushing the both ends into the Fluon(PTFE) plastic sealing ends of the core holder and sealed with plastic O-rings. In the front face of the core, the resin injection face was also mounted on the inlet sealing end of the core holder for distributing the two injection brines, as described in subsection (5.4.2). One pressure transducer was connected to the inlet pipe and the other four were connected to the pressure tappings on the cast resin through 1/8 transparent plastic pipes. The outlet of the core holder was then connected to a vacuum pump and the core was evacuated for at least four hours, followed by saturation of the core with distilled water and ready for core flow. Here the description was given to the preparation of one core. In practice, a number of cores were drilled from a rock block and cast into the resin together at the same time.

The preparation of a resin moulded core was both labour- and time-consuming. It can only be used at ambient temperature and low pressure test. The maximum flow

pressure the cast resin can sustain was 500 psi, above that cracks on the resin would occur. The temperature limit on the cast resin was 50°C.

b. For elevated temperature tests

A much simpler process was involved in preparing a core plug for the 70°C formation damage tests compared to that for the 20°C tests, owing to using the multi-pressure tapped steel core. Core plugs of one inch (25.4mm) diameter and about 3.5 inch(88mm) length were drilled from a Clashach rock block and both ends were cut squarely to give a 3in length. The rock cores were dried in the humidity oven. The dried cores were then stored in a glass desiccator which was connected to either distilled water or a vacuum pump through a three way valve. The cores were first evacuated in the desiccator for at least 24 hours then the distilled water was sucked into the desiccator to saturate the cores. To mount a core into the steel core holder, first a sink was filled with tap water and the core holder was submerged into the water and ensuring any air in the core holder was removed, then a core was quickly taken out of the desiccator and pushed into the rubber sleeve inside the core holder, followed by putting the injection face on the front face of the core. The core plug installed core holder was sealed at both inlet and outlet before being taken out of the sink and quickly connected to the distilled water filled inlet pipes as well as to the plastic pipes from the pressure transducers. After that, any air trapped in the junctions of the inlets and the core holder was bled by pumping the distilled water bypassing the core holder, before the core flow started. The confining pressure space of the core holder was filled with distilled water but left the confining area outlet open. The oven was set 70°C and switched on to heat the core holder to 70°C. The confining pressure was then raised to 1000 psi and the water in the confining area was sealed by closing the outlet valve, ready for core flow.

Test Procedure

Only the main process of the experiment is given description here. The preparatory

work has been described in the early part of this subsection. The four water tanks were filled with distilled water and two opposite brines and covered with 0.2 bar nitrogen. The distilled water was connected to the pumps through the three way valves. The flowrates of two pumps were set to an identical 7.5 ml/min which gave a total 15 ml/min flowrate in the core flow. The outlet screws of the pressure transducers were uncapped to open air and the pressure transducers were balanced to zero. The two three way valves on the flow lines between the pumps and the core holder were switched to the bleeding positions.

The pumps were started by flowing the distilled water , the air in the flow lines were bled and the flow rates on the both pumps were checked and adjusted to 7.5 ml/min each. The three way valves were then switched to flow the distilled water through the core. The distilled water flowed through the core holder to the outlet as well as flowed into the pipes connected to the pressure transducers. Any air trapped in the pipes and the transducers were bled and the caps on the transducers were put on to seal them. The pressure readings and the oven temperature were displayed and collected using the data acquisition unit. The distilled water continued to flow into the core until the line pressure was stabilised. After that, slightly different procedures were adopted for the ambient temperature tests and the elevated temperature tests.

For a 20°C test, the two brines were simultaneously switched on to flow through the core after distilled water while, for a 70°C test, one pump was stopped and the other one started to flow the Ba^{2+} and Sr^{2+} ion rich brine(or formation water) through the core for about half hour before both of the pumps started to flow the two brines together through the core.

The line pressure at the core inlet and the pressures at the ports along the length of the core were constantly recorded on the tape in the computer at one minute intervals to observe the pressure change as a result of permeability damage caused by $(Ba,Sr)SO_4$ scale precipitation in the core.

During some of the tests, the brine effluents from the core were sampled. 1 minute flow of effluent (equivalent to 15 ml) was collected into a calculated volume of distilled water in a beaker (the distilled water volume varied from one test to the other according

to the estimated sulphate supersaturation in the effluent). After the scale precipitation in the core by injecting the brines through the core, distilled water was restarted to flush the core to dissolve any soluble salts retained in the core. At the end of a test, the pumps were either automatically shut down if the pressure limit of one of the pressure transducers had been reached or switched off manually. The core was taken out of the core holder and put into the humidity oven, for porosity measurement and SEM analysis.

Pressure Data Handling

The output from the five pressure transducers during a formation damage test were logged on a data tape, as mentioned above. It was not intended to process or analyse the pressure data on the HP computer due to its limited functions. Instead, the data were transferred from the data tape to the University Vaxcluster mainframe through the Tektronix 4052 computer interface. The transferred data were reorganised or formatted on a data file by a computer programme(REPROC) on the Vaxcluster terminal. The experimental time and date, core porosity(if measured) and flowrate were given in the headings of the data file and followed by the transducers readings in correspondence with the scan number. Another programme (EXANAL) was used to convert the pressure data into permeability changes over the whole core plug and within each section of the core. It was designed also for plotting the core overall pressure and pressure differential across the core sections against the brine injection time or injected brine pore volumes (if the initial core porosity was measured) and similarly, for plotting the overall permeability and the sectional permeability curves. The permeability was calculated from pressure using Darcy's linear flow equation,

$$k_{i,t} = \frac{q \mu L_i}{A \Delta p_{i,t}} \qquad (5.3)$$

Where the subscript i refers to either the entire core plug or one of its sections and

subscript t refers to the time. q is the flowrate, μ the brine viscosity, L_i the core length or section length, A the cross area of the core and $\Delta p_{i,t}$ is the pressure differential across the entire core plug or a section of the core. The brine viscosity was calculated using the correlations proposed by Kestin, et al.[63], as given below.

First, the brine viscosity $\mu(p,t,m)$ at temperature t, pressure p and NaCl concentration m is related to the hypothetical zero-pressure viscosity $\mu^o(t,m)$ by equation (5.4),

$$\mu(p,t,m) = \mu^o(t,m)\,[1 + \beta(t,m)\,p] \tag{5.4}$$

and $\mu^o(t,m)$ is then related to pure water viscosity $\mu^o_w(t)$ at temperature t by equation (5.5),

$$\log_{10}[\,\mu^o(t,m)/\mu^o_w(t)] = A(m) + B(m)\,\log_{10}[\,\mu^o_w(t)\,/\mu^o_w(20°C)] \tag{5.5}$$

Finally, $\mu^o_w(t)$ is calculated from 20°C pure water viscosity $\mu^o_w(20°C)$ using equation (5.6),

$$\log_{10}[\,\mu^o_w(t)\,/\mu^o_w(20°C)] = \{\sum_{i}^{4} \alpha_i\,(20\text{-}t)^i\,\}\,/\,(96+t) \tag{5.6}$$

The parameters involved in the correlations can be found from the paper by Kestin, et al.[63].

The programmes REPROC and EXANAL were originally created by Goulding.[42] Programme EXANAL was developed in this study to be able to plot the permeabilities as a percent of their initial values against time or pore volumes to show the degree of the formation damage in relative terms and to be able to graph the core overall permeability changes from a number of different tests on the same graph. Also a

programme(EXDFIT) was created in this study to smooth the reciprocal of the pressures($1/\Delta p$) recorded during a test with the experimental time or injected brine pore volumes. The pressure data smoothing had a two fold purpose, first, to discard any pressure fluctuations caused by pump pulsation and, second, to be able to characterise the permeability curves numerically. Another programme(EXCALC) was created in the study to perform the numerical characterisation of the permeability curves, which will be described later in chapter 6.

Analytical Techniques

a. Core porosity measurement

For the 20°C tests, the core porosities were not measured because the 3.5 in.(88mm) core length exceeded the capacity of the measurement chamber of the Helium Gas Porosimeter in the Department. The porosities of the cores used in 70°C formation damage experiments were measured by the Helium Gas Porosimeter before and after the scale formation. The purpose of the porosity measurement was to observe the porosity damage resulting from the scale precipitation during a flow test and to calculate the scale volume formed in the rock pores. Also the pore volume of the injected brine during a test was calculated from the rock porosity and subsequently used in graphing the pressure or permeability curves.

b. Brine effluent analysis

The brine effluent samples taken from some of the core flow tests were analysed in IOE(Institute of Offshore Engineering) by Plasma emission spectroscopy (Ionic Emission) to measure the Ba^{2+} and Sr^{2+} ion concentration changes in the brines after scale precipitation in the core during a test. From the effluent analysis results, the Ba^{2+}/Sr^{2+} ratio in the effluent, the profile of sulphate supersaturation change during the test and the scale precipitation rate, etc were calculated.

c. SEM analysis

After the porosity measurement, the scaled core was sliced and the samples were microscopically examined by SEM and a morphological study was made on the printed SEM microphotographs of the scaled core samples. Most of the scaled core samples were taken from the section one(first section in the front of a core) and section five (the last section in the rear of a core) though some samples from middle sections were also examined.

5.6 EXPERIMENTAL RESULTS

5.6.1 Results Obtained from Direct Measurement or Analysis

Summing up the description in section (5.5), the measurements directly obtained during a experiment or from the sample analyses are,

i. overall pressure drop across a core plug and sectional pressure differentials along the length of the core,

ii. core porosities before and after scale-up of a core,**

iii. Ba^{2+} and Sr^{2+} ion concentrations in the brine effluent during a core flow test, and

iv. scanning electron microscopy(SEM) photographs of the scaling crystals precipitated from static bulk solutions and those of the scaled core samples.

The results listed above with ** marked beside are those obtained at 70°C tests only.

5.6.2 Results Derived from the Directly Obtained Results

Subsequent results were derived from the above experimental measurement and analyses. They are listed as,

a. overall permeability and sectional permeability changes during a core flow test,

b. change in the permeability decline rate during a flow test,

c. porosity change due to scale deposition,**

d. perm-poro relations of a core before and after scale formation,**

e. the volume of the $(Ba,Sr)SO_4$ scale deposited in a core and its relation to the permeability reduction,**

f. Ba^{2+}/Sr^{2+} concentration ratio change in the brine effluent during a $(Ba,Sr)SO_4$ scaling test,

g. total scaling rate of $(Ba,Sr)SO_4$ solid solution and the relative scaling rates of $BaSO_4$ and $SrSO_4$ in forming the solid solution, and

h. scaling crystal habits, size, scaling sites on the rock pore surface, scale distribution in the core and scaling crystal orientation in the pore space, etc.

The results marked with ** were available only from the elevated temperature experiments. The above results are presented, later in chapter 6 and chapter 7 in the thesis, either in numerical form(tables) or in graphics accompanied with the result analyses and discussions.

CHAPTER 6

BARIUM SULPHATE AND STRONTIUM SULPHATE SOLID SOLUTION FORMATION AT ROOM TEMPERATURE

6.1 INTRODUCTION

The general purpose and objectives of the investigation of formation damage arising from $(Ba,Sr)SO_4$ solid solution scale precipitation have been outlined in chapter 1 and chapter 5. The aims of the $(Ba,Sr)SO_4$ scaling caused formation damage experiments at room temperature were to physically simulate $(Ba,Sr)SO_4$ solid solution scale formation in porous media in a simple and easy way. From such experiments to obtain some basic information about scale deposition and the effect on the rock permeability to serve as an foundation for further investigation of formation damage caused by the sulphate solid solution carried out in more realistic situations close to the conditions under which the oilfield scale occurs. The information intended to be gathered from the ambient temperature tests were: the nature of the solid solution scale, the mechanism by which the scale forms, the interaction between $BaSO_4$ and $SrSO_4$ in the coprecipitation to form the solid solution, how the rock permeability reduction was caused by the scale precipitation, the extent of permeability decline resulting from the scale formation and the factors influencing the scale deposition and the permeability.

The factors under investigation, the brine compositions, the experimental equipment and methods and the scope of the results obtained were described in the last chapter. This chapter focuses on the experimental result analysis and discussion.

First, the SEM study of the scaling crystals and the scaled core samples is presented in section (6.2). The analysis of the brine effluent ion concentration change is followed in section (6.3). Section (6.4) concentrates on the study of permeability decline curves

and the last section presents the numerical characteristics of the permeability decline trends.

6.2 ANALYSIS OF THE RESULTS OBTAINED FROM SEM MICROPHOTOGRAPH STUDY

Scanning electron microscopy microphotographs were taken for the $(Ba,Sr)SO_4$ crystal samples grown in the brines under static condition and for the core samples scaled with sulphate solid solution. SEM photos of the crystals precipitated from the static brines are shown in figures (6.1) through (6.20) and SEM views of some of the scaled core samples are shown in figures (6.21) through (6.40). The test identification number for each SEM photo is given in the figure caption. The test identification system used in numbering the experiments is similar to that used by Goulding [42] and it is described in Appendix(6.1).

6.2.1 Crystals Formed under Static Conditions

Crystal Morphology

After examining the crystals precipitated from different brines, the typical crystal habits observed from the SEM photos, as shown in figures (6.1) through (6.20), are summarised and illustrated in figures (6.41). To provide a comparison, the perfect $BaSO_4$ and $SrSO_4$ crystals are also presented in figure (6.41).

First, an examination of the crystals precipitated from brines BS0, BS1, BS2 and BS3. As seen in table (5.2), $BaSO_4$ supersaturation was 15 in all the 4 brines but Sr/Ba molar ratios varied from 0.1 to 1.0, 100 up to 1000 from BS0, BS1, BS2 to BS3. The crystals formed from brine BS0(Sr/Ba=0.1) and brine BS1(Sr/Ba=1.0) are similar to each other as seen in figures (6.2) and (6.3) and their typical forms are tabular, as illustrated in figure (6.41). By comparing $BaSO_4$ crystal habit with the crystal habits

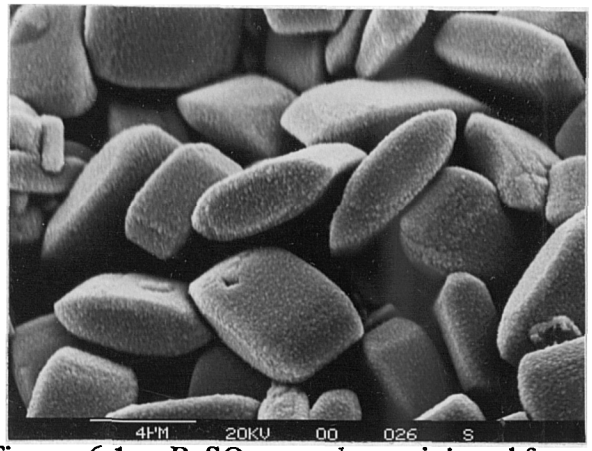

Figure 6.1 $BaSO_4$ crystals precipitated from static brine BA

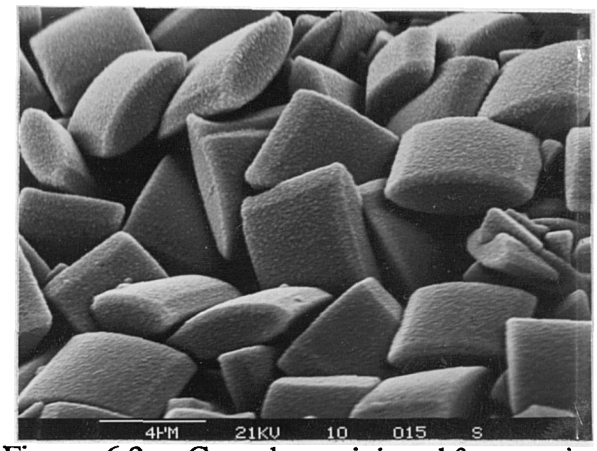

Figure 6.2 Crystals precipitated from static brine BS0, $(Ba+Sr)/SO_4=2$, $Sr/Ba=0.1$

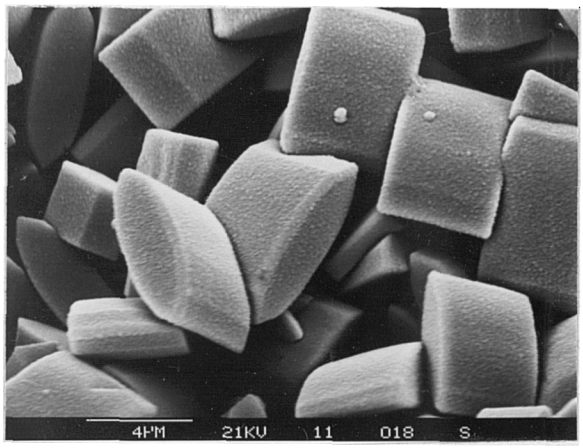

Figure 6.3 Crystals precipitated from static brine BS1, $(Ba+Sr)/SO_4=2$, $Sr/Ba = 1.0$

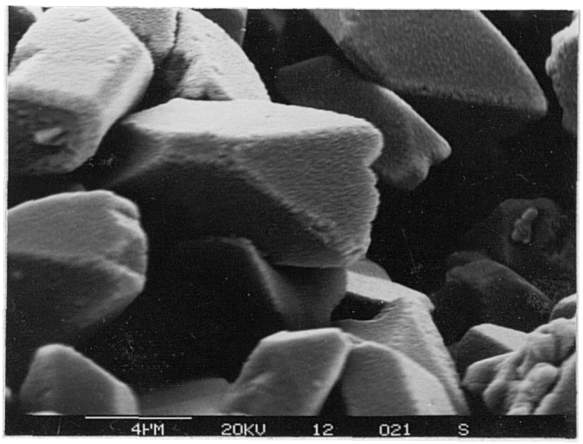

Figure 6.4 Crystals precipitated from static brine BS2, $(Ba+Sr)/SO_4=2$, $Sr/Ba = 100$

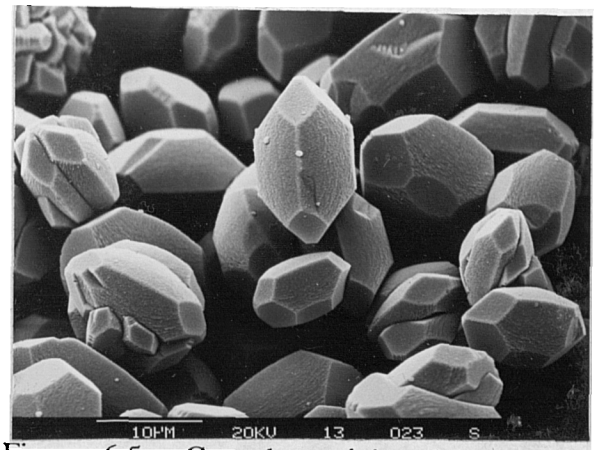

Figure 6.5 Crystals precipitated from static brine BS3, $(Ba+Sr)/SO_4=2$, $Sr/Ba = 1000$

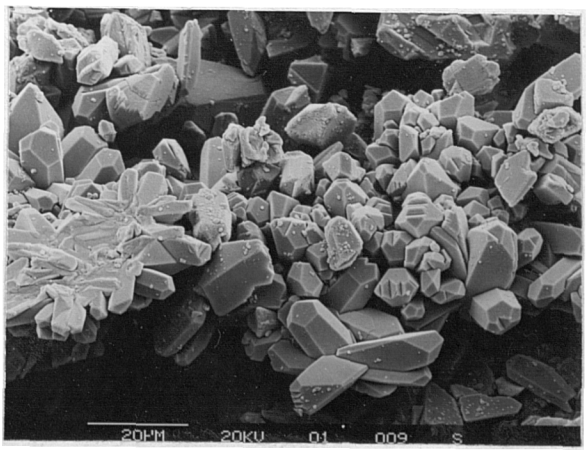

Figure 6.6 $SrSO_4$ crystals precipitated from brine of $SrSO_4$ supersaturation=5

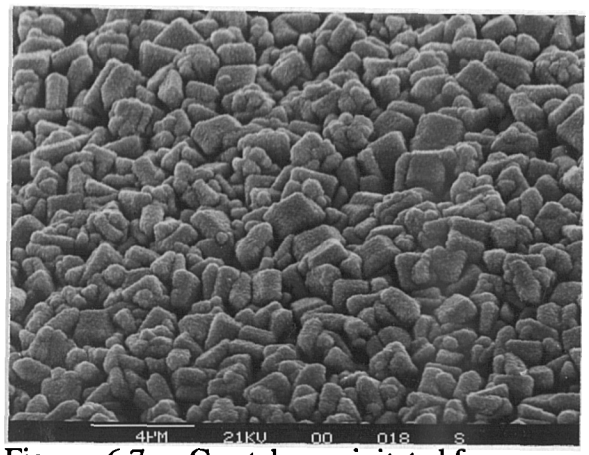

Figure 6.7 Crystals precipitated from unfiltered static brine BS0, compared to figure 6.2

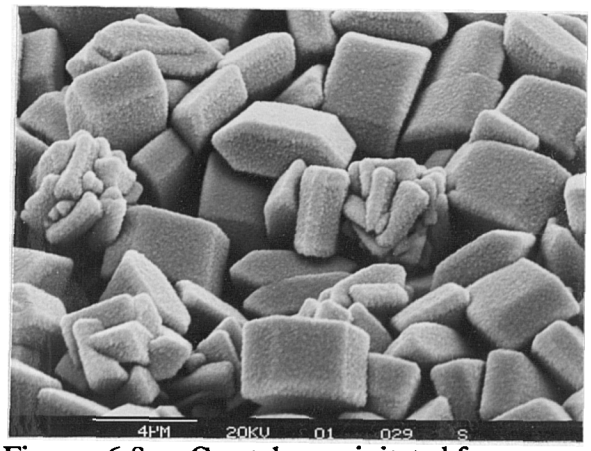

Figure 6.8 Crystals precipitated from unfiltered static brine BS1, compared to figure 6.3

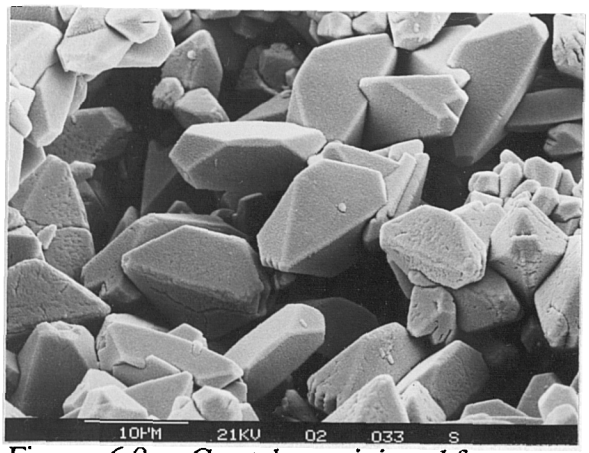

Figure 6.9 Crystals precipitated from unfiltered static brine BS2, compared to figure 6.4

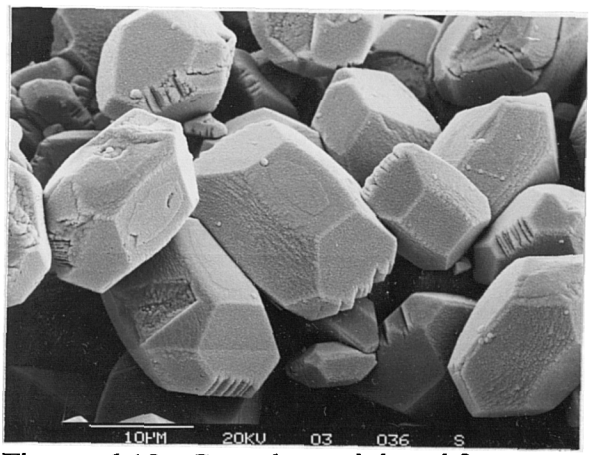

Figure 6.10 Crystals precipitated from unfiltered static brine BS3, compared to figure 6.5

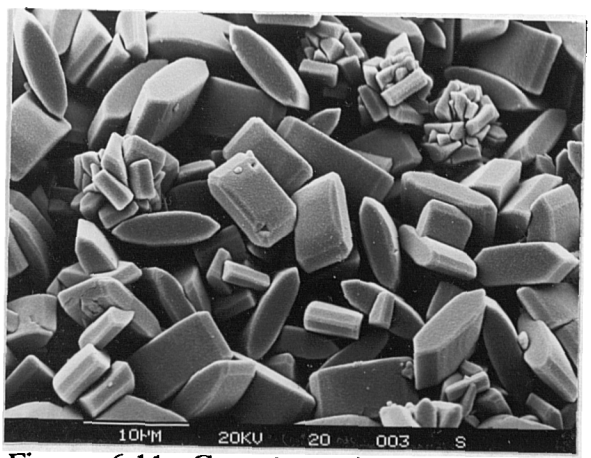

Figure 6.11 Crystals precipitated from static brine BSS0, $(Ba+Sr)/SO_4=1$, $Sr/Ba=0.1$

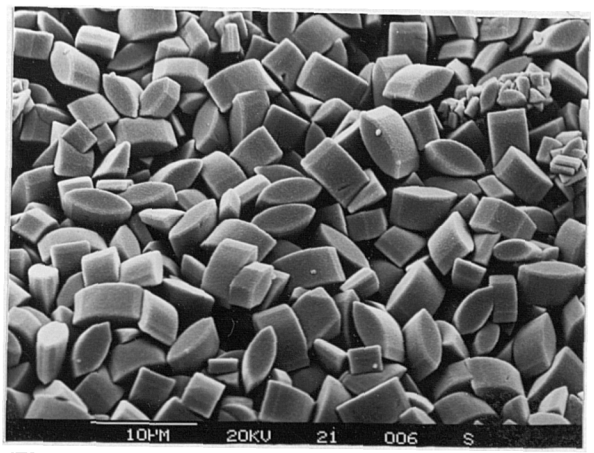

Figure 6.12 Crystals precipitated from static brine BSS1, $(Ba+Sr)/SO_4=1$, $Sr/Ba=1.0$

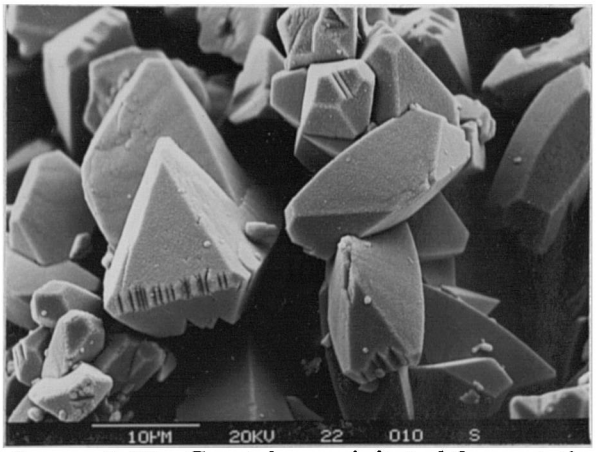

Figure 6.13 Crystals precipitated from static brine BSS2, (Ba+Sr)/SO_4=1, Sr/Ba=100

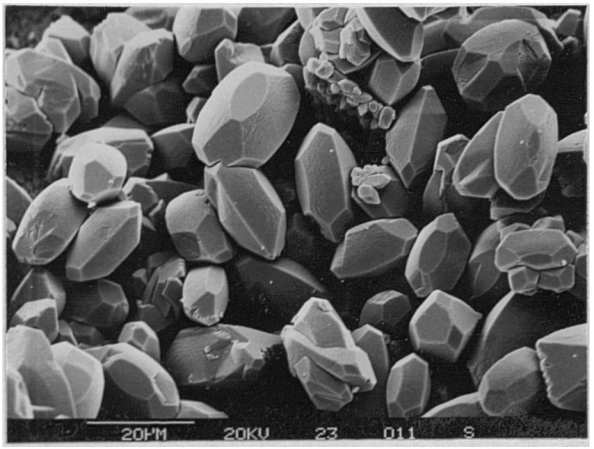

Figure 6.14 Crystals precipitated from static brine BSS3, (Ba+Sr)/SO_4=1, Sr/Ba=1000

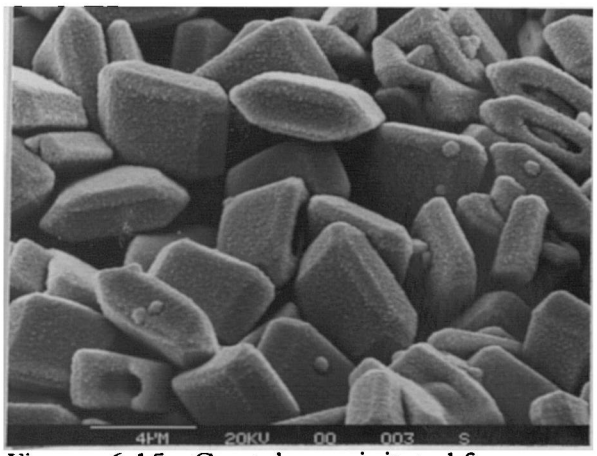

Figure 6.15 Crystals precipitated from unfiltered static brine BSS0, compared to figure 6.11

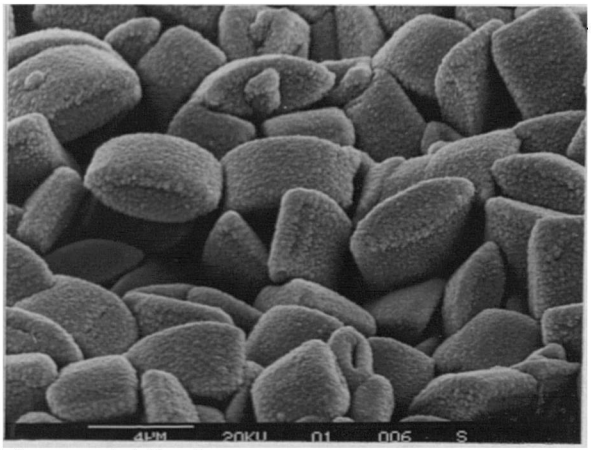

Figure 6.16 Crystals precipitated from unfiltered static brine BSS1, compared to figure 6.12

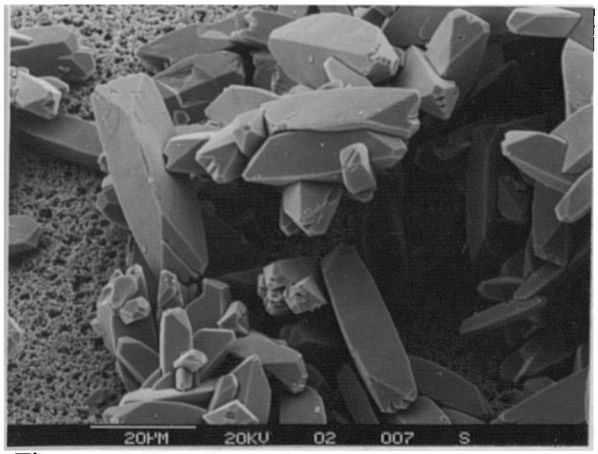

Figure 6.17 Crystals precipitated from unfiltered static brine BSS2, compared to figure 6.13

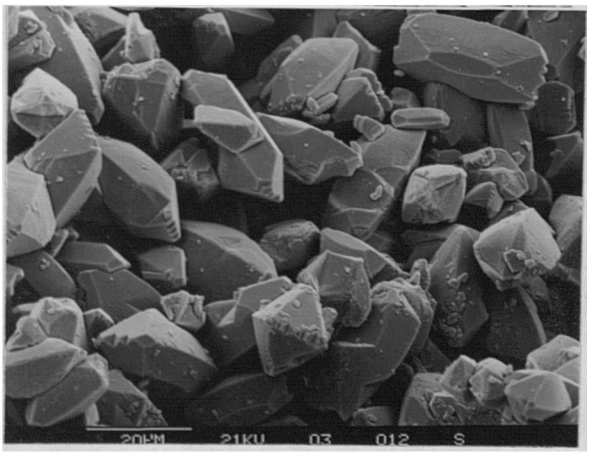

Figure 6.18 Crystals precipitated from unfiltered static brine BSS3, compared to figure 6.14

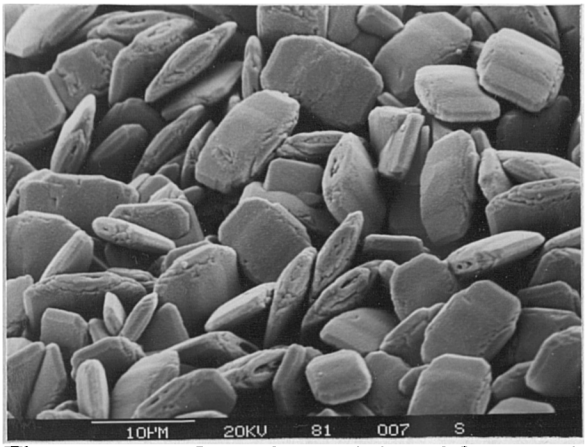

Figure 6.19 Crystals precipitated from static brine BSH1, Sr/Ba=1, $BaSO_4$ SP=30, compared to figure 6.3

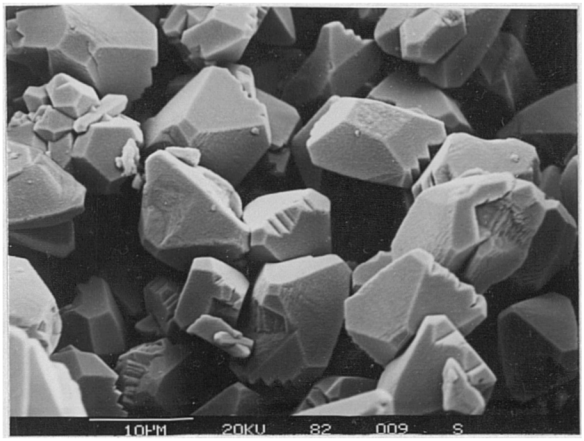

Figure 6.20 Crystals precipitated from static brine BSH2, Sr/Ba=100, $BaSO_4$ SP=30, compared to figure 6.4

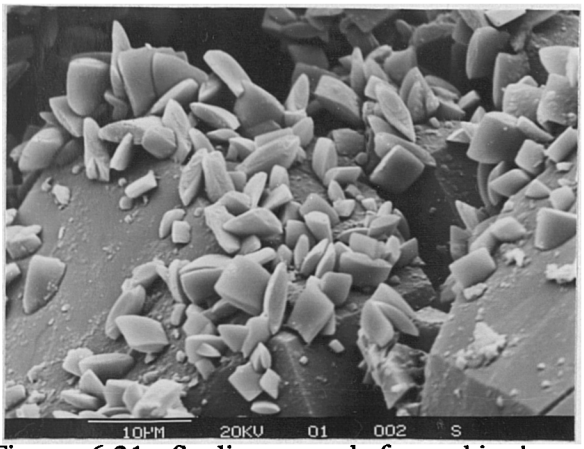

Figure 6.21 Scaling crystals formed in the front section of a core, test C28BS01. Brine $(Ba+Sr)SO_4$=2 and Sr/Ba=0.1. k_i=269md

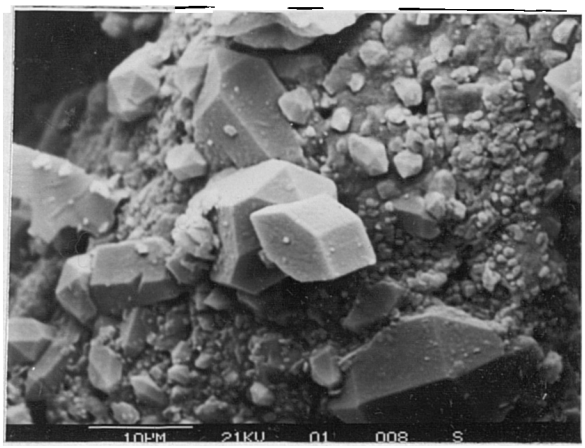

Figure 6.22 Scaling crystals formed in the rear section of a core, test C28BS01

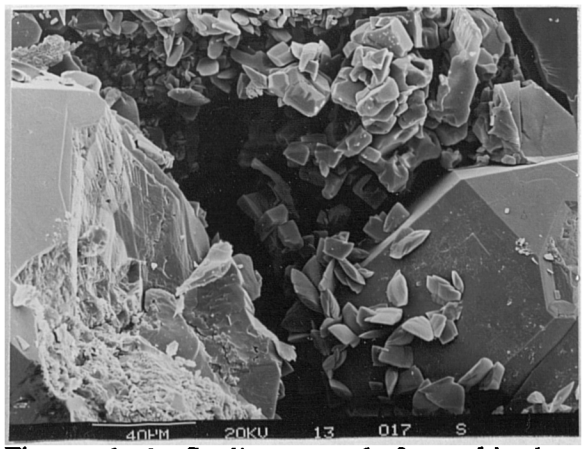

Figure 6.23 Scaling crystals formed in the front section of a core, test C16BS13. Brine $(Ba+Sr)SO_4$=2 and Sr/Ba=1.0. k_i=35md

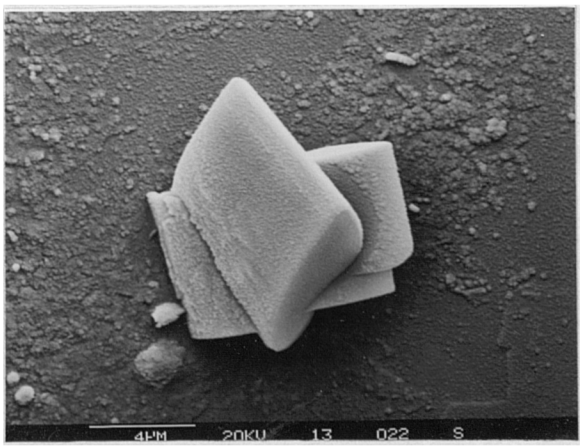

Figure 6.24 Scaling crystals formed in the rear section of a core, test C16BS13

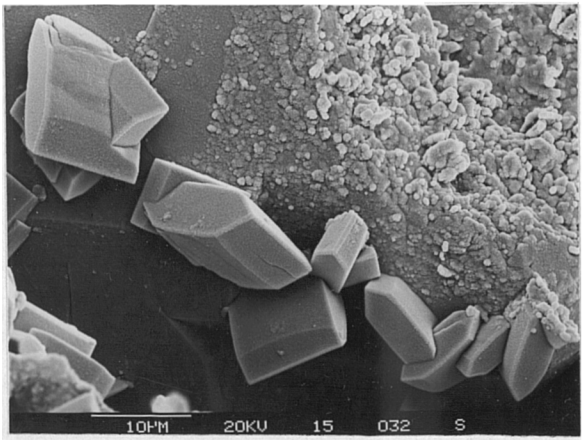

Figure 6.25 Scaling crystals formed in a core, test C25BS15. Brine Sr/Ba=1.0 and $(Ba+Sr)SO_4$ =2. k_i=92md

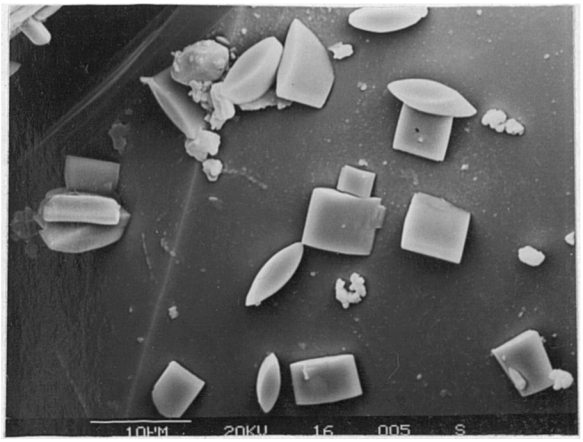

Figure 6.26 Scaling crystals formed in a core, test C16BS16. Brine $(Ba+Sr)SO_4$=2 and Sr/Ba=1.0. k_i=53.5md

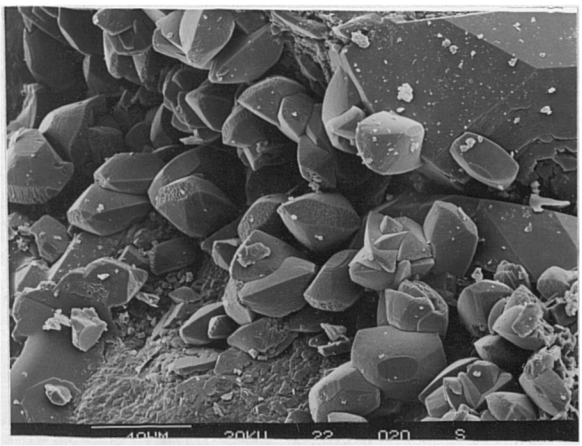

Figure 6.27 Scaling crystals formed in a core, test C25BS22.Brine $(Ba+Sr)SO_4$=2 and Sr/Ba=100. k_i=1025md

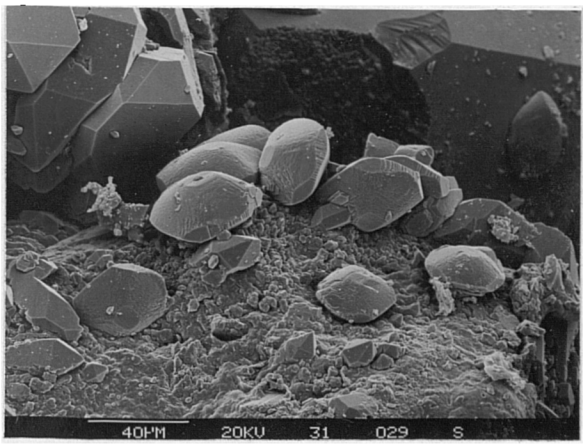

Figure 6.28 Scaling crystals formed in a core, test C25BS32.Brine $(Ba+Sr)SO_4$=2 and Sr/Ba=1000. k_i=940md

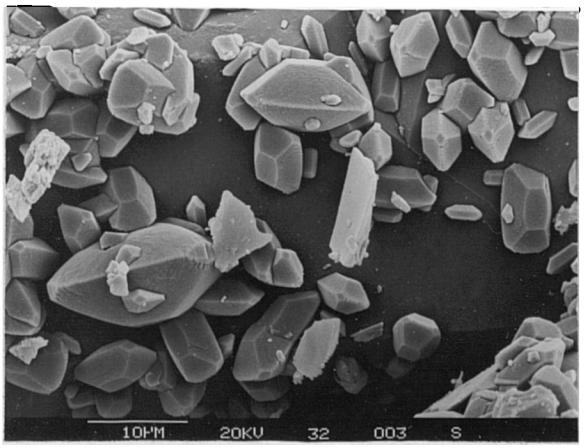

Figure 6.29 Scaling crystals formed in a core, test C16BS33, secondary growth visible. Brine $(Ba+Sr)SO_4$=2 and Sr/Ba=1000. k_i=61md

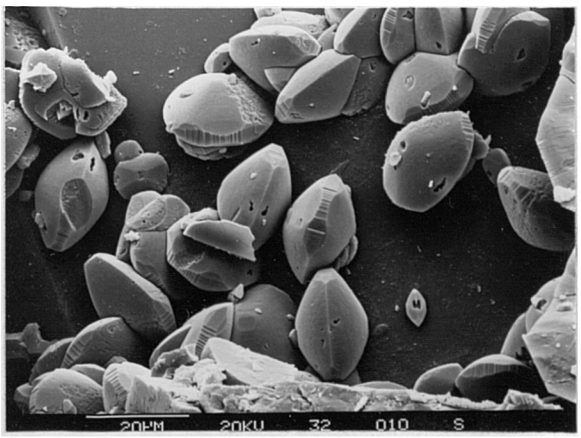

Figure 6.30 Scaling crystals formed in a core, test C16BS33, porous nature

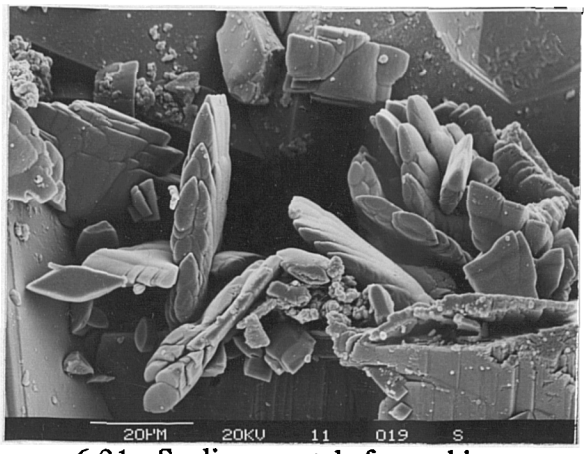

Figure 6.31 Scaling crystals formed in a core, test C28BSH11, protruding into flow. Brine $(Ba+Sr)SO_4$=2 and Sr/Ba=1.0, $BaSO_4$ SP=30 k_i=223md

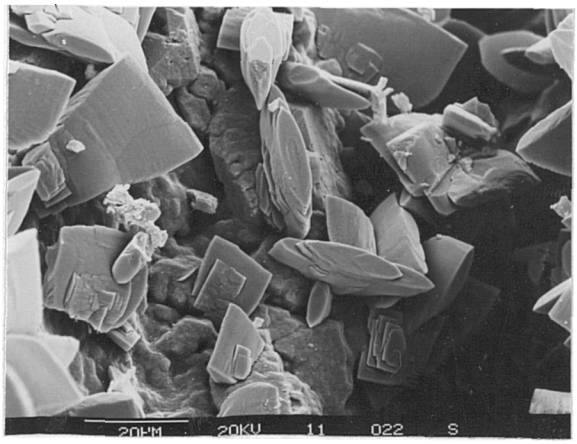

Figure 6.32 Scaling crystals formed in a core, test C28BSH11

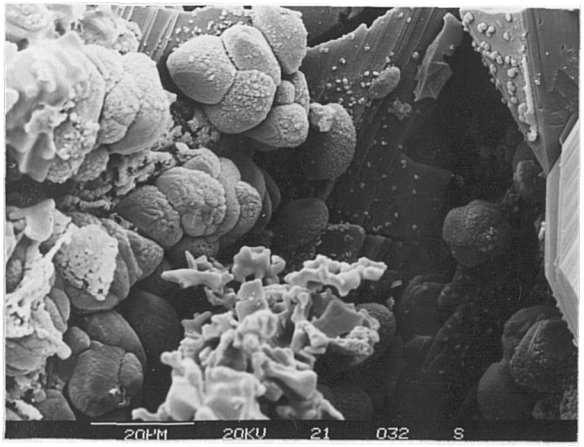

Figure 6.33 Scaling crystals formed in a core, test C28BSH21.Brine $(Ba+Sr)SO_4$=2 and Sr/Ba=100, $BaSO_4$ SP=30. k_i=72.5md

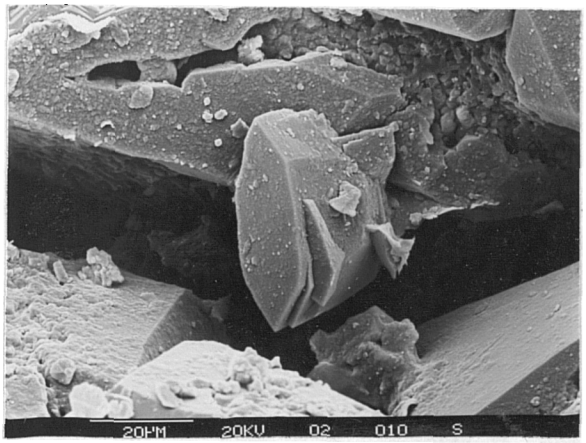

Figure 6.34 Scaling crystals formed in a core, test C25BSS02, dislocation on crystal. Brine $(Ba+Sr)SO_4$=1 and Sr/Ba=0.1. k_i=730md

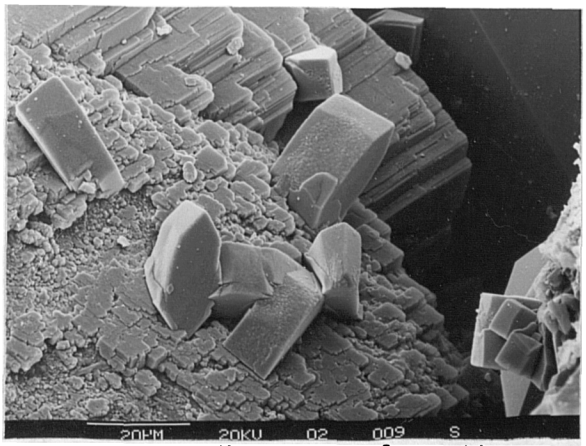

Figure 6.35 Scaling crystals formed in a core, test C25BSS02, grown on feldspars

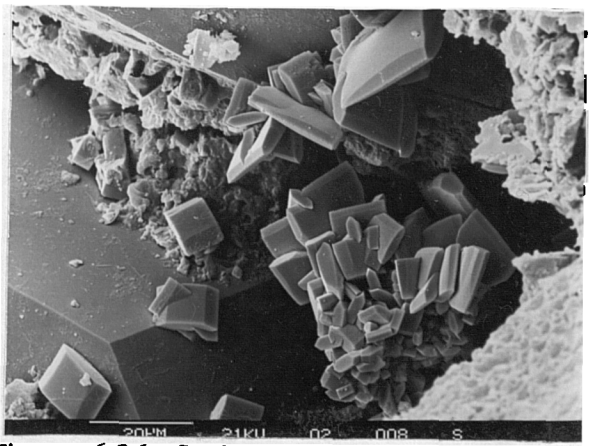

Figure 6.36 Scaling crystals formed in a core, test C25BSS02, cluster of crystals

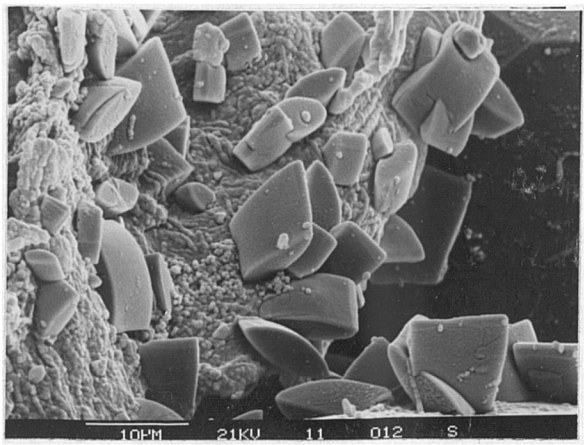

Figure 6.37 Scaling crystals formed in a core, test C27BSS11, protruding into flow. Brine $(Ba+Sr)SO_4$=1 and Sr/Ba=1.0. k_i=35.6md

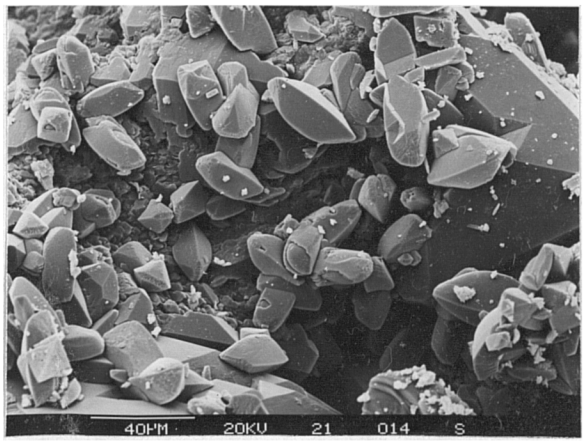

Figure 6.38 Scaling crystals formed in the front section of a core, test C25BSS21, eroded crystals. Brine$(Ba+Sr)SO_4$ =1 and Sr/Ba=100. k_i=573md

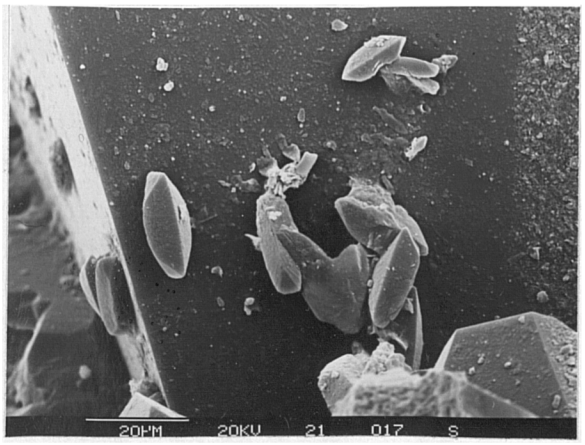

Figure 6.39 Scaling crystals formed in the rear section of a core, test C25BSS21

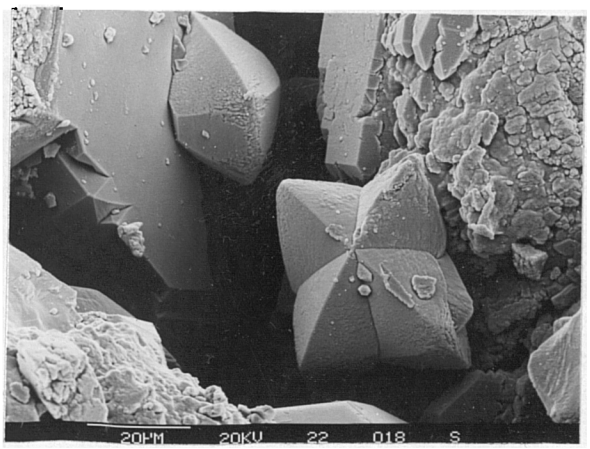

Figure 6.40 Scaling crystals formed in a core, test C25BSS22, twin of crystals. Brine $(Ba+Sr)SO_4$=1 and Sr/Ba=100. k_i=1115md

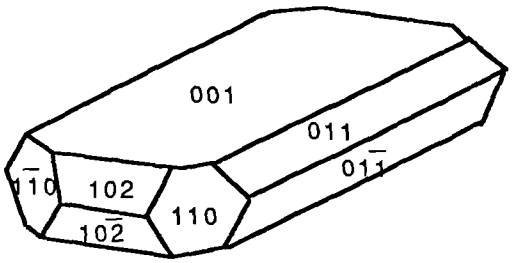

$BaSO_4$

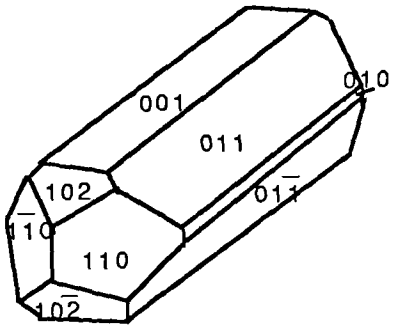

$SrSO_4$

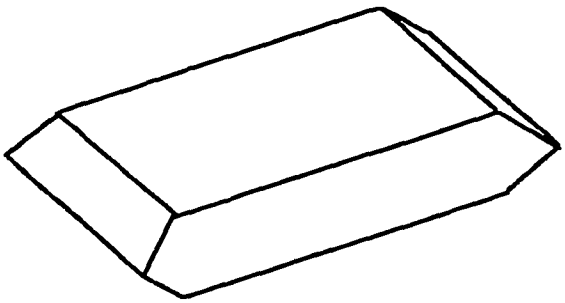

BA,BS0,BSS0,BS1,BSS1or BSH1

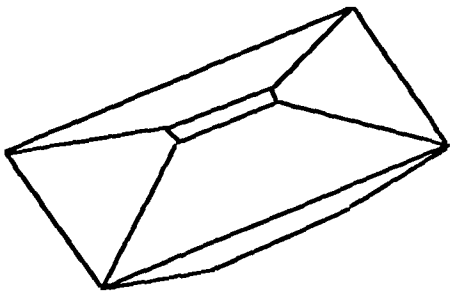

BS2 or BSS2

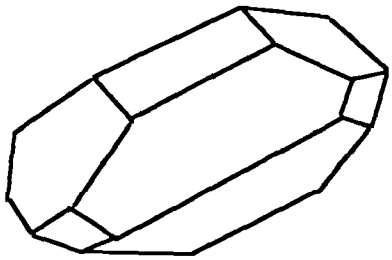

BS3,BSS3 or BSH2

Figure 6.41 **The Typical Habits of (Ba,Sr)SO_4 Crystals Grown at 20°C in Comparison with the Crystal Symmetries Barium Sulphate and Strontium Sulphate**

from brines BS0 and BS1, it becomes clear that BS0 and BS1 crystals bear some resemblance to the perfect $BaSO_4$ crystal but they have fewer faces as if the faces 110 and $1\underline{1}0$ in the perfect $BaSO_4$ have disappeared while faces 102 and $10\underline{2}$ are overgrown, and face 011 and $01\underline{1}$ are overlapped to result in the BS0 and BS1 crystals. The SEM view in figure (6.1) shows the crystals of pure $BaSO_4$ crystals grown in brine BA in this study. The brine BA was the same in $BaSO_4$ supersaturation(15) as brine BS0 but without strontium ion presence therefore only $BaSO_4$ was to precipitate. The BA crystals are very similar to the crystals from brines BS0 and BS1. This is not surprising when we consider that Sr^{2+} was undersaturated in brines BS0 and BS1 and therefore its role in the crystal growth was not important in contrast to Ba^{2+}.

The distinction in morphology is drawn between the crystals formed in brine BS1 in which the Sr/Ba molar ratio was 1 and the crystals precipitated in brine BS2 of Sr/Ba molar ratio equal to 100. The typical BS2 crystal is illustrated in figure (6.4). Whereas the BS1 crystals are tabular, bearing some resemblance to the perfect $BaSO_4$ crystal, BS2 crystals are basically prismatic, having more similarity with the perfect $SrSO_4$ crystal. This difference is again explained from the brine Sr/Ba ratios in the two brines. BS1 brine was undersaturated with $SrSO_4$, whereas $SrSO_4$ had a supersaturation of 4 in the initial mixed brine BS2. Though $SrSO_4$ supersaturation was lower than that of $BaSO_4$ in brine BS2, the quantity of $SrSO_4$ potential of scaling in the aqueous solution was much higher than that of $BaSO_4$ because $SrSO_4$ solubility was about 50 times higher than that of $BaSO_4$ which resulted in $SrSO_4$ being the main component of the precipitated $(Ba,Sr)SO_4$ crystals from BS2 brine. As a result, the crystal growth was most influenced by the presence of $SrSO_4$ and the grown crystals are more like perfect $SrSO_4$ crystal than perfect $BaSO_4$ crystal.

The BS2 crystal may be related to the perfect $SrSO_4$ crystal in the way that faces $110,1\underline{1}0,010$ and $0\underline{1}0$ disappeared, faces 001 and $00\underline{1}$ shrank from the perfect $SrSO_4$

crystal forms, and the other faces had overgrown. The crystal habit again changed significantly from BS2 to BS3 crystals. The crystals precipitated from brine BS3(Sr/Ba=1000) are shown in figure (6.5). Most of the crystals are oval polyhedrons, some are thick tabular like. The tabulars from BS3 are thick and polyhedron, while the tabular crystals from brines BS0 and BS1 are thin and with 8 faces. The BS3 crystal habit, unlike the perfect $SrSO_4$ crystal, is not prismatic although the $SrSO_4$ content in the crystal is predominant. This may be attributed to the very high $SrSO_4$ supersaturation (= 11) in brine BS3 which caused rapid precipitation and irregular growth of the crystal faces.

The pure $SrSO_4$ crystals grown in lower supersaturated $SrSO_4$ brine (SP = 5, similar to that of brine BS2 but without Ba^{2+} presence) in this study are prismatic and show more similarity to the perfect $SrSO_4$ crystal than that of BS3 crystals, as shown in figure (6.6) and compared to figure (6.5) and the crystal symmetry of $SrSO_4$ in figure (6.41). Apart from the significant difference between the BS3 crystals and the perfect $SrSO_4$ crystal, the trace of similar crystal forms between the two crystals can still be seen. As shown in figure (6.41), BS3 crystal is like a crystal transited from the perfect $SrSO_4$ crystal as a result of disappearing faces 010 and 0$\underline{1}$0, shrinking faces 001, 00$\underline{1}$, 110 and 1$\underline{1}$0 and creating a new face 100. The general trend of crystal habits change from BS1 to BS2 until BS3 is tabular to prismatic until oval polyhedron. No distinct difference in morphology between the crystals among BA, BS0 and BS1 is observed though the crystal size difference is visible.

The above described BS crystals were precipitated from the filtered brines. The crystals were also precipitated from the unfiltered BS brines. Their SEM views are seen in figures (6.7) through (6.10). Compared with the crystals precipitated from filtered brines, filtered BS0 crystals have more distinct face and larger size than the unfiltered, in other words, better crystal development. On the other hand, unfiltered BS1 crystals appear more perfect than the filtered BS1 crystals but slightly smaller. The foreign particles in the unfiltered brines probably served as the nuclei for the $(Ba,Sr)SO_4$ solid

solution crystal growth. The difference in morphology between the crystals from filtered BS2 and BS3 brines and the crystals from unfiltered BS2 and BS3 brines are not clearly defined from the SEM photos.

The smaller crystals resulting from secondary nucleation and growth were occasionally found in co-presence with the larger and well developed crystals. These small crystals usually formed clusters, as observed in figures (6.5) and (6.8). Some crystals precipitated from brine BS3 have groove like cuts on the crystal edges.

The crystals precipitated from BSS brines, in which $(Ba^{2+}+ Sr^{2+})/SO_4^{2-}$ molar ratio was one rather two as in BS brines but $BaSO_4$ supersaturation and Sr/Ba ratios were the same as in the corresponding BS brines as shown in table(5.2), are shown in figures (6.11) through (6.14). Comparing these crystal habits with the corresponding crystal habits from BS brines, it is found that the crystals formed in two corresponding brines from the both brine groups are very much similar, e.g, BS1 crystals and BSS1 crystals (Sr/Ba=1.0 in the brines) are like each other in terms of morphology. Like BS crystals, BSS0(Sr/Ba=0.1 in the brine) and BSS1 crystals are 8 face tabulars and similar to one another, The crystals grown in brine BSS2(Sr/Ba=100) are prismatic and the crystals precipitated from brine BSS3(Sr/Ba=1000) are polyhedron or thick tabular like. This demonstrates that, in contrast to the finding by Fischer and Ben Rhinehammer,[34] the change in $(Ba^{2+}+ Sr^{2+})/SO_4^{2-}$ ratio from 1 in BSS brines to 2 in BS brines did not alter the $(Ba,Sr)SO_4$ crystal morphology apparently, as long as the other brine compositional characteristics, e.g, $(Ba,Sr)SO_4$ supersaturation and solution ionic strength, remained the same. Apart from the similarity between the crystals from the two groups of brines, some difference can still be seen. In general terms, BSS crystals are larger but slender than BS crystals, having more distinct tabular or prismatic habits.

To compare the difference between the crystals precipitated from the filtered and unfiltered BSS brines, again, the crystals were precipitated from the unfiltered BSS brines under the same conditions as for growing the filtered BSS crystals. Their SEM microphotographs are given in figures (6.15) through (6.18). Their crystal habits are similar to those filtered crystals, but the unfiltered BSS0 and BSS1 crystals have

rougher surfaces and some cavities or pores are seen on the unfiltered BSS0 crystals while the filtered crystals look smoother and more rigid. This finding is consistent with the observation by Blount[7] that foreign particles affected the crystal perfection.

By doubling the supersaturation of $(Ba,Sr)SO_4$ in the BS1 and BS2 brines, the brines BSH1 and BSH2 were prepared, the brine compositional characteristics are given in table (5.2). The crystals grown in the BSH brines are shown in figures (6.19) and (6.20). The crystals grown from brine BSH1 of $BaSO_4$ supersaturation equal to 30 and Sr/Ba ratio equal to 1 are thin tabulars with cavities(pores) on the crystal faces. The crystal faces are not well developed and the crystals are less regular in contrast to the BS1 crystals, grown from the brine of half the supersaturation of BSH1 brine. This agrees with most of the previous investigations [34,86,90,155] that higher precipitating ion concentrations lead to less perfect crystals. The crystal habit of brine BSH2($BaSO_4$ supersaturation equal to 30 and Sr/Ba ratio equal to 100) has altered from prismatic as observed in crystal BS2($BaSO_4$ supersaturation was 15 in the brine) to polyhedrons. The crystals have groove like cuts on their edges and some of the crystals are broken. The crystal outlook varies largely within the BSH2 crystals. The BSH2 crystals bear more resemblance to BS3 crystals than to BS2 crystals because both BSH2 and BS3 brines were $SrSO_4$ dominant and had closer $SrSO_4$ supersaturations.

Crystal Size

In the last subsection, the morphology of $(Ba,Sr)SO_4$ crystals formed from the static bulk solutions was examined. Here the other aspect of crystal external form, the crystal size, is to be analysed. The crystal size is rather an ambiguous term because most of crystals do not have a spherical or cubic shape and the dimensions of different crystal axes are not the same. In this study, for convenience, the crystal size is defined equivalent to the diameter if a crystal is spherical or circular, otherwise it is equivalent to the longest axis of the crystal.

The crystal size observed among all the ambient temperature beaker tests ranges from

5μm to about 30μm (excluding the much smaller secondary grown crystals) which are considerably smaller than the natural barite or celestite scale which has the usual size of 100-200μm. The size varies from the crystals precipitated in one brine to the others. A difference in crystal size among the crystals precipitated from the same brine were also found, particularly in the brines of very high Sr/Ba ratio(Sr/Ba=100 or 1000). Generally, the crystal size from BS brines of $(Sr+Ba)/SO_4$ ratio equal to 2 increases in the sequence from BS0, BS1, BS2 to BS3 as Sr/Ba ratio in the brines increases from 0.1, 1.0, 100 to 1000. The crystal size change in BSS brines of $(Sr+Ba)/SO_4$ ratio equal to 1 is not in a sequential order as Sr/Ba ratio increase but in the following sequence: BSS1(Sr/Ba=1.0) < BSS0(Sr/Ba=0.1) < BSS2(Sr/Ba=100) < BSS3(Sr/Ba=1000). BSH1 crystals(Sr/Ba=1.0 in the brine) do not have apparent difference from BSH2 crystals (Sr/Ba=100 in the brine) in terms of size, BSH1 crystals appear slightly larger than BSH2 crystals.

BSS crystals are usually larger than BS crystals, only BSS1 crystals are the exception. Also it seems higher supersaturation resulted in larger crystals, as seen from comparison of BS crystals with BSH crystals.

The crystal size difference between crystals precipitated from the filtered brines and those unfiltered has been noticed. The trend is not consistent. Whereas the filtered BS0, BS1, BSS0 and BSS1 brines produced larger crystals than the corresponding unfiltered brines, the contrary seems true for brine BS2, BS3, BSS2 and BSS3. This indicates that the effect of foreign particles in the solutions on crystal size is different between the $BaSO_4$ dominant precipitation and the $SrSO_4$ dominant precipitation.

6.2.2 Microscopic Study of the Scaled Core Samples

The SEM photos were analysed for microscopic study of the scaled core samples. The aspects looked at in the study of the scaled core samples are outlined as below,

i. scaling crystal habits,

ii. crystal size,

iii. deposition sites of the scaling crystals on the rock pore surface,

iv. scaling crystal orientation in the pore space,

v. crystal abundance and distribution within a core, and

vi. the effect of hydrodynamic forces.

In the next section, the SEM views of the scaled core samples are examined and the above listed aspects are looked at.

Crystal Habits

Some of the SEM photos of the scaled core samples are shown in figures (6.21) through (6.40). It is very interesting to note that, when the crystals grew in the rock pores under dynamic flow influence, the basic crystal habits (or crystal forms) did not alter from the crystal habits from static condition. This observation is in accordance with the report by Sarig[122] that stirring did not change crystal habits. This is an important point when relating the crystals formed in the static solutions to those precipitated from flowing brines and it indicates the beaker test is a simple and effective means to study scaling crystal morphology.

The brines BS, BSS and BSH which were used in beaker tests were injected through rock cores to form scale in porous media. The brine compositions are shown in table (5.1) and their characteristics are given in table (5.2) in chapter 5. As shown in table (5.2), $(Ba+Sr)/SO_4$ ratio in BS brines and in BSH brines is 2 and it is 1 in BSS brines, $BaSO_4$ supersaturation is 30 in BSH brines, twice as high as in BS or BSS brines.

By examining the $(Ba,Sr)SO_4$ scaling crystals precipitated from the BS, BSS and BSH brines in the rock pores, it was found that, in general, the crystals precipitated from brines BS0(Sr/Ba=0.1), BS1(Sr/Ba=1.0), BSS0(Sr/Ba=0.1) and BSS1(Sr/Ba=1.0) as well as BSH1(Sr/Ba=1.0) are tabular-like, BS2 and BSS2 crystals(Sr/Ba=100 in both brines) are prismatic, and BS3, BSS3(Sr/Ba=1000) and BSH2(Sr/Ba=100) are oval polyhedrons, which is generally consistent with the crystal

habits formed in the beaker tests with the same brines. Apart from the general similarity, the crystals deposited in the rock pores, unlike those crystals from the beaker tests, are less regular, less uniform and their external morphology and size often vary from site to site in a core. A few scaling crystals have a porous nature, as seen in figure (6.30). Some crystals look like having been eroded or having dissolved into the fluids, as shown in figure (6.38). Also the dislocations on some crystals are observed as in figures (6.32) and (6.34).

The differences between the crystals precipitated from the static solutions and those deposited in cores are believed caused by the porous nature of a rock, the flow condition and the continuous supply of the mixed brine. Firstly, the mixing between the two incompatible brines was bound to be less thorough and varied from one location to the other in a porous medium, in contrast to the homogeneous mixing in a beaker, due to the tortuosity, pore size distribution and the heterogeneity within a rock. Secondly, the fresh brines were continuously pumped through the core during a test while the brine supersaturation was steadily declining as the crystal precipitation took place in a beaker test. Thirdly, the the massive foreign particles such as fines, clay and rock substrates in a core might have influenced the nucleation and subsequent growth of the scaling crystals. Next, the dispersion, convection and local turbulence existing in the flow would have effect on the brine mixing and crystal precipitation in the pore space. Last, the shearing force existing in the flow could have influenced the crystal growth.

Crystal Size

As mentioned in the last subsection, the crystals precipitated in the rock pores from the same brine are not very uniform among themselves in their external morphology. This is also true in respect to crystal size. The size variation in the crystals was found from one location to the other within a core. The causes of such a variation are considered as the same as those causing diversity in crystal morphology, as discussed in the last paragraph. The crystal size observed for the crystals precipitated from all the brines in cores ranged from 5μm to 40μm. The crystals grown in the rock pores were

generally larger (or could grow larger) than the crystals grown from the same brines but under the static condition. This may have been attributed to the continuous supply of the scaling ions from a fresh brine during a core flooding while the brine supersaturation was declining steadily during the scale precipitation in a beaker. The larger crystals formed under flow have the similar dimension to that of average rock pores.

Crystal Growing Sites

After examining all the SEM photos taken for the scaled core samples, it was concluded that the scaling crystals did not have preference on the growing sites on the rock pore surfaces. The crystals were found deposited onto various sites: rock grains, quartz overgrowth, feldspars and fines, as demonstrated in figures (6.23), (6.24), (6.26), (6.33), (6.35) and (6.37). The roughness or smoothness of a rock surface appeared not to affect the scale deposition because both clean, smooth surface and rough, dirty surface attracted the scaling crystals on the surfaces, as seen from these SEM electromicrographs. Due to the limitation of the SEM which can only provide two dimensional view of a rock pore, it is hard to know whether more scale deposited in the pore throats than in the larger pore space or vice versa. The general impression is that the scaling crystals did not deposit at specific sites on the pore walls. No preference in scaling sites may suggest that the nucleation took place in the solution and then precipitated on the pore surface.

Scaling Crystal Orientation

Most of the crystals precipitated from the brines of lower Sr/Ba ratios(0.1 and 1.0) show certain orientation in the rock pore space. They did not lay on the rock surface but somewhat protruded into the flow stream, as shown in figures (6.31), (6.35) and (6.37), which enabled the crystal growth to receive more supply of scaling ions flow the flowing brines. The protruding crystals obviously caused larger resistance to the flow which will result in higher permeability decline. On the other hand, most of the crystals

precipitated from the brines of higher Sr/Ba ratios (100 and 1000) were prone to the pore walls, as indicated in figures (6.28) and (6.30). The difference in the orientation of the scaling crystals may be due to the difference in the mechanism by which the $BaSO_4$ dominant crystals and the $SrSO_4$ dominant crystals grew or may be due to the different crystal habits between the $BaSO_4$ dominant crystals and the $SrSO_4$ dominant crystals.

Crystal Abundance and Distribution in a Core

The quantity of scale formed in a core is dependent on two factors: the brine supersaturation and the brine injection time. From the SEM study, it was noted that for the same experimental condition, the abundance of the $(Ba,Sr)SO_4$ crystals in the cores formed from brines BS0, BS1, BS2, BSS0, BSS1 and BSS2 did not show noticeable differences, while brines BS3, BSH1, BSH2 and BSS3 obviously produced more scales in the cores as expected since much higher scaling ion concentrations existed in these brines. In the case of large scale deposition, the rock pores were almost completely blocked by the massive scaling crystals. On the other hand, few crystals deposited in the rock pores in some of the flow tests.

In general, the crystal abundance declined significantly from the front section to the rear section of a core, as suggested by comparing figure (6.21) to (6.22) and comparing (6.23) to (6.24). This indicates that the mixing of two brines took place immediately after they entered the core and the $(Ba,Sr)SO_4$ crystal nucleation and growth were rapid processes.

The Effect of Hydrodynamic Forces

Most of the solid solution crystals formed during the core flooding did not show any influence of the flow shearing force on their morphology. The crystals had well developed, distinct faces and edges as shown in figures (6.25), (6.29), (6.36) and (6.40), that would not be expected if their growth was disturbed by the flow. The

crystals formed from a few tests with tight cores did have rounded faces, as appeared in figures (6.21) and (6.26), which may have been caused by the stronger shear force present in the tight cores but other causes cannot be ruled out. For example, the crystals perhaps had not grown up at the time of stopping the experiment, due to the short period of brine injection.

The Mechanism of $(Ba,Sr)SO_4$ Crystallisation

Finally, the mechanism by which the nucleation, precipitation and growth of the scaling crystals within the porous media under the flow influence may be speculated from the study of the SEM views of the scaled core samples.

First, the nucleation of $(Ba,Sr)SO_4$ crystals was certain to be heterogeneous, this is because of numerous foreign particles and substrates in the rock pores which may act as the nuclei. Previous investigations [38,83,87,137,153] on $BaSO_4$ and $SrSO_4$ crystals have all confirmed that the homogeneous nucleation was extremely difficult even without any foreign particles present unless the sulphate supersaturation was very high. They also demonstrate that homogeneous nucleation took a longer time to happen, that is contrary to the rapid formation of the scaling crystals in all present core flow tests. Fines or other foreign particles in the brine rather than the rock substrates probably acted as the nuclei, otherwise the crystal deposition sites on the rock pore surface might have shown some preference.

The more interesting point is whether the $(Ba,Sr)SO_4$ crystal growth took place on the rock surface or they first grew up in the flowing brine and then deposited on the pore surface. Two findings all indicate that the process of scaling crystal growth actually took place on the rock pore surface. First, if the growth had occurred in the fluid then the crystals would have travelled with the brine downstream which contradicts the finding that very large numbers of crystals precipitated at the very front section of a core plug. Secondly, most of the crystals, particularly those formed in the lower Sr/Ba ratio brines (Sr/Ba=0.1 or 1.0), were found tightly bound on the rock pore walls, as if they

had grown into the rock matrix. In addition, the time for a brine to travel through a core was less than one minute and a crystal cannot be well developed in such a short period. All these findings evidently rejected the possibility of deposition of the grown-up crystals on the rock surface.

It is not clear whether the sulphate solid solution crystal growth rate was diffusion controlled or surface reaction controlled. The reports [21,38,82,83] on $BaSO_4$ and $SrSO_4$ crystallisation in the static solutions believed this process was surface reaction controlled.

6.3 ANALYSIS OF THE BRINE EFFLUENT FROM CORE TESTS

During a few of the room temperature formation damage experiments, the brine effluents from the cores were sampled at certain time intervals. The Ba^{2+} and Sr^{2+} ion concentrations in the effluents were then analysed in IOE (Institute of Offshore Engineering) by Plasma emission spectroscopy. The analysed concentrations of Ba^{2+} and Sr^{2+} in the brine effluent samples taken during core tests are listed in table (6.1) and the concentration changes from the initial brines to effluent brines are shown in table (6.2). As discussed in subsections (5.5.2) and (5.6.2) of chapter 5, the effluent analysis should be able to provide the information about the Ba^{2+} and Sr^{2+} concentration profile during a test, the Ba^{2+}/Sr^{2+} ratio change, the effluent $(Ba,Sr)SO_4$ supersaturation profile, the volume of scale precipitated from the brine and the sulphate scaling rate.

Disappointingly, the analysed brine effluent data appears inconsistent, as seen in table (6.1), and it is considered due to errors in sampling and measurement. Three factors may have contributed to such errors in the analysis of Ba^{2+} and Sr^{2+} concentrations in the effluents. Firstly, in the original sampling method which was discarded in 70°C tests, the sampled brine effluents were still supersaturated with $BaSO_4$ or SrSO4 and they may have precipitated out before any dilution was taken. Next, the sampled effluents were diluted by adding distilled water into the samples and about 15 ml of each diluted brine was stored in a test tube waiting for the analysis. Sometimes,

Table 6.1 Ion Concentration Changes in the Brine Effluents during 20°C Core Tests

Test	Brine	Sampling time (mins)	Ba(mg/l)	Sr (mg/l)
C16BS21	BS2	16	-	1205
		38	-	1240
		61	-	1192
C25BS22	BS2	13	-	1136
		40	-	1172
		100	-	1100
		164	-	1116
		300	-	1156
C25BS32	BS3	13	-	2510
		44	-	2480
		72	-	2480
C27BSS01	BSS0	14	34.5	7.9
		31	86.0	7.9
		56	78.0	8.1
		186	62.0	7.6
C27BSS11	BSS1	15	30.1	66.0
		32	60.0	42.0
		49	45.1	72.0
C25BSS21	BSS2	19	-	936
		38	-	948
		69	-	960

Table 6.2 Ion Concentrations in the Brine Effluents from 20°C Core Tests

Tests	Brine	$Ba_{,i}$ (molar)	$Sr_{,i}$ (molar)	$Ba_{,e}$ (molar)	$Sr_{,e}$ (molar)	$Ba_{,e}/Ba_{,i}$	$Sr_{,e}/Sr_{,i}$	$Ba_{,i}/Sr_{,i}$	$Ba_{,e}/Sr_{,e}$	$SP_{Ba,i}$	$SP_{Ba,e}$	$SP_{Sr,i}$	$SP_{Sr,e}$
C16BS21	BS2	0.00015	0.01536	no	0.01384	no	0.90	no	no	15.0	no	3.8	3.2
C25BS22	BS2	0.00015	0.01536	no	0.01297	no	0.84	no	no	15.0	no	3.8	2.9
C25BS32	BS3	0.00005	0.04878	no	0.02842	no	0.58	no	no	15.0	no	11.9	3.7
C27BSS01	BSS0	0.00104	0.00010	0.000474	0.000090	0.46	0.90	10	5.3	15.0	7.1	0.12	0.08
C27BSS11	BSS1	0.00077	0.00077	0.000329	0.000685	0.43	0.89	1.0	0.48	15.0	8.0	0.38	0.29
C25BSS21	BSS2	0.00011	0.01086	no	0.01082	no	0.97	no	no	15.0	no	3.8	3.7

* $Ba_{,i}$ —— barium concentration in initial brine, $Sr_{,i}$ —— strontium concentration in initial brine,
$Ba_{,e}$ —— average barium concentration in brine effluent samples from one core test
$Sr_{,e}$ —— average strontium concentration in brine effluent samples from one core test
SP —— supersaturation of barium sulphate or strontium sulphate
no —— no effluent analysis

the original effluent may not have thoroughly mixed with the added distilled water when the 15 ml of the mixed water was taken into the test tube. Thirdly, owing to improper arrangement, most of the samples had waited for at least a couple of weeks for the Plasma analysis.

Though these effluent data were not very reliable, they do give a general impression on the changes in $BaSO_4$ and $SrSO_4$ concentrations in the initial brines to the brine effluents resulting from the scale formation within the rock cores, as shown in table (6.2). From table (6.2), it is clear that the brine supersaturations had reduced significantly in the effluents but the brines were still supersaturated with sulphates, bearing in mind that the time for an injected brine to travel through a core plug was less than 1 minute which was the period allowed for the scale to deposit from the brine to the rock pore surface. Also it indicates from table (6.2) that the $BaSO_4$ scaling rate was much faster than that of $SrSO_4$.

6.4 PERMEABILITY DECLINE DUE TO SOLID SOLUTION SCALE FORMATION

As described in the last chapter, the recorded pressure data during a formation damage experiment in a core were subsequently converted to the overall core permeability and sectional permeabilities. The core permeability damages due to scale formation were calculated and presented in table (6.3). From the calculated permeability vs time relation, five different results were derived.

Firstly, the overall core permeability and sectional permeabilities were graphed against the brine injection time, as demonstrated in figures (6.42) and (6.43). Secondly, the permeabilities as the percent of the initial values were plotted against the brine injection time, as shown in figures (6.44) and (6.45). Thirdly, the permeability decline rate (dk_t/dt) versus time curves were drawn, as shown in figure (6.46). fourthly, the time at which the core permeability decline rate had just reduced to the half of its initial value($t_{1/2}$) was calculated from the numerical permeability - time relation. Lastly, the brine injection time corresponding to the nominal maximum curvature of a

Table 6.3 Core Permeability Decline due to Scaling at 20°C

Test	Brine used	Brine injection time (mins)	k_i (md)	k_f (md)	Δk_f (md)	$(\Delta k_f/k_i)\times 100$
C28BS01	BS0	226.	269.0	28.0	241.0	89.6
C16BS14	BS1	8	46.0	41.5	4.5	9.8
C25BS15	BS1	306	92.0	49.0	43.0	46.7
C16BS16	BS1	45	53.5	21.5	32.0	59.8
C25BS17	BS1	209	1100.0	736.0	364.0	33.1
C16BS21	BS2	59	45.6	20.5	25.1	55.0
C25BS22	BS2	276	1025.0	465.0	560.0	54.6
C25BS32	BS3	179	940.0	53.0	887.0	94.4
C28BSH11	BSH1	139	223.0	60.0	163.0	73.1
C29BSH13	BSH1	17	19.5	13.3	6.2	31.8
C28BSH21	BSH2	25	72.5	22.5	50.0	69.0
C27BSS01	BSS0	183	160.0	73.0	87.0	54.4
C25BSS02	BSS0	310	730.0	510.0	220.0	30.1
C27BSS11	BSS1	48	35.6	25.0	10.6	29.8
C16BSS12	BSS1	37	32.5	21.0	11.5	35.4
C25BSS21	BSS2	369	573.0	455.0	118.0	20.6
C25BSS22	BSS2	97	1115.0	1060.0	55.0	4.9

* k_i —— initial core permeability, k_f (md) —— final core permeability after scale formation
Δk_f —— final permeability reduction due to scaling, $(\Delta k_f/k_i)\times 100$ —— final permeability reduction as % of k_i

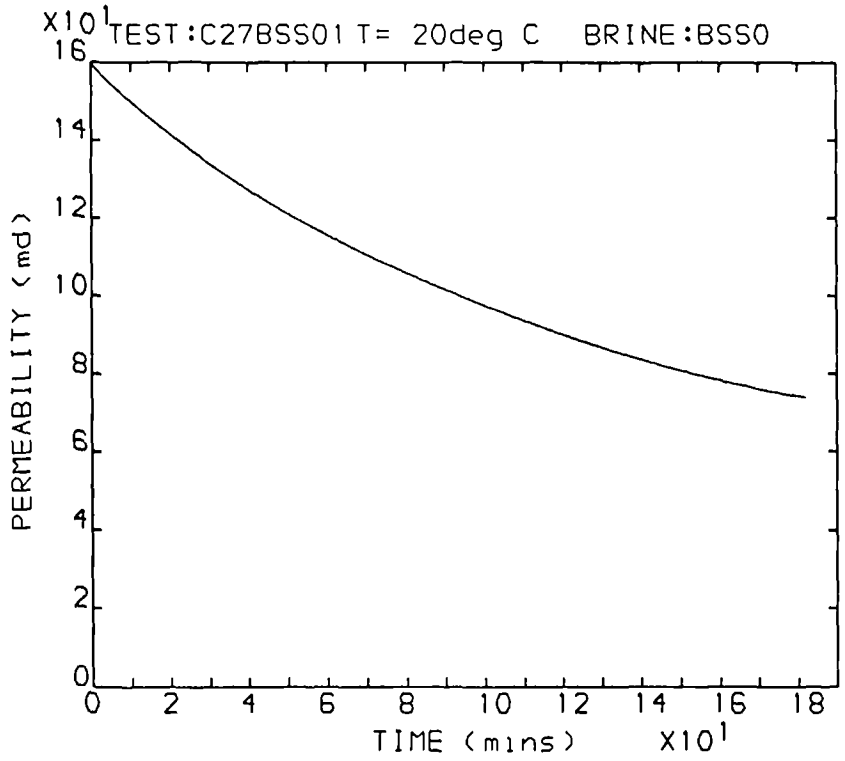

Figure 6.42 Overall core permeability - brine injection time curve

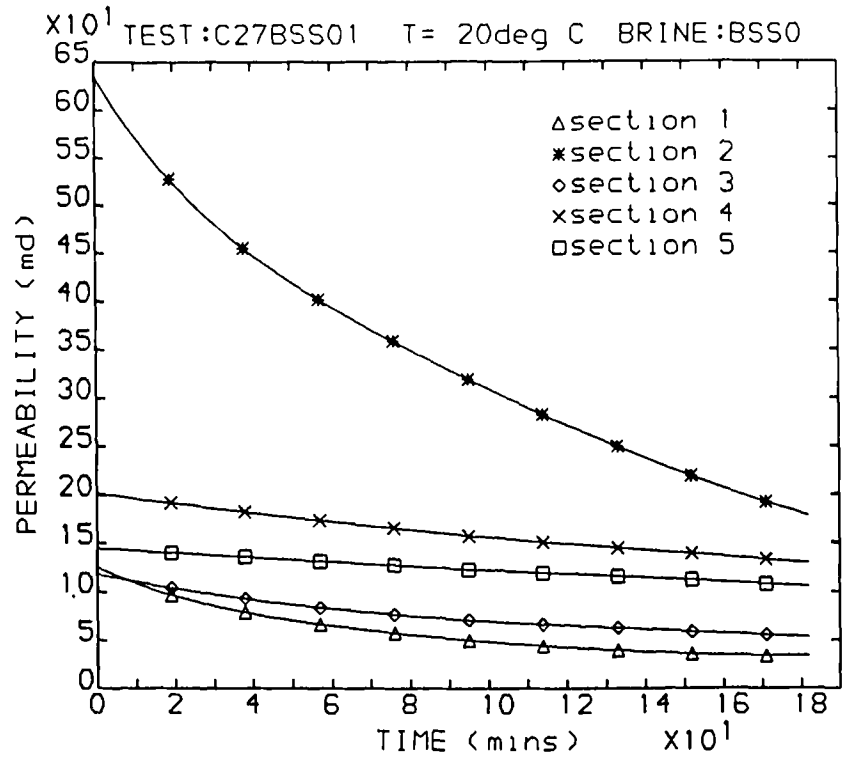

Figure 6.43 Core section permeability - brine injection time curves

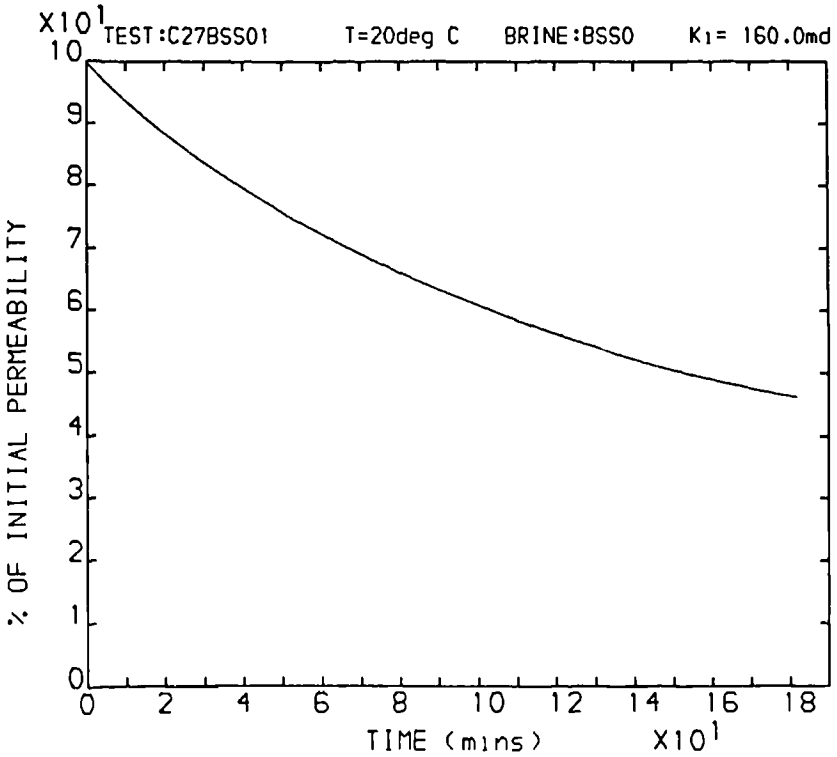

Figure 6.44 Overall core permeability curve, y axis is the permeability as percent of initial permeability

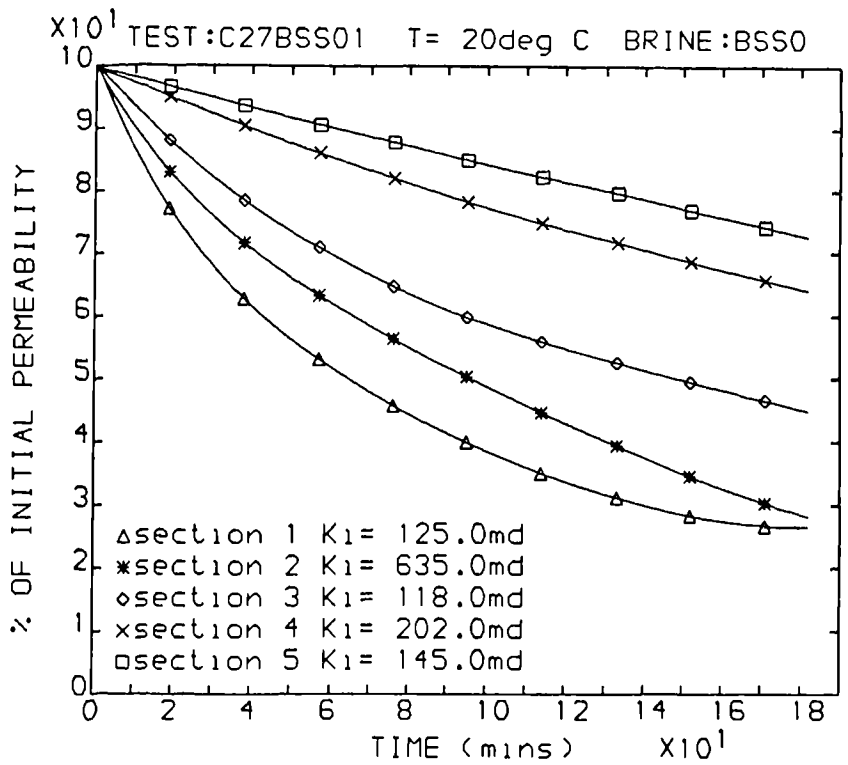

Figure 6.45 Core section permeability curves, y axis are section permeabilities as percent of initial section permeabilities

permeability - time curve(t_c) was calculated. The definition of t_c will be given in subsection (6.4.2).

By analysing all the curves and calculated data, the extent of permeability damage caused by the $(Ba,Sr)SO_4$ solid solution scale precipitation, the pattern or trend of the overall and sectional permeability reduction, the permeability decline rate and the rate change during a test, and the numerical characteristics of the permeability curves may be understood from this study. Also the influencing factors may be clarified. In the following subsections, these results are discussed in detail.

6.4.1 Permeability Decline Trend

Overall Permeability

Figures (6.47) and (6.48) show two extremes of the permeability damage arising from $(Ba,Sr)SO_4$ scale deposition in the porous media. Figure (6.47) shows less than 10% of initial core permeability was reduced after an entire core flow test and figure (6.48) shows more than 90% of the initial permeability was impaired in a heavily scaled core. Medium range of permeability damage was observed more frequently, as shown in table (6.3).

The permeability - brine injection time profile also shows differences between the curves in figure (6.47) and (6.48). The permeability reduction curve in figure (6.47) is linear like but the curve in figure (6.48) has a concave profile. It was found from most of the 20°C tests, that the curve shape in figure (6.47) is typical when the permeability damage extent was small (approximately less than 30% of k_i), while the concave curve is the case of large permeability damage. It seems that the first section of a permeability reduction curve, at which the permeability decline extent was small, is almost linear, no matter what extent of permeability was finally reduced by the scale formation. This was demonstrated by plotting only the first section of the concave curve in figure (6.48), as shown in figure (6.49). There are a few factors having effects on the permeability

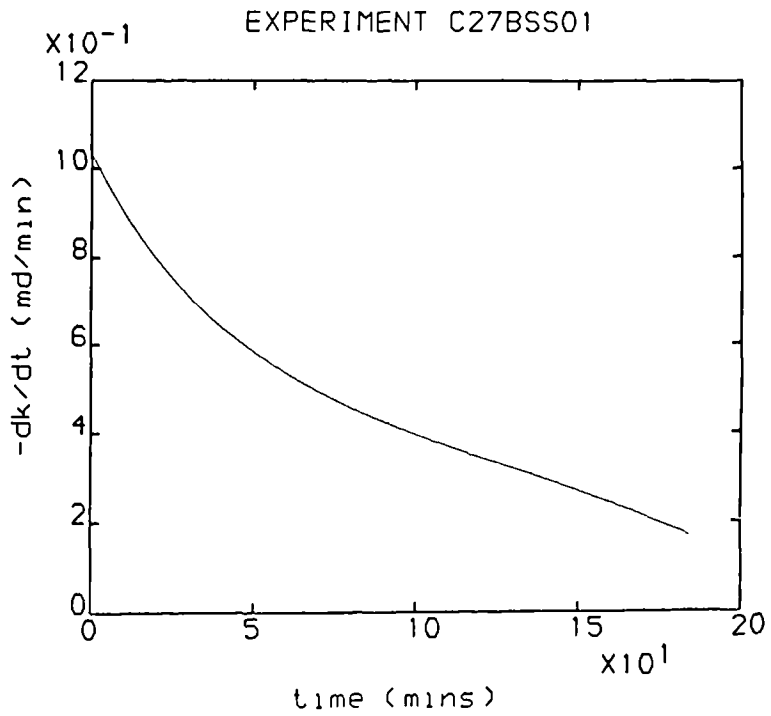

Figure 6.46 Core permeability decline rate curve

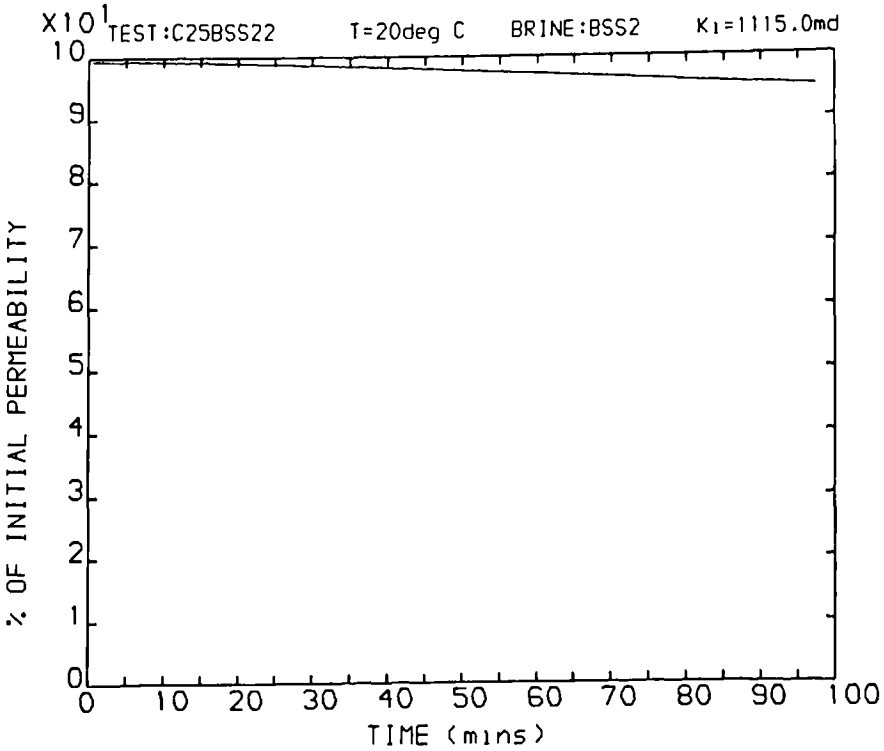

Figure 6.47 Permeability damage curve in a lightly scaled case

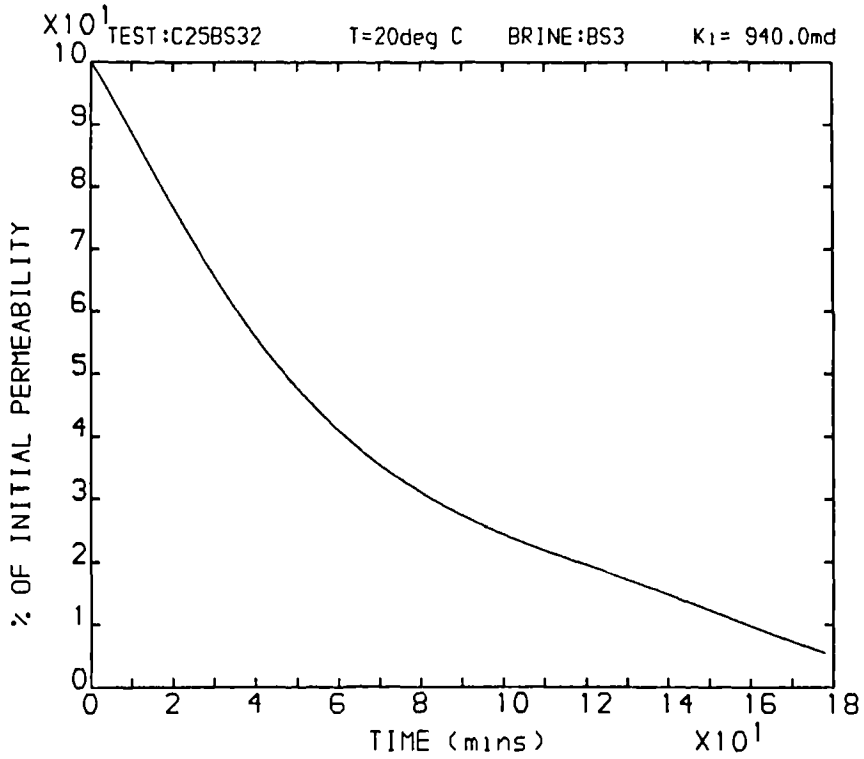

Figure 6.48 Permeability damage curve in a heavily scaled case

damage extent and the trend of permeability decline during a flow test. The following text is given to the discussion of these factors.

a. Initial core permeability

In most of the core tests, a core with lower initial permeability usually suffered higher percent loss of its initial permeability, as seen in figure (6.50) but less permeability loss in absolute terms, as shown in figure (6.51), when the tests were carried out at similar conditions. This observation was the case particularly when comparing the formation damage in two cores largely different in their initial permeabilities. This is not difficult to understand because the relative degree of resistance to the flow raised by the same amount of scale precipitation is always larger in a tight core than to a more open core. As exceptions, a few cores experienced the reverse situation as indicated in figure(6.52).

b. Sulphate supersaturation

The (Ba,Sr)SO_4 supersaturation was found to play an important role in determining the extent of permeability decline. Figure (6.53) shows the permeability declines in the rock cores injected with the brines of different supersaturations, the tests were conducted at similar conditions. The doubling in the initial brine supersaturation resulted in a much significant loss of the core permeability, as a result of a larger quantity of scale deposition in the rock pores, which can be seen by comparing the SEM views in figures (6.26) and (6.31).

c. Scaling ion concentration ratio

Formation damage experiments were also carried out with the brines of different Sr/Ba ratios but constant $BaSO_4$ supersaturation. Their permeability curves are presented in figures (6.54), (6.55) and (6.56). The variation in permeability reduction

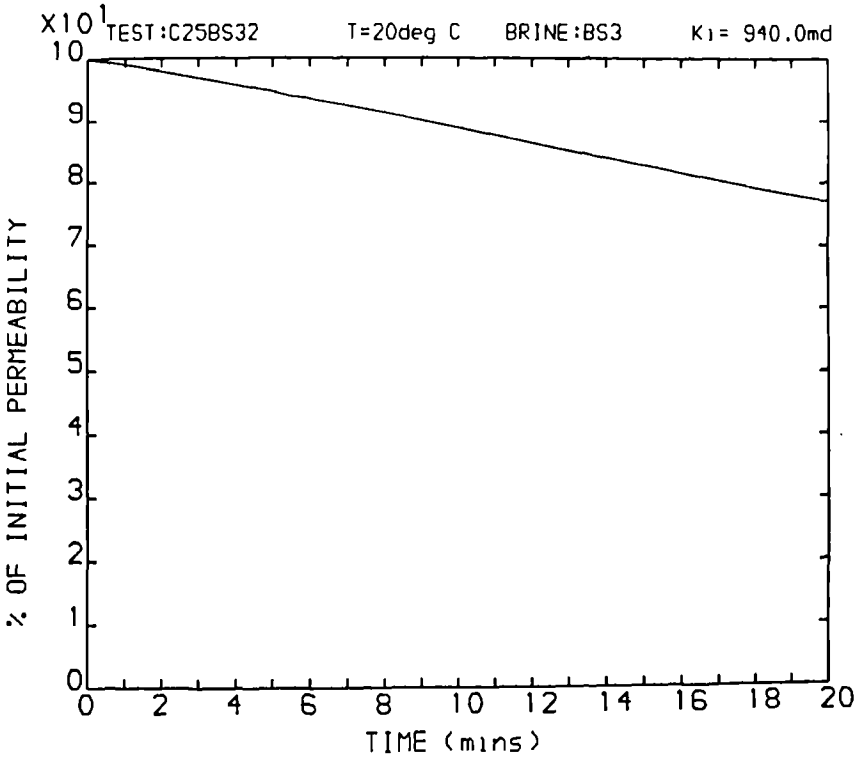

Figure 6.49 First section of the permeability curve in figure 6.48, the permeability - time relation is almost linear

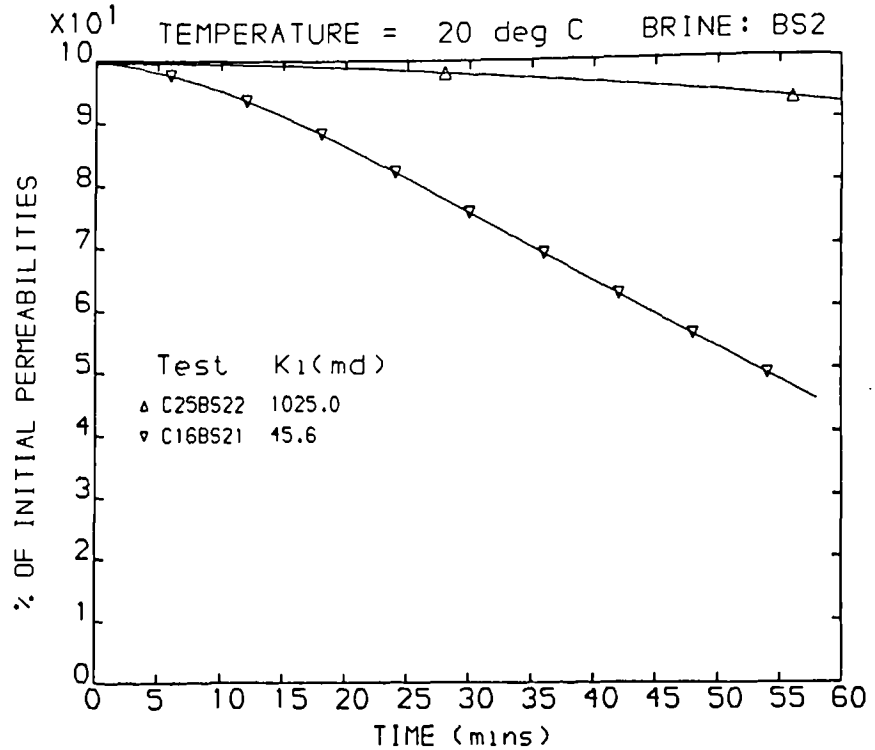

Figure 6.50 Percent permeability damages due to scaling in two cores of different initial permeabilities injected with the same brine.

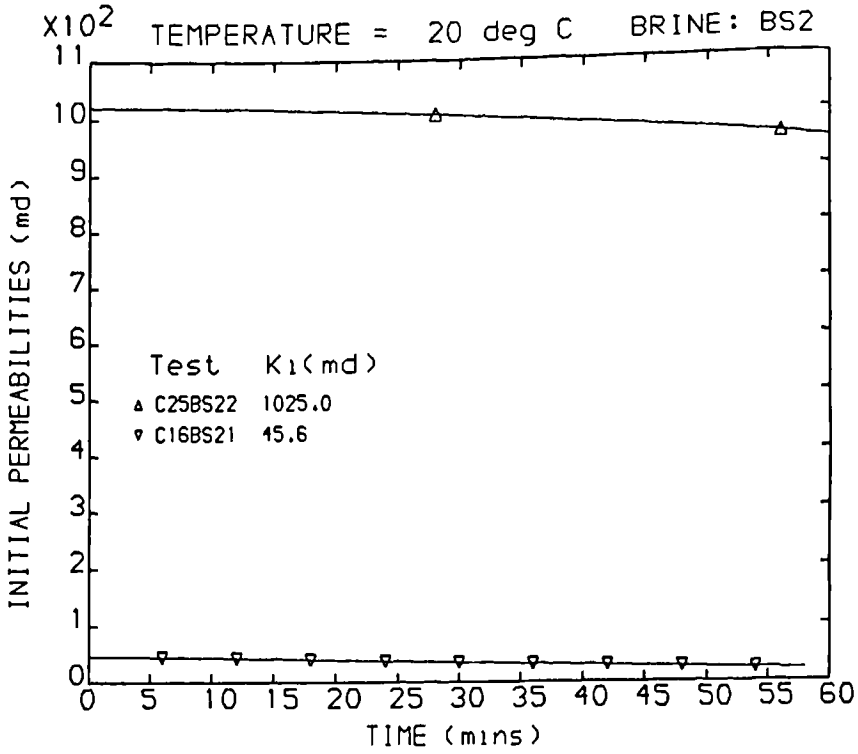

Figure 6.51 Permeability damages in absolute terms, compared to figure 6.50

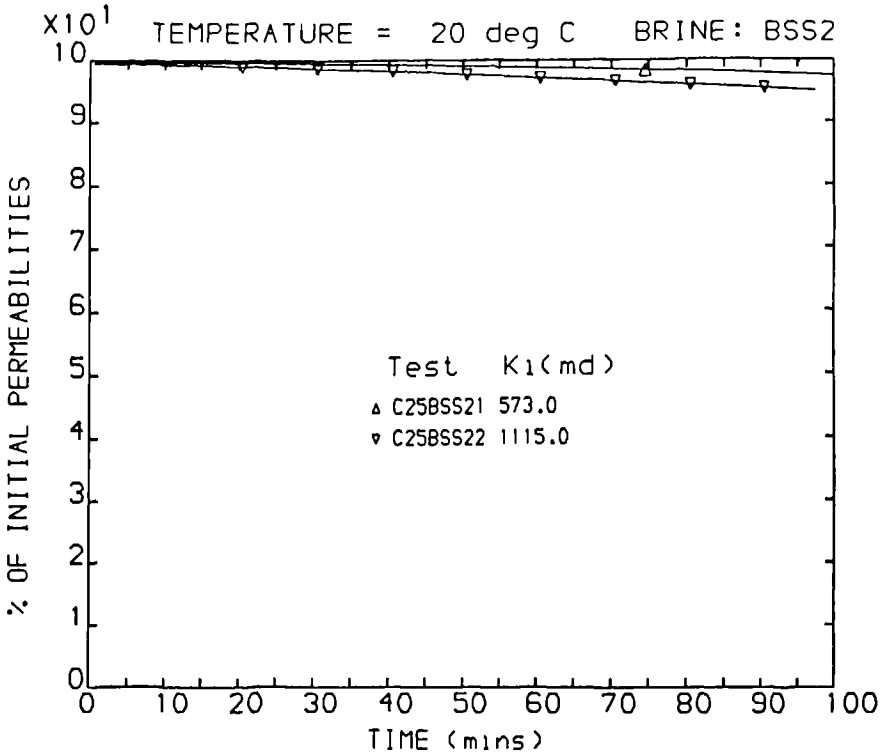

Figure 6.52 Permeability damages due to scaling in two cores of different initial permeabilities injected with the same brine, more permeability damage in relative terms occurred in more permeable core, an unusual case

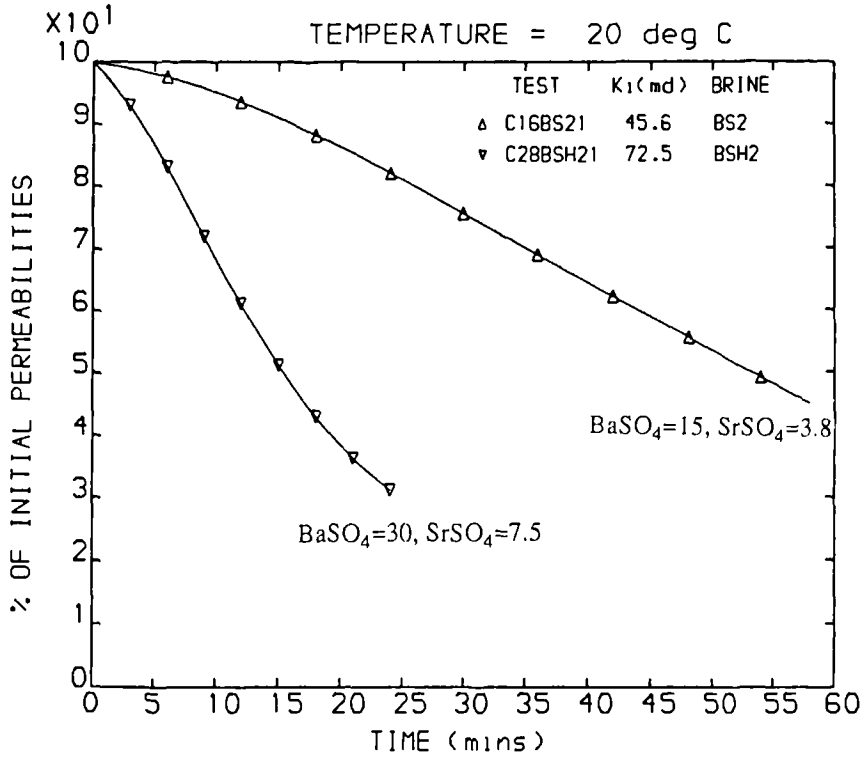

Figure 6.53 Permeability damages in two cores injected with brines of different supersaturations

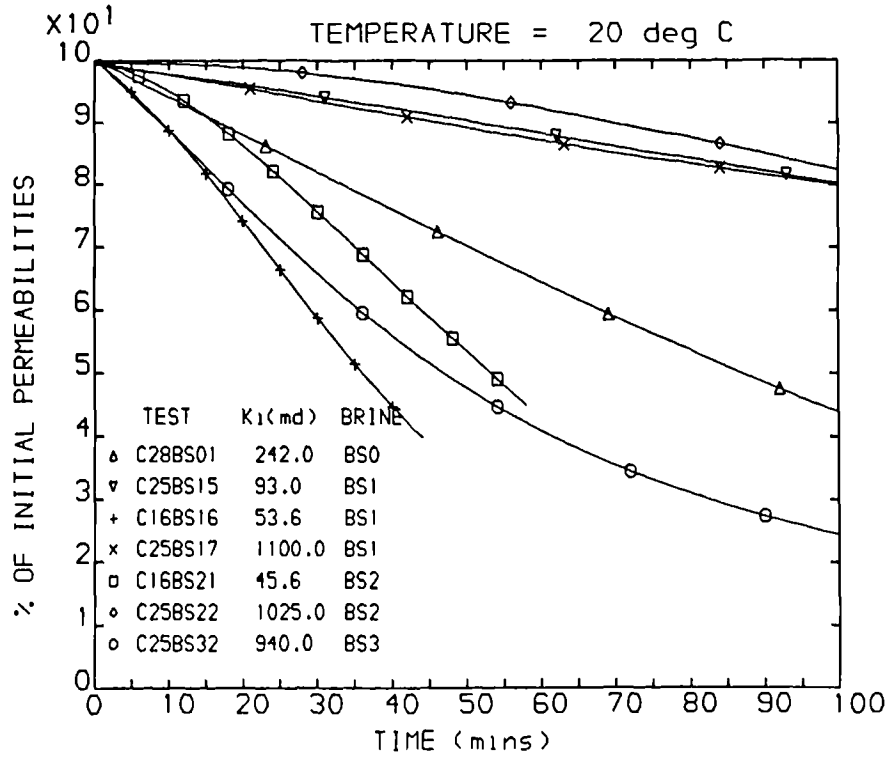

Figure 6.54 Permeability damages due to injecting BS brines of different Sr/Ba molar ratio.

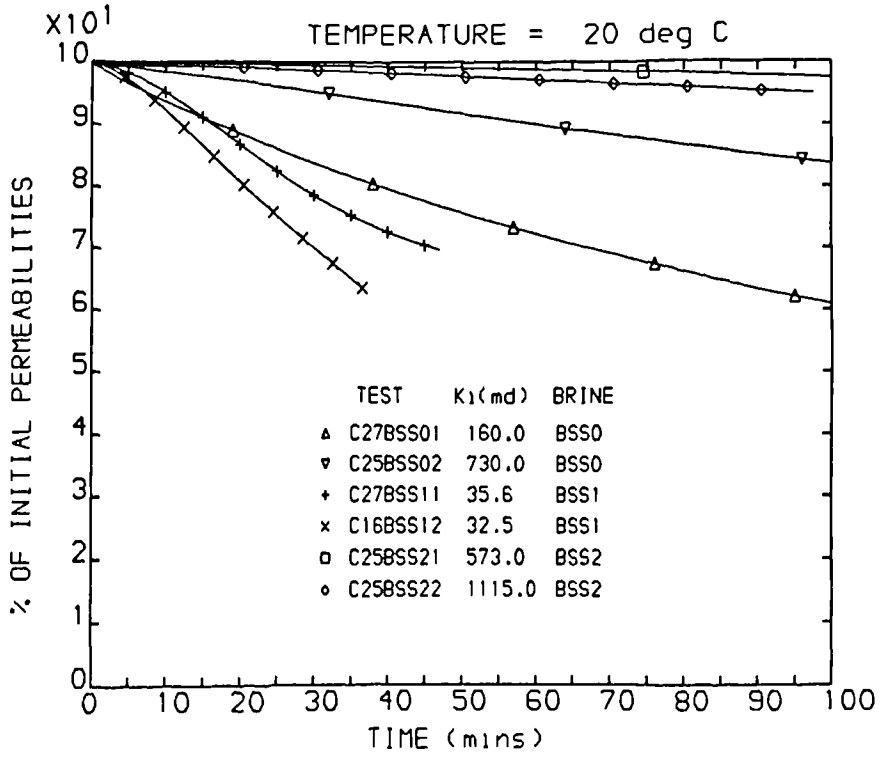

Figure 6.55 Permeability damages due to injecting BSS brines of different Sr/Ba molar ratio.

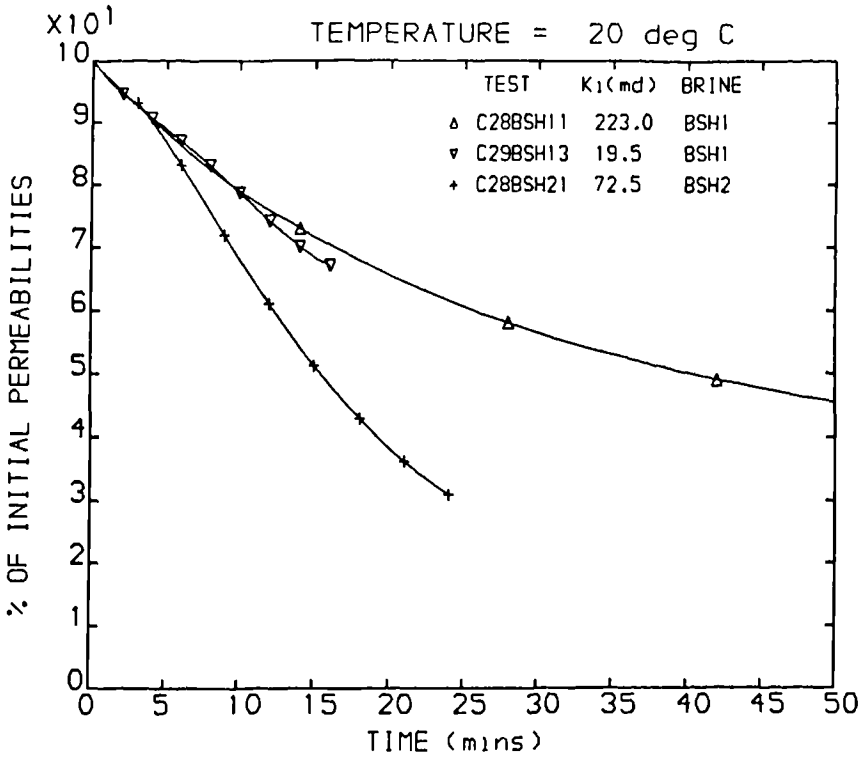

Figure 6.56 Permeability damages due to injecting BSH brines of different Sr/Ba molar ratio.

caused by the scale formation in the cores of similar initial permeabilities was subject to the difference in the brines. The brines rated according to causing permeability damage extent from high to low, may be listed as BS3(Sr/Ba=1000) > BS0(Sr/Ba=0.1) ≥ BS1(Sr/Ba=1.0) ≥ BS2(Sr/Ba=100), BSS3(Sr/Ba=1000) > BSS0(Sr/Ba=0.1) ≈ BSS1(Sr/Ba=1.0) ≥ BSS2(Sr/Ba=100) and BSH2(Sr/Ba=100) > BSH1(Sr/Ba=1.0).

Brines BS3 and BSS3 had the highest Sr/Ba molar ratio (1000) at which the $SrSO_4$ supersaturation was 11. A large amount of $SrSO_4$ was supersaturated in the two brines and subsequently a substantial quantity of scale deposition resulted in severe loss of core permeability. In the brines BS0, BS1, BSS0, BSS1, the $SrSO_4$ was undersaturated and $BaSO_4$ supersaturation was 15, therefore about the same amount of scaling damage was expected to be caused to the cores by injecting these brines. The investigation by Gardner and Nancollas[38] found that $SrSO_4$ had a lower precipitation rate than $BaSO_4$. Their finding explains why more severe permeability loss resulted from BS0 or BSS0 brine than that from BS1 or BSS1 because of the retarding effect of Sr^{2+} ions on scale precipitation, bearing in mind $SrSO_4$ was undersaturated in these four brines.

$SrSO_4$ in brines BS2 and BSS2 were supersaturated but the supersaturation was only about 3.7. The permeability loss caused by injecting brines BS2 or BSS2 was less than that by injecting the brine of lower Sr/Ba ratio(brines BS0, BSS0, BS1, or BSS1). This was probably because the permeability reduction contributed from $SrSO_4$ precipitation in the core was relieved by the retardation in the scaling rate (or precipitation rate) and depletion of SO_4^{2-} ions for $BaSO_4$ precipitation in the presence of higher Sr^{2+} concentration in BS2 and BSS2 brines. On the other hand, BSH2 brine injection resulted in more severe permeability reduction than injecting BSH1 brine. $SrSO_4$ supersaturation in brine BSH2 was 8 compared to 4 in brine BSH1 and both brines had $BaSO_4$ supersaturation equal to 30. Like brine BS3, the higher $SrSO_4$ supersaturation in brine BSH2 led to more $SrSO_4$ precipitation in the rock pores and heavier permeability impairment.

The alteration of $(Ba^{2+} + Sr^{2+})/SO_4^{2-}$ molar ratio from 1 in BSS brines to 2 in BS brines while $(Ba,Sr)SO_4$ supersaturation was held constant also had an effect on the rock permeability reduction, as indicated in figures (6.57), (6.58) and (6.59). The cores suffered slightly more damage resulting from injection of BS brines than from injection of BSS brines. No convincing explanation has yet been found.

Sectional Permeabilities

The sectional permeability decline curves produced by most of the formation damage tests conform to one of the two patterns. The first pattern shows the permeability declines, expressed as the percent of their initial values in the sections along the length of a core, were sequential from the first section in the core front to the last section in the rear of the core, as illustrated in figure (6.60). The other pattern is different from the first pattern as the permeability declines in the first two sections were reversed, that is, the permeability decline in the section 2 rather than section 1 was the largest, as shown in figure (6.61). Other patterns of the sectional permeability curves also resulted from a few core tests but viewed as non-typical, one of such non-common patterns is presented in figure (6.62). In general, the core tests with lower Sr/Ba ratios (0.1 and 1.0) brines were more likely to conform to the pattern 1 while those tests with the brines of higher Sr/Ba ratios (100 and particularly 1000) were inclined to produce pattern 2 sectional permeability decline distribution. The explanation for such phenomenon is again found from the retardation of scale precipitation in rock pores from the brines of higher Sr/Ba ratios. The retardation meant the $SrSO_4$ dominant solid solution scale deposition in section 2 rather than section 1 of a core was more likely. Curiously, the difference in scale abundance in section 1 and section 2 was not evident from the SEM photos of the core tests showing pattern 2 curves. The possible reason is that the SEM photos only show the localised views of the scaled core samples and the scale distribution cannot be identified if the difference in scale abundance from one site to another was slight.

Permeability Decline Rate

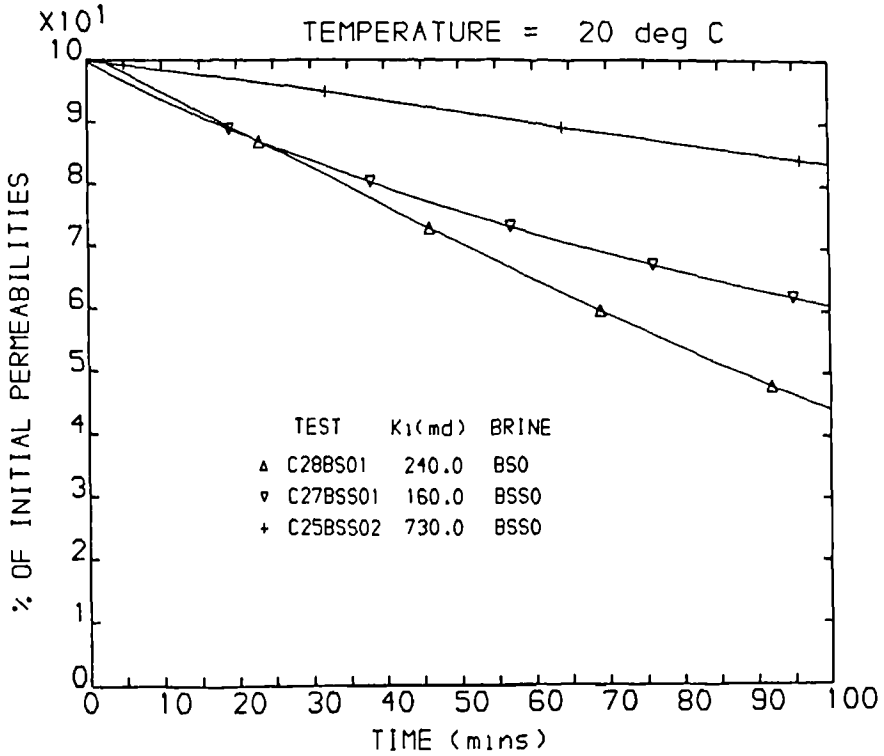

Figure 6.57 Comparison of permeability damages between the cores injected with BS0 brine and the cores injected with BSS0 brine. (Ba+Sr)/SO_4=1 in BSS0 brine and 2 in BS0 brine

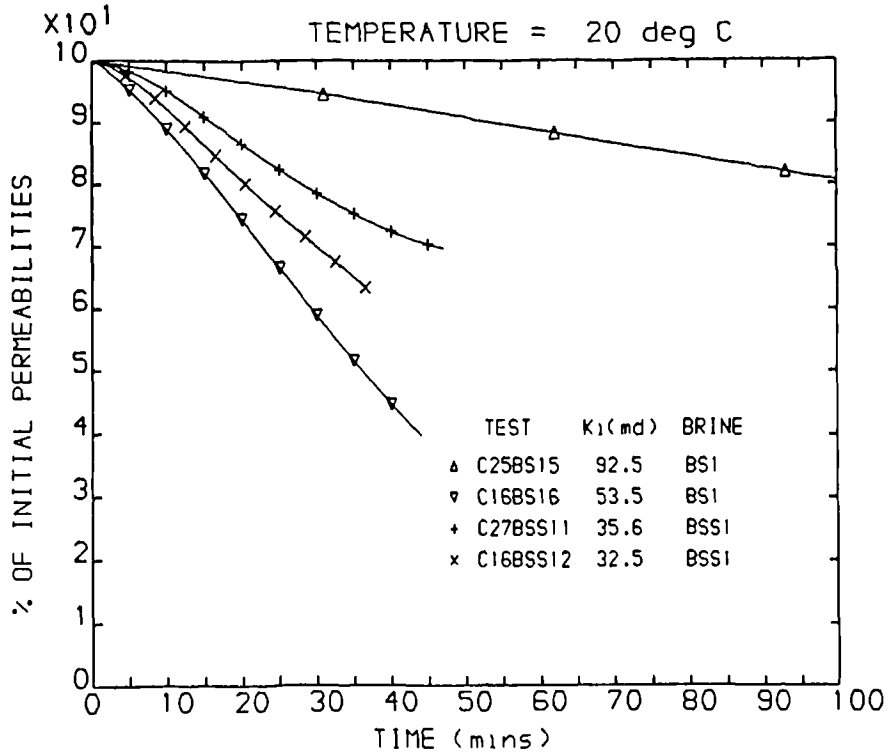

Figure 6.58 Comparison of permeability damages between the cores injected with BS1 brine and the cores injected with BSS1 brine. (Ba+Sr)/SO_4=1 in BSS1 brine and 2 in BS1 brine

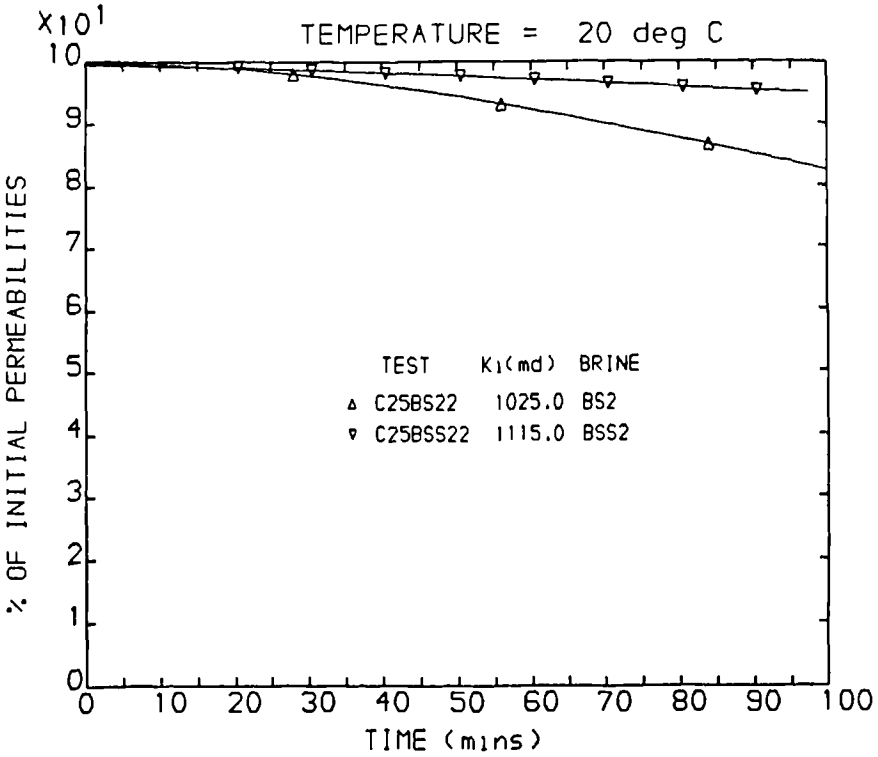

Figure 6.59 Comparison of permeability damages between the cores injected with BS2 brine and the cores injected with BSS2 brine. $(Ba+Sr)/SO_4$=1 in BSS2 brine and 2 in BS2 brine

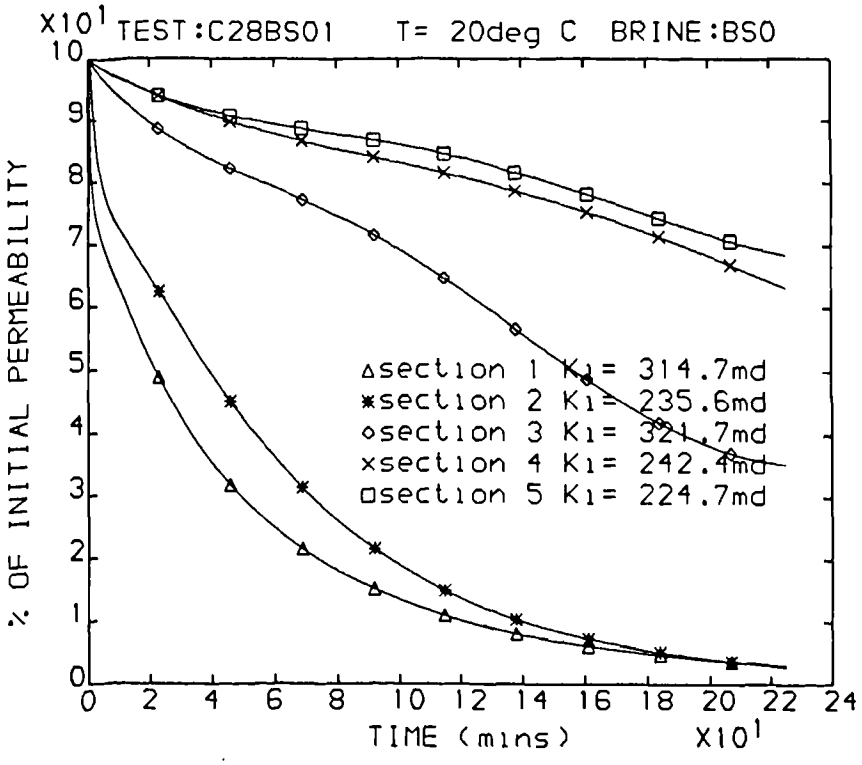

Figure 6.60 Core section permeability declines due to scale formation, sequential from front to rear in the extent of damage, pattern 1

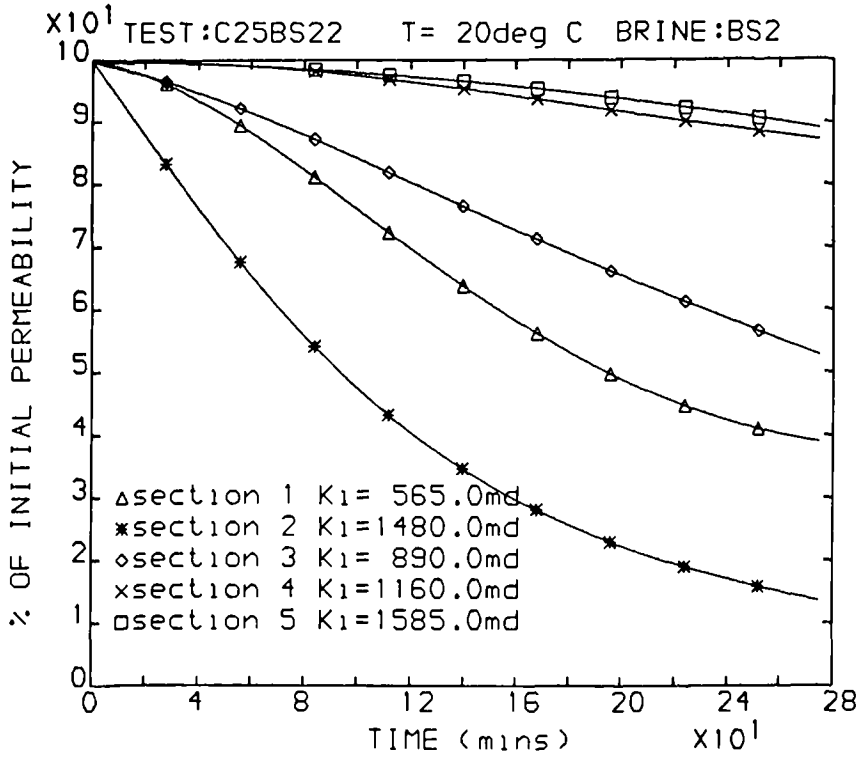

Figure 6.61 Section permeability declines, section 2 decline is the highest, pattern 2

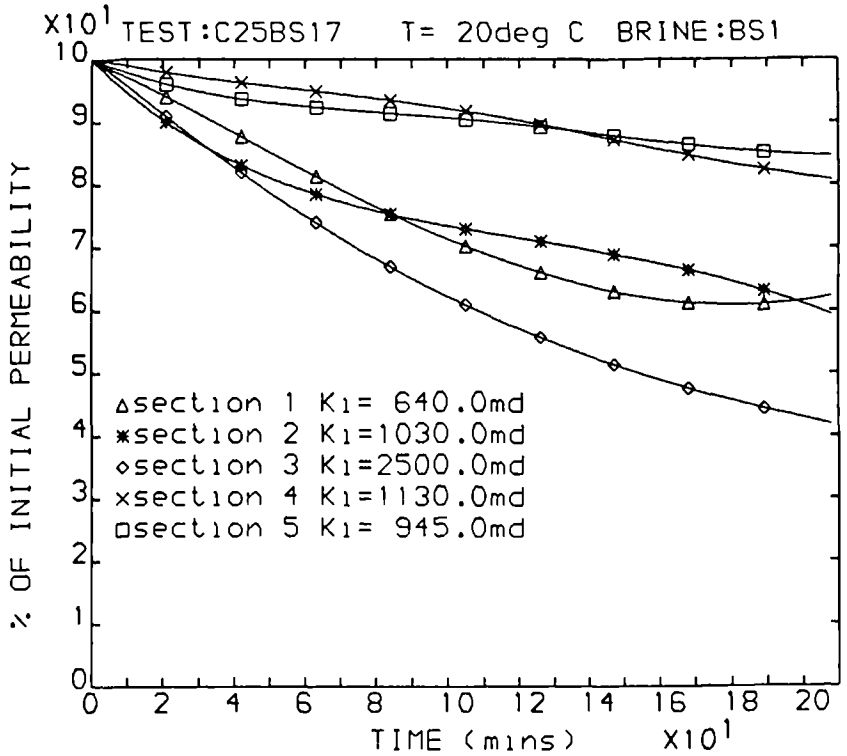

Figure 6.62 Section permeability declines, other pattern

In order to have insight into the changing trend of permeability decline rate during a scale formation experiment, core permeability decline rates (dk_t/dt) were calculated from the numerical expressions of the permeability - brine injection time relations obtained from the smoothed $1/\Delta p$ - t data. The permeability decline rate for each test was then plotted versus the brine injection time. Typical dk_t/dt - t curves from the ambient temperature tests are shown in figures (6.63) through (6.68).

Four types of the dk_t/dt - t trend were summarised from the curves. In type 1, the permeability decline rate steadily decreased throughout an entire flow test, as demonstrated in figure(6.63). Type 2 curve was only seen in one test which shows the permeability decline rate went through three stages. First, the permeability decline rate reduced sharply versus the time, then it started to increase and after a period of increase, the decline rate began to decrease with the time again, as shown in figure (6.64). Type 3 curve shows two different trends in the permeability decline rate during a test, as illustrated in figures (6.65) and (6.67). The first section of the type 3 curve shows the permeabililty decline rate at the beginning of the scale deposition was not the fastest but gradually increased as the brine was continuously injected into a core for a certain period (ranging from 8 mins to 230 mins, depending on the individual tests). The decline rate then started to decrease until the end of the experiment. Three stages of the permeability rate change can be seen in type 4 curve, as seen in figures(6.66) and(6.68). The first two stages are the same as in type 3 but the permeability decline rate was found to start to increase again in the last period of a formation damage test after the decrease in the stage 2.

It is assumed that the unchanged mechanism of $(Ba,Sr)SO_4$ scaling in the porous media was held throughout the experiments showing type 1 curve. A more complicated process must have been involved in the scaling in the cores producing the other three permeability decline rate curve types. The first stage of increase in permeability decline rate from its initial rate as shown in types 3 and 4 suggests some kind of retardation in the scale formation was the cause. Possibly the initial rate of crystal precipitation(or

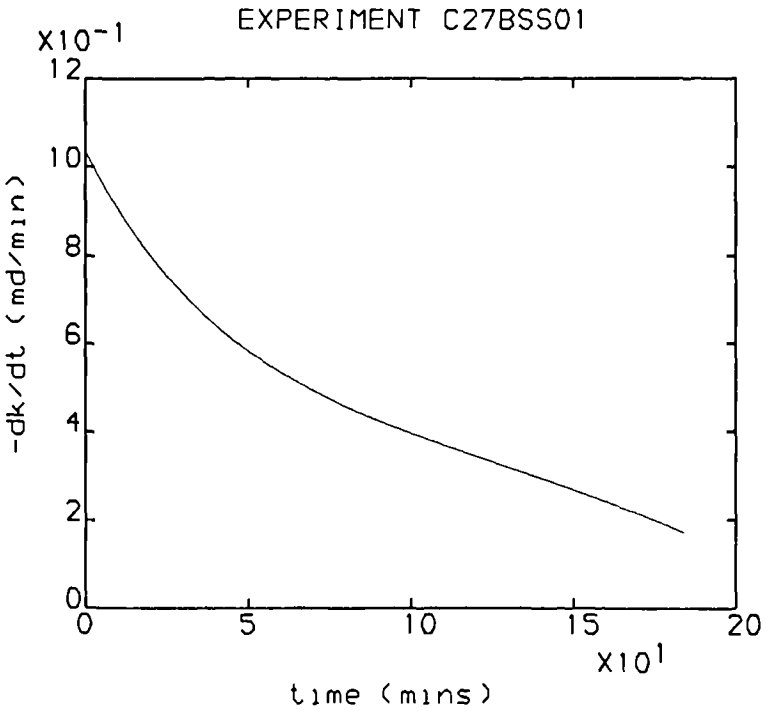

Figure 6.63 Core permeability decline rate change during scaling, steady decline, type 1

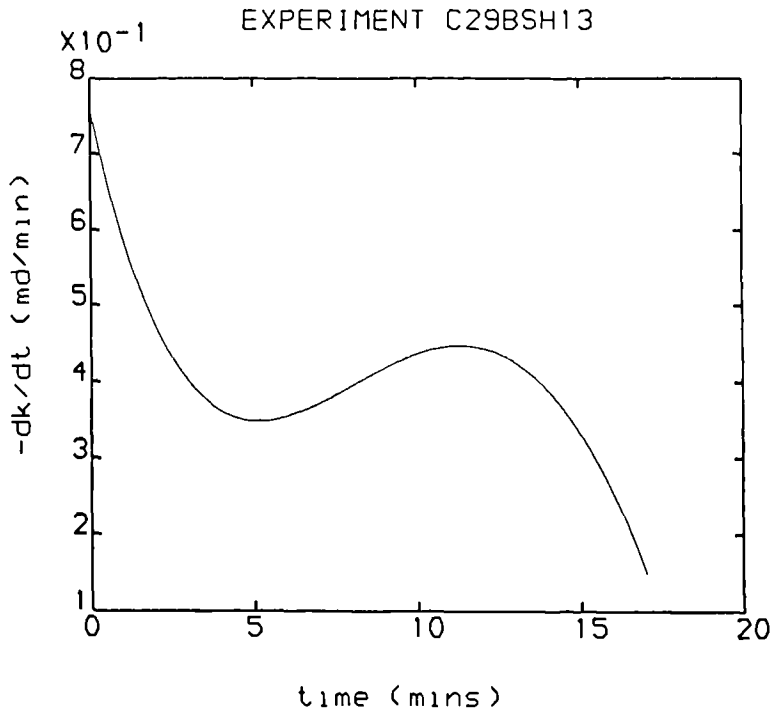

Figure 6.64 Core permeability decline rate change during scaling, decline-increase-decline, type 2

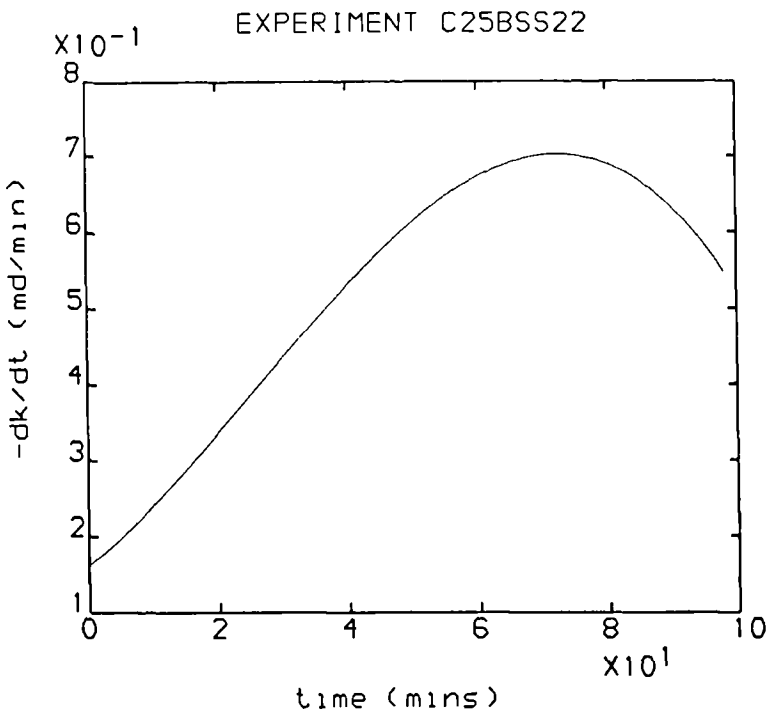

Figure 6.65 Core permeability decline rate change during scaling, increase then decline, type 3

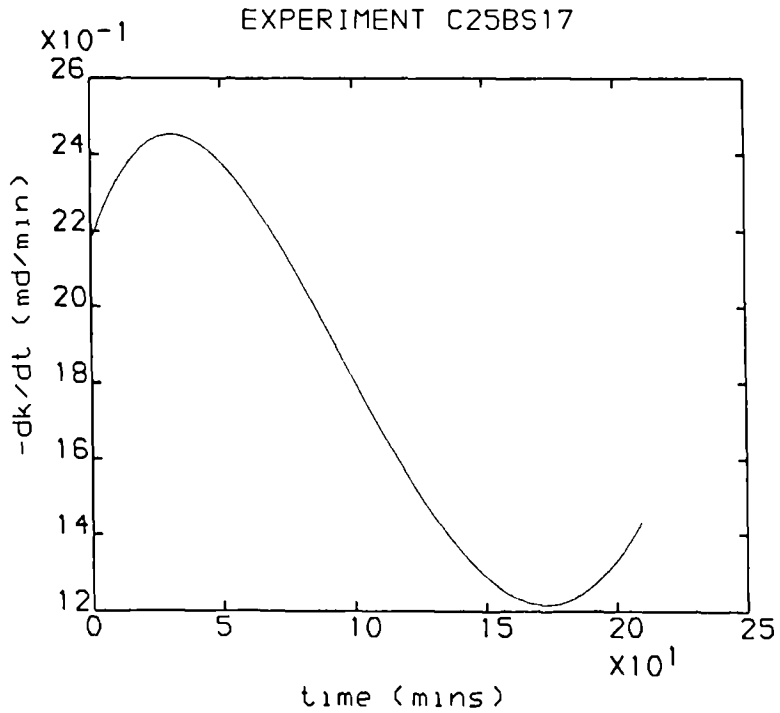

Figure 6.66 Core permeability decline rate change during scaling, increase-decline-increase, type 4

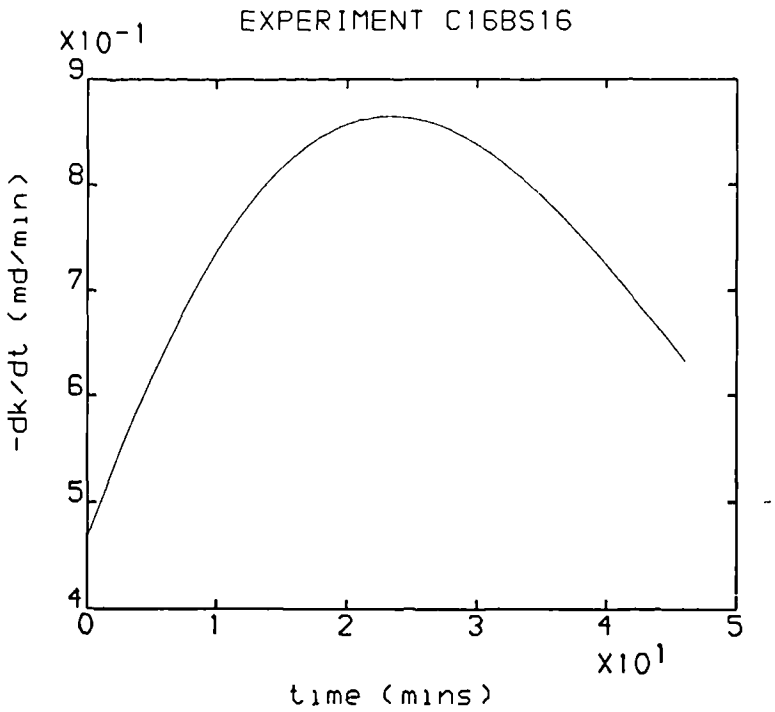

Figure 6.67 Core permeability decline rate change during scaling, no $t_{1/2}$

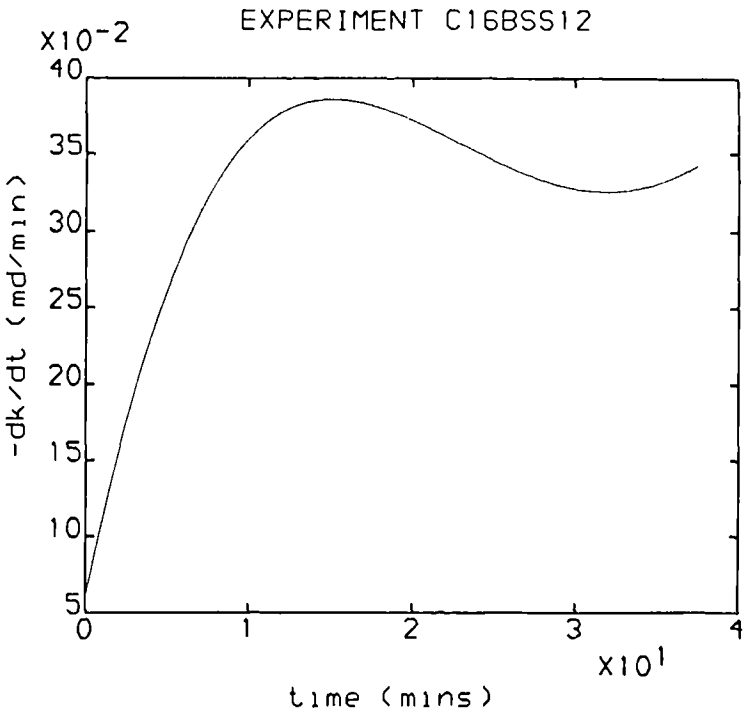

Figure 6.68 Core permeability decline rate change during scaling, no $t_{1/2}$

growth rate) onto the rock pore surface was lower and gradually accelerated. The decrease in permeability decline rate as found in all four types of curves was probably due to increasing hindrance of the flow shear force on the further crystal growth into the flow stream as the flow path increasingly narrowed. Owing to the difficulty for the scaling crystal growth to take place in the flow stream, the crystal precipitation and growth were then diverted to the pore space less affected by the flow, such as the dead pore ends and the small pores. The increase in permeability decline rate after a certain period of reduction, as seen in type 2 and 4 curves, is a very interesting trend. The only explanation of such a trend is that the secondary crystal nucleation and growth had taken place after substantial amount of the scaling brine had flown through the core.

It is still not clear why that not one but four types of the permeability decline rate curves were produced from the $(Ba,Sr)SO_4$ scale formation in the cores. The rock property was ruled out from the factor determining the curve type because different curve types resulted from the cores cut from the same Clashach rock block. The fact that the type 1 curves all resulted from the experiments with the brines of low Sr/Ba ratios (0.1 and 1.0) may suggest that the Sr/Ba ratio was one of the determining factors.

6.4.2 Characterisation of the Permeability Curves

Besides the analysis of the permeability - time curves and the permeability decline rate - time curves, numerical calculations were carried out to characterise these curves in hope that they might give insight into the trend of permeability damage as the result of the $(Ba,Sr)SO_4$ solid solution scale formation.

The numerical calculations provided the following information: the initial permeability decline rate, i.e, $(dk/dt)_i$ and $(dk/dt)_i/k_i$; the maximum permeability decline rate, i.e, $(dk/dt)_m$ and $(dk/dt)_m/k_i$; the time at which the permeability decline rate had just reduced to half of its initial rate($t_{1/2}$) and the time corresponding to the maximum curvature of a k - t curve (t_c). $t_{1/2}$ calculation was initially proposed in Goulding's PhD thesis[42] and was called characterisation time. t_c concept was first used in this study in

an attempt to characterise the k - t curve shape and to observe if there is any relation between t_c and $t_{1/2}$.

Analysis of $(dk/dt)_i$, $(dk/dt)_m$ and $t_{1/2}$

Table (6.4) presents the calculated $(dk/dt)_i$, $(dk/dt)_i/k_i$, $(dk/dt)_m$, $(dk/dt)_m/k_i$, $t_{1/2}$ and t_c. As we know from dk/dt - t curve analysis in the last subsection, $(dk/dt)_i$ is not necessarily $(dk/dt)_m$, which is confirmed by the calculated results in table (6.4) showing the initial permeability decline rates were not the highest in over half of the core tests.

As shown in table (6.4), the $(dk/dt)_i$ ranges from -0.0008 to -9.9118(md/min) and $(dk/dt)_i/k_i$ ranges from -1.429E-6 to -3.889E-2(1/min)(the minus sign indicates the decline of core permeability as scale builds-up), depending on the individual tests. The maximum permeability decline rates have approximately the same ranges. $t_{1/2}$, i.e, the time at which the permeability decline rate reduced to half of its initial value, did not exist in more than half of the core tests because the permeability decline rate was gradually increasing from the beginning of these tests, which can be seen from the dk/dt - t curves shown in figures (6.65) and (6.68). The initial permeability decline rates were then plotted versus the corresponding initial rock permeabilities and displayed in figures (6.69) and (6.70). The curves do not show certain correlations between the initial permeability decline rate and initial permeability which is understandable because the permeability reduction was subject to scaling brine composition. By correlating $(dk/dt)_i$ and $(dk/dt)_i/k_i$ with $t_{1/2}$ as shown in figures (6.71) and (6.72), it is found that whereas the $(dk/dt)_i$ - $t_{1/2}$ relation is not obvious, $t_{1/2}$ was smaller at a higher $(dk/dt)_i/k_i$, which is a measure of initial permeability decline rate in a relative term by excluding the effect of different initial permeability values.

Analysis of the Nominal Maximum Curvature Time t_c

Table 6.4 Numerical Characterisation of Permeability Decline at 20°C

Test	Brine used	k_i (md)	Brine injection time (mins)	$(dk/dt)_i$ (md/min)	$(dk/dt)_m$ (md/min)	$(dk/dt)_i/k_i$ (1/min)	$(dk/dt)_m/k_i$ (1/min)	t_m (mins)	$t_{1/2}$ (mins)	t_c (mins)
C28BS01	BS0	269.0	226	-1.5022	-1.5022	-6.207E-3	-6.207E-3	0.0	144.5	145.1
C16BS14	BS1	46.0	8	-0.6157	-1.0029	-1.338E-2	-2.179E-2	8.0	no	5.5
C25BS15	BS1	92.0	306	-0.1341	-0.1980	-1.458E-3	-2.154E-3	67.0	no	151.8
C16BS16	BS1	53.5	45	-0.4664	-0.8646	-8.718E-3	-1.616E-2	23.0	no	no
C25BS17	BS1	1100.0	209	-2.1743	-2.4528	-1.976E-3	-2.230E-3	31.0	no	94.9
C16BS21	BS2	45.6	59	-0.0678	-0.5294	-1.487E-3	-1.161E-2	36.0	no	no
C25BS22	BS2	1025.0	276	-0.2869	-2.7833	-2.799E-4	-2.715E-3	106.0	no	172.4
C25BS32	BS3	940.0	179	-9.9118	-11.6166	-1.054E-2	-1.235E-2	14.0	68.9	60.5
C28BSH11	BSH1	223.0	139	-6.2611	-6.2611	-2.808E-2	-2.808E-2	0.0	15.3	25.8
C29BSH13	BSH1	19.5	17	-0.7583	-0.7583	-3.889E-2	-3.889E-2	0.0	3.5	2.1
C28BSH21	BSH2	72.5	25	-0.9263	-2.7259	-1.278E-3	-3.761E-3	8.9	no	no
C27BSS01	BSS0	160.0	183	-1.0350	-1.0350	-6.469E-3	-6.469E-3	0.0	63.9	123.5
C25BSS02	BSS0	730.0	310	-0.9506	-1.2751	-1.302E-3	-1.746E-3	49.0	180.9	137.8
C27BSS11	BSS1	35.6	48	-0.0017	-0.3160	-4.848E-5	-8.878E-3	19.0	no	42.3
C16BSS12	BSS1	32.5	37	-0.0597	-0.3858	-1.837E-3	-1.187E-2	15.0	no	23.6
C25BSS21	BSS2	573.0	369	-0.0008	-0.3506	-1.429E-6	-6.118E-4	231.0	no	no
C25BSS22	BSS2	1115.0	97	-0.1619	-0.7029	-1.452E-4	-6.304E-4	73.0	no	25.2

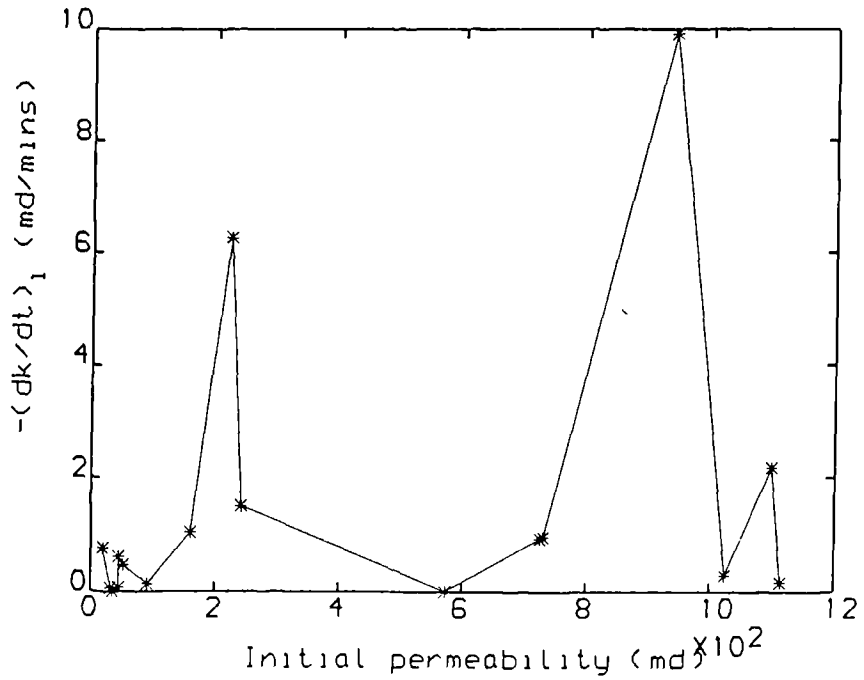

Figure 6.69 Permeability decline rate - initial permeability correlation, decline rate in absolute term

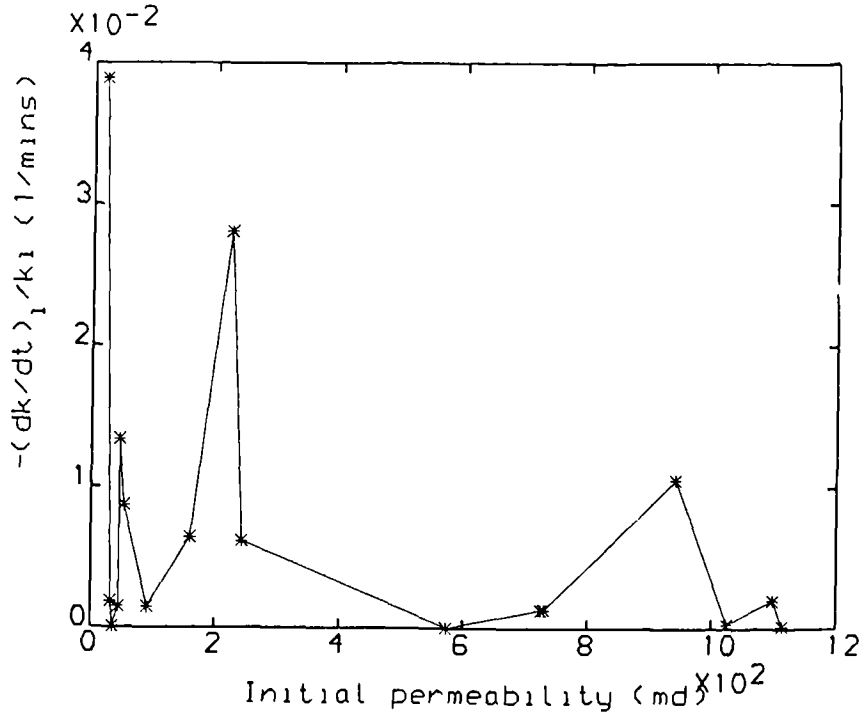

Figure 6.70 Permeability decline rate - initial permeability correlation, decline rate in relative term

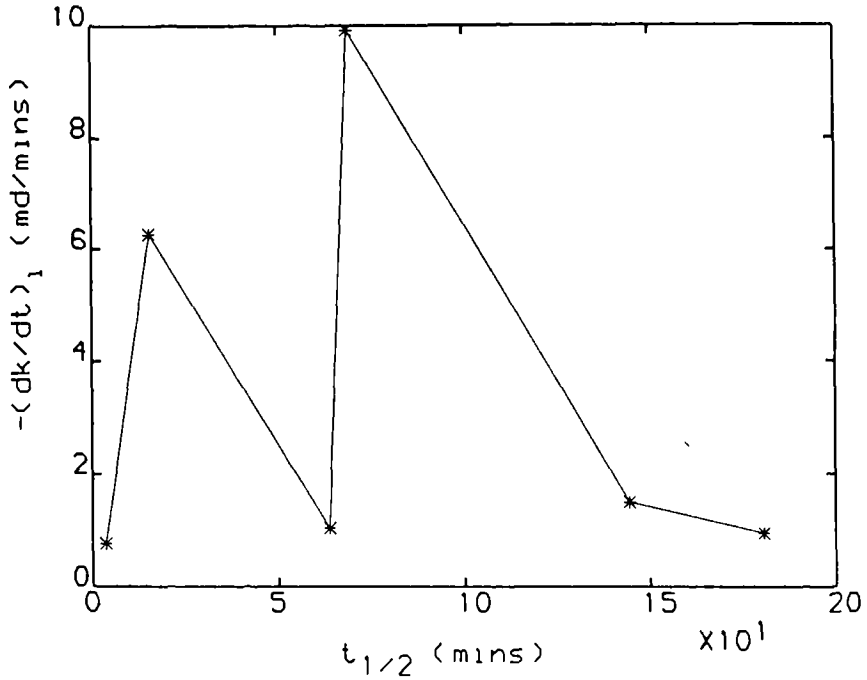

Figure 6.71 Permeability decline rate - $t_{1/2}$ correlation, decline rate in absolute term

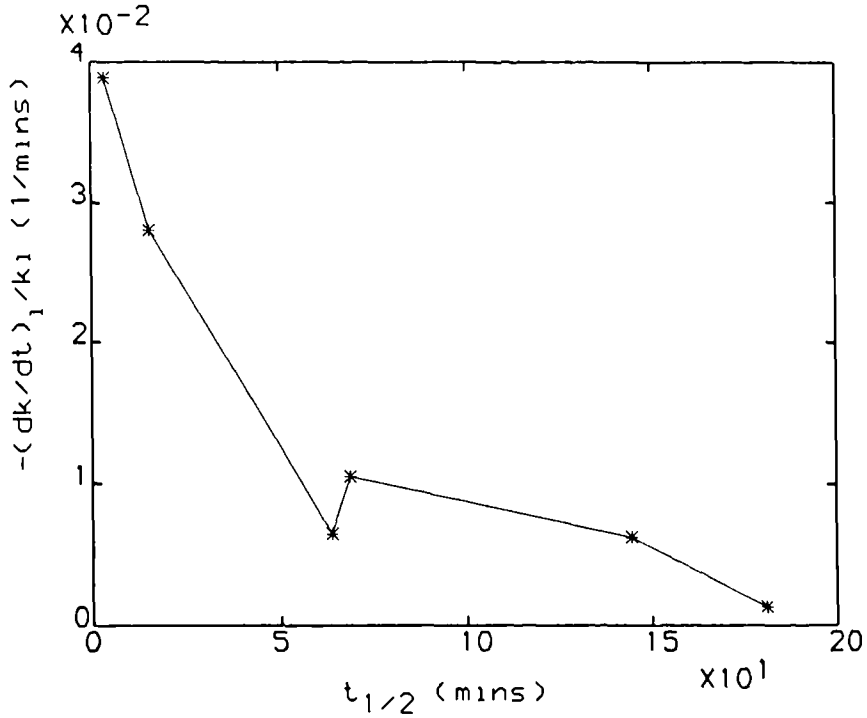

Figure 6.72 Permeability decline rate - $t_{1/2}$ correlation, decline rate in relative term

For a k - t curve, the time at the maximum curvature point, opposed to what was expected, is not a constant but rather changing with the axis scales chosen in plotting the curve, that is, the maximum curvature is not an invariant point. This is demonstrated by plotting the same k - t curve from a core test on different graphs with different axis scales, as shown in figures (6.73) and (6.74). Figure (6.73) is the k - t curve using the initial core permeability k_i as the full scale of the ordinate and the abscissa scale is set by the whole period of the brine injection. In figure (6.74), the ordinate scale is the same as in figure (6.73) but only a section of the k - t curve was graphed with 14.5 minutes as the full scale of the abscissa, in contrast to 55 minutes in figure (6.73). The maximum curvature time for each curve in figures (6.73) and (6.74) was calculated and they are not equal, t_c is 15.1 minutes from figure (6.73) while it is 3.1 minutes from figure (6.74). Therefore, it is meaningless to characterise a k - t curve using t_c without certain restrictions to make the calculated t_c values from different k - t curves comparable. To avoid the above described ambiguity, it was decided to chose k_i as the full scale of the ordinate and 100 minutes as the full scale of the abscissa for every k - t curve and then the y-axis and x-axis were normalised to 1. After such a treatment, the t_c was calculated for each normalised k - t curve and this t_c is called the time at the **nominal** maximum curvature because it is subject to artificial restriction. The t_c values are given in table (6.4) together with $t_{1/2}$. Their correlation curve is presented in figure (6.75). Figure (6.75) shows there exists a consistence between t_c and $t_{1/2}$ that a larger $t_{1/2}$ usually corresponded a larger t_c or vice versa, which proves that t_c is a valuable measurement of the permeability - time curve characteristics.

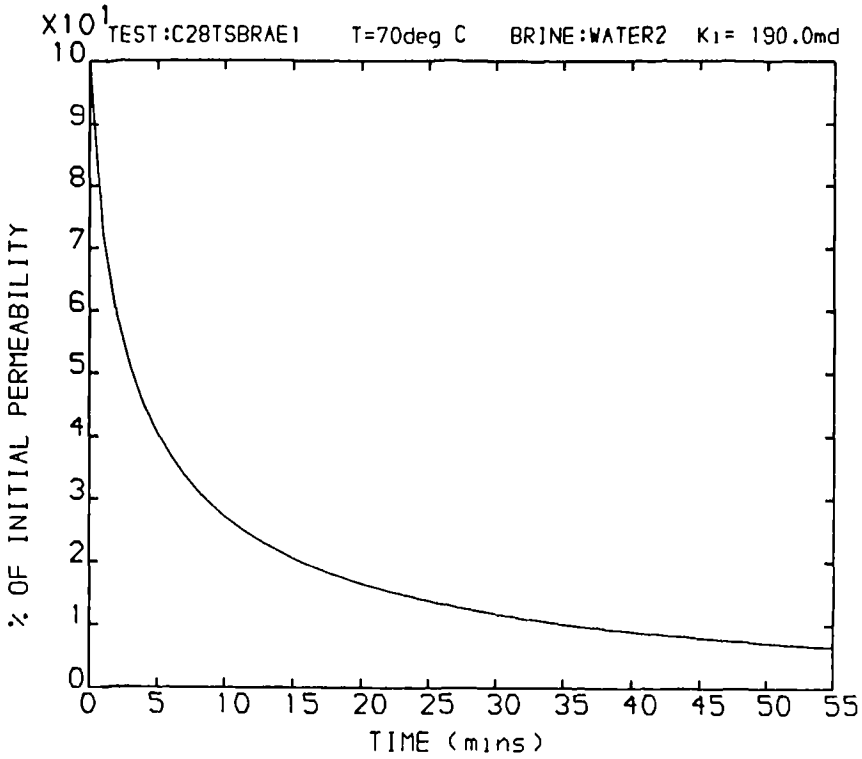

Figure 6.73 Core permeability - time curve, the total brine injection time as the full scale of abscissa

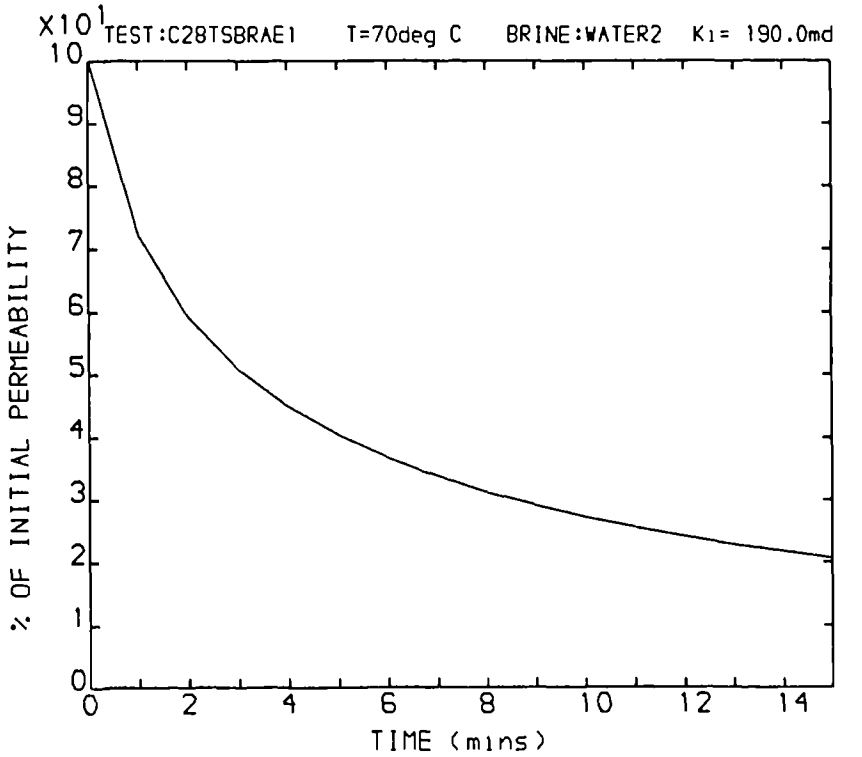

Figure 6.74 Core permeability - time curve, the same experiment as in figure 6.73 but only first 15 minutes plotted

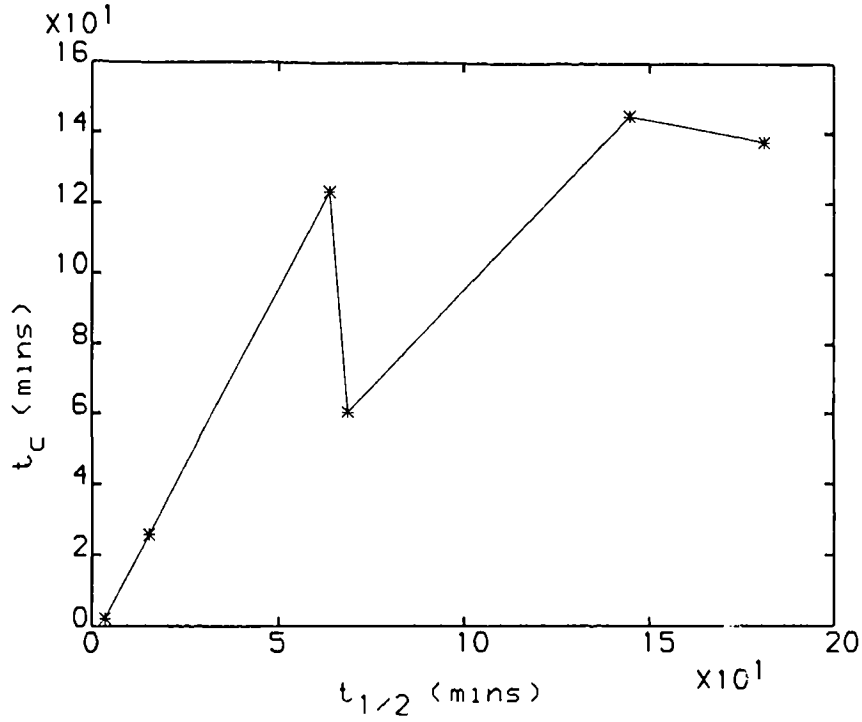

Figure 6.75 t_c - $t_{1/2}$ correlation

CHAPTER 7

BARIUM SULPHATE AND STRONTIUM SULPHATE SOLID SOLUTION FORMATION AT ELEVATED TEMPERATURE

7.1 INTRODUCTION

Since higher temperatures than 20°C exist in reservoir formations, it was felt necessary to carry out an investigation of sulphate scale formation and the formation damage at an elevated temperature to give a closer simulation of reservoir scaling conditions. The change in temperature has an effect on sulphate solubilities, sulphate precipitation kinetics and sulphate crystal growth. In turn, the rock permeability damage arising from the scale deposition can be expected to be affected by temperature change. In comparison with the results obtained at 20°C formation damage experiments described in chapter 6, the temperature effect can be analysed from the high temperature experiments.

In the present study, static beaker(jar) tests and dynamic core flow tests were conducted at 70°C by mixing both simple brines and a synthetic full component North Sea water and formation waters. The brines were described in chapter 5 and their compositions and compositional characteristics are given in tables (5.1) through (5.4). The experimental equipment used in the elevated temperature experiments and the test method and procedure were also described in chapter 5, although some changes had been made from the 20°C tests in some aspects. The factors affecting the scale precipitation and the formation damage which had been investigated at 70°C were also listed in chapter 5. The core test identification system is similar to that used in 20°C experiments and described in Appendix(6.1).

In this chapter, the results obtained at the elevated temperature tests are presented; the nature of sulphate solid solution scales, the scaling mechanism and the permeability decline behaviour at 70°C are examined and compared to the room temperature

experimental findings. The differences in scale formation between mixing the simple brines and the full component field brines are analysed. From the comparison and the analysis, the implications are drawn from the elevated temperature tests and from the tests with the full component brines.

7.2 ANALYSIS OF SEM ELECTROMICROGRAPHS

7.2.1 Study of the Crystals Precipitated from the Static Bulk Brines

The crystal growth in the BS brines and BSS brines were carried out under static conditions. The brine compositions are shown in table (5.1) and the composition characteristics are given in table (5.2). As mentioned in chapter 6, the corresponding BS brines and BSS brines, e.g, BS1 vs. BSS1, were the same except that $(Sr+Ba)/SO_4$ ratio in BSS brines was 1 and it was 2 in BS brines. The Sr/Ba ratio increased from 0.1, 1.0, 100 to 1000 from brine BS0, BS1, BS2 to BS3, and the same ratio change was observed between brines BSS0, BSS1, BSS2 and BSS3.

The electromicrographs of the precipitated crystals from these brines are shown in figures (7.1) through (7.10). We start by examining the crystals formed in BSS brines. Both BSS0 and BSS1 crystals look like tabular rhombi, but BSS0 crystals have 2 to 4 small extra faces. The distinct difference in crystal habits emerged from BSS2 crystals. The BSS2 crystals present tabular - prismatic habits with clear and deep jigsaw like grooves on both top sides of the longest axis. Further transition in crystal forms due to changing Sr/Ba ratio is observed in BSS3 crystals. The oval polyhedrons are the dominant crystal habits in the BSS3 crystals and a few crystals appear like thick polyhedron tabulars. Most of the crystals precipitated from brine BSS3 have a porous nature and the groove like cuts on the crystals are also visible. The crystal size was also influenced by the different Sr/Ba ratios in the brines. The crystal size varies from about 6μm to 20μm in the sequence from BSS0, BSS1, BSS2 to BSS3.

The transition in $(Ba,Sr)SO_4$ crystal morphology similar to that among BSS crystals was found in the BS crystals resulting from changing Sr/Ba ratio in the BS brines from

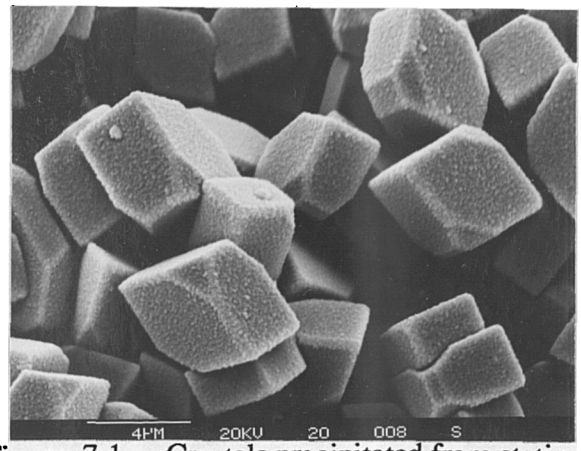

Figure 7.1 Crystals precipitated from static brine BSS0 at 70°C, (Ba+Sr)/SO_4 =1, Sr/Ba=0.1

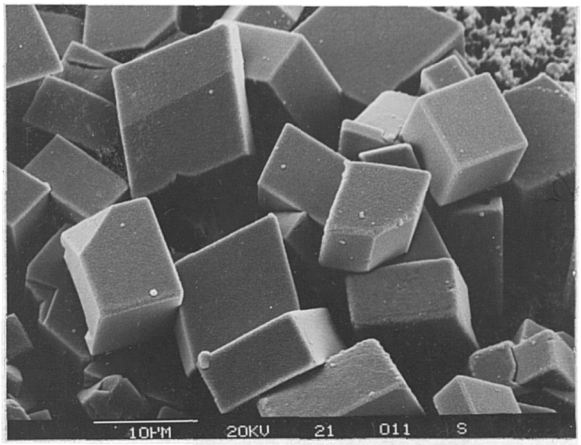

Figure 7.2 Crystals precipitated from static brine BSS1 at 70°C,(Ba+Sr)/SO_4 =1, Sr/Ba=1.0

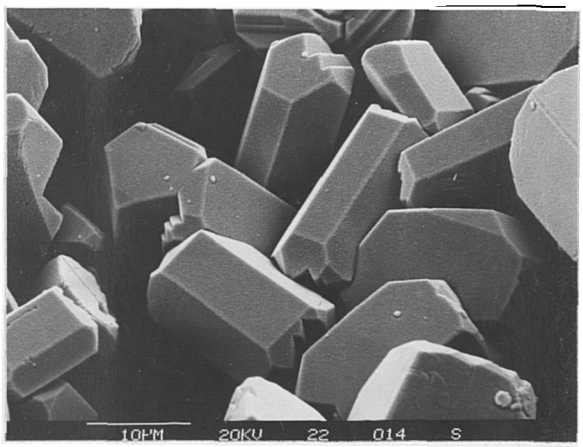

Figure 7.3 Crystals precipitated from static brine BSS2 at 70°C, (Ba+Sr)/SO_4 =1, Sr/Ba=100

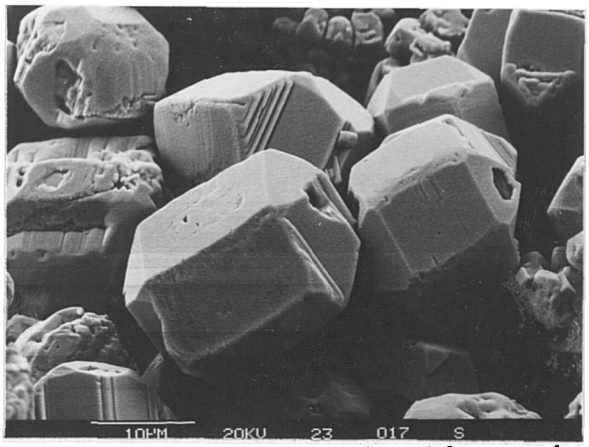

Figure 7.4 Crystals precipitated from static brine BSS3 at 70°C,(Ba+Sr)/SO_4 =1, Sr/Ba=1000

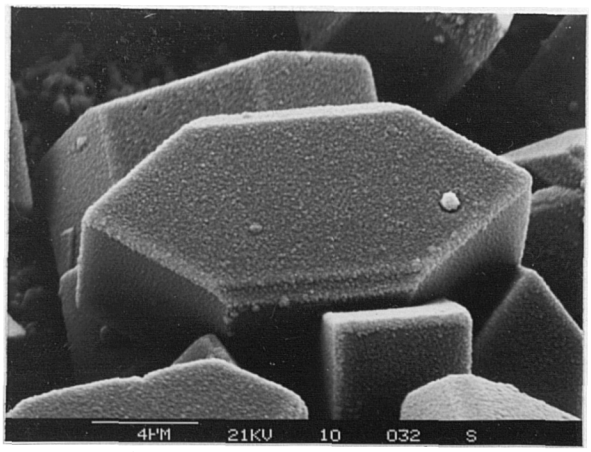

Figure 7.5 Crystals precipitated from static brine BS0 at 70°C, (Ba+Sr)/SO_4 =2, Sr/Ba=0.1, 8 face tabular

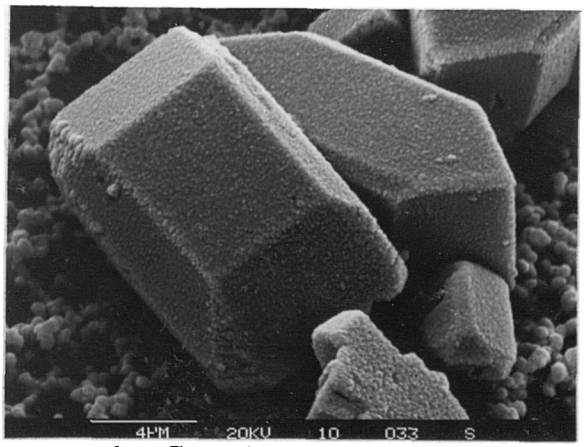

Figure 7.6 Crystals precipitated from static brine BS0 at 70°C, (Ba+Sr)/SO_4 =2, Sr/Ba=0.1, 10 face tabular

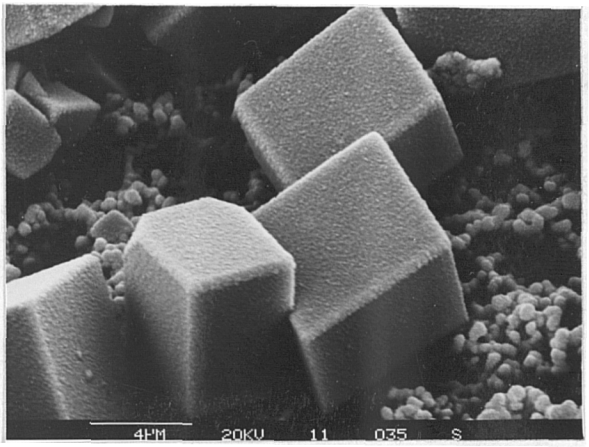

Figure 7.7 Crystals precipitated from static brine BS1 at 70°C, (Ba+Sr)/SO_4 =2, Sr/Ba=1.0, rhombus

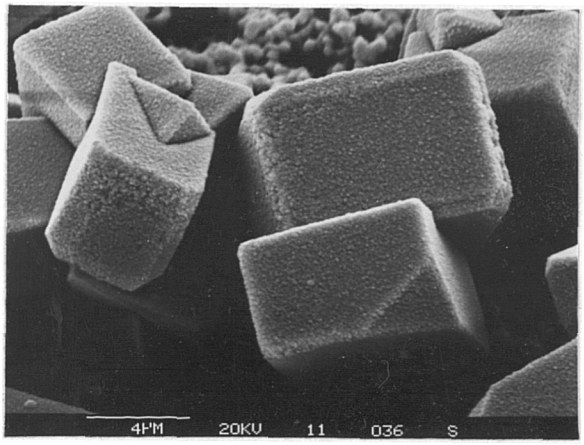

Figure 7.8 Crystals precipitated from static brine BS1 at 70°C, (Ba+Sr)/SO_4= 2, Sr/Ba=1.0, thick tabular blocks

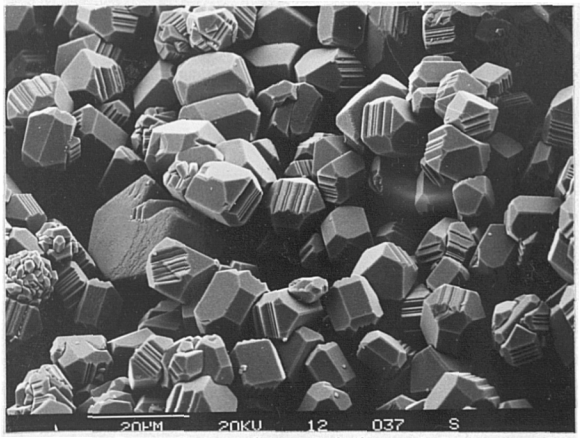

Figure 7.9 Crystals precipitated from static brine BS2 at 70°C, (Ba+Sr)/SO_4 =2, Sr/Ba=100

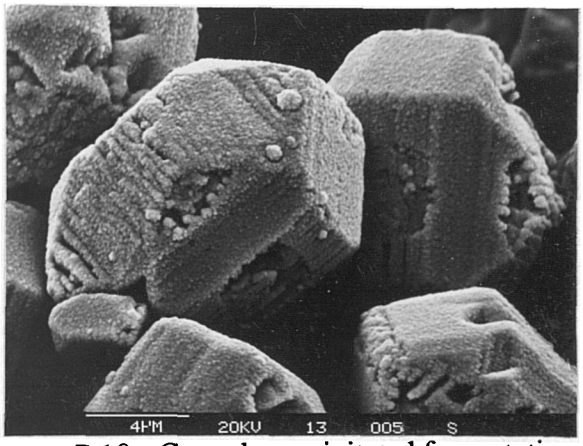

Figure 7.10 Crystals precipitated from static brine BS3 at 70°C, (Ba+Sr)/SO_4 =2, Sr/Ba=1000

0.1, 1.0, 100 to 1000. Unlike BSS0 crystals which have unique crystal forms, two different crystal habits were formed from brine BS0, most of the BS0 crystals are eight face thick tabulars as shown in figure (7.5) but a few crystals are ten face tabulars which is similar to the perfect $BaSO_4$ crystal, as noticed in figure (7.6). Both crystals of the two different habits are of the similar size about 13μm. BS1 crystals are rhombi or cubic blocks, as shown in figures (7.7) and (7.8). Thick tabulars and polyhedrons with deep cut grooves are the apparent habits of $(Ba,Sr)SO_4$ crystals precipitated from brine BS2. Figure (7.9) shows the SEM electromicrograph of the BS2 crystals. Eroded, porous and rounded crystals were formed in BS3 brine, in which the Sr/Ba molar ratio was the highest (1000). The BS crystal size change does not conform to a sequential trend as observed in the BSS crystals. The typical crystal sizes of the BS crystals are, BS0 13μm, BS1 8μm, BS2 12μm and BS3 12μm.

The difference between the crystals formed from the corresponding BS brines of $(Ba+Sr)/SO_4$ equal to 2 and BSS brines of $(Ba+Sr)/SO_4$ equal to 1, e.g, BS1 vs BSS1, is not as noticeable as that between the crystals formed from different brines within the same brine group, e.g, BS1 vs BS2. BSS0 crystals are more or less rhombi while BS0 crystals are two different tabulars. BS1 and BSS1 crystals are both rhombic though BS1 crystals look thicker and more square. BSS2 crystals have a better development in the longest axis (x-axis) and are more prismatic than the crystals formed in brine BS2. Both crystals from brines BS3 and BSS3 are similar oval polyhedrons but BS3 crystals are more porous, rounder and less distinct in the external morphology. After examining these crystals grown from the simple brines at 70°C, their typical habits are illustrated in figures (7.11) and (7.12).

7.2.2 Analysis of Electromicrographs of the Scaled Core Samples

As stated in chapter 6, the purpose of microscopically examining the scaled core samples is to have insight into the $(Ba,Sr)SO_4$ scale nature, the scaling mechanism and to have a general impression of the quantity of scale deposited in the rock pores. The

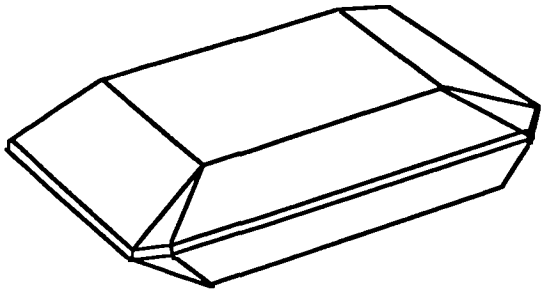

BS0, form 1

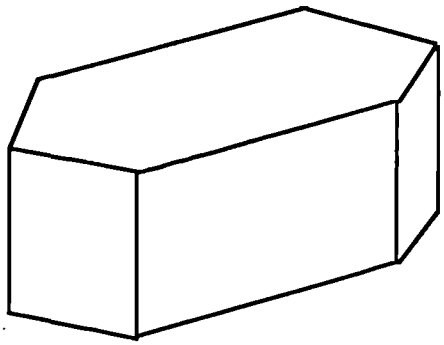

BS0, form 2

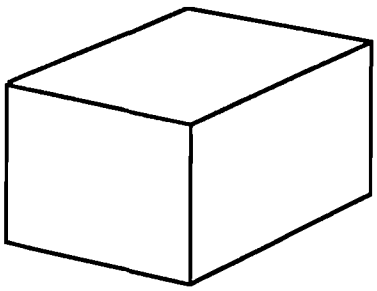

BS1

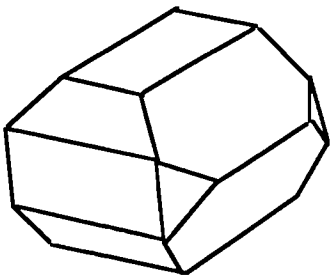

BS2 or BS3

Figure 7.11 Typical Habits of (Ba,Sr)SO_4 Crystals Grown from BS Brines at 70°C

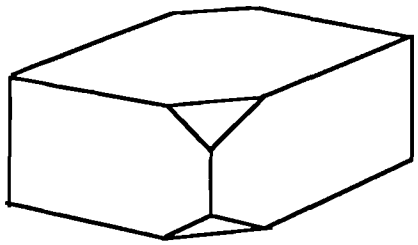

BSS0, form 1

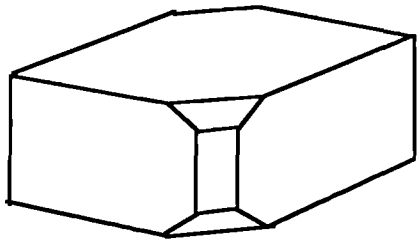

BSS0, form 2

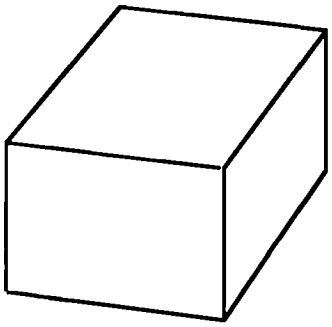

BSS1, form 1

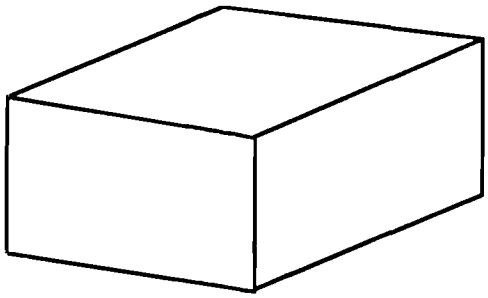

BSS1, form 2

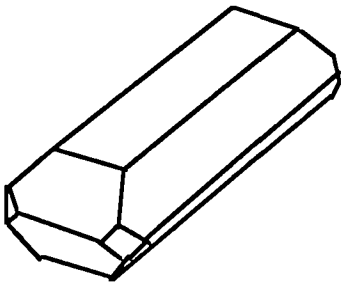

BSS2

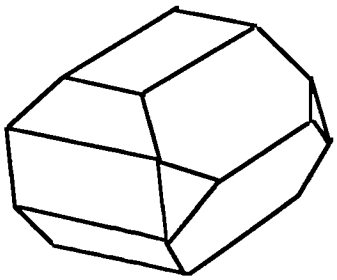

BSS3

Figure 7.12 Typical Habits of (Ba,Sr)SO_4 Crytsals Grown from BSS Brines at 70°C

SEM micrographs of the scaled core samples obtained from 70°C core tests are presented here in figures (7.13) through (7.23). After looking at these SEM pictures and comparing with those of the crystals grown in the beakers, it was concluded that the $(Ba,Sr)SO_4$ scaling crystals formed from the same brines but under both static and flow conditions did not have obvious difference in terms of their external morphology, as also was found from the 20°C experiments. The difference lies on the irregularity, dislocations and size variation occurring in the crystals deposited in the rock pores. The SEM views in figures (7.1) through (7.10) and in figures (7.13) through (7.23) show these differences between the crystals precipitated under flow and under static conditions. The crystals precipitated in the cores have more variable sizes but generally they are larger than those formed in the beaker. This was probably caused by the continuous supply of fresh supersaturated brine during a core flow test which, on one hand, created different stages of crystal nucleation and, on the other hand, enabled the precipitated crystals to continue growth into a larger dimension. The findings about the scaling sites and scale distribution within a core from the room temperature tests were confirmed again by the elevated temperature test results. That is, the scaling crystals did not show preference on the scaling sites on rock surface. Also the sharp reduction in the scaling crystal abundance was observed along the length of a core from the front of the core to its rear section. Unlike the scaling crystals deposited in the pore space at room temperature, most of the scaling crystals precipitated at 70°C appear to be prone on the rock surface without protruding into the flow.

7.3 ROCK PERMEABILITY REDUCTION CAUSED BY $(Ba,Sr)SO_4$ DEPOSITION

The conversion of the pressure data recorded during a core test to the permeability change was described in section (5.5.2). The rock permeability reduction was always the focal point of the present investigation of the barium and strontium sulphate scale formation. The extent of permeability decline, the permeability decline rate, the permeability decline distribution into the depth of a core, the permeability curve characteristics and the affecting factors were the aspects of the formation damage

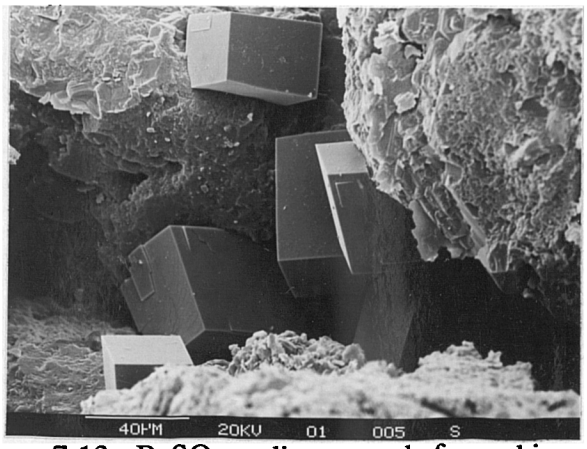

Figure 7.13 $BaSO_4$ scaling crystals formed in a core, test C28TBA1. Brine BA. k_i=42md

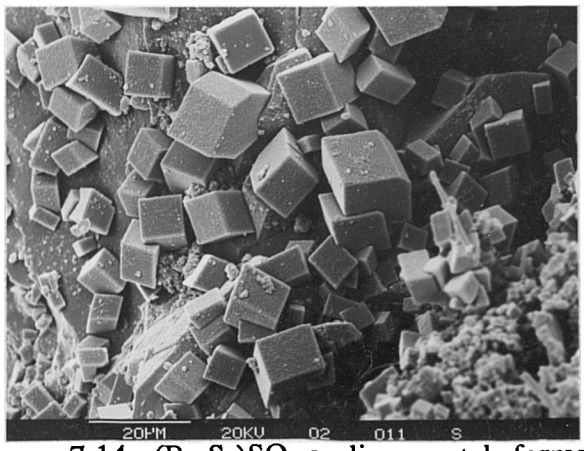

Figure 7.14 $(Ba,Sr)SO_4$ scaling crystals formed in a core, test C28TBSS02. Brine BSS0, $(Ba+Sr)SO_4$=1, Sr/Ba=0.1. k_i=12.1md

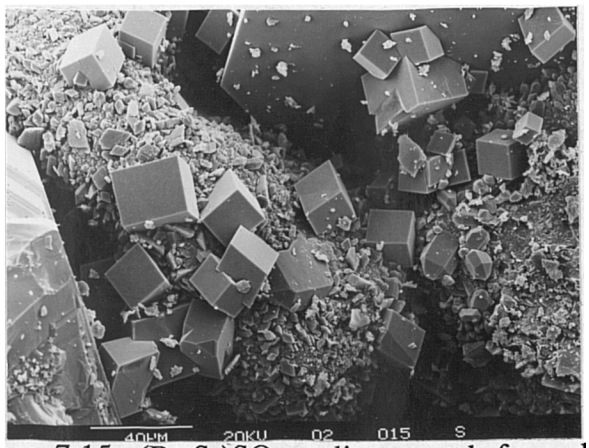

Figure 7.15 $(Ba,Sr)SO_4$ scaling crystals formed in a core, test C28TBSS02, crystals grown on fines

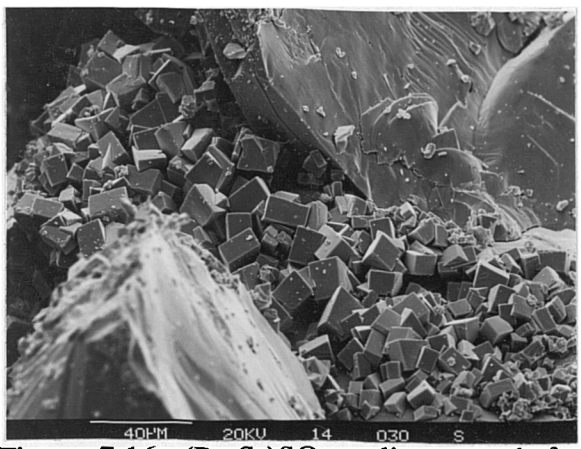

Figure 7.16 $(Ba,Sr)SO_4$ scaling crystals formed in a core, test C32TBSS14. Brine BSS1, $(Ba+Sr)SO_4$=1, Sr/Ba=1.0. k_i=10.2md

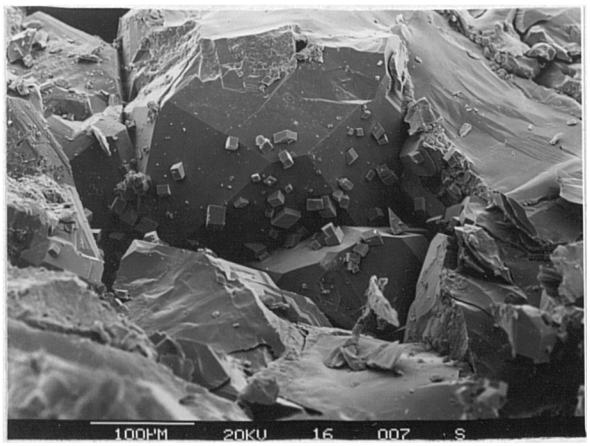

Figure 7.17 $(Ba,Sr)SO_4$ scaling crystals formed in a core, test C33TBSS16. Brine BSS1, $(Ba+Sr)SO_4$=1, Sr/Ba=1.0. k_i=31.8md

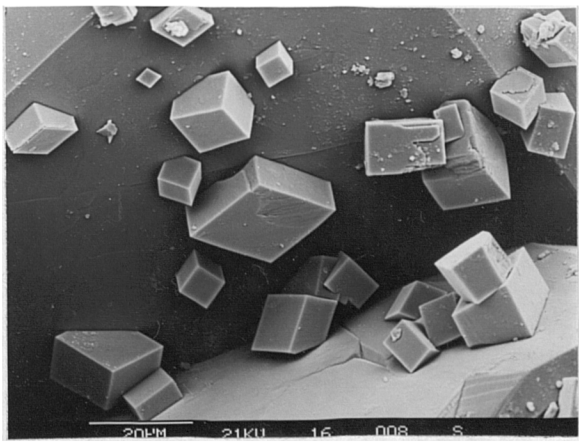

Figure 7.18 $(Ba,Sr)SO_4$ scaling crystals formed in a core, test C33TBSS16

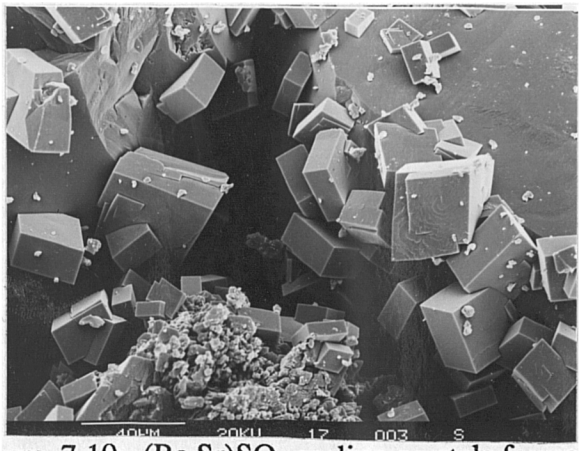

Figure 7.19 $(Ba,Sr)SO_4$ scaling crystals formed in a core, test C33TBSS17,dislocation on crystals. Brine BSS1, $(Ba+Sr)SO_4$=1,Sr/Ba=1.0. k_i=36.5md

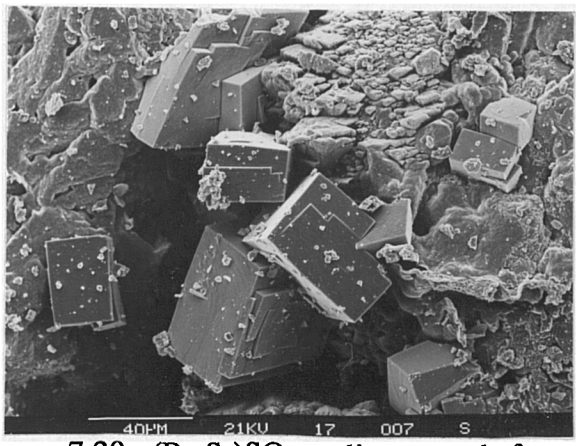

Figure 7.20 $(Ba,Sr)SO_4$ scaling crystals formed in a core, test C33TBSS17

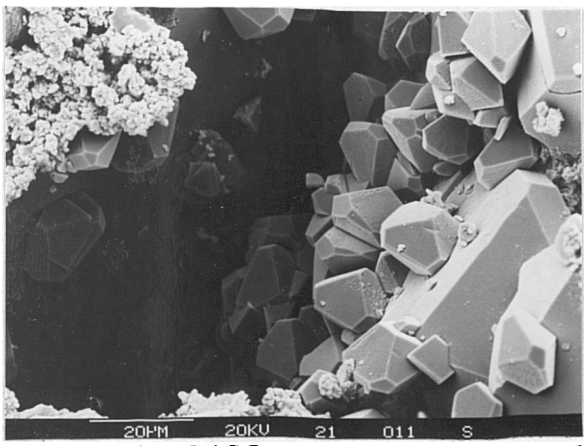

Figure 7.21 $(Ba,Sr)SO_4$ scaling crystals formed in a core, test C33TBSS21. Brine BSS2,$(Ba+Sr)SO_4$=1,Sr/Ba=100. k_i=18md

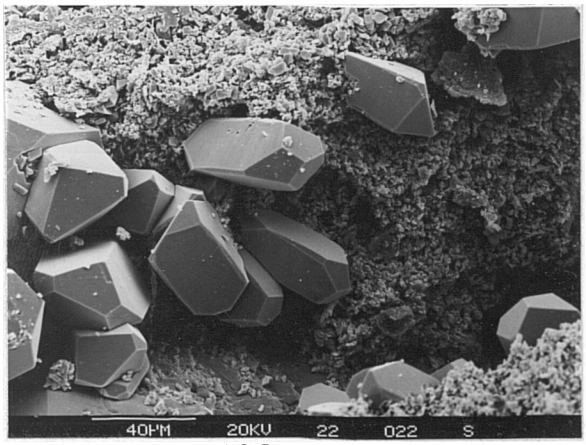

Figure 7.22 $(Ba,Sr)SO_4$ scaling crystals formed in a core, test C25TBSS22. Brine BSS2, $(Ba+Sr)SO_4$=1, Sr/Ba=100. k_i=147.5md

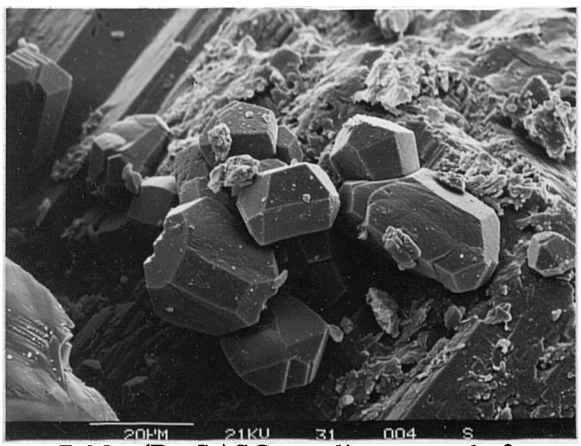

Figure 7.23 $(Ba,Sr)SO_4$ scaling crystals formed in a core, test C28TBSS31. Brine BSS3,$(Ba+Sr)SO_4$=1,Sr/Ba=1000. k_i=51md

investigation. The permeability decline to porosity reduction, permeability decline to the scale quantity precipitated in a core and the permeability decline rate to $(Ba,Sr)SO_4$ scaling(precipitation) rate were the three relations to be studied in the elevated temperature core flow experiments.

7.3.1 Analysis of the Overall Core Permeability Curves

The k - t curves from some of the elevated temperature formation damage experiments are presented in figures (7.24) through (7.30). Most of the curves have a concave shape. Even the final extent of the permeability reduction is relatively small, e.g, in the cases of the tests shown in figures (7.25) and (7.26). This was seen at 20°C only in the heavily damaged cores. As an exception to the concave k - t curve, two curves of different shapes were also noticed. One curve from a core test in figure(7.29) shows a slightly convex trend and the other curve from another test shown in figure(7.27) is slightly convex in the first section followed by a slightly concave section. It cannot be explained why the first section of the k - t curve in figure (7.27) is convex while the curve in figure(7.26), using a similar core and the same brine, resulted in a common concave curve. Nor is it clear about the cause of the k - t curve from the test shown in figure(7.29). The only difference of the test shown in figure (7.29) from the tests shown in figure(7.28)) and figure(7.30) is that the core used in the test in figure (7.29) had a much higher initial porosity which might have caused the $(Ba,Sr)SO_4$ scaling in the core in a different way or by a different mechanism.

The overall extent of permeability damage at the elevated temperature was also diverse, ranging from 12.4% to 88.2% of the initial permeabilities, as displayed in table (7.1).

Comparisons were made in the core tests carried out with the same brines but in cores of different initial permeabilities. The general observation is that a core of lower initial permeability was inclined to suffer more impairment on the relative scale but less permeability reduction in absolute term, as illustrated in figures (7.31) and (7.32), which is consistent with the findings from the 20°C tests. The only exception was a test

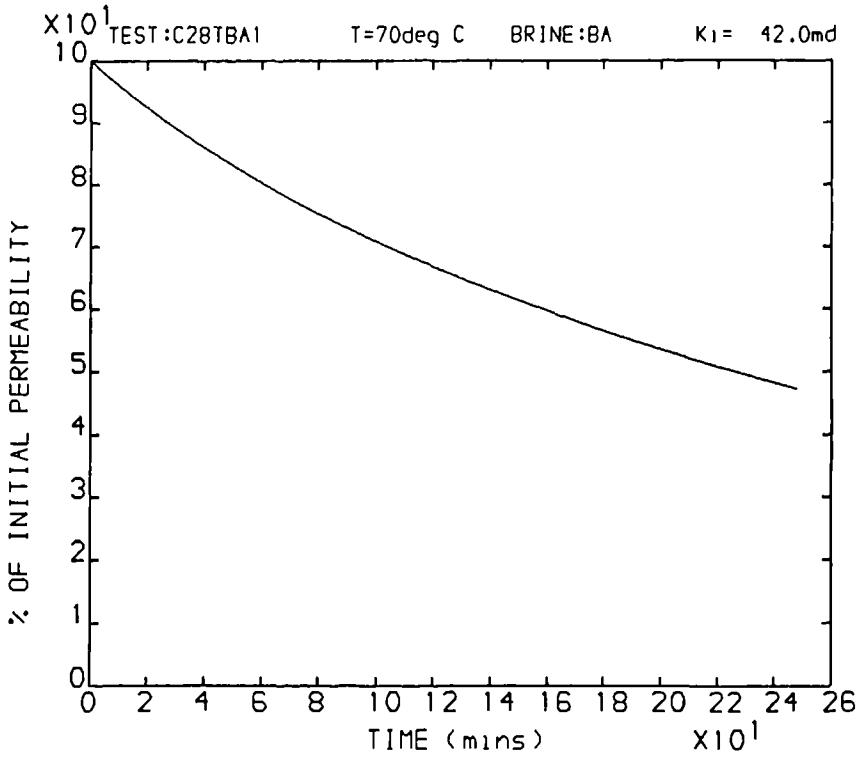

Figure 7.24 Core overall permeability curve, concave shape

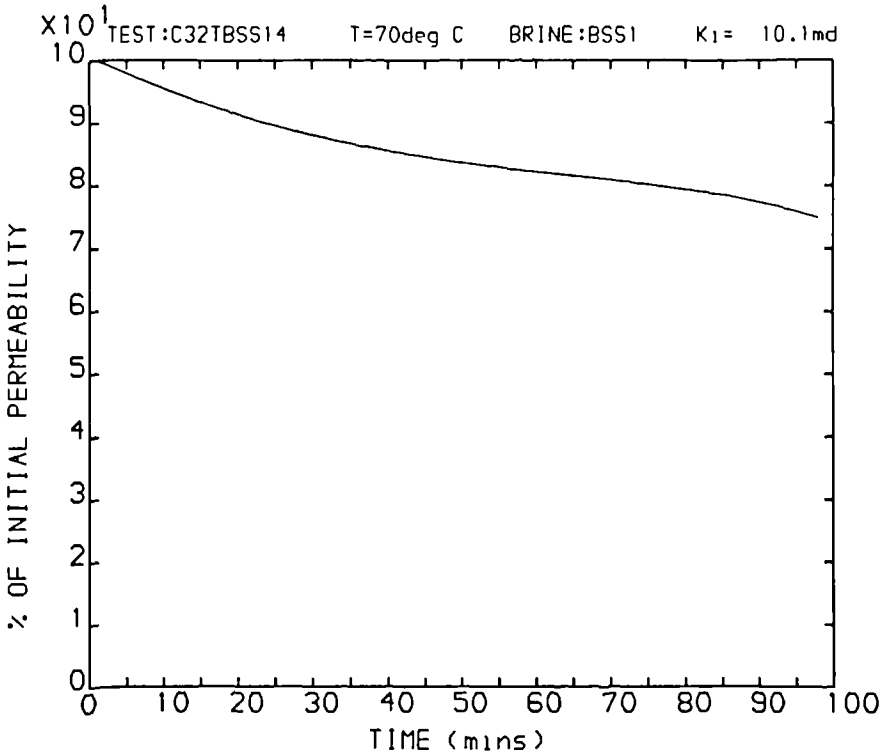

Figure 7.25 Core overall permeability curve, concave shape

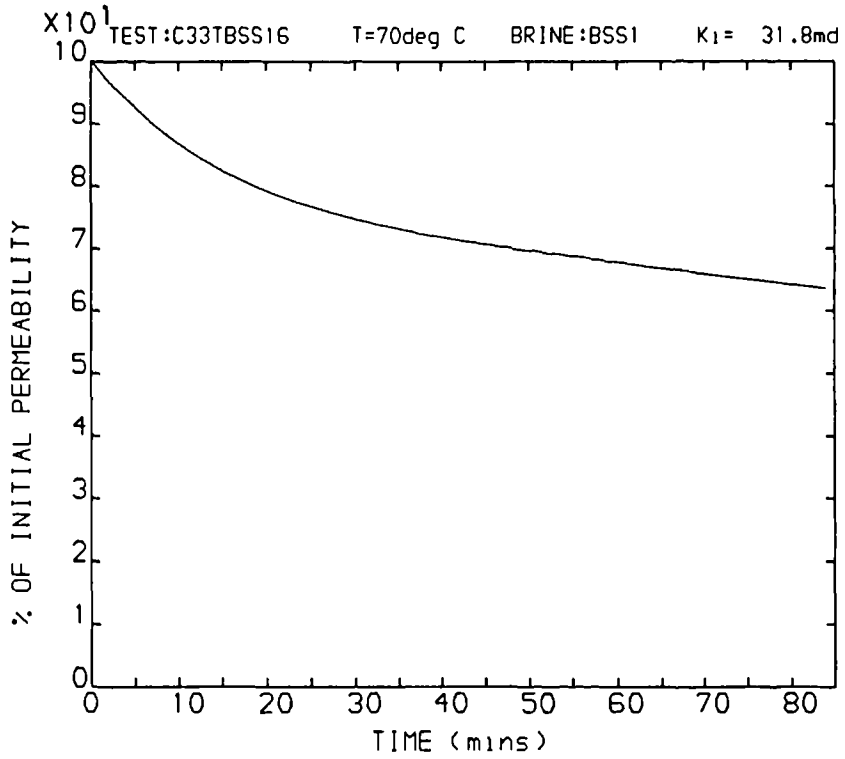

Figure 7.26 Core overall permeability curve, concave shape

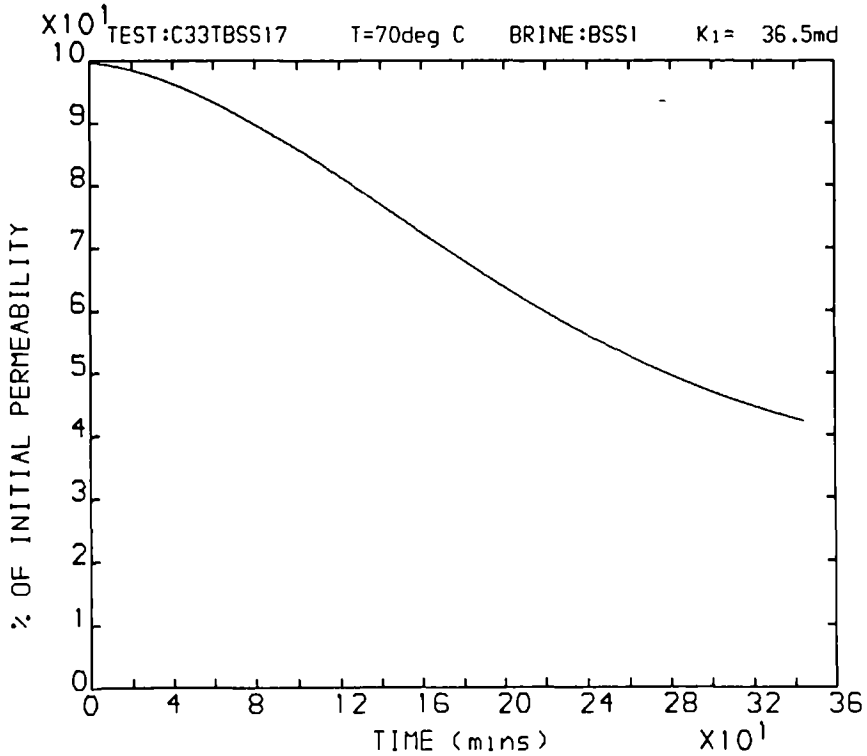

Figure 7.27 Core overall permeability curve, convex in first section and then concave

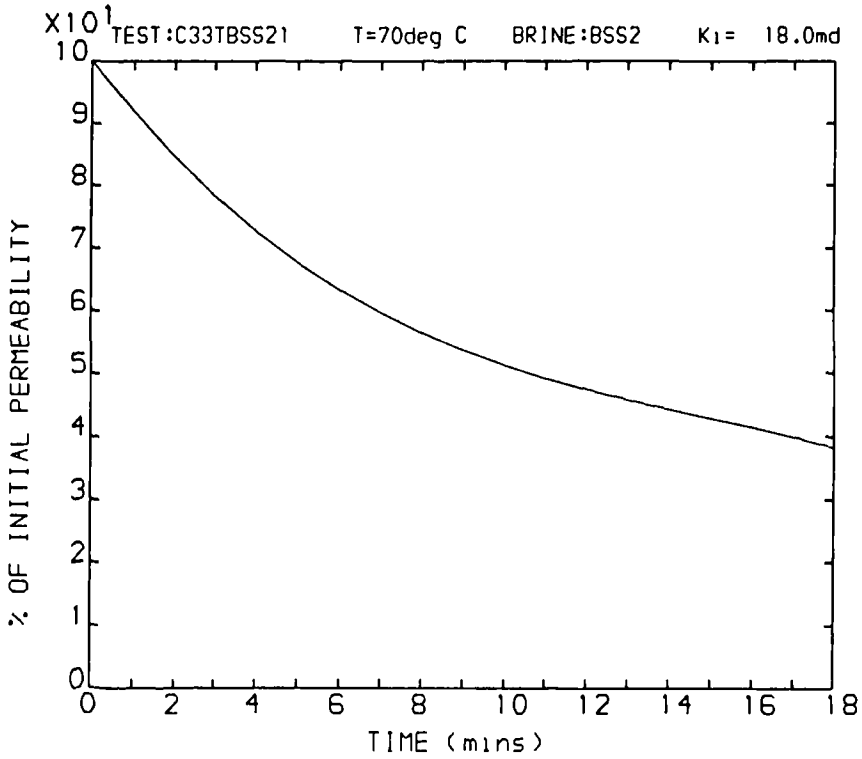

Figure 7.28 Core overall permeability curve, concave shape

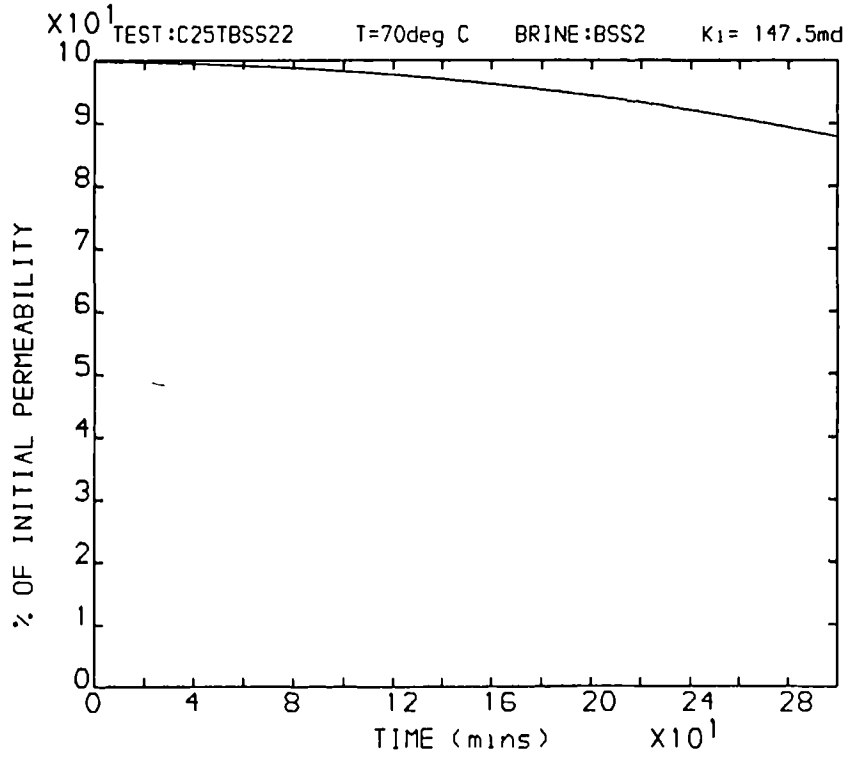

Figure 7.29 Core overall permeability curve, slightly convex shape

Table 7.1 Permeability and Porosity Changes and Amount of Scale Formed during Core Tests at 70°C

Test	Brine	Brine injection time (mins)	Permeability reduction				Porosity damage				Scale volume(ml)	
			k_i (md)	k_f (md)	Δk_f (md)	$(\Delta k_f/k_i)\times 100$	ϕ_i	ϕ_f	$\Delta\phi_f$	$(\Delta\phi_f/\phi_i)\times 100$	$V_{s,\phi}$	$V_{s,e}$
C28TBA1	BA	249	42.0	20.0	22.0	52.4	12.78	8.84	3.94	30.83	1.5	0.118
C29TBSS04	BSS0	120	12.1	5.6	6.5	53.7	14.17	13.93	0.24	1.69	0.096	0.067
C32TBSS14	BSS1	98	10.15	7.6	2.25	25.1	13.43	13.71	no	no	no	no
C33TBSS16	BSS1	84	31.8	20.5	11.3	35.5	13.33	13.73	no	no	no	no
C33TBSS17	BSS1	347	36.5	15.0	21.5	58.9	14.20	10.36	3.84	27.04	1.47	0.1533
C33TBSS21	BSS2	19	18.0	6.9	11.1	61.7	13.75	10.75	3.00	21.82	1.15	1.51
C25TBSS22	BSS2	295	147.5	129.2	18.3	12.4	21.33	16.62	4.71	22.08	1.81	no
C33TBSS23	BSS2	303	238.0	28.0	210.0	88.2	14.67	9.89	4.78	32.58	1.83	no
C28TBSS31	BSS3	12	51.0	20.0	31.0	60.8	13.98	9.81	4.17	29.83	1.60	no
C28TFORT1	Water1	120	68.5	13.5	55.0	80.3	13.41	9.38	4.03	30.05	1.55	no
C28TFORT2	Water1	107	123.5	24.0	99.5	80.6	14.74	10.73	4.01	27.20	1.54	0.213
C28TSBRAE1	Water2	56	190.0	13.0	177.0	93.2	14.23	10.07	4.16	29.23	1.60	no

* k_i —— initial core permeability, k_f (md) —— final core permeability after scale formation
Δk_f —— final permeability reduction due to scaling, $(\Delta k_f/k_i)\times 100$ —— final permeability reduction as % of k_i
ϕ_i —— initial porosity(%), ϕ_f —— final porosity(%) after scale formation, $\Delta\phi_f$ —— final porosity reduction(%) due to scaling
$(\Delta\phi_f/\phi_i)\times 100$ —— final porosity reduction as % of initial porosity, $V_{s,\phi}$ —— scale volume calculated from porosity reduction
$V_{s,e}$ —— scale volume calculated from effluent analysis, no —— no data available

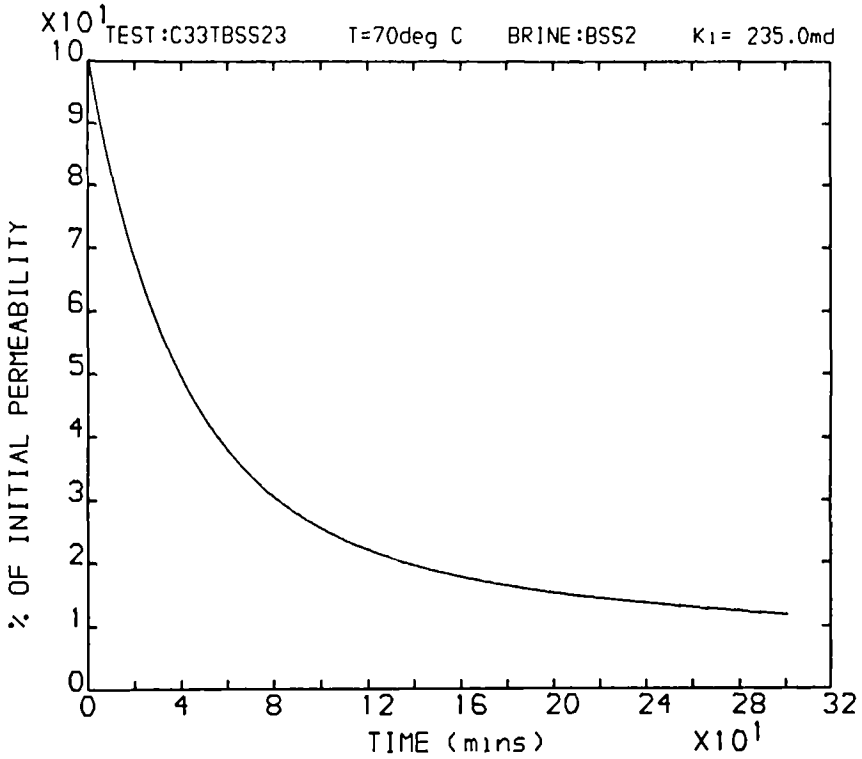

Figure 7.30 Core overall permeability curve, concave shape

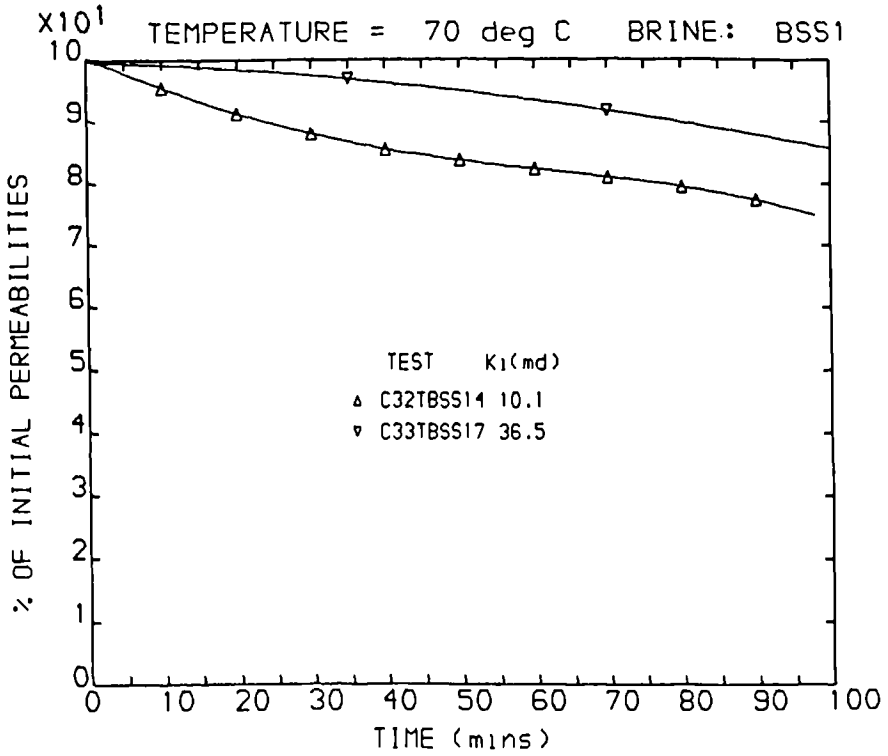

Figure 7.31 Permeability damages in two cores of different initial permeabilities injected with the same brine,permeability decline in relative term

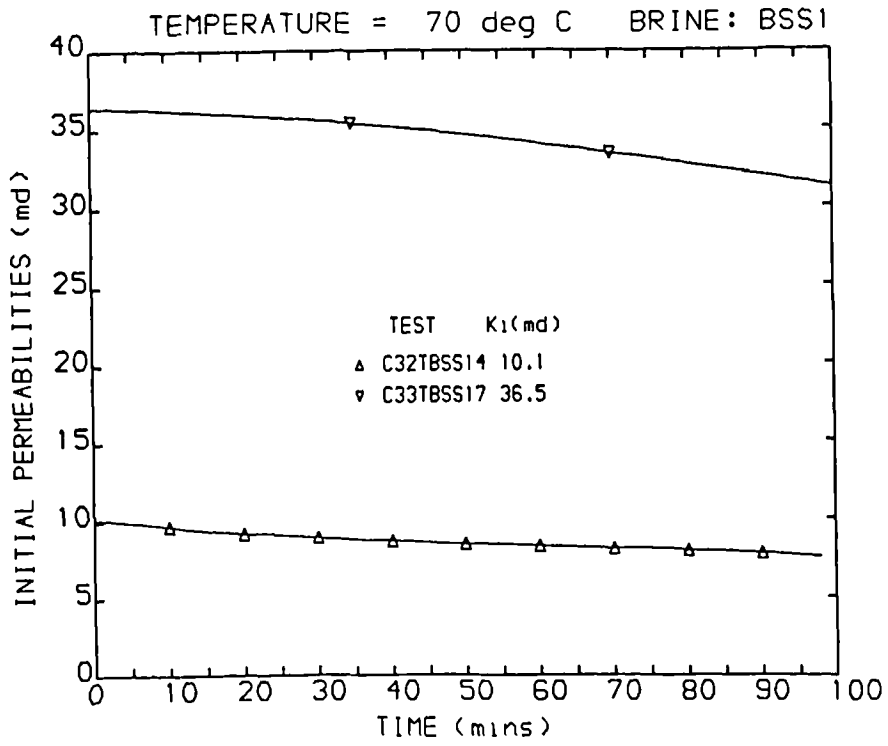

Figure 7.32 Permeability damages in two cores of different initial permeabilities injected with the same brine,permeability decline in absolute term

injected with brine BSS1 of Sr/Ba ratio equal to 1.0 (test C32TBSS14). The core used in this test had lower k_i than the core used in another test injected with the same brine (test C33TBSS16) but it underwent less permeability loss relatively after the same period of injecting the same brine as shown in figure (7.33). After examining the rock porosities, it was found the initial porosity of C32TBSS14 core (13.43%) was slightly higher than the core used in C33TBSS16 (13.33%). Based on this finding, the initial porosities of all the cores used in 70°C tests were related to the rock permeability damage. It was revealed that a core of lower initial porosity(even though it might be of higher k_i) had suffered higher permeability loss in a relative term (as % k_i) when the same brine was used under the same experimental conditions.

Considering the effect of changing Sr/Ba ratio in the brines, it was observed that at similar rock and test conditions, injecting BSS3 brine (Sr/Ba=1000) caused the most severe damage, then BSS2(Sr/Ba=100) and BSS0(Sr/Ba=0.1) brines, and injection of BSS1(Sr/Ba=1.0) had the least effect on rock permeability, as indicated in figure (7.34).

7.3.2 The Pattern of Sectional Permeability Decline Distribution

In general, the permeability in the core front was reduced more than that in the rear of a core as a result of the sulphate solid solution scale formation, as shown in the sectional permeabilities - time curves in figures (7.35) through (7.39). The same result was produced from the 20°C core tests. The two patterns in the permeability decline distribution into the depth of a core, originally found from the room temperature experiments, were roughly applicable to the results at 70°C. That is, the permeability decline extent reduced sequentially from section 1 through section 5 of a core (pattern 1) or section 2 rather than section 2 had the heaviest permeability loss (pattern 2). But such trends were not so evident at 70°C as at 20°C because the rear sections of a core (sections 4 and 5) had larger permeability reductions than that in the middle sections of a core in a few core tests carried out at the elevated temperature. The transition from one pattern to the other were not found to be related to the Sr/Ba ratio change in the injected brines. The retardation theory, which explained the cause of the two patterns of permeability

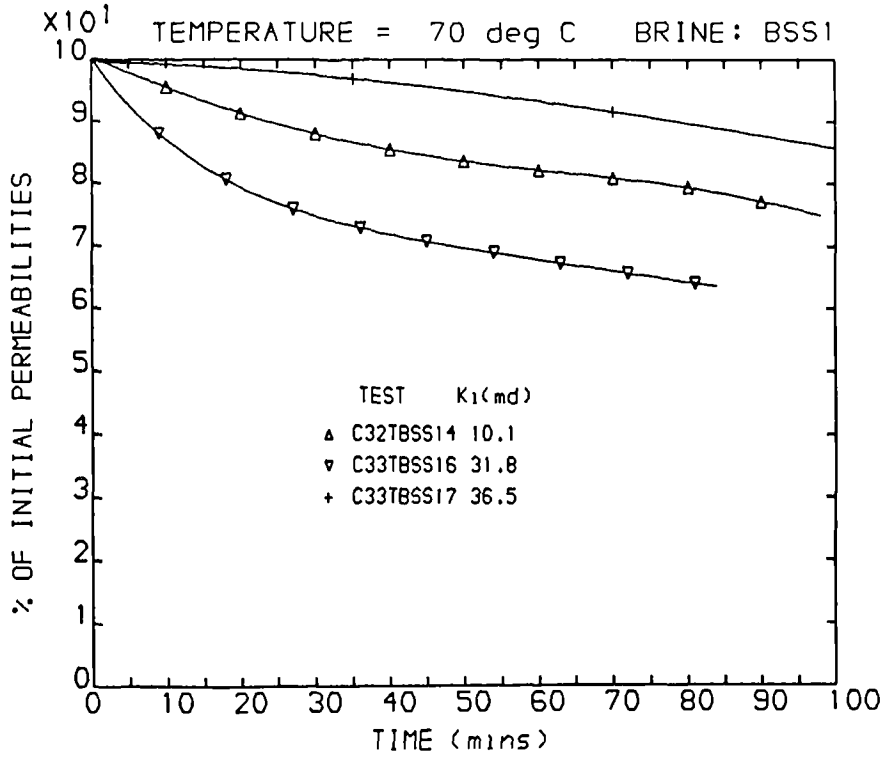

Figure 7.33 Permeability damages in the cores injected with the same brine, TBSS16 core had higher initial permeability than TBSS14 core and had larger permeability loss in relative term, an unusual case

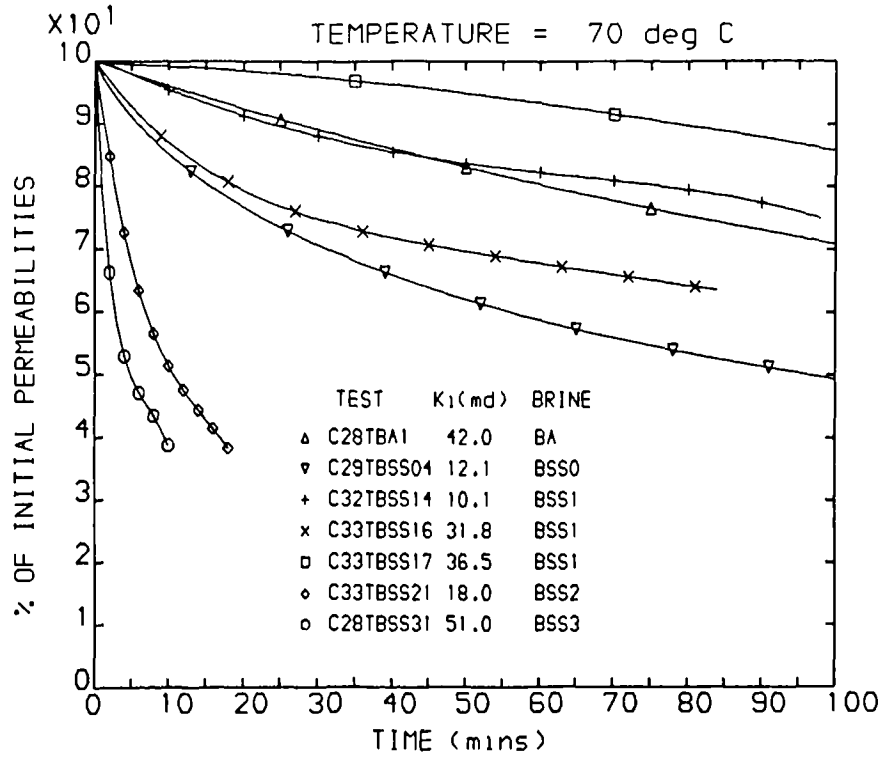

Figure 7.34 Core permeability damages resulting from injecting brines of different Sr/Ba molar ratio

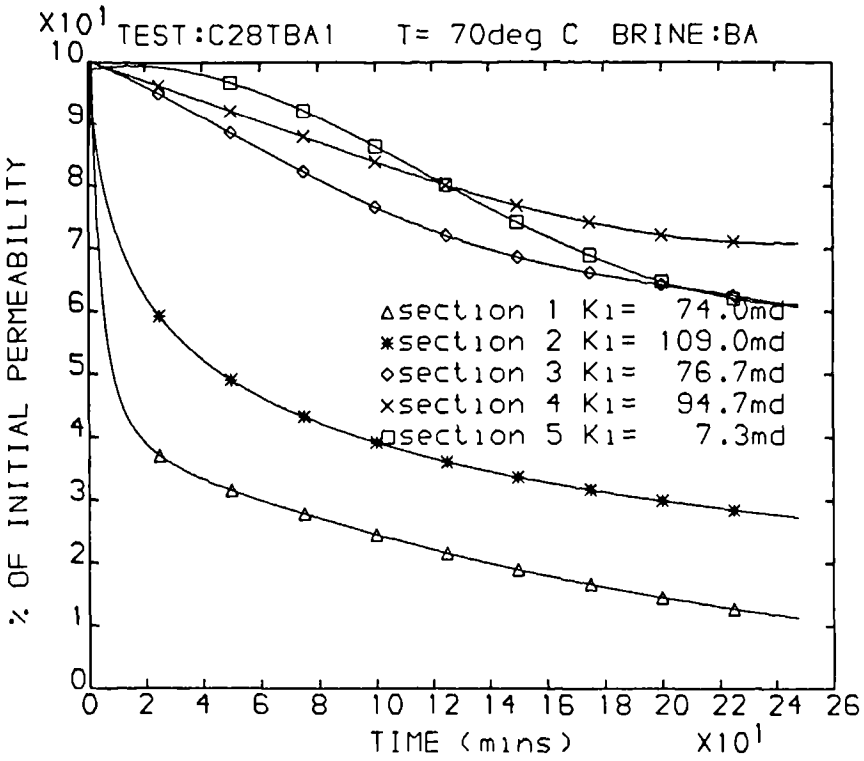

Figure 7.35 Permeability changes in sections of a core due to scaling

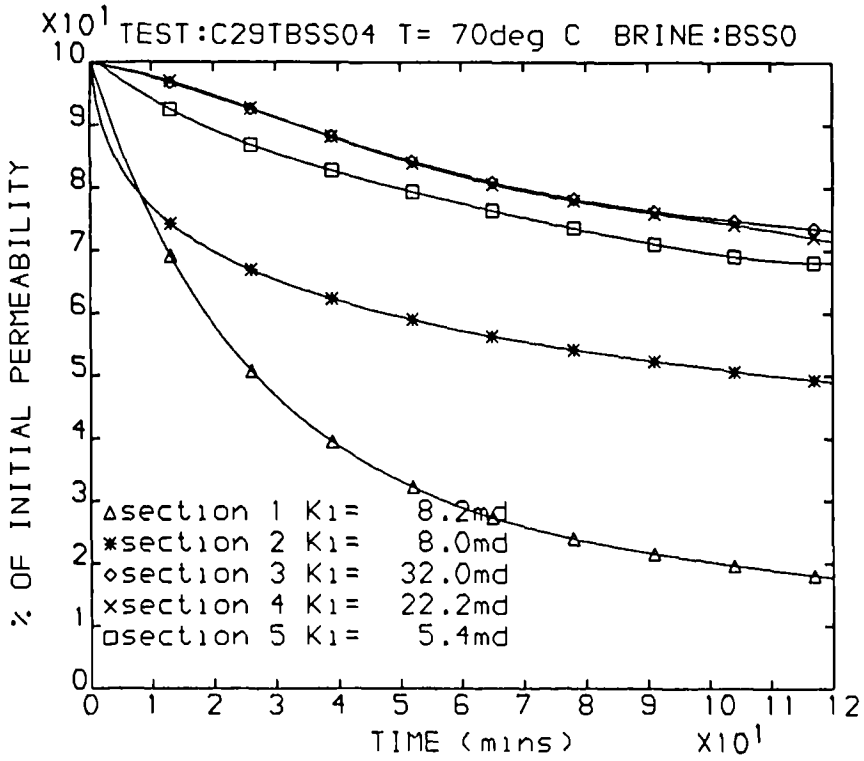

Figure 7.36 Permeability changes in sections of a core due to scaling

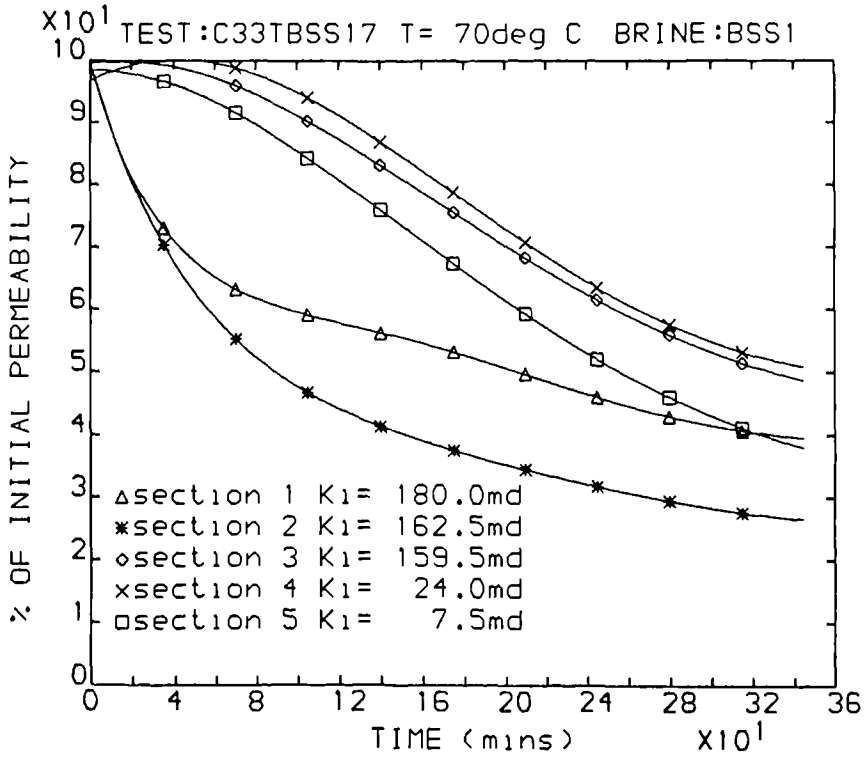

Figure 7.37 Permeability changes in sections of a core due to scaling

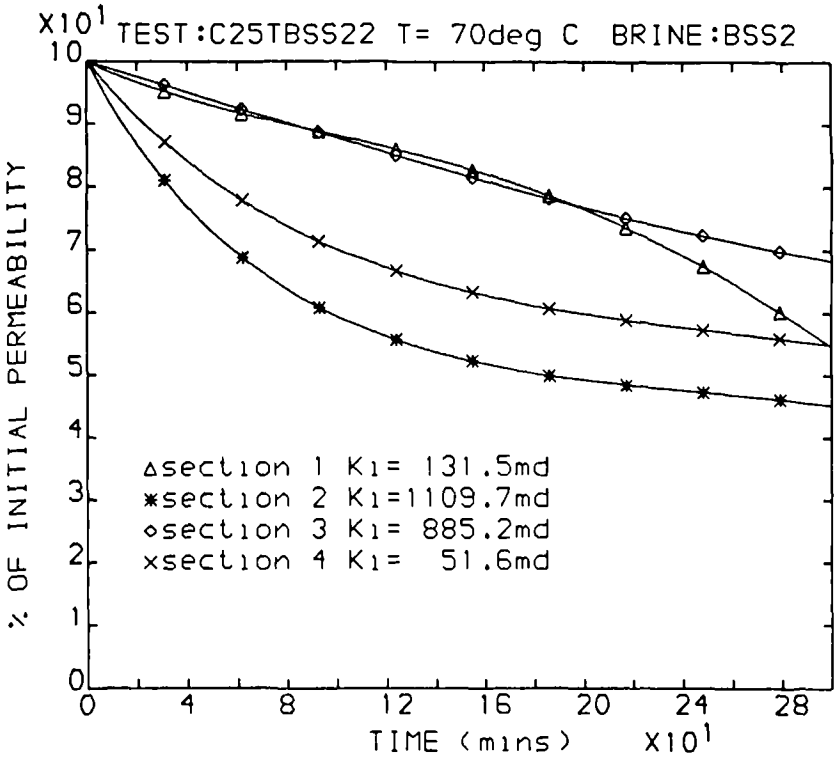

Figure 7.38 Permeability changes in sections of a core due to scaling

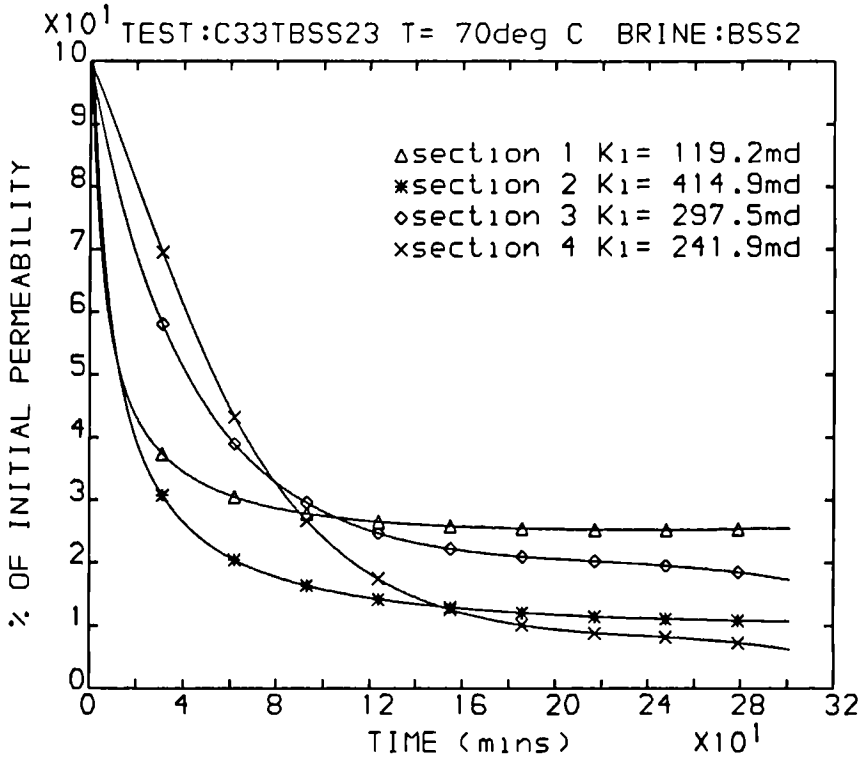

Figure 7.39 Permeability changes in sections of a core due to scaling

damage distribution resulting from the 20°C scale formation experiments, seems unable to give a satisfactory explanation to the cause of the distribution difference produced from the 70°C tests. More discussion on this point will be followed in section (7.5) when the temperature effect is addressed.

7.3.3 The Trend of Permeability Decline Rate

As described in subsection (6.4.1) of chapter 6, the core permeability decline rate trends during the formation damage core tests at 20°C fell into four types. The typical dk/dt - t curves obtained from 70°C core tests are shown in figures (7.40) through (7.45). The majority of the curves show type 1 trend, that is, dk/dt steadily decreased as the brine injection continued. Three curves show type 2 trend, first dk/dt decreasing then increasing. Only one of the 70°C tests produced type 3 trend of permeability decline rate change, which shows the dk/dt climbing at the first stage of the core flow experiment then declining. No type 4 dk/dt change trend is observed among the dk/dt - t curves resulting from 70°C tests. Type 1 curves indicate that scale precipitation took place rapidly soon after the incompatible brines started mixing in the rock pores at 70°C and the few type 2 curves suggest the secondary crystal growth could have occurred in some of the formation damage experiments at 70°C, but not as frequently as at 20°C, probably because the crystal growth at the higher temperature competed with the secondary nucleation more favourably. The fact that only one type 3 curve, no type 4 curve and mostly type 1 curves were the results of 70°C core tests indicates the difference in the precipitation kinetics at 70°C compared to that at 20°. That is, the scaling rate at 70°C was higher than that at 20°C. This is consistent with the finding by Gardner and Nancollas.[38]

7.3.4 Characterisation of the Permeability Curves

Similar treatment to the 20°C permeability curves was carried out to 70°C results. The initial permeability decline rates and the maximum permeability rates were calculated

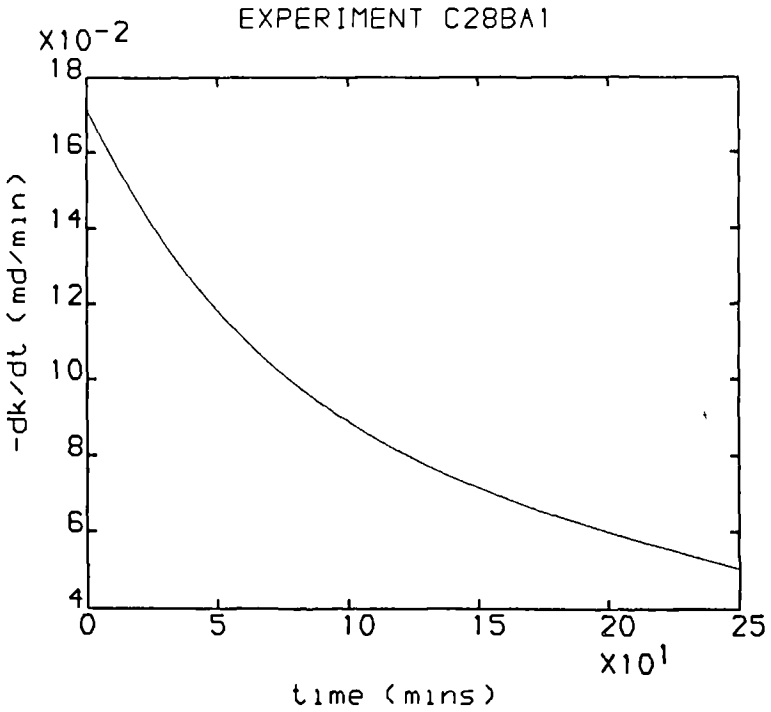

Figure 7.40 Core permeability decline rate curve, type 1

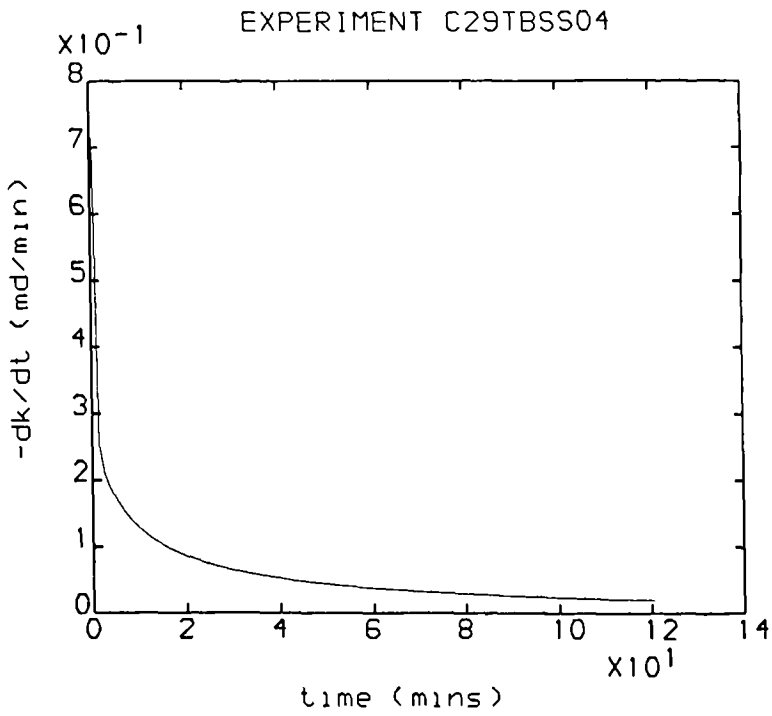

Figure 7.41 Core permeability decline rate curve, type 1

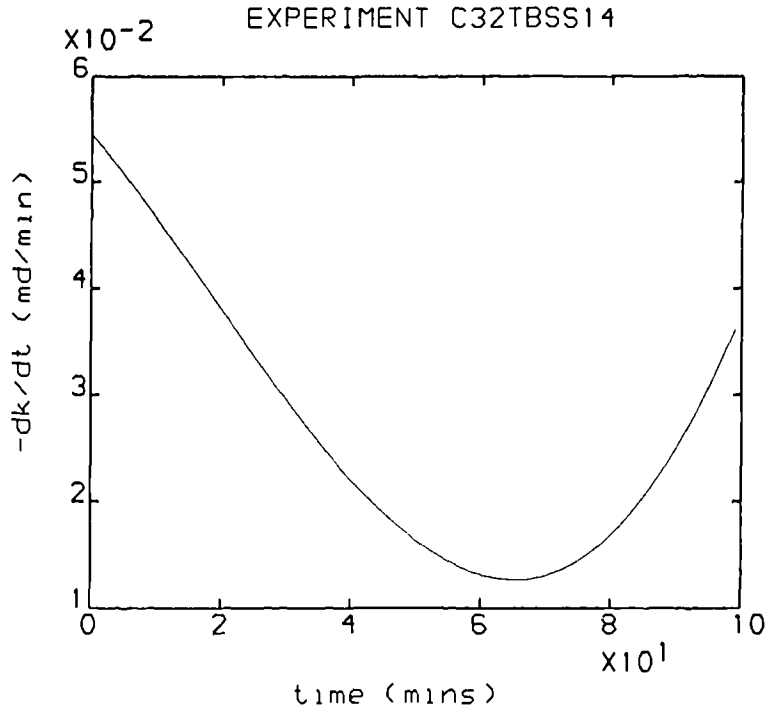

Figure 7.42 Core permeability decline rate curve, type 2

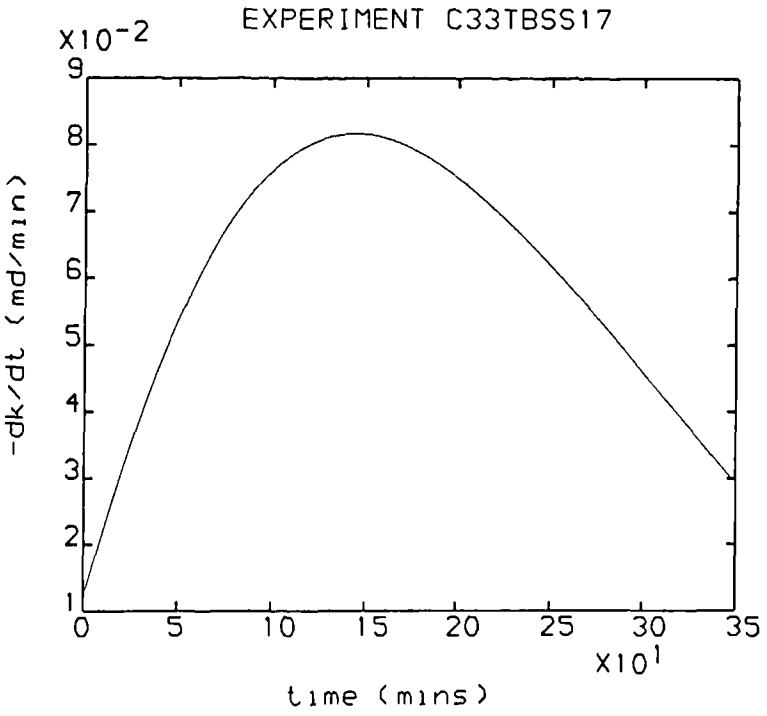

Figure 7.43 Core permeability decline rate curve, type 3

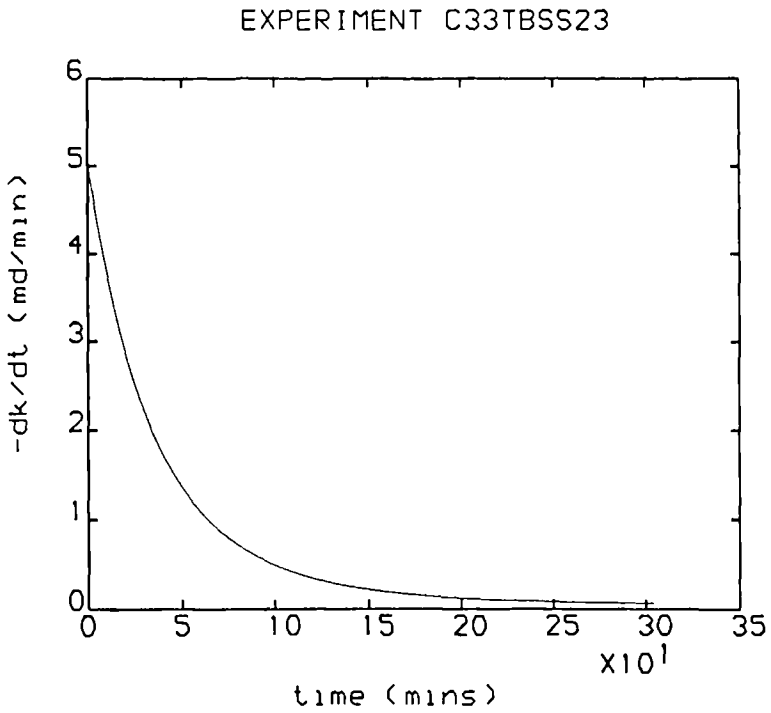

Figure 7.44 Core permeability decline rate curve, type 1

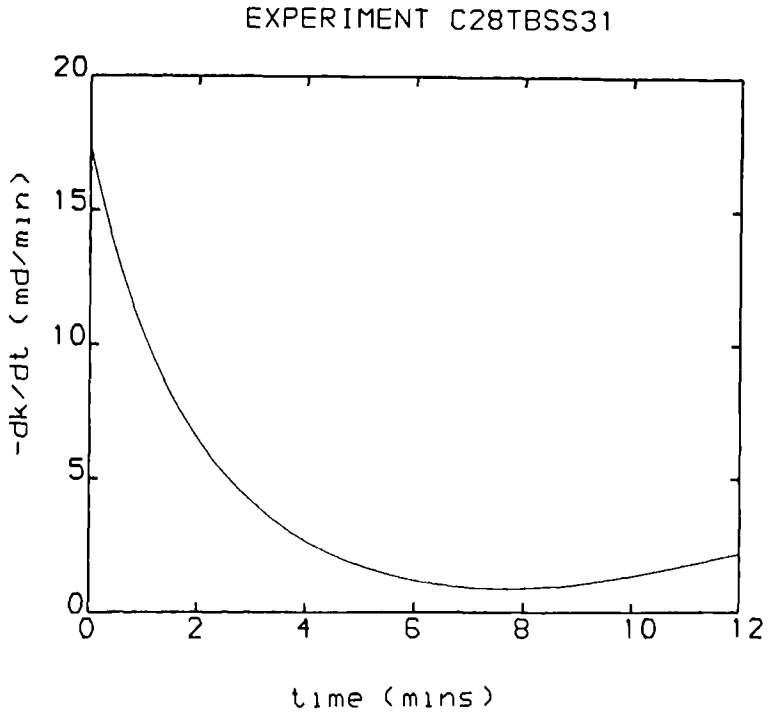

Figure 7.45 Core permeability decline rate curve, type 2

from the numerical expressions for dk/dt - t and k - t curves at 70°C and are presented in table (7.2). They show at 70°C, different results from the 20°C tests, all but two $(dk/dt)_i$ or $(dk/dt)_i/k_i$ values are identical to the corresponding $(dk/dt)_m$ or $(dk/dt)_m/k_i$ values, suggesting the rapid start of the scale precipitation in the cores at the elevated temperature and this was confirmed by comparing the $(dk/dt)_i/k_i$ values between the two temperatures.

The average $(dk/dt)_i/k_i$ values in the 20°C core tests injected with brines BSS0(Sr/Ba=0.1), BSS1(Sr/Ba=1.0) and BSS2(Sr/Ba=100) are -3.886E-3, -0.943E-3 and -0.733E-4 (1/min), respectively. In comparison, the average $(dk/dt)_i/k_i$ values in the 70°C core tests injected with brines BSS0, BSS1 and BSS2 are -5.917E-2, -7.729E-3 and -4.400E-2 (1/min), which indicates that the solid solution precipitation rate increased at the higher temperature.

The time at half of the initial permeability decline rate, i.e, $t_{1/2}$, and the nominal maximum curvature time t_c were also calculated from the numerical expression of a dk/dt curve and a k - t curve from each core test, respectively. The calculated permeability change characteristics are also listed in table (7.2). As seen from table (7.2), $t_{1/2}$ did not exist for dk/dt - t curve produced from test C33TBSS17 injected with brine BSS1 of Sr/Ba molar ratio equal to 1.0 because the initial permeability decline rate at the start of the brine injection was the lowest. Again, as found from 20°C experiments, the trend of the t_c value change from one test to the other is generally consistent with the change in $t_{1/2}$ as suggested in figure (7.46). Also, the time when the initial permeability decline rate reduced to its half ($t_{1/2}$) was shorter if the initial permeability decline rate $(dk/dt)_i/k_i$ was higher, as shown in figure (7.47)

7.3.5 Correlation of Permeability Damage with Porosity Reduction and Scale Volume

In order to find out if there is any relation between the extent of rock permeability

Table 7.2 Numerical Characterisation of Permeability Decline at 70°C

Test	Brine	k_i (md)	Brine injection time (mins)	$(dk/dt)_i$ (md/min)	$(dk/dt)_m$ (md/min)	$(dk/dt)_i/k_i$ (1/min)	$(dk/dt)_m/k_i$ (1/min)	t_m (mins)	$t_{1/2}$ (mins)	t_c (mins)
C28TBA1	BA	42.0	249	-0.1716	-0.1716	-4.086E-3	-4.086E-3	0.0	107.0	no
C29TBSS04	BSS0	12.1	120	-0.7160	-0.7160	-5.917E-2	-5.917E-2	0.0	0.9	0.7
C32TBSS14	BSS1	10.2	98	-0.0545	-0.0545	-5.369E-3	-5.369E-3	0.0	32.7	24.8
C33TBSS16	BSS1	31.8	84	-0.5560	-0.5560	-1.748E-2	-1.748E-2	0.0	12.5	14.9
C33TBSS17	BSS1	36.5	347	-0.0121	-0.0817	-3.315E-4	-2.238E-3	144.0	no	no
C33TBSS21	BSS2	18.0	19	-1.5830	-1.5830	-8.794E-2	-8.794E-2	0.0	5.8	11.8
C25TBSS22	BSS2	147.5	295	-0.0084	-0.1134	-5.708E-5	-7.687E-4	295.0	no	no
C33TBSS23	BSS2	238.0	303	-5.0500	-5.0500	-2.122E-2	-2.122E-2	0.	24.7	35.3
C28TBSS31	BSS3	51.0	12	-17.378	-17.378	-0.3408	-0.3408	0.	1.4	6.1
C28TFORT1	Water1	68.5	120	-2.959	-2.959	-4.320E-2	-4.320E-2	0.	9.1	19.6
C28TFORT2	Water1	123.5	107	-2.686	-2.686	-2.175E-2	-2.175E-2	0.	24.1	30.4
C28TSBRAE1	Water2	190.0	56	-94.520	-94.520	-0.4975	-0.4975	0.	1.0	15.1

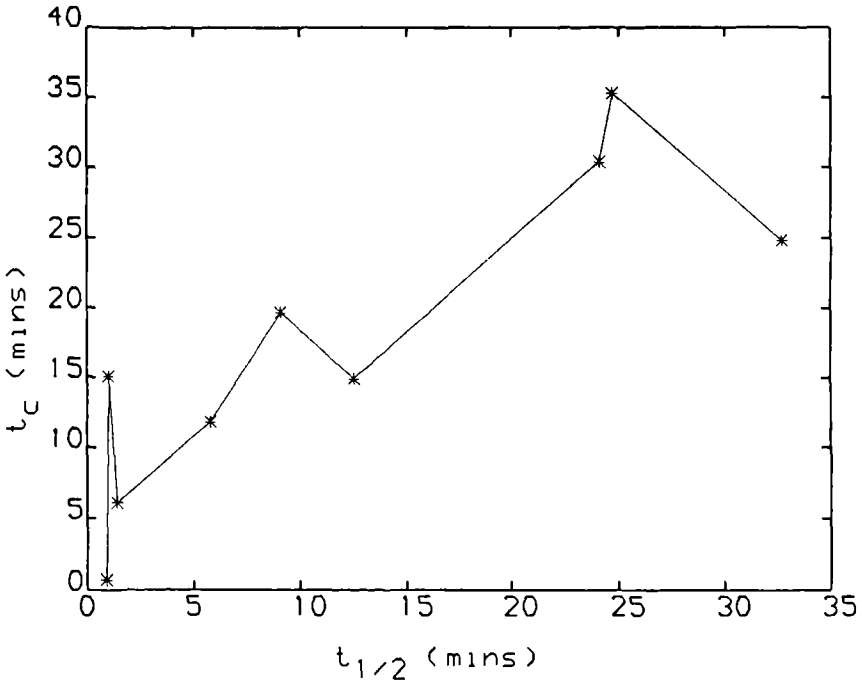

Figure 7.46 t_c - $t_{1/2}$ correlation from 70°C core test results

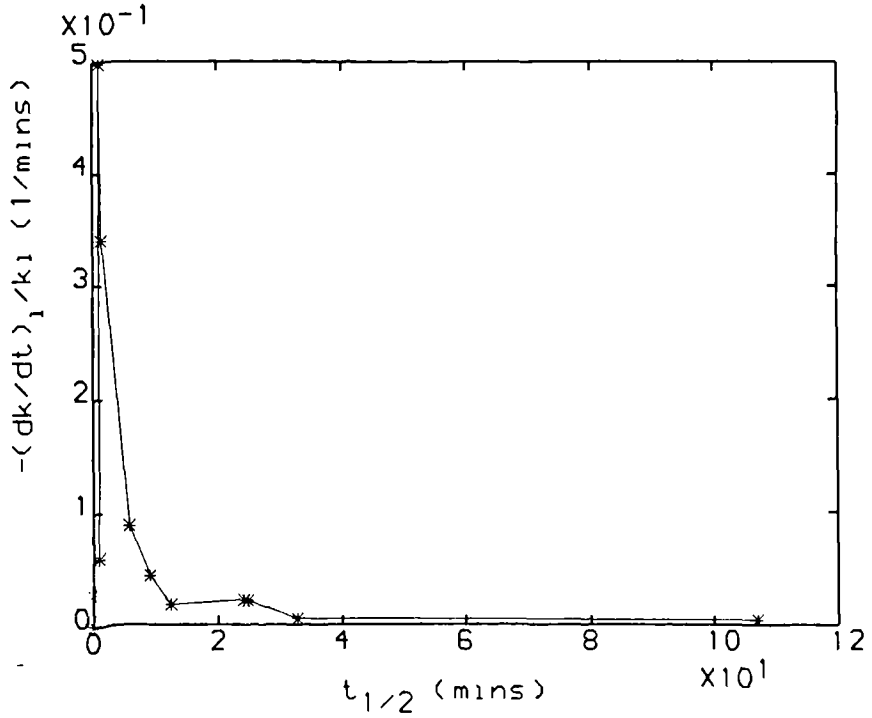

Figure 7.47 Initial permeability decline rate - $t_{1/2}$ correlation

damage and the extent of rock porosity reduction caused by the $(Ba,Sr)SO_4$ solid solution scale formation or between the permeability reduction and the volume of scale deposited in a core, permeability - porosity correlation and permeability - scale volume correlation were made and are presented in figures (7.48) to (7.51).

No clear relation is observed between initial core permeability and its initial porosity. The permeability reduction does not seem obviously related to porosity reduction but an indication is given that higher porosity damage resulted in a larger permeability loss. Similar observation applies to the permeability reduction - scale volume relation, which indicates that the permeability change due to solid solution scaling was not a unique function of the porosity change or amount of scale formed. The other aspects such as the scaling sites, scaling crystal morphology and scale distribution in the core, etc. might also be responsible for the extent of permeability reduction. The findings from the present study were not conclusive because the fines migration out of the core during a test might have produced some error in porosity measurement. Also some other factors, e.g, the different brine composition and diversity in the cores used in the tests, might have complicated the permeability - scale volume relation. It is felt further investigation should be conducted in this aspect with more rigid experimental tests, which would exclude the interference by other factors.

7.4 THE PROFILES OF BARIUM AND STRONTIUM ION CONCENTRATIONS IN THE CORE FLOW BRINE EFFLUENTS

During some of the core flow tests, the brine effluents from the scaling cores were sampled and subsequently Plasma analysis was made to measure the Ba^{2+} and Sr^{2+} ion concentrations. Table (7.3) and figures (7.52) through (7.56) present the analysed results. Table (7.3) suggests that the scaling rate of barium sulphate in the porous media was higher than that of strontium sulphate. The sulphate supersaturations reduced significantly after flowing through a core though the effluent brines were still supersaturated. These results were consistent with those from the 20°C experiments. The Ba^{2+} concentration in the brine effluents during a test generally shows a downward

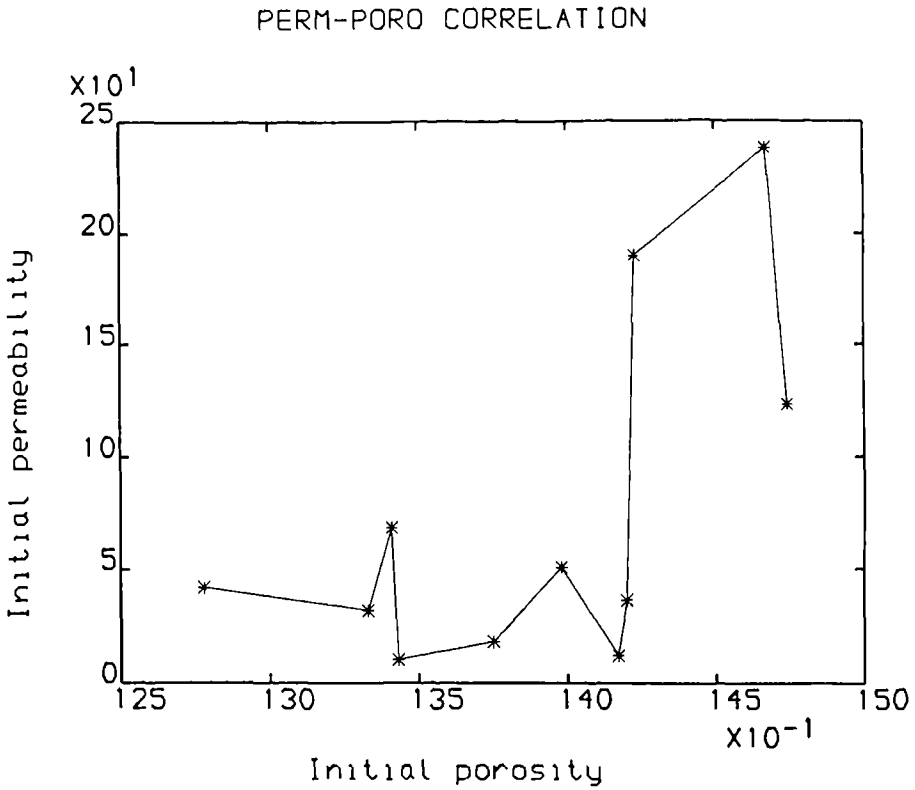

Figure 7.48 Clashach core permeability - porosity correlation

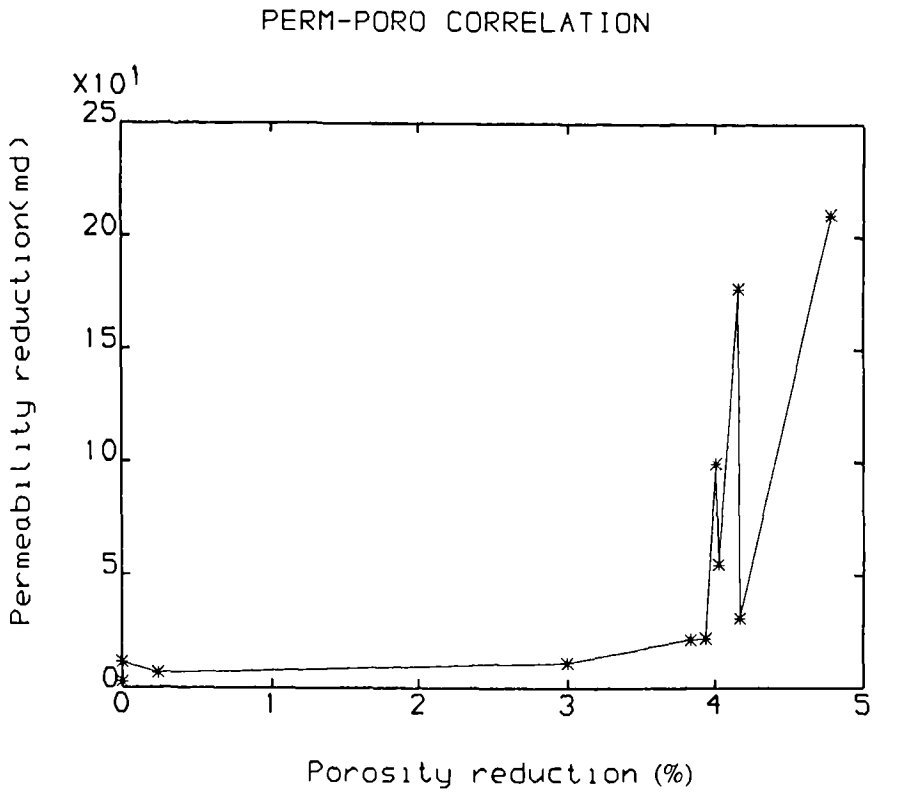

Figure 7.49 Scale formation permeability reduction - porosity reduction correlation

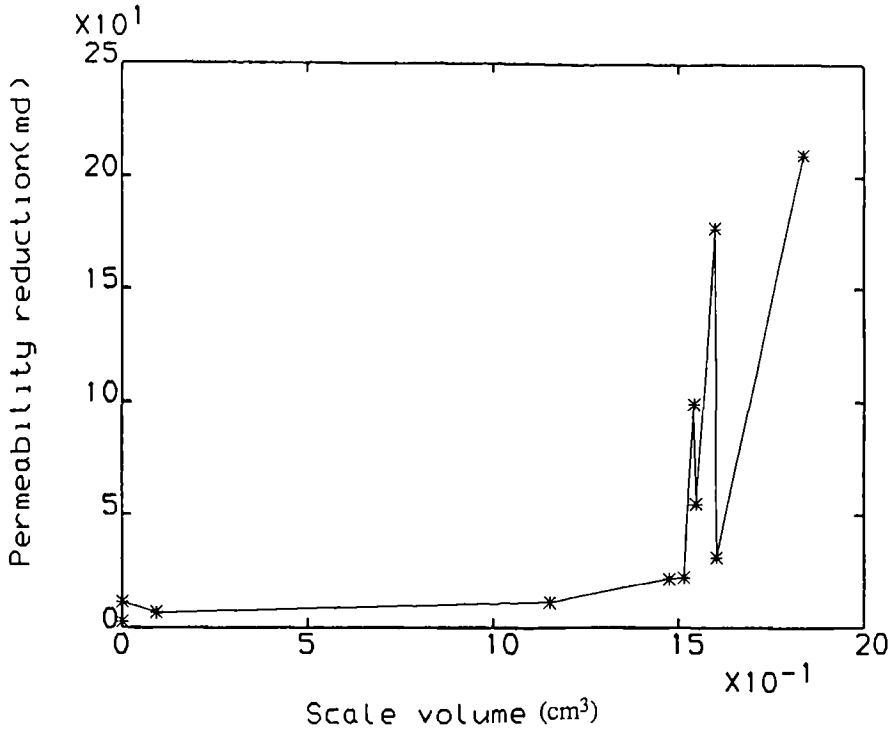

Figure 7.50 *Correlation of permeability reduction - volume of scale deposited in the cores, permeability decline in absolute term*

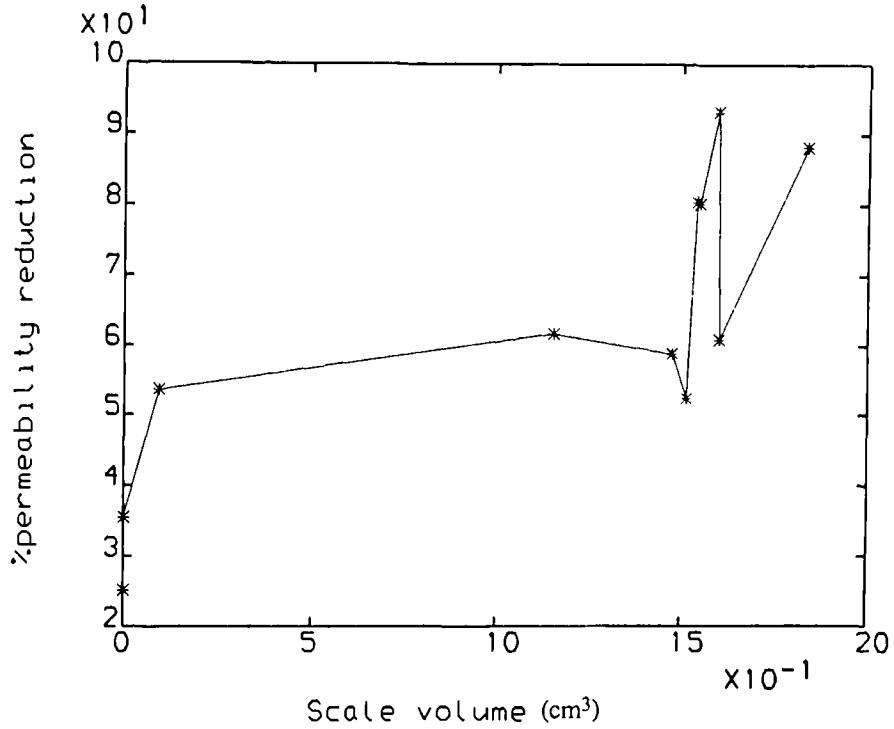

Figure 7.51 *Correlation of permeability reduction - volume of scale deposited in the cores, permeability decline in relative term*

Table 7.3 Ion Concentrations in the Brine Effluents from 70°C Core Tests

Test	Brine	$Ba_{,i}$ (molar)	$Sr_{,i}$ (molar)	$Ba_{,e}$ (molar)	$Sr_{,e}$ (molar)	$Ba_{,e}/Ba_{,i}$	$Sr_{,e}/Sr_{,i}$	$Ba_{,i}/Sr_{,i}$	$Ba_{,e}/Sr_{,e}$	$SP_{Ba,i}$	$SP_{Ba,e}$	$SP_{Sr,i}$	$SP_{Sr,e}$
C28BA1	BA	0.00109	no	0.000488	no	0.45	no	no	no	8.4	4.2	no	no
C29TBSS04	BSS0	0.00104	0.00010	0.000378	no	0.36	no	no	no	8.4	3.5	no	no
C33TBSS17	BSS1	0.00077	0.00077	0.000307	0.00067	0.40	0.87	1.0	0.46	8.4	4.7	0.46	0.34
C25TBSS22	BSS2	0.00011	0.01086	no	0.00523	no	0.48	no	no	8.4	no	4.6	2.2
C28TFORT2	Water1	0.00090	0.00335	0.000005	0.00178	0.005	0.53	0.27	0.003	22.7	1.5	2.0	1.4

* $Ba_{,i}$ —— barium concentration in initial brine, $Sr_{,i}$ —— strontium concentration in initial brine

$Ba_{,e}$ —— average barium concentration in brine effluent samples from one core test

$Sr_{,e}$ —— average strontium concentration in brine effluent samples from one core test

SP —— supersaturation of barium sulphate or strontium sulphate

no —— no effluent analysis

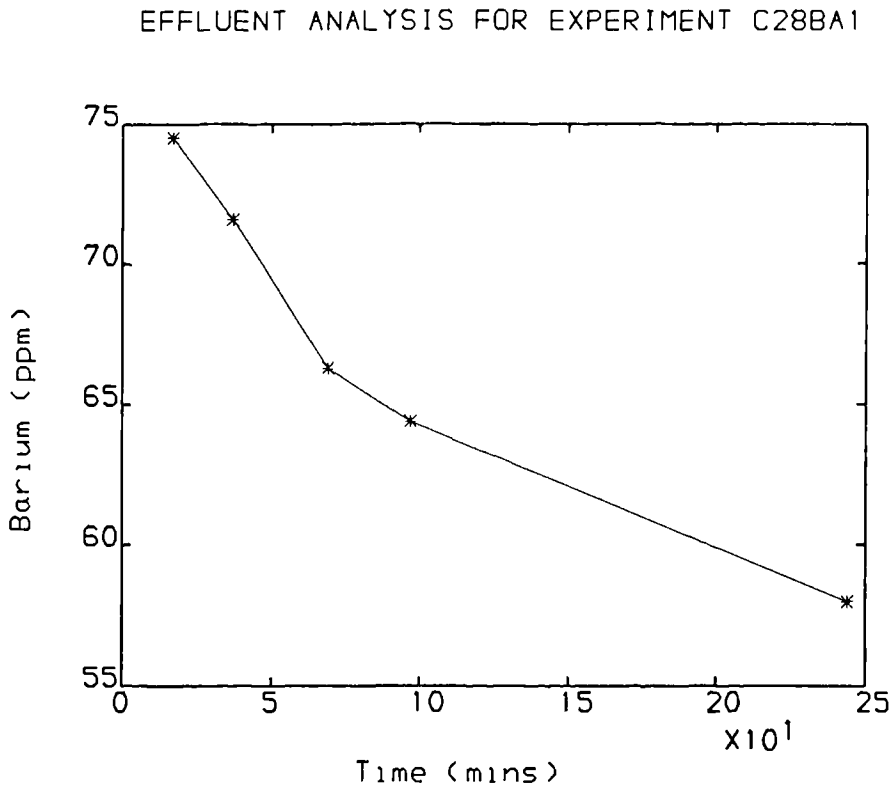

Figure 7.52 Barium ion concentration change in the brine effluents during a core test

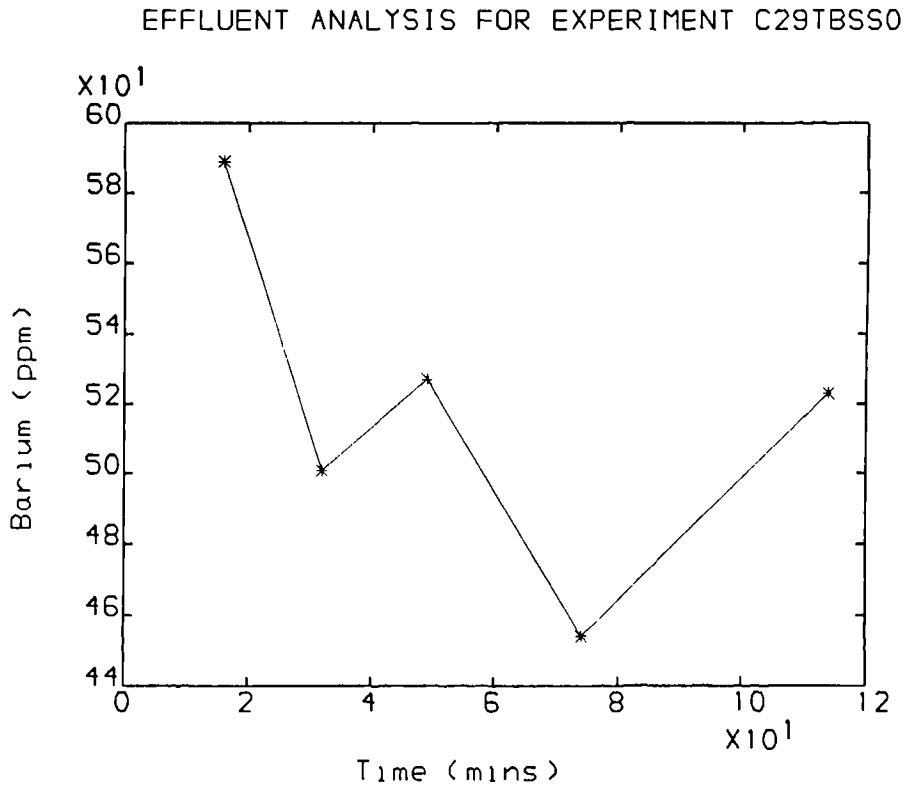

Figure 7.53 Barium ion concentration change in the brine effluents during a core test

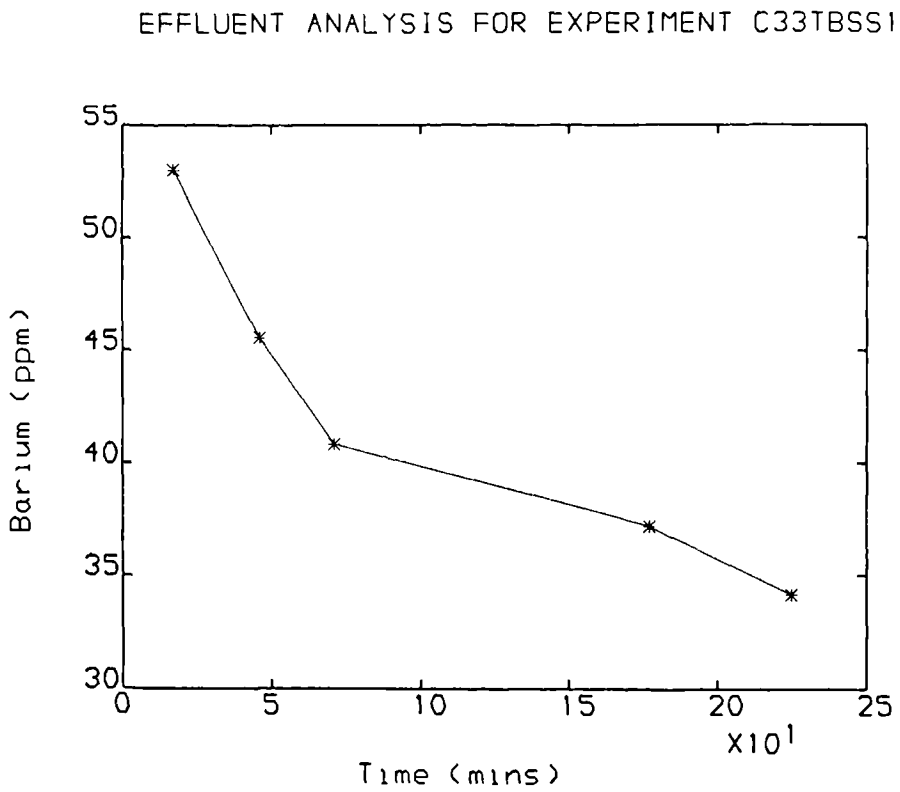

Figure 7.54 Barium ion concentration change in the brine effluents during a core test

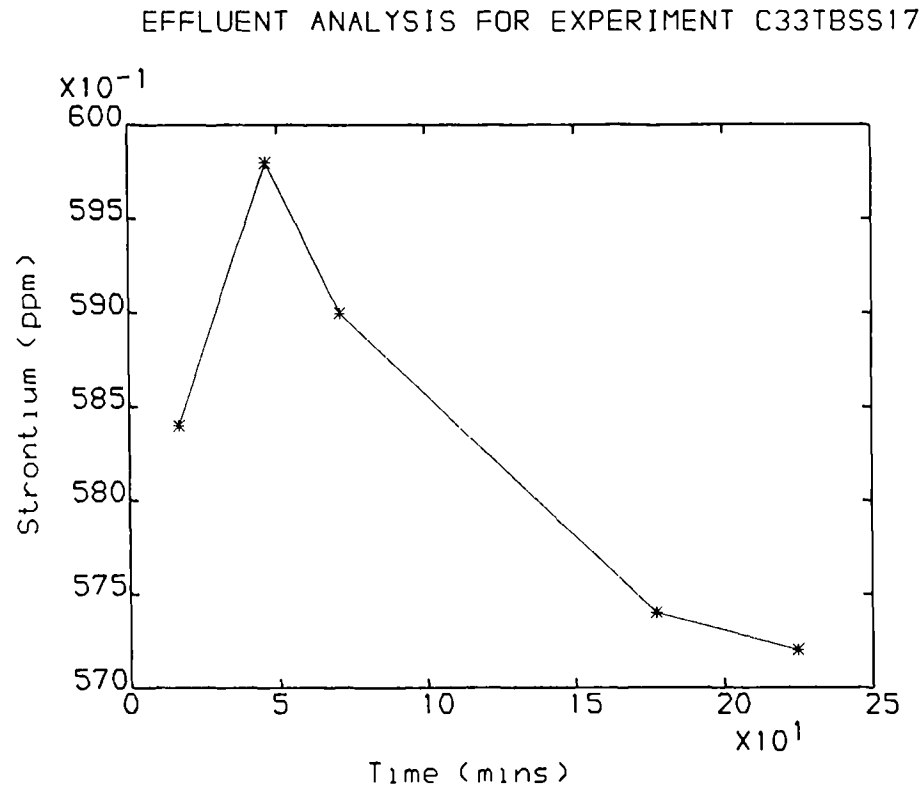

Figure 7.55 Strontium ion concentration change in the brine effluents during a core test

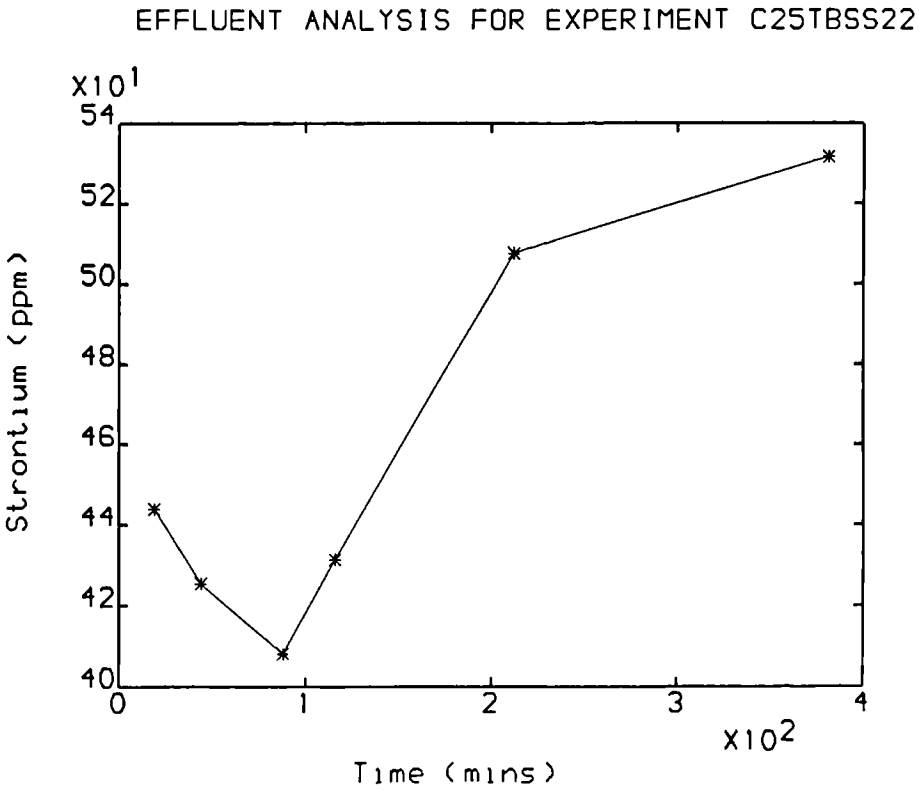

Figure 7.56 Strontium ion concentration change in the brine effluents during a core test

trend as shown in figures from (7.52) to (7.54). It implies that the $BaSO_4$ scaling rate accelerated gradually as the core flow test proceeded. Contrary to this trend, the permeability decline rate usually was decreasing gradually during a core test, as discussed in subsections (7.3.1) and (7.3.3). The logical conclusion is that the scale precipitation was increasing during the test, but due to the increasing flow shearing forces in the flow path caused by the scale build-up, less and less scale deposition or scaling crystal growth occurred in the flow stream and most of the precipitation was diverted to the pore space bypassed or less affected by the brine flow. This resulted in the permeability decline rate not increasing but decreasing during a test. The variation in Sr^{2+} ion concentration change in the brine effluents showed no clear trend during a core test and between the different core flow tests. This may be the true reflection of the $SrSO_4$ precipitation in the core or may be due to the inaccurate sampling and dilution procedures. It is not possible therefore to know precisely the $SrSO_4$ precipitation rate change during a core from the present investigation. More formation damage experiments are suggested with improved brine effluent sampling and dilution methods, as recommended in chapter 9.

7.5 TEMPERATURE EFFECT ON THE SOLID SOLUTION SCALE FORMATION AND THE RESULTED FORMATION DAMAGE

The results obtained from the scale formation study at both 20°C and 70°C so far have been discussed and the findings are presented in chapter 6 and in the early part of this chapter. The temperature varies at different locations and during the production history in oilfields, hence, it is important to understand the influence of temperature change on the barium sulphate and strontium sulphate scale formation and the permeability damage resulting from the scale formation. In this section, the differences in the scale nature, scaling mechanism and permeability damage trend caused by the experimental temperature change from 20°C to 70°C are analysed and how the temperature change affects the $(Ba,Sr)SO_4$ scale formation is suggested.

7.5.1 Temperature Effect on the Morphology of the Solid Solution Crystals

The morphology change of the $(Ba,Sr)SO_4$ scaling crystals are apparent as a result of increasing the precipitation temperature from 20°C to 70°C, as clearly seen from the SEM electromicrographs of the crystals grown at the two different temperatures both in the static solutions and in the cores. In general, the crystals precipitated at the elevated temperature are more perfect and have fewer crystal faces, in accordance with the literature. [26,33,34]

Nancollas et al. [21,38,80,82-84] found that $BaSO_4$ and $SrSO_4$ crystal growths were both surface reaction controlled. As the temperature is raised, the $BaSO_4$ supersaturation reduced in the same brine and the surface reaction intensified, hence, the perfection of the $BaSO_4$ dominant solid solution crystals was more likely than at a lower temperature. In the $SrSO_4$ predominant solid solution crystal growth, the $SrSO_4$ supersaturation increase resulting from the temperature rise and its effect of causing crystals less perfect was probably overcome by the increase in the surface reaction and its role of improving crystal perfection. Thus, the $(Ba,Sr)SO_4$ scaling crystals grown from the brines of Sr/Ba ratios ranging from 0.1 to 1000 appear always more perfect at a higher temperature.

The change in crystal habits also resulted in a change in the scaling crystal orientation in the rock pore space, as demonstrated from comparing figures (6.31) and (6.37) to figures (7.14) and (7.17). The crystals formed at 20°C tended to protrude into the flow stream in the rock pores while the crystals precipitated at 70°C were usually prone on the pore surface.

The other difference of the crystals formed at the two different temperatures is that the dislocations were more often found on the crystals formed at the elevated temperature, as shown in the SEM view in figure (7.13), (7.19) and (7.20). The increase in the surface reaction at the higher temperature was the possible cause.

The amount of the scale deposition which occurred in the pores appears unaffected

by the temperature change, judging from the SEM views of the 20°C and 70°C core samples. From the solubility or supersaturation point of view, the increase in temperature should lead to less $BaSO_4$ precipitation and more $SrSO_4$ precipitation. But the scale formation in a core under the flow influence was affected by factors other than supersaturation but also the precipitation kinetics, hydrodynamic forces and the interaction between the rock surface and the scaling crystals, etc. Owing to such complexity, the explanation about the scale abundance at the different temperatures is not straightforward.

7.5.2 Temperature Effect on Permeability Decline

Because insufficient core tests were performed and the cores used at both of the temperatures were not often of similar initial permeabilities, no conclusive trend has been found on the temperature effect on the permeability - brine injection time curves. The basic profile of the k - t curve did not alter from 20°C to 70°C tests. However, by comparing the dk/dt - t curves in figures (7.40) through (7.45) from 70°C tests to those shown in figures (6.63) through (6.68) from 20°C, it is apparent that most of the dk/dt - t curves at 70°C are type 1 (dk/dt steadily declining throughout a core test) and the 70°C type curves were usually steeper than those type 1 curves at 20°C. In addition, the $(dk/dt)_i/k_i$ values at 70°C were normally higher than the $(dk/dt)_i/k_i$ values at 20°C, as discussed in subsection (7.3.4). Both $(dk/dt)_i/k_i$ values and the dk/dt - t curves indicate that the core permeability declined faster at 70°C than it did at 20°C when injected with the same brine under the similar experimental conditions. This is attributed to a higher scaling rate at 70°C.

As pointed out in subsection (6.4.1) of chapter 6, pattern 2 sectional permeability decline distribution along a core length, i.e, the second section of a core having the highest permeability reduction, was more likely to occur at 20°C when using higher Sr/Ba ratio brines(Sr/Ba=100 or 1000), due to the retardation caused by a slower $SrSO_4$ precipitation. Such a conclusion was found not entirely true when the experimental

temperature was raised to 70°C, as discussed in section (7.3.2). It is believed that the precipitation retardation in the higher Sr/Ba ratio brines at the elevated temperature was overwhelmed by the increase in both $SrSO_4$ supersaturation and its scaling rate. This was supported by the finding that the trend of the variation in the extent of permeability reduction as a result of injecting different brines into the cores was different between the two experimental temperatures. At 20°C, the brines, according to their effects on the damage to permeability from large to small, were in the sequence: BSS3(Sr/Ba=1000) > BSS0(Sr/Ba=0.1) ≥ BSS1(Sr/Ba= 1.0) ≥ BSS2(Sr/Ba=100) while the sequence at 70°C was: BSS3>BSS2>BSS0≥BSS1. This means whereas brine BSS2, which had a higher Sr/Ba ratio than BSS0 and BSS1, caused the least damage to the core permeability among the four brines at 20°C, it resulted in heavier permeability reduction than brines BSS0 and BSS1 at 70°C. This is likely due to the increasing $SrSO_4$ precipitation and relatively less $BaSO_4$ scaling at a higher temperature.

7.6 FORMATION DAMAGE DUE TO MIXING NORTH SEA WATER AND THE FORMATION WATERS

The investigation of the $(Ba,Sr)SO_4$ scale formation was carried out using the simple brines to systematically look at the various aspects of the sulphate solid solution scaling and its effect on the rock permeability and the results were already presented and discussed in chapter 6 and the previous sections of this chapter. As a step forward, the investigation of the $(Ba,Sr)SO_4$ scaling problem caused by mixing North Sea water with Forties formation water and with South Brae formation water was followed so as to give a more realistic view of the sulphate scale occurrence in offshore operations. These fields were chosen as examples to simulate a range of scaling tendencies in the North Sea. Of the two fields, Forties is found to have medium scaling problems and severe scaling tendency is observed when North Sea water mixes with South Brae formation water.

The sea water and the formation waters were synthesised in the laboratory by adding

the full ion components into distilled water. Their compositions and compositional characteristics are given in table (5.3) and table (5.4) in chapter 5. In the tables and figures, for convenience, the equal volume mixed North Sea water and Forties formation water is referred to as water 1 and the equal volume mixed North Sea water and South Brae formation water is referred to as water 2.

A number of differences can be noticed when the full component field waters are compared to the simple brines listed in tables (5.1) and (5.2) in chapter 5. First, other ions besides sodium, chloride and the scaling ions were present in the field waters. Secondly, the 50:50 mixed sea water with either one of the formation waters gave higher solution ionic strengths than that in the simple brines. Thirdly, the brine made of 50:50 mixed sea water and South Brae water (water 2) was far more supersaturated with $BaSO_4$ than any of the simple brines. Also the Sr/Ba ratios and the $(Sr+Ba)/SO_4$ ratios in the mixed full component brines were different from those in the simple brines. Because of the involvement of the other ions such as Mg^{2+} and HCO_3^- ions and the change in brine characteristics, it was interesting to know how the $(Ba,Sr)SO_4$ scaling take place and how the rock permeability was impaired as a result by mixing the full component brines in the porous media.

In the next subsections, analysis is applied to the results, similar to that used in the simple brines. The nature of scale, the scaling mechanism and the scaling effect on the permeability and porosity resulting from using the field waters are studied by means of SEM technique, the brine effluent analysis and the permeability curve analysis.

7.6.1 SEM Study of the Scaling Crystals and the Scaled Core Samples

The sulphate solid solution crystals precipitated from the static solution of mixed sea water and Forties water (water 1) show uniform crystal habit and size, as seen in figure (7.57). The crystals were the 'desert roses', which is one of the typical barite crystal forms. The average crystal size was about 15μm. Each 'desert rose' was actually made of a number of tabular crystals, probably as a result of continuous secondary nucleation

and growth of the smaller crystals on the larger ones. Uniform $(Ba,Sr)SO_4$ crystals were also formed when North Sea water mixed with South Brae water (water 2) in the beaker test, as shown in figure (7.58). The crystals show entirely different habit from that precipitated from mixing sea water and Forties water. Each of the crystals looks like a butterfly made of 4 pieces of tabular, tree leaf like crystals. The typical crystal size (length) was about 40μm, 2 - 3 times larger than the 'desert rose'. Comparing these two forms of crystals with the crystals grown in the simple brines seen in figures (7.1) through (7.10), it is remarkable that the crystals precipitated from the full component waters preserve totally different habits from the simple brine produced crystals. The crystals precipitated from mixing the sea water and formation waters appear much more sophisticated, suggesting that the presence of the other ions in the brines had complicated the process of $(Ba,Sr)SO_4$ crystal growth.

Consistent to the previous findings from the simple brine experiments on the flow effect on crystal habits, the SEM views of the scaled core samples concurrently injected with the sea water and either of the two formation waters show that the basic crystal forms were not influenced by the flow in the porous media, as illustrated in figures (7.59) through (7.64). This also indicates that the mechanism of the solid solution scaling crystal growth was not changed from the static condition to the dynamic condition. The 'desert roses' crystals were less regular and have variation from one location to the other in a core as the possible result of the effects of flow or rock property. The crystals formed from mixing the sea water and South Brae water in the cores were often found fragmented, as seen in figures (7.63) and (7.64). The scaling crystals were abundant in the rock pores in the front section of a core, particularly the crystals deposited from mixing the sea water and the South Brae water. Again the scaling sites appear arbitrary, the rock grains, the quartz overgrowth and the feldspars all acted as the likely scaling crystal growth sites.

7.6.2 Analysis of the Brine Effluents from Core Flow

Brine effluent samples were taken only during one of the core tests injected with the

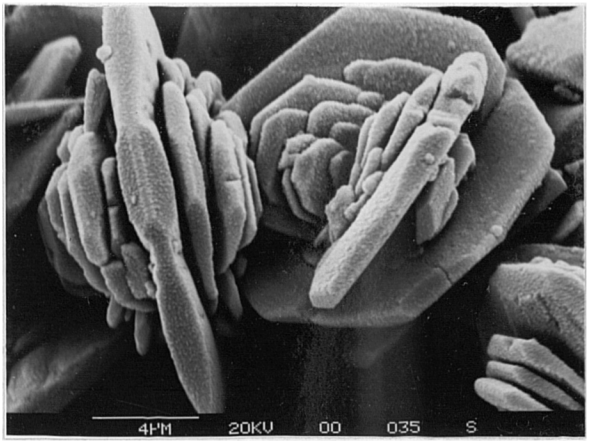

Figure 7.57 Crystals grown from 50:50 mixed North sea water and Forties water under static condition, 'desert roses' crystals

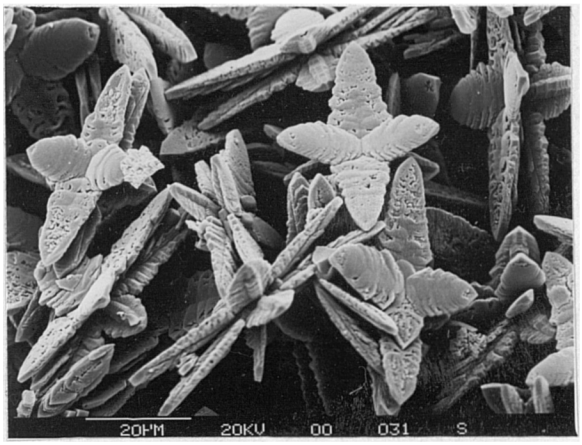

Figure 7.58 Crystals grown from 50:50 mixed North sea water and South Brae water under static condition, 'tree leaves' crystals

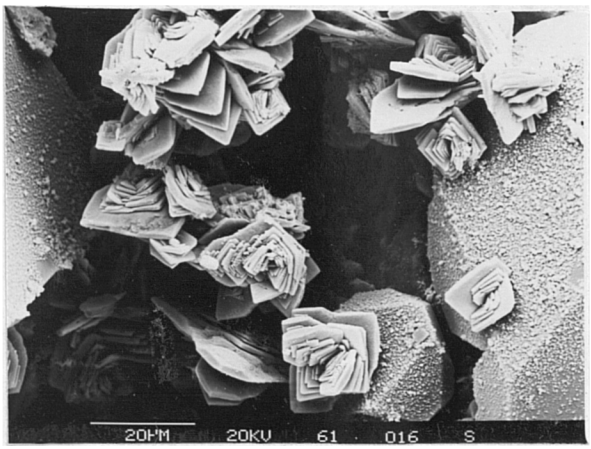

Figure 7.59 Scaling crystals formed in a core injected North sea water and Forties water

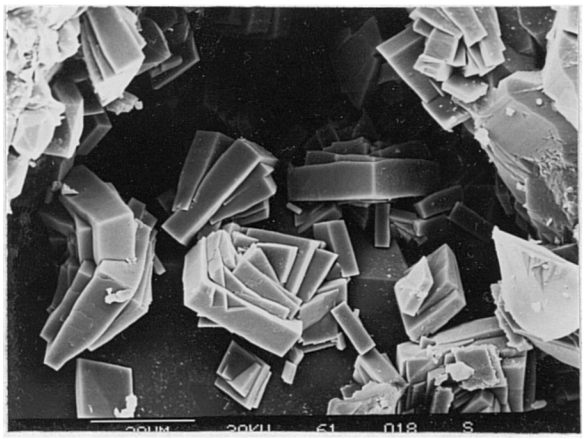

Figure 7.60 Scaling crystals formed in a core injected North sea water and Forties water

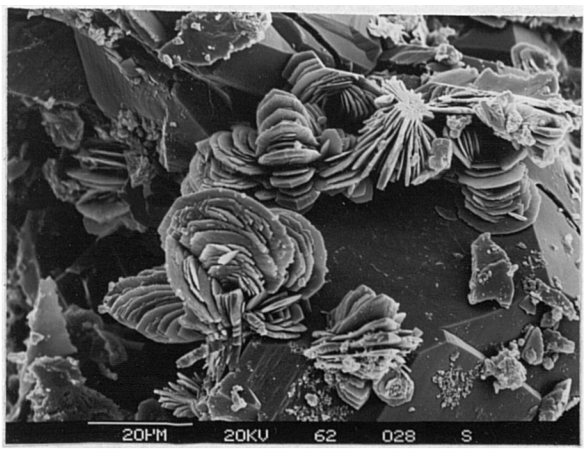

Figure 7.61 Scaling crystals formed in a core injected North sea water and Forties water

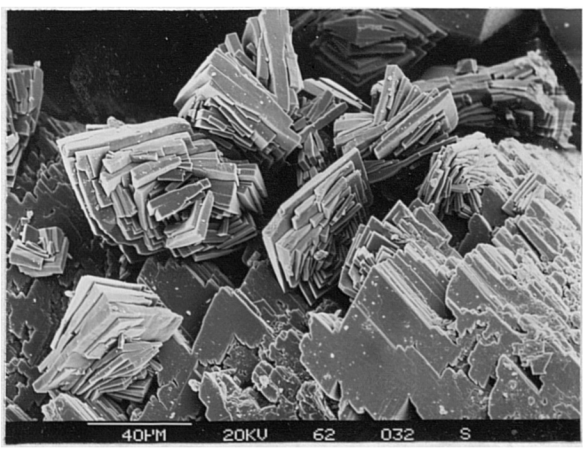

Figure 7.62 Scaling crystals formed in a core injected North sea water and Forties water

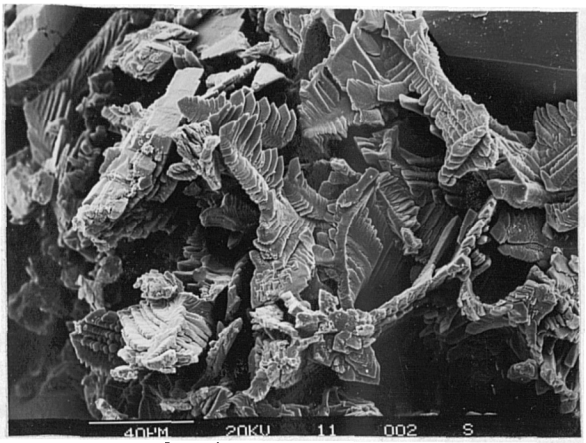

Figure 7.63 Scaling crystals formed in a core injected North sea water and South Brae water

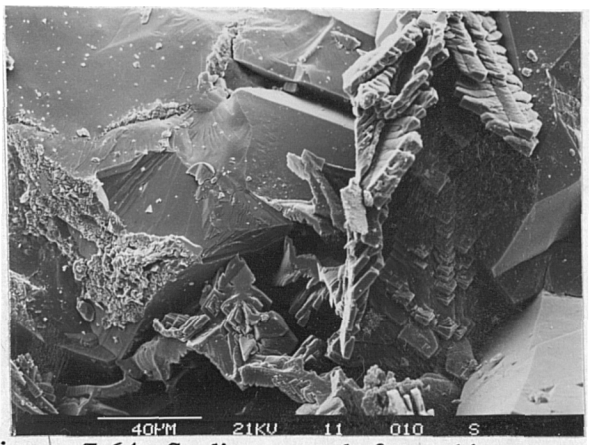

Figure 7.64 Scaling crystals formed in a core injected North sea water and South Brae water

full component brines. The scaling ion concentration changes from the initial brine to its effluent from the core are presented in table (7.3) and the changing trend of ion concentrations in the effluents during the scale formation test is shown in figures (7.65) and (7.66). The barium ion concentration shows a steadily decline during the scale formation test, the same trend as observed in the simple brine core tests. The Sr^{2+} concentration change during brine injection did not show a general trend, which is also the case in the simple brine core tests and the cause is speculated in section 7.4.

7.6.3 Analysis of Permeability Decline Pattern

A large degree of permeability damage was caused by injecting the incompatible field brines into the Clashach cores. 80% of the initial core permeability reduction was the result of two core flow tests injected with sea water and Forties water (water 1) and a more severe 93% of the initial permeability damage to the core scaled with the solid solution by injecting sea water and South Brae water (water 2). The permeability losses and porosity reductions occurred in these tests are listed in table (7.1). The curves of the overall core permeability change during these tests are typical concave shape, comparable with the k - t curves from some of the tests with the simple brines, as shown in figures (7.67) through (7.69). The discussion of the concave curves are given in subsections (6.4.1) and (7.3.1).

The core section permeability decline curves resulting from injecting the mixed field waters are displayed in figures (7.70), (7.71) and (7.72). The sectional permeability decline distribution along the length of a core as the $(Ba,Sr)SO_4$ scaling in a core by mixing the sea water and Forties water generally conformed to pattern 1, i.e, the extent of damage within section 1 of a core was the largest and followed by the damage within section 2. On the other hand, the section permeability decline distribution produced from injecting sea water and South Brae water was similar to pattern 2, i.e, highest damage in section 2 and followed by the damage in section 1 of a core. This again proves that the retardation theory, which was believed to be true at 20°C, could not explain the change in the pattern of the sectional permeability decline curves because the

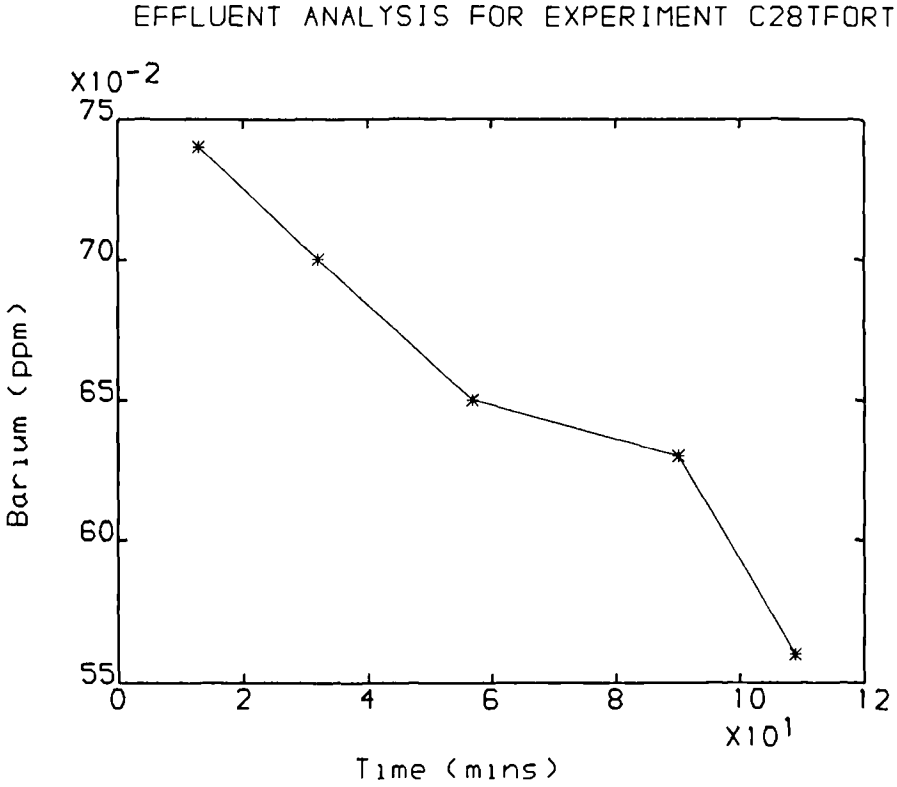

Figure 7.65 Barium ion concentration change in the brine effluents during a core test injected with North sea water and Forties water

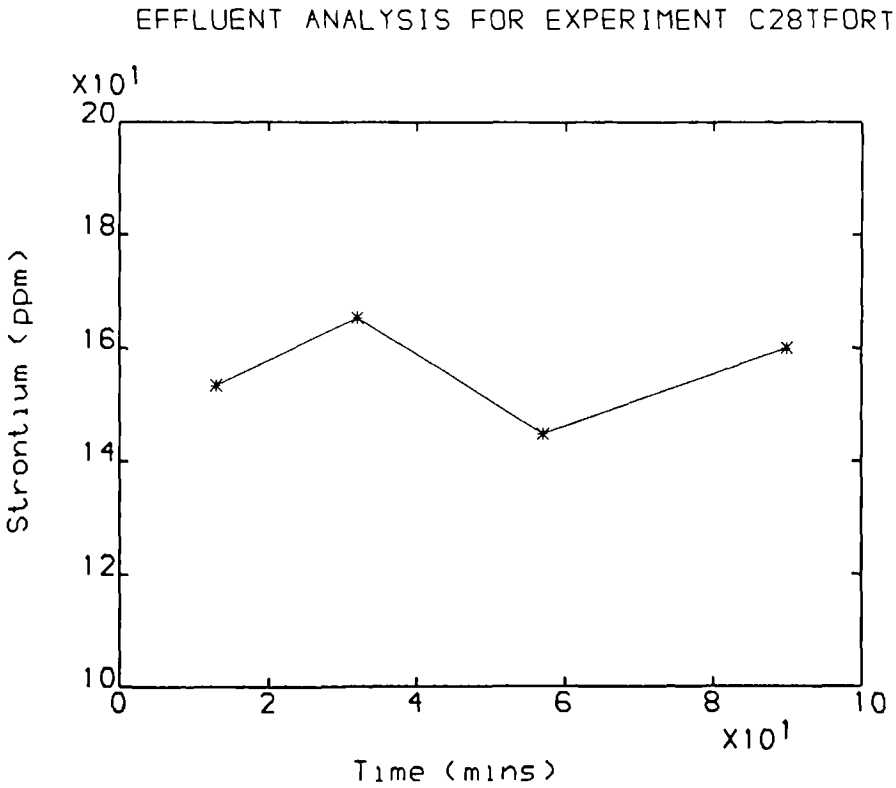

Figure 7.66 Strontium ion concentration change in the brine effluents during a core test injected with North sea water and Forties water

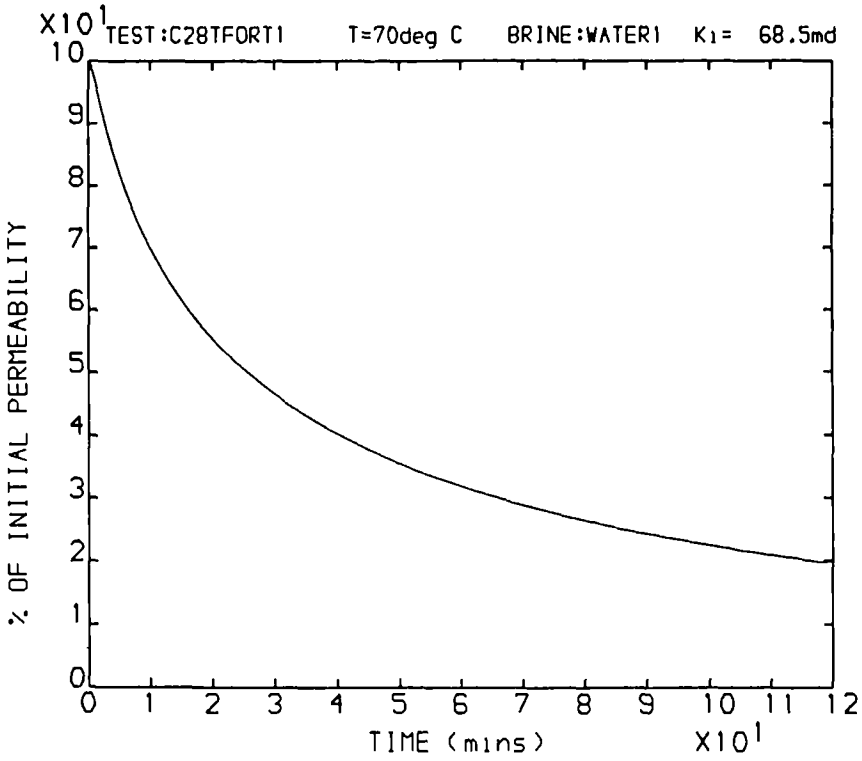

Figure 7.67 Core overall permeability decline due to scale formation by injecting North sea water and Forties water

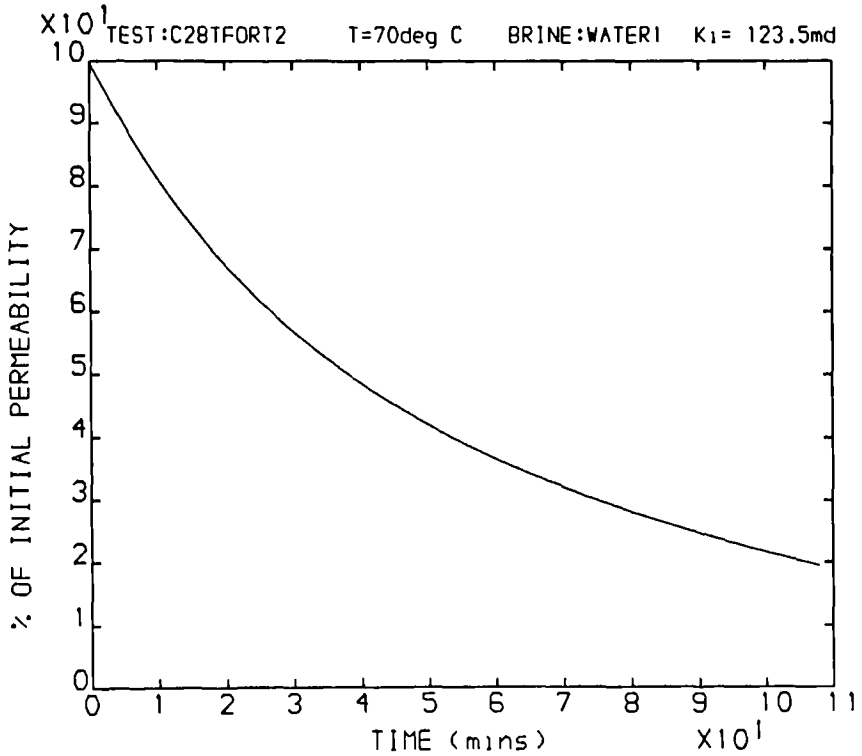

Figure 7.68 Core overall permeability decline due to scale formation by injecting North sea water and Forties water

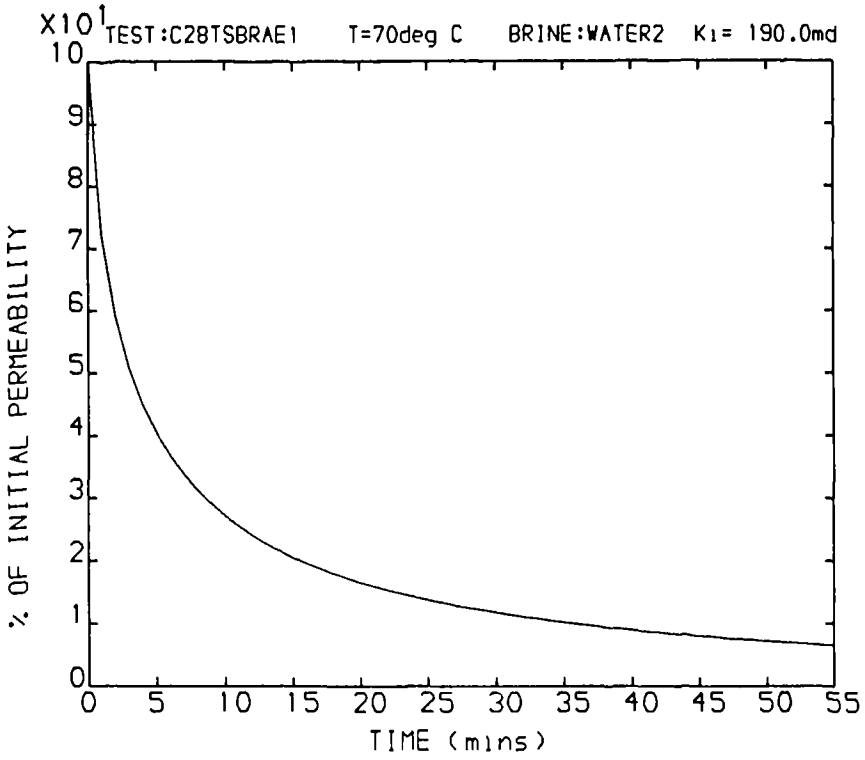

Figure 7.69 Core overall permeability decline due to scale formation by injecting North sea water and South Brae water

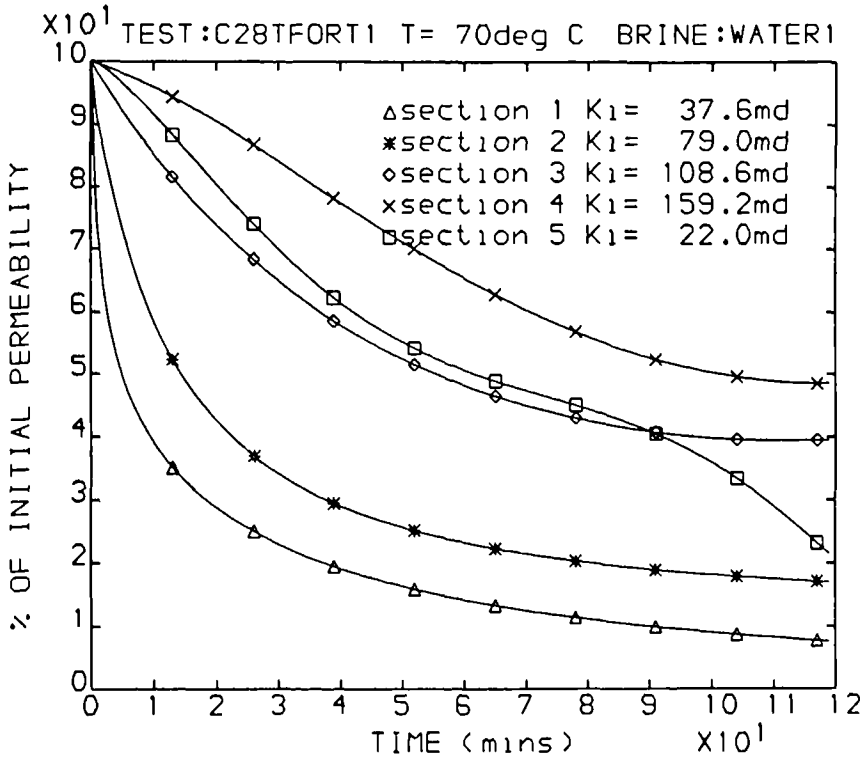

Figure 7.70 Section permeability change during injecting North sea water and Forties water

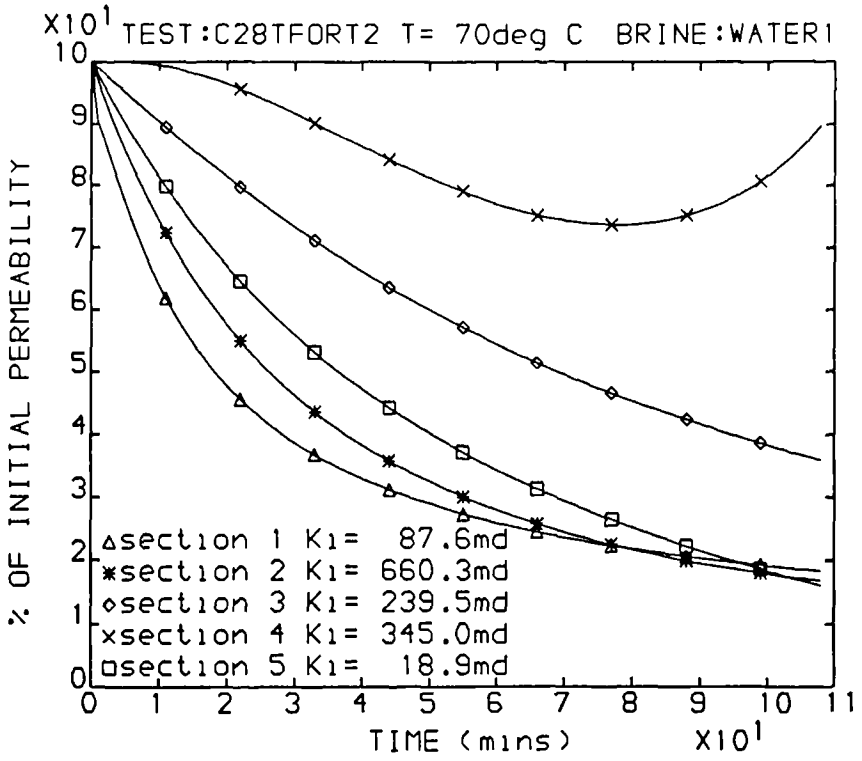

Figure 7.71 Section permeability change during injecting North sea water and Forties water

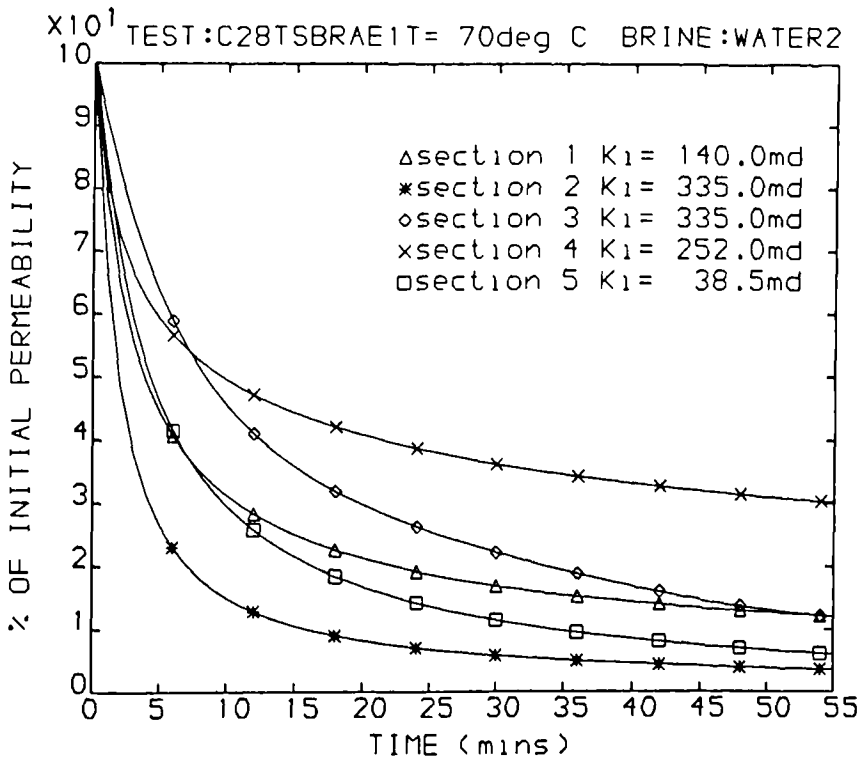

Figure 7.72 Section permeability change during injecting North sea water and South Brae water

Sr/Ba ratio in the mixed sea water and South Brae water was higher than the ratio in mixed sea water and Forties water. The detailed discussion about the retardation theory is referred to sections (7.3.2) and (6.4.1). It is interesting to note that from all the scale formation tests by injecting the mixed field waters, the extent of permeability damage in the last section of the cores was medium, lower than the reductions in the core front sections but higher than the reductions in the middle sections. This was considered to be the result of considerably lower initial permeability in the last section of a core than the permeabilities in the rest sections, caused by fines downstream migration during line pressure stabilisation period before both brines were switched on to mix in the core.

The dk/dt - t curves from all the core tests with the full component brines all show the same trend of steady decline in the permeability decline rate during the cores, as demonstrated in figures (7.73), (7.74) and (7.75), which had been found to be the general case in the elevated temperature core tests with the simple brines.

The numerical characteristics of the permeability curves, i.e, $(dk/dt)_i$, $(dk/dt)_m$, $(dk/dt)_i/k_i$, $(dk/dt)_m/k_i$, $t_{1/2}$ and t_c, are summed up in table (7.2). Again, it shows higher $(dk/dt)_i/k_i$ or $(dk/dt)_m/k_i$ led to shorter $t_{1/2}$ and t_c. Comparing these values with those obtained from the simple brine flow tests, it is clear that mixing of North Sea water and South Brae brine produced the worst $(Ba,Sr)SO_4$ scale deposition.

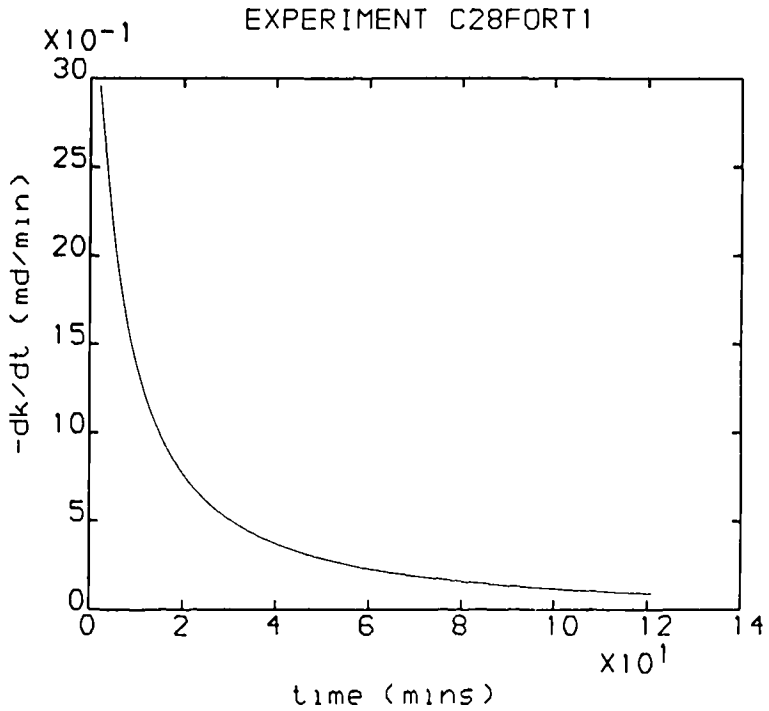

Figure 7.73 Core permeability decline rate curve, core injected with North sea water and Forties water

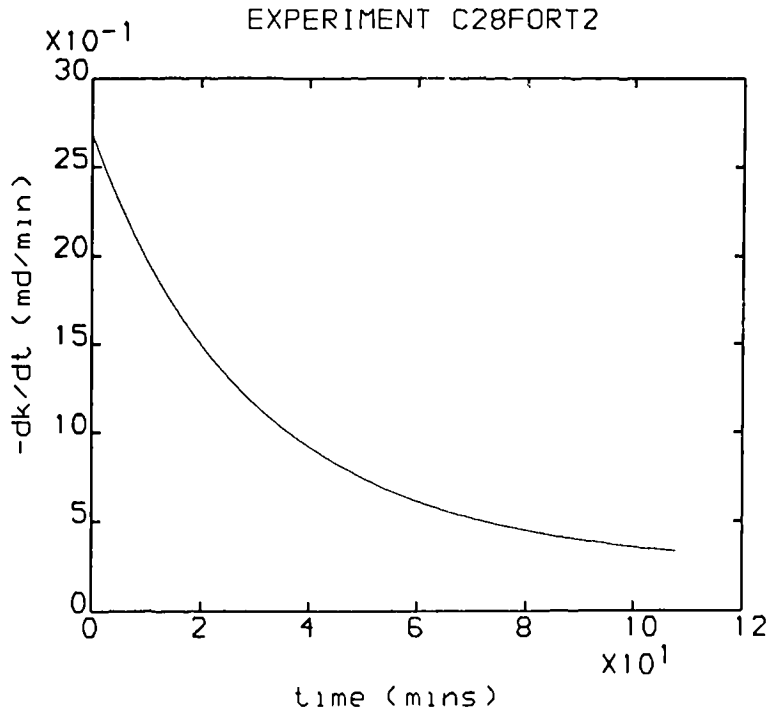

Figure 7.74 Core permeability decline rate curve, core injected with North sea water and Forties water

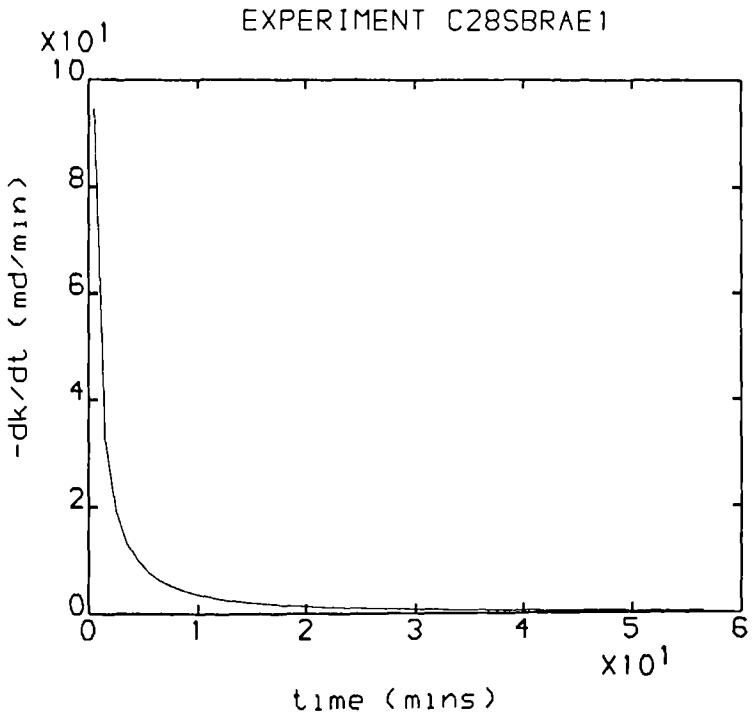

Figure 7.75 Core permeability decline rate curve, core injected with North sea water and South Brae water

CHAPTER 8

CONCLUSIONS

8.1 INTRODUCTION

This PhD study involved two areas of work related to sulphate scaling problems: computer modelling of the scaling tendencies of barium, strontium and calcium sulphates in the brines, and a laboratory investigation of the formation damage arising from the $(Ba,Sr)SO_4$ solid solution scale formation in the porous media. The two research areas seems independent to each other but in fact they are related in two aspects: the scale prediction model was used in the formation damage experiments to formulate the brines by predicting the sulphate supersaturations and potential precipitations and to help examine the brine compositional characteristics before and after a core test, and both the prediction model and the experimental results can be applied to the construction of a reservoir simulation model for the scaling damage. The description of developing the sulphate scaling tendency prediction model was presented in chapter 2 and chapter 3, and the results obtained from the experimental study of the solid solution scaling and the discussions of the results were given in chapters 5, 6 and 7. The conclusions are presented in this chapter from the description, analyses and discussion presented in the previous chapters.

8.2 THE MODEL FOR PREDICTING SULPHATE SCALING TENDENCY

A scaling tendency prediction model has been developed for predicting the supersaturations and precipitations of barium sulphate, strontium sulphate, gypsum and anhydrite in the oilfield waters as a result of commingling of incompatible waters as well as temperature and pressure changes. The model is capable of predicting the scaling tendencies of the sulphates at various brine compositions, temperatures and pressures

covering oilfield operation conditions.

The simultaneous coprecipitation of more than one of the sulphates, which is the common phenomenon in oilfield scale occurrence, is reflected in the model by taking the interactions among the precipitations of different sulphates into account.

An iterative process is used in the model to ensure that the precipitation - dissolution equilibria existing between the scaling ions in the aqueous solution and their solid precipitates have been established in the scaling prediction.

This model has proved successful in predicting the sulphate scaling tendencies in both the single brines and mixed incompatible waters at various temperatures and pressures.

The model was constructed using a thermodynamic sulphate solubility prediction model which was developed from the application of the Pitzer's equation for electrolyte mean activity coefficient.

It is believed that this study is the first to extend the Pitzer's approach to calculate the solubilities of $BaSO_4$, $SrSO_4$, gypsum and anhydrite in the aqueous solutions at the temperatures other than the ambient temperature. The sulphate solubilities predicted from this solubility model are in reasonably good agreement with the measured data.

As a result of adopting the Pitzer's equation, the sulphate solubility prediction model and the scaling tendency prediction model are theoretically more consistent, less empirical and more comprehensive in their applications, as compared to the previous models.

8.3 THE LABORATORY INVESTIGATION OF FORMATION DAMAGE DUE TO SULPHATE SOLID SOLUTION FORMATION

The $(Ba,Sr)SO_4$ solid solution scale precipitation in the porous media was initiated from the heterogeneous nucleation and followed by rapid scaling ion precipitation and crystal growth. The scaling crystal growth took place on the rock pore substrates. It was found that $BaSO_4$ had a higher precipitation rate than $SrSO_4$ in forming the solid solution scale, resulting in a higher Ba/Sr ratio in the formed scale than the ratio in the

scale-forming brine. It appears that the solid solution precipitation did not have preference to the sites on the rock pore surfaces and it shows no evidence suggesting that the scaling crystals had preference to the rock pores or pore throats for growth. The most abundant scale was seen in the front section of a core and the scale abundance was significantly reduced into the depth of the core. Although the scaling crystals deposited in the rock pores were less regular in shape and more variable in size, the basic morphology of the solid solution crystals were not altered from growing in the static bulk solutions to precipitating in the rock pores under flow influence. The crystals precipitated in the rock pores had the size ranging from 5μm to 50μm. The largest crystals precipitated from flow in the cores were usually larger that those grown from the same brines but under static condition.

Permeability loss caused by the $(Ba,Sr)SO_4$ scale formation in the cores ranged from less than 5% to more than 95% of the initial permeability, depending on the brine composition, core initial permeability and brine injection period, etc. The concave shape of the permeability - time curves was the common feature of the majority of the core flow tests. The permeability decline distribution along the length of a core during a formation damage experiment showed that the front section of the core suffered considerably more severe permeability reduction as compared with the rear section. In some cases, the second section from the front of a core(about 10 mm into the core) had the largest extent of the permeability reduction, resulting from the solid solution scale formation.

Heavy loss of core permeability was caused by concurrently injecting either North Sea water and Forties formation water or the sea water and South Brae formation water through a core, which underlines the severity of the potential formation damage due to commingling incompatible injection seawater with the formation water in some North Sea reservoirs. The profiles of the permeability decline curves produced from injecting the field waters through the cores were typical concave curves observed in most of the flow tests with the simple brines. On the other hand, entirely different $(Ba,Sr)SO_4$ scaling crystals were precipitated from mixing the sea water and the formation waters, in contrast to the crystals grown in the simple brines.

Comparing the permeability reductions with the corresponding porosity damages resulting from the scaling in the cores, no clear and consistent correlation between the two aspects of the formation damage was revealed in this study, nor any consistent relation between the permeability loss and the scale quantity deposited in a core. This indicates that the scale volume or quantity was not the sole determining factor on the permeability damage.

A few influencing factors on the $(Ba,Sr)SO_4$ scale formation and the formation damage were examined. Temperature change had a remarkable effect on the scaling crystal morphology and a higher scaling rate was observed at the elevated temperature. The importance of $SrSO_4$ scaling in forming the $(Ba,Sr)SO_4$ solid solution scale at a higher temperature increased because of the temperature effect on $BaSO_4$ and $SrSO_4$ solubilities and the precipitation rates. A significant increase in the amount of scale deposition and in the permeability damage was observed as the brine supersaturation was doubled. Alteration of Sr/Ba molar ratio in the simple brine from 0.1, 1.0, 100 to 1000 caused transition in the solid solution crystal morphology from tabular, prismatic to oval polyhedrons but it was less evident in changing the extent of core permeability reduction, unless the Sr/Ba ratio had reached 1000. In general, a lower initial permeability core suffered more damage in respect to its initial permeability.

The many questions raised from the experiments demonstrate that there is still much work to be done in this subject area, to understand and predict the complex nature of oilfield scale deposition.

CHAPTER 9

RECOMMENDATIONS FOR FUTURE WORK

9.1 INTRODUCTION

Chapters 2, 3, 5, 6, and 7 of this thesis reported the work carried out in this study and the conclusions from the study were summarised in chapter 8. The two goals set for this PhD programme, i.e, to develop an improved sulphate scaling tendency prediction model and to have insight into the formation damage arising from the $(Ba,Sr)SO_4$ scale formation, have so far been realised. However, it is considered, from the research experience and examination of the experimental results obtained from the present study, that it is far from the completion for the investigation of the barium sulphate related scale formation and its formation damage impact and there are still a number of interesting aspects yet to look at. As for the scaling tendency prediction, the improvement and further development on the current model are considered possible and worthwhile. The recommendations for further work regarding both the scaling prediction and the laboratory investigation of formation damage resulting from the sulphate scaling are presented in the next two sections.

9.2 PREDICTION OF OILFIELD SCALE OCCURRENCE

The specific ion effects on barium sulphate solubility are unable to be reflected in the current sulphate solubility and scale prediction model because of insufficient solubility data to make solubility correlations in aqueous systems other than in sodium chloride solutions. Due to data shortage or inaccuracy, the quality of solubility prediction for other sulphates, particularly strontium sulphate, is also affected. These shortcomings can be overcome if more extensive and reliable sulphate solubility data become available in the future. Some literature reports [8,38] suggested that the solubilities of barium

sulphate and strontium sulphate in their solid solution differ from their solubilities behaved when the two sulphates are in separate solid phase of precipitation, that is, the solid solution formation has altered the solubility behaviour of the two sulphates. Again, due to a lack of solubility data on the barium sulphate and strontium sulphate in the solid solution, the molecular interaction between $BaSO_4$ and $SrSO_4$ and the effect on their solubilities in the solid solution was not identified and subsequently ignored in the present model for scaling tendency prediction. Nevertheless, it is felt that the relation between the $BaSO_4$ and $SrSO_4$ solubilities and their ratio in the solid solution may be established from the newly emerged data in the future and such a relation can be then incorporated into the present model to improve the prediction of the $(Ba,Sr)SO_4$ scale formation.

The present model is restricted to the sulphate scale prediction. In the oilfield operations, calcium carbonate scale is also one of the common scales. Hence, it is desirable if this model can be extended to comprehend the calcium carbonate scaling tendency prediction. The incorporation of $CaCO_3$ scale prediction should not be difficult, provided a reliable solubility prediction model for $CaCO_3$ covering oilfield brines and conditions has been developed. Unlike the sulphates, the precipitation - dissolution equilibrium between $CaCO_3$ in the aqueous solution and its solid precipitate is determined not only by the brine composition, temperature and pressure but also by the solution pH value and CO_2 pressure. Therefore, more extensive solubility data are needed and more effort has to be made to develop a $CaCO_3$ solubility prediction model, which was not achieved in this study because of time limitation.

9.3 LABORATORY INVESTIGATION OF THE FORMATION DAMAGE DUE TO SCALING

Most of the scale formation experiments in this study were carried out using the simple brines in order to identify the different factors affecting the $(Ba,Sr)SO_4$ scale

formation and its damage to rock permeability. It was found from the study that the nature of the scale precipitated from mixing North Sea water and the offshore formation waters differed remarkably from that precipitated from the simple brines, presumably because of the presence of other ion species, e.g, Ca^{2+}, Mg^{2+}, K^{+} and HCO_3^{-} etc. To have a closer simulation of the reservoir sulphate scaling, it is considered that the future study on $BaSO_4$ related scale formation and the formation damage due to the scaling should be concentrated on using the full component North Sea water and the North Sea offshore reservoir waters.

So far, substantial knowledge on sulphate scale formation and resulting formation damage has been gathered from this study and Goulding's work[42], but some quantitative relations have to be identified for the purpose of reservoir modelling of the scale formation. In future work, it is recommended that the main objective is to clarify three relations: between the brine sulphate supersaturation and the amount of scale precipitation, between the brine supersaturation and the permeability decline rate, and between the extent of permeability damage and the quantity of scale deposited in a core.

In this study, the flowrate used throughout all the flow tests was 15 ml/min. and the volume mixing ratio between two opposite brines was 50:50. Only ambient pressure was presented in the formation damage tests and oil was absent in the rock cores. Owing to the importance of flowrate, brine mixing ratio, pressure and oil presence to the scale formation in a reservoir while not sufficiently represented in the present laboratory investigation, some changes concerning these four aspects are recommended for the future study.

First, a very low flowrate($\leq$1.0 ml/min) should be used in some of the core tests to provide a comparison with the results from 15 ml/min tests and to see if the flowrate change has a noticeable effect on the sulphate scale formation and the permeability decline trend. Second, a larger portion of formation water(higher flowrate) and a relatively smaller portion of sea water(lower flowrate) should be mixed in the core flow, as found from the scale prediction model that the scale precipitation was the most severe when sea water ratio to formation water ratio was small. Thirdly, a few tests may be carried out with back pressure to raise the pressure inside a core during a formation damage test to

investigate the pressure effect on scale formation. Lastly, the cores with residual oil saturation should be used in some of the formation damage experiments to compare with the experiments without oil presence. It is suggested that the new changes proposed above should be phased in during the future experiments, avoiding complication of identifying the influencing factors.

It is believed there is room for improvement on the present experimental technique. The rock cores where possible should be preselected based on their initial permeabilities. For example, the cores of similar initial permeabilities may be used in the tests with the same brine under the same experimental conditions to test the repeatability, or the cores with rather different initial permeabilities may be tested to observe the effect of the core initial permeability on scale formation and permeability.

Another modification is recommended for the brine effluent sampling and analysis because of the inconsistence of the water analysis results using the present sampling and dilution methods. It is believed that the brine effluent analysis is an important means to study the scaling mechanism, in particular, the scaling rate.

Regrettably, the ion composition of the scale crystals formed in the experiments was not quantitatively analysed, due to the difficulty with EDAX (Energy Dispersive X-ray Analysis) which so far has not been solved. The morphological study of solid solution scale would be improved considerably if the scale composition can be determined by EDAX or by other means, for example, the laser spectrometer.

In addition, it is interesting to run a few core tests with the full component field waters but excluding Sr^{2+} ions in order to understand the role of Sr^{2+} ions on the solid solution scale formation.

APPENDIX 2.1

THE LEAST SQUARES METHOD

The least squares method is one of the standard methods for modelling experimental data and its introduction can be found in most engineering mathematics textbooks. A description is given for the convenience of reference. The principle of the method is to minimise the deviation of the reproduced data from the experimental data or any measured data. First, a model or a function with a number of parameters is supposed, then the least squares method is to find the parameters to give the optimal fitting of the measured data. In the case of a polynomial function, as used in this study to correlate sulphate solubility with ion concentrations, it may be demonstrated below.

Assume we are fitting m measured data points and the measured data y_i(e.g, solubility) is a function of variables $x_{1,i}$, $x_{2,i}$,...$x_{n,i}$(e.g, the concentrations of Na, Cl ions, etc) in a polynomial form of n terms. The subscript i represents the ith data point and i = 1, m. The n parameters in the polynomial are a_1,a_2...a_n in correspondence with variables $x_{1,i}$, $x_{2,i}$,...$x_{n,i}$. The least squares method is to find the n parameters by minimising the calculated data from the measured. The function may be expressed as

$$y_i = a_1 x_{1,i} + a_2 x_{2,i} + ... a_n x_{n,i} \qquad i=1, m \qquad (A.1)$$

To minimise the deviation of y_i calculated from equation (A.1) from the measured data, that is, to minimise S,

$$S = \sum_{i=1}^{m} [y_i - (a_1 x_{1,i} + a_2 x_{2,i} + ... a_n x_{n,i})]^2 \qquad (A.2)$$

it must satisfy the following conditions,

$$\frac{\partial S}{\partial a_1} = \frac{\partial S}{\partial a_2} = \frac{\partial S}{\partial a_3} = \cdots \frac{\partial S}{\partial a_n} = 0 \qquad \text{(A.3)}$$

or it may be written as,

$$\begin{aligned}
&\sum_{i=1}^{m} x_{1,i} [\, y_i - (a_1 x_{1,i} + a_2 x_{2,i} + \ldots a_n x_{n,i})] = 0 \\
&\sum_{i=1}^{m} x_{2,i} [\, y_i - (a_1 x_{1,i} + a_2 x_{2,i} + \ldots a_n x_{n,i})] = 0 \\
&\sum_{i=1}^{m} x_{3,i} [\, y_i - (a_1 x_{1,i} + a_2 x_{2,i} + \ldots a_n x_{n,i})] = 0 \\
&\vdots \qquad \text{(A.4)} \\
&\sum_{i=1}^{m} x_{n,i} [\, y_i - (a_1 x_{1,i} + a_2 x_{2,i} + \ldots a_n x_{n,i})] = 0
\end{aligned}$$

The equations in (A.4) constitute a group of n linear equations with n unknown parameters a_1, a_2, a_3 .... a_n. By solving these equations, the parameters a_1, a_2, a_3 .... a_n are determined. In the sulphate solubility correlations, a NAG library routine was called to give their values.

APPENDIX 2.2

REDUCTION OF EQUATION (2.23) TO EQUATION (2.33)

Equation (2.23) in chapter 2 is a general expression of the relation between the square root of stoichiometric solubility product of a sulphate mineral and its thermodynamic solubility product and mean activity coefficient. The equation was used for correlating sulphate solubility with ionic strength and ion concentrations to parameterise the unknown coefficients used in solubility prediction. The general equation was reduced to simpler equations for sulphate solubility correlations in specific aqueous sysytems. The reduction process to equation (2.33) for sulphate in pure water or NaCl solutions is given below, similar reductions were carried out for other aqueous systems. The symbols in the following equations may be referred to in chapter 2 and in the nomenclature of the thesis.

Equation (2.23) is given as,

$$
\begin{aligned}
-\ln Q_{sp,MX} = {} & -1/2 \ln K_{sp,MX} + n/2 \ln \gamma_{H2O} + |z_M z_X| f^{\gamma} + \\
& (2\nu_M/\nu) \sum_a m_a [B_{Ma} + (\Sigma m z) C_{Ma} + (\nu_X/\nu_M) \theta_{Xa}] + \\
& (2\nu_X/\nu) \sum_c m_c [B_{cX} + (\Sigma m z) C_{cX} + (\nu_M/\nu_X) \theta_{Mc}] + \\
& \sum_c \sum_a m_c m_a \{ |z_M z_X| B'_{ca} + \nu^{-1} [2\nu_M z_M C_{ca} + \\
& \nu_M \psi_{Mca} + \nu_X \psi_{caX}] \} + 1/2 \sum_c \sum_{c'} m_c m_{c'} [(\nu_X/\nu) \psi_{cc'X} + \\
& |z_M z_X| \theta'_{cc'}] + 1/2 \sum_a \sum_{a'} m_a m_{a'} [(\nu_M/\nu) \psi_{Maa'} + \\
& |z_M z_X| \theta'_{aa'}] \qquad (2.23)
\end{aligned}
$$

For a sulphate mineral MX($BaSO_4$, $SrSO_4$ or $CaSO_4$) in NaCl solution, $z_M=z_X=2$,

$\nu_M=\nu_X=1$, and $\nu=2$. Subscripts a and a' stand for cations M(Ca, Ba or Sr) or N(Na) and c and c' represent anions $X(SO_4)$ or Y(Cl). The equation can be expanded as,

$$
\begin{aligned}
-\ln Q_{sp,MX} = \; & -1/2 \ln K_{sp,MX} + n/2 \ln \gamma_{H2O} + 4f^{\gamma} + \\
& m_X B_{MX} + m_X(\Sigma\, m\, z)\, C_{MX} + m_Y B_{MY} + \\
& m_y(\Sigma\, m\, z)\, C_{MY} + m_y \theta_{XY} + m_M B_{MX} + \\
& m_M(\Sigma\, m\, z)\, C_{MX} + m_N B_{NX} + m_N(\Sigma\, m\, z)\, C_{NX} + \\
& m_N \theta_{MN} + \\
& 4m_M m_X B'_{MX} + 2m_M m_X C_{MX} + \\
& 4m_M m_Y B'_{MY} + 2m_M m_Y C_{MY} + 1/2 m_M m_Y \psi_{MXY} + \\
& 4m_N m_X B'_{NX} + 2m_N m_X C_{NX} + 1/2 m_N m_X \psi_{MNX} + \\
& 4m_N m_Y B'_{NY} + 2m_N m_Y C_{NY} + 1/2 m_N m_Y \psi_{MNY} + \\
& 1/2\, m_N m_Y \psi_{NXY} + \\
& 1/4 m_M m_N \psi_{MNX} + 2m_M m_N \theta'_{MN} + \\
& 1/4 m_N m_M \psi_{NMX} + 2m_N m_M \theta'_{NM} + \\
& 1/4 m_X m_Y \psi_{MXY} + 2m_X m_Y \theta'_{XY} + \\
& 1/4 m_Y m_X \psi_{MYX} + 2m_X m_Y \theta'_{YX}
\end{aligned}
\qquad \text{(A.5)}
$$

In the equation, $\psi_{MNX} = \psi_{NMX}$, $\psi_{MXY} = \psi_{MYX}$, $\theta'_{MN} = \theta'_{NM}$ and $\theta'_{XY} = \theta'_{YX}$. After re-grouping the terms in equation (A.5) and substituting $S\theta+E\theta$ for θ and $E\theta'$ for θ', we obtain equation (A.6),

$$
\begin{aligned}
-\ln Q_{sp,MX} = \; & 4f^{\gamma} + (m_M + m_X)B_{MX} + m_Y B_{MY} + m_N B_{NX} + \\
& 4m_M m_X B'_{MX} + 4m_M m_Y B'_{MY} + 4m_N m_X B'_{NX} + \\
& 4m_N m_Y B'_{NY} + [(m+ m_X)(\Sigma\, m\, z) + 2m_M m_X]\, C_{MX} + \\
& m_y[(\Sigma\, m\, z) + 2m_M]\, C_{MY} + m_N[(\Sigma\, m\, z) + 2m_X] C_{NX} + \\
& 2m_N m_Y C_{NY} + m_N E\theta_{MN} + m_y E\theta_{XY} + 4m_M m_N E\theta'_{MN} +
\end{aligned}
$$

$$4m_X m_Y E\theta'_{XY} + n/2 \ln \gamma_{H2O} +$$
$$-1/2\ln K_{sp,MX} +$$
$$m_N S\theta_{MN} + m_y E\theta_{XY} +$$
$$1/2m_N m_X \psi_{MNX} + 1/2m_M m_N \psi_{MNX} +$$
$$1/2m_M m_Y \psi_{MXY} + 1/2m_X m_Y \psi_{MXY} +$$
$$1/2m_N m_Y \psi_{MNY} +$$
$$1/2\, m_N m_Y \psi_{NXY} \qquad (A.6)$$

Since the concentrations of Na ion and Cl ion are identical in such a aqueous system, i.e, $m_N = m_y$, also the concentrations of M(Ba, Ca or Sr ion) and X(SO_4 ion) are identical($m_M = m_X$), equation (A.6) is further reduced to equation (A.7),

$$-\ln Q_{sp,MX} = 4f^{\gamma} + (m_M + m_X)B_{MX} + m_Y B_{MY} + m_N B_{NX} +$$
$$4m_M m_X B'_{MX} + 4m_M m_Y B'_{MY} + 4m_N m_X B'_{NX} +$$
$$4m_N m_Y B'_{NY} + [(m+ m_X)(\Sigma\, m\, z) + 2m_M m_X]\, C_{MX} +$$
$$m_y[(\Sigma\, m\, z) + 2m_M]\, C_{MY} + m_N[(\Sigma\, m\, z) + 2m_X]C_{NX} +$$
$$2m_N m_Y C_{NY} + m_N E\theta_{MN} + m_y E\theta_{XY} + 4m_M m_N E\theta'_{MN} +$$
$$4m_X m_Y E\theta'_{XY} + n/2 \ln \gamma_{H2O} +$$
$$-1/2\ln K_{sp,MX} +$$
$$m_N(S\theta_{MN} + E\theta_{XY}) +$$
$$m_M m_N(\psi_{MNX} + \psi_{MXY}) +$$
$$1/2m_N^2 \psi_{MNY} \qquad (A.7)$$

Finally, equation(A.7) is written as equation (2.33),

$$-\ln Q_{sp,MX} = K - 1/2\ln K_{sp,MX} + m_N S\theta + m_M m_N \psi_1 +$$
$$1/2\, m_N^2 \psi_2 \qquad (2.33)$$

where,

$$S\theta = S\theta_{MN} + S\theta_{XY}, \tag{2.34}$$

$$\Psi_1 = \Psi_{MNX} + \Psi_{MXY}, \tag{2.35}$$

$$\Psi_2 = \Psi_{MNY} + \Psi_{NXY} \tag{2.36}$$

and

$$\begin{aligned} K = {} & 4f^{\gamma} + (m_M + m_X)B_{MX} + m_Y B_{MY} + m_N B_{NX} + \\ & 4m_M m_X B'_{MX} + 4m_M m_Y B'_{MY} + 4m_N m_X B'_{NX} + \\ & 4m_N m_Y B'_{NY} + [(m_M + m_X)(\Sigma mz) + 2 m_M m_X]C_{MX} + \\ & m_Y [(\Sigma mz) + 2 m_M]C_{MY} + m_N [(\Sigma mz) + 2m_X]C_{NX} + \\ & 2m_N m_Y C_{NY} + m_N E\theta_{MN} + m_Y E\theta_{XY} + 4m_M m_N E\theta'_{MN} + \\ & 4 m_X m_Y E\theta'_{XY} + n/2 \ln\gamma_{H2O} \end{aligned} \tag{2.37}$$

APPENDIX 6.1

EXPERIMENTAL IDENTIFICATION SYSTEM

For the crystals precipitated from a labelled brine in a beaker test, the identification is a simple matter. The crystals are referred to the same as the brine. For example, the crystals grown from brine BS0 are referred to as BS0 crystals. A more complicated identification system is used to number the core tests conducted in this study to provide information of the core material used, the rock block number from which the core was drilled, experiment temperature, the brine injected and the number of test using this brine. The flow rate is not included in the identification system because the flow rate of 7.5milliliter/minute for each unmixed brine was used throughout the present study.

The identification system for a room temperature core test consists of four parts: first, a capital letter C representing the Clashach sandstone used as core material, then a two figure number indicating the rock block for coring, the third part is the brine label and finally a number showing the test number using this specific brine. The system can be illustrated by an example of test C25BSS02:

part 1	part 2	part 3	part 4
C	**25**	**BSS0**	**2**
Clashach	block 25	brine BSS0	test 2

An extra capital letter T is inserted between the block number and brine label to number the 70°C core tests, e.g, test C33TBSS16. If mixed field waters instead of the simple brines were used in a core test, then FORT is in place of brine label to represent the 50:50 mixed North Sea water and Forties water(water 1) and SBRAE is to indicate that 50:50 mixed North Sea water and South Brae water(water 2) was used in a test, e.g, test C28TFORT1.

REFERENCES

1. Alder, M.S., Glater, J. and McCutchan, J.W.: "*Prediction of Gypsum Solubility and Scaling Limits in Saline Waters*", J. Chem. & Eng. Data (1979), 24(3), 187-92.

2. Babcock, K.L. and Marion, G.M.: "*Effect of Ion-pair Formation on the Solubility Product*", Soil Sci. Soc. Amer. Proc. (1972), 36, 689-91.

3. Barba, D., Brandani,V. and Di Giacomo, G.: "*Solubility of Calcium Sulfate Dihydrate in the System Na_2SO_4-$MgCl_2$-H_2O*", J. Chem. & Eng. Data (1984), 29, 42-5.

4. Bennett, A.C. and Adams, F.: "*Solubility and Solubility Product of Gypsum in Soil Solutions and Other Aqueous Solutions*", Soil Sci. Amer. Soc. Proc. (1972), 36, 288-91.

5. Berto, L. et al.: "*Chemical Equilibrium Models: Their Use in Simulating the Injection of Incompatible Waters*", paper SPE 14126 presented at the SPE 1986 International Meeting on Petroleum Engineering held in Beijing, China, March 17-20, 1986.

6. Block, J. and Waters, O.B.Jr.: "*The $CaSO_4$-Na_2SO_4-NaCl-H_2O System at 25°to 100°C*", J. Chem. & Eng. Data (1968), 13(3), 336-44.

7. Blount, C.W.: "*Synthesis of Barite, Celestite, Anglestite, Witherite, and Strontianite from Aqueous Solutions*", Amer. Mineralogist (1974), 59, 1209-19.

8. Blount, C.W.: "*Barite Solubilities and Thermodynamic Quantities up to 300°C and 1400 Bars*", Amer. Mineralogist (1977), 62, 942-57.

9. Blount, C.W. and Dickson, F.W.: "*The Solubility of Anhydrite ($CaSO_4$) in NaCl-H_2O from 100 to 450°C and 1 to 1000 Bars*", Geochim. Cosmochim. Acta (1969), 33, 227-45.

10. Blount, C.W. and Dickson, F.W.: "*Gypsum-Anhydrite Equilibria in Systems $CaSO_4$-H_2O and $CaSO_4$-NaCl-H_2O*", Amer. Mineralogist (1973), 58, 323-31.

11. Bock, E.: "*On the Solubility of Anhydrous Calcium Sulphate and of Gypsum in Concentrated Solutions of Sodium Chloride at 25°C, 30°C, 40°C, and 50°C*", Can. J. Chemistry (1961), 39, 1746-51.

12. Booth, H.S. and Bidwell, R.M.: "*Solubilities of Salts in Water at High Temperatures*", J. Amer. Chem. Soc. (1950), 72(1), 2567-75.

13. Booth, H.S. and Pollard, E.F.: "*Conversion of Celestite to Strontium Carbonate*", Ind. & Eng. Chem. (1948), 40(10), 1986-88.

14. Bovington, C.H.: "*The Effect of Labelling on the Solubilities of Crystalline Substances*", J. Inorg. Nucl. Chem. (1965), 27, 1975-79.

15. Boyle, M.J. and Mitchell, R.W.: "*Scale Inhibition Problems Associated with North Sea Oil Production*", paper SPE 8164 presented at Offshore Europe 79 Conference held in Aberdeen, Scotland, Sept.3-7, 1979.

16. Brower, E.: "*Synthesis of Barite, Celestite and Barium-Strontium Sulfate Solid Solution Crystals*", Geochim. Cosmochim. Acta (1973), 37, 155-8.

17. Brower, E. and Renault, J.: "*Solubility and Enthalphy of the Barium-Strontium Sulfate Solid Solution Series*", Circular 116, New Mexica State Bureau of Mines and Mineral Resources (1971).

18. Burkhard, A.: "*Optische und Rontgenographische Untersuchungen am System $BaSO_4$- $SrSO_4$*", Schweiz. Mineral. Petrogr. Mitt. (1973), 53, 185-97.

19. Cameron, F.K.: "*Solubility of Gypsum in Aqueous Solutions of Sodium Chloride*", J. Phys. Chem. (1901), 5, 556-76.

20. Campbell, A.N. and Cook, E.J.: "*A Study of Precipitation from Supersaturated Solutions of Strontium Sulfate*", J. Amer. Chem. Soc. (1935), 57(3), 387-90.

21. Campbell, J.R. and Nancollas, G.H.: "*The Crystallization and Dissolution of Strontium in Aqueous Solution*", J. Phys. Chem. (1969), 73(6), 1735-40.

22. Case, L.C.: "*Here are Some Common Waterflood Problems and Their Solutions*", Oil and Gas J. (Aug.3, 1970), 92-6.

23. Case, L.C.: *Water Problems in Oil Production*, 2nd ed., The Petroleum Publishing Co., Tulsa, OK. (1976).

24. Case, L.C.: "*Water Analysis Prevents Injection-well Plugging*", Oil & Gas J. (Dec.12, 1983), 128-32.

25. Collins, F.C. and Leineweber, J.P.: "*The Kinetics of the Homogeneous Precipitation of Barium Sulfate*", J. Phys. Chem. (1956), 69, 389-94.

26. Cowan, J.C. and Weintritt, D.J.: *Water-Formed Scale Deposits*, Gulf Publishing Co., Houston (1976).

27. Davis, J.W. and Collins, A.G.: "*Solubility of Barium and Strontium Sulfates in Strong Electrolyte Solutions*", Envir. Sci. & Tech. (1971), 5(10), 1039-43.

28. Dawson, I.M. and McGaffney, A.I.: "*The Structure of Colloid Barium Sulfate*", Intern. Kongr. Electroneumikroskopie (1958), 4(1), 736.

29. Deer, W.A., Howie, R.A. and Zussman, J.: *An Introduction to the Rock Forming Minerals*, Longman, London (1966).

30. Denman, W.L.: "*Maximum Re-Use of Cooling Water*", Ind. & Eng. Chem. (1961), 53(10), 817-22.

31. Dickson, F.W., Blount, C.W. and Tunell, G.: "*Use of Hydrothermal Solution Equipment to Determine the Solubility of Anhydrite in Water from 100°C to 275°C and from 1 Bar to 1000 Bars Pressure*", Amer. J. Sci. (1963), 261, 61-78.

32. Essel, A.J. and Carlberg, B.C.: "*Strontium Sulfate Scale Control by Inhibitor Squeeze Treatment in the Fateh Field*", JPT (June 1982), 1302-6.

33. Fischer, R.B.: "*Precipitation of Barium Sulfate*", Analytical Chem. (1951), 23(11), 1667-71.

34. Fischer, R.B. and Ben Rhinehammer, T.: "*Rapid Precipitation of Barium Sulfate*", Analytical Chem. (1953), 25(10), 1544-8.

35. Fletcher, G.E., French, T.R. and Collins, A.G.: "*Method for Calculating Strontium Sulfate Solubility*", Report DOE/BETC-80/10 (Apr. 1981).

36. Furby, E., Glueckauf, E. and McDonald, L.A.: "*The Solubility of Calcium Sulphate in Sodium Chloride and Sea Salt Solutions*", Desalination (1968), 4, 264-76.

37. Gardner, A.W. and Glueckauf, E.: "*Ionic Association in Aqueous Solutions of Bivalent Sulphates*", Proc. Roy. Soc. Lond. A. (1969), 313, 131-47.

38. Gardner, G.L. and Nancollas,G.H.: "*Crystal Growth in Aqueous Solution at Elevated Temperatures. Barium Sulfate Growth Kinetics*", J. Phys. Chem. (1983), 87(23), 4699-703.

39. Gates, G.L. and Caraway, W.H.: "*Oil Well Scale Formation in Waterflood Operations Using Ocean Brines, Wilmington, Calif.*", Report of Investigations 6658, Bureau of Mines (1965).

40. Glew, D.N. and Hames, D.A.: "*Gypsum, Disodium Pentacalcium Sulfate, and Anhydrite Solubilities in Concentrated Sodium Chloride Solutions*", Can. J. Chem. (1970), 48, 3733-38.

41. Gordon, L., Reimer, C.C. and Burtit, B.P.: "*Distribution of Strontium within Barium Sulfate Precipitated from Homogeneous Solution*", Analytical Chem. (1954), 26(5), 842-6.

42. Goulding, P.S.: *Formation Damage Arising from Barium Sulphate Scale Precipitation*, Ph.D thesis, Heriot-Watt University, Edinburgh, 1987.

43. Gundlach, H., Stoppel, D. and Strubel, G.: "*Zur Hydrothermalen Loslichkeit von Baryt*", Neus. Jahrb. Miner. Abh. (1972), 116(3), 321-38.

44. Haarberg, T. et al.: "*Scale Formation in Reservoir and Production Equipment during Oil Recovery.I. An Equilibrium Model*", poster presented at the Chemicals in the Oil Industry held in Manchester, England, Apr. 19-20, 1988.

45. Hall, R.E., Robb, J.A. and Coleman, C.E.: "*The Solubility of Calcium Sulfate at Boiler-Water Temperatures*", J. Amer. Chem. Soc. (1926), 48, 927-38.

46. Hamilton, W.R., Woolley, A.R. and Bishop, A.C.: *The Hamlyn Guide to Minerals, Rocks and Fossils*, The Hamlyn Publishing Group Ltd., London (1975).

47. Hanor, J.S.: "*Frequency Distribution of Compositions in the Barite-Celestite Series*", Amer. Mineralogist (1968), 53, 1215-22.

48. Hara, R., Tanaka, T. and Nakamura, K.: "*On the Calcium Sulphate in Sea Water.I. Solubilities of Dihydrate and Anhydrite in Sea Waters of Various Concentrations at 0°- 200℃*", Tech. Reports. Tohoku. Imp. Univ. (1934), 11, 199-221.

49. Harned, H.S. and Owen, B.B.: *The Physical Chemistry of Electrolytic Solutions*, 3rd ed., Reinhold Publishing Co., New York (1958).

50. Harvie, C.E. and Weare, J.H.: "*The Prediction of Mineral Solubilities in Natural Waters: The Na-K-Mg-Ca-Cl-SO_4-H_2O System from Zero to High Concentration at 25℃*", Geochim. Cosmochim. Acta (1980), 44, 981-97.

51. Harvie, C.E., Moller, N. and Weare, J.H.: "*The Prediction of Mineral Solubilities in Natural Waters: The Na-K-Mg-Ca-H-Cl-SO_4-OH-HCO_3-CO_3-CO_2-H_2O System to High Ionic Strengths at 25℃*", Geochim. Cosmochim. Acta (1984), 48, 723-51.

52. Hausler, R.H.: "*Predicting and Controlling Scale from Oilfield Brines*", Oil and Gas J. (Sept.18, 1978), 146-54.

53. Hill, A.E.: "*Ternary Systems. XIX. Calcium Sulfate, Potassium Sulfate and Water*", J. Amer. Chem. Soc. (1934), 56, 1071-8.

54. Hill, A.E.: "*The Transition Temperature of Gypsum to Anhydrite*", J. Amer. Chem. Soc. (1937), 59, 2242-4.

55. Hill, A.E. and Wills, J.H.: "*Ternary Systems. XXIV. Calcium Sulfate, Sodium Sulfate and Water*", J. Amer. Chem. Soc. (1938), 60, 1647-55.

56. Holmes, H.F., Baes, C.F.Jr. and Mesmer, R.E.: "*Isopiestic Studies of Aqueous Solutions at Elevated Temperatures.I. KCl, $CaCl_2$, and $MgCl_2$*", J. Chem. Thermodynamics (1978), 10, 983-96.

57. Holmes, H.F. and Mesmer, R.E.: "*Isopiestic Studies of Aqueous Solutions at Elevated Temperatures.V. $SrCl_2$, and $BaCl_2$*", J. Chem. Thermodynamics (1981), 13, 1025-33.

58. Hughes, C.T. and Whittingham, K.P.: "*The Selection of Scale Inhibitors for Forties Field*", paper EUR 313 presented at Europe Petroleum Conference held in London, Oct. 25-28, 1982.

59. Hulett, G.A. and Allen, L.E.: "*Solubility of Gypsum*", J. Amer. Chem. Soc. (1902), 24, 667-79.

60. Jacques, D.F. and Bourland, B.I.: "*A Study of Solubility of Strontium Sulfate*", SPEJ (Apr. 1983), 292-300.

61. Jacques, D.F., Gollberg., B.J. and Whiteside, W.C.: "*Strontium Sulfate Solubility and the Effects of Scale Inhibitors*", paper presented at the BSE/NACE Middle East Corrosion Conference held in Bahrain, Apr. 15-17, 1979.

62. Johnson, K.S. and Pytkowicz, R.M.: "*Ion Association and Activity Coefficients in Multicomponent Solutions*", *Activity Coefficients in Electrolyte Solutions*, R.M.Pytkowicz (ed.), CRC Press, Florida (1979).

63. Kestin, J., Khalifa, H.E. and Correia, R.J.: "*Tables of the Dynamic and Kinematic Viscosity of Aqueous NaCl Solutions in the Temperature Range 20-250°C and the Pressure Range 0.1-35 MPa*", J. Phys. Chem. Ref. Data (1981), 10(1), 71-87.

64. King, G.E. and Warden, S.L.: "*Introductory Work in Scale Inhibitor Squeeze Performance: Core Tests and Field Results*", paper SPE 18485 presented at the SPE International Symposium on Oilfield Chemistry held in Houston, Texas, Feb. 8-10, 1989.

65. Langelier, W.F.: "*The Analytical Control of Anti-Corrosion Water Treatment*", J.Amer. Works Assn. (1936), 28(10),1500-21.

66. Lieser, K.H.: "*Radiochemische Messung der Loslichkeit von Erdalkalisulfaten in Wasser und in Natriumsulfatlosungen*", Zeitschrift fur Anorganische und Allegemeine Chemie (Feb. 1965), 335, 225-31.

67. Lindlof, J.C. and Stoffer, K.G.: "*A Case Study of Seawater Injection Incompatibility*", JPT (July 1983), 1256-62.

68. Lucchesi, P.J. and Whitney, E.D.: "*Solubility of Strontium Sulphate in Water*

and Aqueous Solutions of Hydrogen Chloride, Sodium Chloride, Sulphuric Acid and Sodium Sulphate by the Radiotracer Method", J. Appl. Chem. (1962), 12, 277-9.

69. MacDonald, R.W. and North, N.A.: "*The Effect of Preesure on the Solubility of $CaCO_3$, CaF_2, and $SrSO_4$ in Water*", Can. J. Chem. (1974), 52, 3181-6.

70. Madgin, W.M. and Swales, D.A.: "*Solubilities in the System $CaSO_4$-NaCl-H_2O at 25° and 35°*", J. Appl. Chem. (1956), 6, 482-487.

71. Marshall, W.L. and Slusher, R.: "*Thermodynamics of Calcium Sulfate Dihydrate in Aqueous Sodium Chloride Solutions, 0-100°*", J. Phys. Chem. (1966), 70(12), 4015-27.

72. Marshall, W.L. and Slusher, R.: "*Aqueous Systems at High Temperature. Solubility to 200°C of Calcium Sulfate and Its Hydrates in Sea Water and Saline Water Concentrates, and Temperature-Concentration Limits*", J. Chem. & Eng. Data (1968), 13(1), 83-93.

73. Mazo, R.M. and Mou, C.Y.: "*Introduction to the Statistical Mechanics of Solutions*", *Activity Coefficients in Electrolyte Solutions*, R.M. Pytkowicz (ed.), CRC Press, Florida (1979).

74. Melcher, A.C.: "*The Solubility of Silver Chloride, Barium Sulphate, and Calcium Sulphate at High Temperatures*", J. Amer. Chem. Soc. (1910), 32, 50-66.

75. Metler, A.V. and Ostroff, A.G.: "*The Proximate Calculation of the Solubility of Gypsum in Natural Brines from 28°C to 70°C*", Envir. Sci. & Tech. (1967), 1(10),815-9.

76. Millero, F.J. and Schreiber, D.R.: "*Use of the Ion Pairing Model to Estimate Activity Coefficients of the Ionic Components of Natural Waters*", Amer. J. Sci. (1982), 282, 1508-40.

77. Mitchell, R.W., Grist, D.M. and Boyle, M.J.: "*Chemical Treatments Associated with North Sea Projects*", JPT (May 1980), 904-12.

78. Moore, E.S.: "*Oolitic and Pisolitic Barite from the Saratoga Oilfield, Texas*", Bull. of Geol. Soc. Amer. (1914), 25, 77-9.

79. Muller, G.: "*Die Loslichkeit von Coelestin ($SrSO_4$) in Wasserigen NaCl- und KCl- Losungen*", Neus. Jahrb. Mineral. Monatsh. (1960), 237-9.

80. Nancollas, G.H.: "*Kinetics of Crystal Growth from Solution*", J. Crystal Growth (1968)), 3-4, 335-9.

81. Nancollas, G.H. and Gill, J.S.: "*Formation and Dissolution of High Temperature Forms of Calcium Sulfate Scales: The Influence of Inhibitors*", SPEJ (Dec. 1979), 423-9.

82. Nancollas, G.H. and Liu, S.T.: "*Crystal Growth and Distribution of Barium Sulfate*", SPEJ (Dec. 1975), 509-16.

83. Nancollas, G.H. and Purdie, N.: "*Crystallization of Barium Sulphate in Aqueous Solution*", Trans. Faraday Soc. (1963), 59, 735-40.

84. Nancollas, G,H and Reddy, M.M.: "*The Kinetics of Crystallization of Scale-Forming Minerals*", SPEJ (Apr. 1974), 117-26.

85. Neuman, E.W.: "*Solubility Relations of Barium Sulfate in Aqueous Solutions*

of Strong Electrolytes", J. Amer. Chem. Soc. (1933), 55, 879-84.

86. Nielsen, A.E.: "*The Kinetics of Crystal Growth in Barium Sulfate Precipitation*", Acta. Chem. Scand. (1958), 12, 951-8.

87. Nielsen, A.E.: "*Homogeneous Nucleation in Barium Sulfate Precipitation*", Acta Chem. Scand. (1961), 15(2), 441-2.

88. Nielsen, A.E.: "*Nucleation and Growth of Crystals at High Supersaturation*", Kristall Und Technik (1969), 4(1), 17-38.

89. North, N.A.: "*Pressure Dependence of $SrSO_4$ Solubility*", Geochim. Cosmochim. Acta (1974), 38, 1075-81.

90. Okada, S. and Magari, S.: "*Morphology of Barium Sulfate as Seen through Electron Microscopy*", Analytical Chem. (1955), 27(9), 1481-4.

91. Ostroff, A.G. and Metler, A.V.: "*Solubility of Calcium Sulfate Dihydrate in the System $CaSO_4$-$MgCl_2$-H_2O from 28° to 70°C*", J. Chem. & Eng. Data (1966), 11(3), 346-50.

92. Packter, A.: "*The Precipitation of Strontium and Lead Sulphates from Aqueous Solution. Kinetics of the Crystal Growth*", Kristall und Technik (1974), 9(3), 249-56.

93. Partridge, E.P and White, A.H.: "*The Solubility of Calcium Sulfate from 0 to 200°*", J. Amer. Chem. Soc. (1929), 51, 360-70.

94. Patton, C.C.: "*Water Quality Control and Its Importance in Waterflooding Operations*", JPT (Sept. 1988), 1123-6.

95. Phutela, R.C. and Pitzer, K.S.: "*Thermodynamics of Aqueous Calcium Chloride*", J. Solution Chem. (1983), 12(3), 201-7.

96. Phutela, R.C. and Pitzer, K.S.: "*Heat Capacity and Other Thermodynamic Properties of Aqueous Magnesium Sulfate to 473K*", J. Phys. Chem. (1986), 90, 895-901.

97. Pitzer, K.S.: "*Thermodynamics of Electrolytes.I. Theoretical Basis and General Equations*", J. Phys. Chem. (1973), 77(2), 268-77.

98. Pitzer, K.S.: "*Thermodynamics of Electrolytes.V. Effects of Higher-Order Electrostatic Terms*", J. Solution Chem. (1975), 4(3), 249-65.

99. Pitzer, K.S.: "*Theory: Ion Interaction Approach*", *Activity Coefficients in Electrolyte Solutions*, R.M. Pytkowicz (ed.), Vol.1, CRC Press, Florida (1979).

100. Pitzer, K.S.: "*Thermodynamics of Aqueous Electrolytes at Various Temperatures, Pressures, and Compositions*", ACS Symposium Series 133 (1980), S.A. Newman (ed.)

101. Pitzer, K.S.: "*Thermodynamics of Electrolyte Solutions over the Entire Miscibility Range*", Chem. Eng. Thermodynamics, S.A. Newman (ed.), Butterworths, England (1983).

102. Pitzer, K.S. and Kim, J.J.: "*Thermodynamics of Electrolytes.IV. Activity and Osmotic Coefficients for Mixed Electrolytes*", J. Amer. Chem. Soc. (1974), 96(18), 5701-7.

103. Pitzer, K.S. and Mayorga, G.: "*Thermodynamics of Electrolytes.II. Activity*

and Osmotic Coefficients for Strong Electrolytes with One or Both Ions Univalent", J. Phys. Chem. (1973), 77(19), 2300-8.

104. Pitzer, K.S. and Mayorga, G.: "*Thermodynamics of Electrolytes.III. Activity and Osmotic Coefficients for 2-2 Electrolytes*", J. Solution Chem. (1974), 3(7), 539-46.

105. Pitzer, K.S., Peiper, J.C. and Busey, R.H.: "*Thermodynamic Properties of Aqueous Sodium Chloride Solutions*", J. Phys. Chem. Ref. Data (1984), 13(1), 1-102.

106. Ponizovskii, A.M. et al.: "*Solubility of Gypsum and Hemihydrate in Solutions of Magnesium and Calcium Chloride*", Tekhnol. Proizvod. Magnez. Prod. (1974), 42-7.

107. Posnjak, E.: "*The System, $CaSO_4$-H_2O*", Amer. J. Sci. (1938), 35A, 247-72.

108. Posnjak, E.: "*Deposition of Calcium Sulfate from Sea Water*", Amer. J. Sci. (1940), 23, 559-68.

109. Power, W.H., Fabuss, B.M. and Satterfield, C.N.: "*Transient Solubilities in the Calcium Sulfate-Water System*", J. Chem. & Eng. Data (1964), 9(3), 437-42.

110. Power, W.H., Fabuss, B.M. and Satterfield, C.N.: "*Transient Solute Concentrations and Phase Changes of Calcium Sulfate in Aqueous Sodium Chloride*", J. Chem. & Eng. Data (1966), 11(2), 149-55.

111. Przybylinski, J.L.: "*Adsorption and Desorption Characteristics of Mineral Scale Inhibitors as Related to the Design of Squeeze Treatments*", paper SPE 18486 presented at the SPE International Symposium on Oilfield Chemistry held in Houston, Texas, Feb.8-10, 1989.

112. Puchelt, H.: "*Zur Geochemie des Bariums im Exogenen Zyklus*", Proc. of Heidelberg Academy of Science, Heidelberg, 1967. Springer-Verlag.

113. Pucknell, J.: *Oilfield Scale*, Ph.D Thesis, Heriot-Watt University, Edinburgh, 1983.

114. Ralston, P.H.: "*Scale Control with Aminomethylenephosphonates*", JPT (Aug. 1969), 1029-36.

115. Read, P.A. and Ringen, J.K.: "*The Use of Laboratory Tests to Evaluate Scaling Problems during Water Injection*", paper SPE 10593 presented at the SPE International Symposium on Oilfield and Geothermal Chemistry held in Dallas, Texas, Jan. 25-7, 1982.

116. Reardon, E.J.: "*Determination of $SrSO_4$ Ion Pair Formation Using Conductimetric and Ion Exchange of Techniques*", Geochim. Cosmochim. Acta (1983), 47, 1917-22.

117. Renon, H., Planche, H., Furst, W. and Ball, F-X.: "*Models for Thermodynamics of Electrolyte Solutions*", Chem. Eng. Thermodynamics, S.A.Newmann(ed.), Butterworths, England (1983), 379-90.

118. Rogers, P.S.Z.: "*Thermodynamics of Geothermal Fluids*", Report LBL-12356 (Mar. 1981).

119. Rogers, P.S.Z. and Pitzer, K.S.: "*High-Temperature Properties of Aqueous Sodium Sulfate Solutions*", J. Phys. Chem. (1981), 85(20), 2886-95.

120. Rosseinsky, D.R.: "*The Solubilities of Sparingly Soluble Salts in Water. Part.5.- The Solubility of Barium Sulphate at 25 °C*", Trans, Faraday Soc. (1958), 54, 116-7.

121. Rowe, A.M. and Chou, J.C.S.: "*P-V-T-Concentration Relation of Aqueous NaCl Solutions*", J. Chem. & Eng. Data (1970), 15(1), 61-7.

122. Sarig, S.: "*Crystal Habit Modification by Water Soluble Polymers*", J.Crystal Growth (1974), 24-25, 338-41.

123. Schulien, S.: "*High-Temperature/High-Pressure Solubility Measurements in the Systems $BaSO_4$-NaCl-H_2O and $SrSO_4$-NaCl-H_2O in Connection with Scale Studies*", paper SPE 16264 presented at the SPE International Symposium on Oilfield Chemistry held in San Antonio, Texas, Feb.4-6, 1987.

124. Seidell, A. and Linke, W.F.: *Solubilities of Inorganic and Metal Organic Compounds*, 4th ed., Van Norstrand Co., Princeton, New Jersey (1958).

125. Shaffer, L.H.: "*Solubility of Gypsum in Sea Water and Sea Water Concentrates at Temperatures from Ambient to 65 °C*", J. Chem. & Eng. Data (1967), 12(2), 183-9.

126. Shen, J. and Crosby, C.C.: "*Insight into Strontium and Calcium Sulfate Scaling Mechanisms in a Wet Producer*", JPT (July. 1983), 1249-55.

127. Shternina, E.B.: "*On the Maximum of the Solubility Isotherms of Calcium Sulfate and Carbonate*", Zhurnal Neorganicheskoi Khimi (1957), 2(4), 933-7.

128. Shternina, E.B.: "*Solubility of Gypsum in Aqueous Solutions of Salts*", Int. Geology Rev. (1960), 2(5-8), 605-16.

129. Silvester, L.F. and Pitzer, K.S.: "*Thermodynamics of Electrolytes.8. High-Temperature Properties, Including Enthalpy and Heat Capacity, with Application to Sodium Chloride*", J. Phys. Chem. (1977), 81(19), 1822-28.

130. Skillman, H.L., McDonald, J.P.Jr. and Stiff, H.A.: "*A Simple, Accurate, Fast Method for Calculating Calcium Sulfate Solubility in Oil Field Brine*", paper 906-14-I presented at the Spring Meeting of the Southwestern District, Division of Production, American Petroleum Institute, Dallas, Texas, march 12-14, 1969.

131 Stiff, H.A.Jr. and Davis, L.E.: "*A Method for Prediciting the Tendency of Oilfield Waters to Deposit Calcium Sulfate*", Trans. of AIME (1952), 195, 25-8.

132 Stiff, H.A.Jr. and Davis, L.E.: "*A Method for Prediciting the Tendency of Oilfield Waters to Deposit Calcium Carbonate*", Trans. of AIME (1952), 195, 213-6.

133. Stoughton, R.W. and Lietzke, M.H.: "*Calculation of Some Thermodynamic Properties of Sea Salt Solutions at Elevated Temperatures from Data on NaCl Solutions*", J. Chem. & Eng. Data (1965), 10(3), 254-60.

134. Straub, F.G.: "*Solubility of Calcium Sulfate and Calcium Carbonate at Temperatures between 182 ° and 316 °C*", Ind. & Eng. Chem. (1932), 24(8), 914-7.

135. Strubel, G.: "*Zur Kenntnis und Genetischen Bedeutung des Systems $BaSO_4$ - NaCl - H_2O*", Neus. Jahrb. Mineral. Monatsh. (1967), 15. 223-34.

136. Strubel, G.: "*Die Hydrothermale Loslichkeit von Colestin im System $SrSO_4$ - NaCl - H_2O*", Neus. Jahrb. Mineral. Monatsh. (1966), 99-108.

137. Suhnel, O. and Handlirova, M.: "*Precipitation of Strontium Sulphate*", Crystal Res. & Technol. (1984), 19(4), 477-490.

138. Suito, E. and Takiyama, K.: "*Formation and Aging of Precipitates.I. Electron Microscopic Studies of the Formation of Barium Sulfate Precipitates*", Bull. Chem. Soc. Japan (1954), 27, 121-5.

139. Takiyama, K.: "*Formation and Aging of Precipitates.X. An Electron Micro-Diffusion Study on Crystal Habit of Barium Sulfate Precipitates*", Bull. Chem. Soc. Japan (1959), 32(1), 68-70.

140. Takiyama, K.: "*Formation and Aging of Precipitates.XI. An Electron Micro-Diffusion Study on Nucleation of Barium Sulfate Precipitate from Homogeneous Solution*", Bull. Chem. Soc. Japan (1959), 32(4), 287-91.

141. Tanner, R.N. and Wittingham, K.P.: "*Scale Control during Waterflooding Operations: A Field Appraisal of Inhibitor Requirement and Performance*", paper SPE 14127 presented at the SPE 1986 International Meeting on Petroleum Engineering held in Beijing, China, Mar. 17-20.

142. Templeton, C.C.: "*Solubility of Barium Sulfate in Sodium Chloride Solutions from 25° to 95°C*", J. Chem. & Eng. Data (1960), 5(4), 514-6.

143. Todd, A.C. and Yuan, M.D.: "*Barium and Strontium Sulfate Solid Solution Formation in Relation to North Sea Scaling Problems*", paper SPE 18200 presented at the SPE 63rd Annual Conference held in Houston, Texas, Oct. 2-5, 1988.

144. Todd, A.C. and Yuan, M.D.: "*Barium and Strontium Sulfate Solid Solution Scale Formation at Elevated Temperatures*", paper SPE 19762 to be presented at the SPE 64th Annual Conference held in San Antonio, Texas, Oct. 8-11, 1989.

145. Uchameyshvili, N.Ye., Malinin, S.D. and Khitarov, N.I.: "*Solubility of Barite in Concentrated Chloride Solutions of Some Metals at Elevated Temperatures in Relation to Problems of the Genesis of Barite Deposits*", Geochem. Int. (1966), 3, 951-63.

146. Vetter, O.J.G.: "*How Barium Sulfate Is Formed: An Interpretation*", JPT (Dec. 1975), 1515-24.

147. Vetter, O.J.G.: "*Oilfield Scale - Can We Handle It?*", JPT (Dec. 1976), 1402-8.

148. Vetter, O.J. and Kandarpa, V.: "*Scale Formation at Various Locations in a Geothermal Operation Due to Injection of Imported Waters*", DOE/ET/27146-T13 (June 1982).

149. Vetter, O.J., Kandarpa, V. and Harouaka, A.: "*Prediction of Scale Problems due to Injection of Incompatible Waters*", JPT (Feb. 1982), 273-84.

150. Vetter, O.J.G. and Phillips, R.C.: "*Prediction of Deposition of Calcium Sulfate Scale under Down-Hole Conditions*", JPT (Oct. 1970), 1299-308.

151. Vetter, O.J.G., Vandenbroek, I. and Nayberg, J.: "*$SrSO_4$: The Basic Solubility Data*", paper SPE 11803 presented at the SPE International Symposium on Oilfield and Geothermal Chemistry held in Denver, Colorado, June 1-3, 1983.

152. Walton, A.: "*Nucleation*", International Sci. & Technol., (1966), 60, 28-40.

153. Walton, A.G. and Hlabse, T.: "*Nephelometric Examination of Barium Sulphate Precipitation*", Talanta (1963), 10, 601-10.

154. Walton, G. and Walden, G.H.Jr.: "*The Contamination of Precipitated Barium Sulfate by Univalent Cations*", J. Amer. Chem. Soc. (1946), 68, 1742-53.

155. Weintritt, D.J. and Cowan, J.C.: "*Unique Characteristics of Barium Sulfate Scale Deposition*", JPT (Oct. 1967), 1381-94.

156. Whitfield, M.: "*A Chemical Model for the Major Electrolyte Component of Seawater Based on the Bronsted-Guggenheim Hypothesis*", Marine Chemistry (1973), 1, 251-66.

157. Whitfield, M.: "*An Improved Specific Interaction Model for Seawater at 25 °C and 1 Atmosphere Total Pressure*", Marine Chemistry (1975), 3, 197-213.

158. Whitfield, M.: "*The Extension of Chemical Models for Seawater to Include Trace Components at 25 °C and 1 Atm Pressure*", Geochim. Cosmochim. Acta (1975), 39, 1545-57.

159. Yeatts, L.B. and Marshall, W.L.: "*Apparent Invariance of Activity Coefficients of Calcium Sulfate at Constant Ionic Strength and Temperature in the System $CaSO_4$-Na_2SO_4-$NaNO_3$-H_2O to the Critical Temperature of Water. Association Equilibria*", J. Phys. Chem. (1969), 73(1), 81-90.

160. Yeatts, L.B. and Marshall, W.L.: "*Solubility of Calcium Sulfate Dihydrate and Association Equilibria in Several Aqueous Mixed Electrolyte Salt Systems at 25 °C*", J.Chem. & Eng. Data (1972), 17(2), 163-8.

161. Yuan, M.D. and Todd, A.C.: "*Prediction of Sulphate Scaling Tendency in Oilfield Operations*", paper SPE 18484 presented at the SPE International Symposium on Oilfield Chemistry held in Houston, Texas, Feb. 8-10, 1989.

162. Zdanovskii, A.B.: "*Heterogeneous Salt Equilibria*", Tr. Vses. Nauchn.-Issled Inst. Galurgii (1949), 21, 336-58.

163. Zen, E-An.: "*Solubility Measurements in the System $CaSO_4$-$NaCl$-H_2O at 35 °, 50 °, and 70 °C and One Atmosphere Pressure*", J. Petrology (1965), 6(1), 124-64.